Technische Universität München

TECHNISCHE UNIVERSITÄT MÜNCHEN
TUM School of Natural Sciences

Excitons in Mono- and Bilayers of Transition-Metal Dichalcogenides

Malte Kremser, M. Sc.

Vollständiger Abdruck der von der TUM School of Natural Sciences der Technischen Universität München zur Erlangung des akademischen Grades eines

Doktors der Naturwissenschaften
(Dr. rer. nat.)

genehmigten Dissertation.

Vorsitz:	Prof. Dr. David Egger
Prüfer*innen der Dissertation:	Prof. Jonathan J. Finley, Ph.D. Prof. Dr. Christian Back

Die Dissertation wurde am 12.06.2023 bei der Technischen Universität München eingereicht und durch die TUM School of Natural Sciences am 14.07.2023 angenommen.

"God made the bulk;
the surface was invented by the devil."

Wolfgang Pauli

To Barbara

Abstract

Within this thesis we study the excitonic properties of monolayers and artificial bilayers of semiconducting transition metal dichalcogenides (TMDs). Both hetero- and homo-bilayers are explored for bilayers placed onto different substrates and incorporated into both dielectric heterostructures and van-der-Waals (vdW) heterostructures with complete hexagonal-boron-nitride (hBN) encapsulation.

Firstly, we outline the basic structural, electronic and optical properties of few-layer TMD crystals and their heterobilayers in chapter 2. We continue in chapter 3 to build on this foundation, by presenting photoluminescence (PL) studies of localized excitons in monolayer tungsten diselenide (WSe_2) trapped at strain perturbations induced by nanoscale-patterned substrates. These localized excitons display pronounced spectral wandering on the sub-Hertz timescale. We study the impact of the substrate material on the spectral stability of the excitons and find that we can reduce the spectral wandering by a factor of 6 to $(0.32 \pm 0.36)\,\mathrm{eV}$ and the linewidth by a factor of 1.5 to $(2.0 \pm 1.3)\,\mathrm{eV}$ by switiching from resist-based nanopillars to aluminum-gallium-arsenide (AlGaAs) pillars, grown by molecular beam epitaxy (MBE) and defined by local etching.

Chapter 4 continues to demonstrate that this strain-trapping approach via substrate patterning can be applied to dipolar interlayer excitons in heterobilayers of WSe_2 and molybdenum disulfide ($MoSe_2$). We perform spectroscopy studies on localized low-energy PL peaks and confirm the interlayer

character via the excitation-power dependent blueshift, the characteristic radiative decay timescales ((118.8 ± 2.1) ns and (8.1 ± 0.5) ns) and the excitation resonances at the $MoSe_2$ and WSe_2 exciton energies. Furthermore, we present magnetic-field dependent PL spectra, revealing an excitonic g-factor of (-6.4 ± 0.1), that does not coincide with the g-factor of the free interlayer exciton, possibly hinting at different orbital contributions for the coupled bilayer.

Chapter 5 then discusses the dipolar character of the interlayer excitons combined with the nanoscale trapping potential. We show how pronounced inter-exciton interactions allow us to identify states of one to five excitons in the potential trap via their distinct excitation-power dependencies. Biexcitons are found to be blueshifted by (8.4 ± 0.6) meV with respect to single excitons. We reproduce the increasing blueshifts for complexes featuring higher numbers of excitons with a model of point dipoles in a two-dimensional harmonic potential. Switching to a fully quantum-mechanical description of the interlayer biexciton, we explain the observed biexciton splitting of (1.2 ± 0.5) meV in terms of exchange interaction.

After exploring the interactions of trapped interlayer excitons in TMD heterobilayers, we continue in chapter 6 to present a detailed spectroscopy study of different exciton species in twisted bilayers of $MoSe_2$. Homobilayers feature a multitude of optically adressable intra-layer and interlayer excitons. We find pronounced differences between "low-angle" (less than 10° from 0° or 60°) samples and "high-angle" (10° to 50°) samples. The A exciton shows only little dependence on the twist angle in the high-angle range but abruptly redshifts by more than 10 meV when approaching 0° or 60°. Low-energy PL spectra feature signatures of momentum-indirect excitons only in low-angle samples. The brightness of the A exciton in PL experiments, however, is higher in the high-angle samples. We explain these findings by employing a continuum model of the excitons moving through a periodic moiré potential.

Zusammenfassung

Im Rahmen dieser Arbeit untersuchen wir die exzitonischen Eigenschaften von Monolagen und künstlichen Bilagen von halbleitenden Übergangsmetall-Dichalcogeniden (TMDs). Sowohl Heterobilagen als auch Homobilagen werden auf verschiedenen Substraten und als Bestandteil von dielektrischen und hBN-ummantelten van-der-Waals-Heterostrukturen untersucht.

Zunächst stellen wir in Kapitel 2 die grundlegenden strukturellen, elektronischen und optischen Eigenschaften von TMD-Kristallen, die nur aus wenigen Lagen bestehen, und von TMD-Hetero-Bilagen vor. Darauf aufbauend präsentieren wir in Kapitel 3 Studien zur Photolumineszenz (PL) von lokalisierten Exzitonen in Monolagen von Wolframdiselenid (WSe_2), die durch die lokale Verspannung des Materials durch auf der Nanoskala strukturierte Substrate gefangen werden. Diese lokalisierten Exzitonen weisen deutliche spketrale Schwankungen über Sekunden hinweg auf. Wir untersuchen die Auswirkungen des Substrats auf die spektrale Stabilität der Exzitonen und demonstrieren, dass ein Wechsel von Säulen aus Lithografie-Lack hin zu Säulen aus Aluminium-Gallium-Arsenid (AlGaAs), die durch Molekularstrahlepitaxie (MBE) hergestellt und durch lokale Ätzung definiert wurden, das spektrale Wandern um einen Faktor von 6 auf $(0.32 \pm 0.36)\,\mathrm{eV}$ und die Linienbreite um einen Faktor von 1.5 auf $(2.0 \pm 1.3)\,\mathrm{eV}$ reduziert.

In Kapitel 4 demonstrieren wir, dass sich der verspannungsbasierte Ansatz zur Exzitonenlokalisierung durch strukturierte Substrate auf dipolare Interlagen-Exzitonen in Heterobilagen von WSe_2 und Molybdändisulfit ($MoSe_2$)

übertragen lässt. Wir führen spektroskopische Studien an lokalisierten PL-Spitzen durch und bestätigen deren Interlagen-Charakter über ihre anregungsleistungsabhängige Blauverschiebung, die charakteristischen Zerfallszeiten ((118.8 ± 2.1) ns und (8.1 ± 0.5) ns) und die Anregungsresonanzen bei den Energien von Exzitonen in $MoSe_2$ und WSe_2. Darüberhinaus präsentieren wir magnetfeldabhängige PL-Spektren, die einen exzitonischen g-Faktor von (-6.4 ± 0.1) offenbaren, welcher nicht mit dem g-Faktor freier Interlagen-Exzitonen übereinstimmt. Dies könnte auf eine im Vergleich zu freien Interlagen-Exzitonen geänderte orbitale Zusammensetzung hindeuten.

Der dipolare Charakter der Interlagen-Exzitonen in Kombination mit den Einfangpotentialen auf Nanometer-Skala führen zu ausgeprägten Wechselwirkungseffekten zwischen den Exzitonen, wie wir in Kapitel 5 diskutieren. Wir identifizieren Zustände aus einem bis fünf Exzitonen in der selben Potentialfalle über ihre distinkten Abhängigkeiten von der Anregungsleistung. Wir ermitteln eine Blauverschiebung der Biexzitonen gegenüber einzelnen Exzitonen von (8.4 ± 0.6) meV. Wir reproduzieren die zunehmenden Blauverschiebungen für Komplexe mit höherer Anzahl an Exzitonen mithilfe eines Modells von Punkt-Dipolen in einem zweidimensionalen, harmonischen Potential. Durch einen Wechsel zu einer vollständig quantenmechanischen Beschreibung des Interlagen-Biexzitons können wir die Aufspaltung des Biexzitons von (1.2 ± 0.5) meV über die Austauschwechselwirkung erklären.

Nach der Erforschung der Wechselwirkungen von eingefangen dipolaren Exzitonen präsentieren wir in Kapitel 6 eine detaillierte Spektroskopie-Studie verschiedener Arten von Exzitonen in verdrehten $MoSe_2$-Bilagen. Homobilagen von TMDs beherbergen eine Vielzahl an optisch ansprechbaren Interlagen- und Intralagen-Exzitonen. Wir entdecken ausgeprägte Unterschiede zwischen Proben mit „kleinen Winkeln“ (weniger als 10° von 0° oder 60° entfernt) und Proben mit „großen Winkeln“ (zwischen 10° und 50°). Das A-Exziton zeigt nur sehr begrenzte Abhängigkeit vom Verdrehwinkel innerhalb des Bereichs „großer Winkel“, aber reduziert seine Energie abrupt um mehr als 10 meV, wenn der Winkel sich 0° oder 60° annähert. Photolumineszenz-Spektren im Bereich niedriger Energien weisen nur in Proben mit „kleinen Winkeln“ Signaturen (impuls-)indirekter Exzitonen auf. Die Helligkeit von A-Exzitonen

ist hingegen in Proben mit „großen Winkeln“ höher. Diese Entdeckungen erklären wir mithilfe eines Kontinuumsmodells für Exzitonen, die sich durch ein periodisches Moiré-Potential bewegen.

Contents

CHAPTER 1

Designer materials from two-dimensional crystals

Since Novoselov et al. reported the successful isolation of monoatomic layers from graphite crystals in 2004, [Nov04] two-dimensional (2D) materials have risen to become one of the most active research areas in condensed-matter physics. The term two-dimensional material is almost interchangeably used with the terms layered material and van der Waals material/crystal. These terms describe a crystal with a structure that can be divided into layers. Within the layers, adjacent atoms are strongly bound together by covalent bonds, whereas only weak van der Waals (vdW) forces act between adjacent layers.

The terms mentioned above do however not contain any information on the precise crystal structure, the number of layers that constitute a specific crystal, or the electronic properties of the material. In fact, most material classes available in three-dimensional (3D) materials also have a 2D counterpart: For example, graphene is a Dirac semi-metal [Nov05], hexagonal BN (hBN) is a wide-bandgap insulator, [Wat04] Bi_2Te_3 is a topological insulator, [Che09] and $NbSe_2$ exhibits a superconducting and a charge-density-wave phase. [Wil75, Xi15] The research presented in this thesis is cen-

tered around semiconducting materials from the family of transition metal dichalcogenides (TMDs). These materials have been studied since the 1960s [Fri66, Eva67, Joe86] but have attracted new interest, to a large extent due to the discovery of an indirect-to-direct-bandgap transition. [Mak10, Spl10]

The layered structure, which is the only property that all 2D materials share, already has profound consequences: The weak forces between adjacent layers allow for a relatively effortless cleaving between layers using the Scotch tape method, in which a crystal is placed between two adhesive tapes, which are then pulled apart. [Nov04, Tan14] This simple technique allows to exfoliate few-layer structures of the materials down to the monolayer limit. For most materials, the exact number of layers greatly influences the electronic properties. For example, bilayer graphene becomes a semiconductor instead of a semi-metal [Cas07] and CrI_3 displays ferromagnetic behavior only for odd layer numbers. [Hua17] More advanced techniques even allow to deterministically separate monolayers (with thicknesses below 1 nm) from bulk crystals with a lateral extent of $\sim 1\,\mathrm{cm}$. [Liu20a] For many 2D materials, exfoliation is still preferred over more scalable fabrication techniques, such as chemical-vapor deposition (CVD) [Wan09] or molecular-beam epitaxy (MBE) [Mor10, Par10], due to its simplicity combined with high material quality. [Ky18]

However, the most compelling feature of 2D materials may be the prospect of combining arbitrary sets of them to form new metamaterials with novel functionalities. [Gei13] Since no covalent bonds need to be formed between the layers, creating a heterostructure between two 2D materials is as easy as placing one on top of the other, for which a variety of techniques exists. [Fri18] Unlike in epitaxy of traditional materials, no constraints on lattice matching are imposed on subsequent layers. It is therefore possible to combine materials regardless of crystal structure and lattice constants with arbitrary twist angles. The twist angle, in particular, can widely tune the properties of the metamaterials in some cases. The most well-known example for this is twisted bilayer graphene, which exhibits Mott insulation [Cao18a], unconventional superconductivity [Cao18b] and strange-metal behavior, [Cao20] if the two layers have a relative twist corresponding to so-

called “magic angles”. [Tar19] The almost limitless material combinations with twist angles as an additional tuning knob present a promising route towards designer metamaterials.

Within this thesis, we study the excitonic properties of transition metal dichalcogenides integrated on different substrates and in different few-layer combinations. Using patterned substrates, we introduce strain perturbations into monolayer WSe_2, which will give rise to the formation of in-plane trapping potentials for excitons. We study the influence of substrate material on the spectral stability of these localized states (Chapter 3). Thereafter, we demonstrate that an analogous approach can be followed to trap dipolar excitons in a $MoSe_2$-WSe_2 heterobilayer in a nanoscale potential (Chapter 4), which leads to pronounced direct and exchange interaction effects (Chapter 5). Finally, we examine high-quality artificial bilayers of $MoSe_2$ and study the influence of the twist angle on different excitonic species (chapter 6).

CHAPTER 2

Two-dimensional transition metal dichalcogenides

In this chapter, we provide an introduction to the field of transition metal dichalcogenides (TMDs) and in particular their monolayers. We will review existing literature to provide context to the experimental findings of the following chapters. After describing the crystal structure and symmetry of TMDs, we explore their electronic and excitonic properties. We then continue to discuss heterostructures of TMDs and the formation of interlayer excitons.

For alternative overviews over these topics, we recommend general review papers on 2D TMDs [Man17] or more specialized reviews on optical properties of 2D TMDs [Mak16] and interlayer excitons in TMD heterobilayers. [Riv18]

2.1 Crystal structure

As indicated by the name, transition metal dichalcogenides have a stoichiometric representation of MX_2, where M is a group-VI (or sometimes group-V) transition-metal atom (Mo, W, Nb, Ta) and X is a chalcogen atom (e.g. S, Se, Te). The crystal structure in the common 2H polytype is illustrated

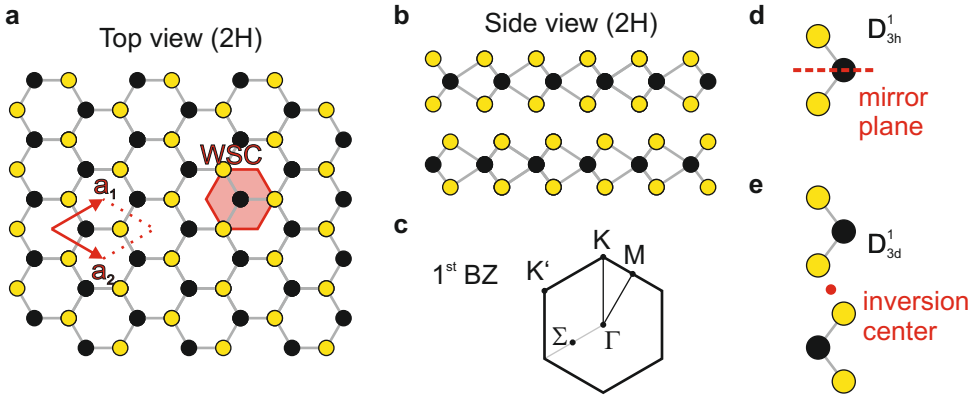

Figure 2.1: **Crystal structure of transition metal dichalcogenides. (a)** Top view of the TMD honeycomb lattice. The black (yellow) circles represent transition metal (chalcogen) atoms. The red arrows denote the lattice vactors spanning the primitive cell. A transition-metal-centered Wigner-Seitz cell is given by the red hexagon. **(b)** Side-view of the TMD crytsal structure in 2H stacking. **(c)** The hexagonal first Brillouin zone of monolayer TMDs with marked symmetry points. **(d)** Side view of a TMD monolayer with the red dashed line denoting the mirror plane. **(e)** Side view of a bilayer TMD with the inversion center marked by the red point. Adapted from [Wie19].

in Fig. 2.1a in top view and in Fig. 2.1b in side view. As stated previously, the crystal can be divided into layers, such that strong, covalent bonds are only formed within a layer and weak van-der-Waals forces act between layers. When a single layer is viewed from the top, the atoms form a honeycomb lattice, in which the lattice sites are occupied by a single M atom, or two X atoms in alternation. The M atoms of one layer all lie within one plane, whereas the X atoms form two planes, which encapsulate the M atoms. [Wil69, Ver70] Each M atom forms six covalent bonds with its neighboring X atoms, whereas X atoms form three covalent bonds to neighboring M atoms. This lattice features a three-fold rotational symmetry, i.e. it is symmetric w.r.t. rotations by 120°. The two lattice vectors a_1 and a_2, depicted by the red arrows in Fig. 2.1a, span the primitive cell of the lattice. The Wigner-Seitz cell (WSC), centered at a transition-metal site, is denoted by the red hexagon in Fig. 2.1a.

In 2H stacking, which is the most common polytype for the TMDs discussed in this thesis, [Wil69] adjacent layers are rotated relatively by 180° (or, equivalently due to the rotational symmetry, 60° or 300°). The chalcogen (transition metal) atoms of the upper layer are positioned above the transition metal (chalcogen) atoms of the lower layer. Another common configuration is the rhombohedral 3R polytype, in which the individual layers have the same structure as in 2H but adjacent layers are not rotated relatively but only offset. Finally, in the octahedral 1T polytype, already the atomic configuration within one layer is altered: [Wan18] There, one of the chalcogen planes is shifted to fill the interstitial lattice of the honeycomb structure. However, if not stated otherwise, we will restrict our discussion to the 2H polytype within this thesis.

The properties of a material are, to a great extent, dictated by its symmetries. The symmetry of TMD crystals depends on the number of layers: if they are odd-numbered, such as the monolayer depticted in Fig. 2.1d, they exhibit mirror symmetry w.r.t. the central transition-metal plane and therefore belong to the D^1_{3h} point group. Most notably they do not exhibit inversion symmetry, unlike even-numbered layers (e.g. the bilayer depicted in Fig. 2.1e) belonging to the D^3_{3d} point group. [Zha13b] These, on the other hand break mirror symmetry. These different symmetries will be relevant for the electronic structure discussed in the next section, in particular the phenomenon of spin-valley locking.

The hexagonal first Brillouin zone (BZ) of a monolayer TMD is shown in Fig. 2.1c. We marked the high-symmetry points, Γ in the center of the BZ, K at the corners and M at the center of the edges. Neighboring corners cannot be transformed into one another by the symmetry operations of the lattice (translation by the lattice vectors and rotation by 120°) and are therefore inequivalent. To discriminate between them, they are commonly referred to as either K and K' or K^+ and K^- depending on the authors. The M points, on the other hand, are equivalent under the available lat-

tice symmetries.[1] Furthermore, we marked the lower-symmetry Σ point at $\sim 0.55\overline{\Gamma K}$, a point in the Brillouin zone sometimes referred to as Q or Λ, where the conduction-band minimum (CBM) is situated (more details in the next section). Unfortunately, the nomenclature pertaining to the BZ symmetry points is not unique in the literature. Specifically older papers tend to use Herring's notation, [Her42] in which Σ denotes a point on the line $\overline{\Gamma M}$, whereas other papers refer to the corners of the Brillouin zone as the P points and to the centers of the edges using the terminology Q. [Bro71] Most current publications, however, use a nomenclature similar to the one introduced here.

2.2 Electronic bandstructure

Figure 2.2 displays density-functional-theory calculations of the bandstructure of MoS_2 as a prototypical TMD adapted from [Spl10]. The effects discussed here for MoS_2 analogously apply to $MoSe_2$, WS_2 and WSe_2. If there are major discrepancies between the materials, we will point them out explicitly. The thickness of the crystal in Fig. 2.2 is successively reduced when moving from panel (a) to panel (d), going from a bulk crystal over a quadrilayer and a bilayer to a monolayer. The solid black arrows in each panel denote the transition from the valence-band maximum (VBM) to the conduction-band minimum (CBM), i.e. the bandgap. The monolayer shows a contrasting behavior to all other crystal thicknesses: Instead of an indirect bandgap with the VBM at the Γ point and the CBM the Σ point, [Mat73b, Li07, Spl10, Che12] it features a direct bandgap at the K points. [Leb09, Li07, Spl10, Che12] A direct consequence of this is that MoS_2 [Spl10] and other TMDs [Gut13, Ton13b] exhibit much stronger photoluminescence in their monolayer form compared with multilayer crystals.

The reason for the transition from an indirect to direct bandgap is the different orbital contributions to the states at the Γ, Σ and K points. The elec-

[1] To see this, start at the center of one edge. Translation to the center of the opposing edge corresponds to a reciprocal lattice vector. The remaining four centers are reached via rotation by $\pm 120^\circ$ around Γ starting from either of the two points.

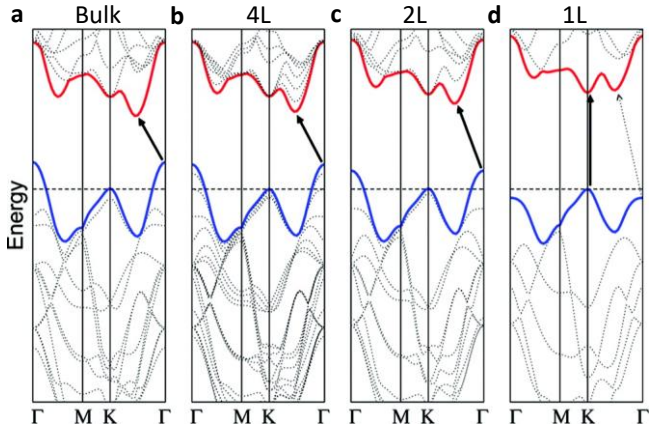

Figure 2.2: **Layer-dependent band structure of TMDs. (a-d)** Calculated electronic band structure of MoS_2 for the case of a bulk crystal (a), a quadrilayer (b), a bilayer (c) and a monolayer (d). Spin-orbit splitting is not included. The solid arrows indicate the transition from the valence-band maximum to the conduction-band minimum. Reprinted (adapted) from Andrea Splendiani, Liang Sn, Yuanbo Zhang, et al.: Emerging Photoluminescence in Monolayer $MoS2_2$, Nano Letters **10**, 1271–1275 [Spl10]. Copyright 2010 American Chemical Society.

tronic configuration of molybdenum and sulfur are $[Kr]4d^5 5s^1$ and $[Ne]3s^2 3p^4$, respectively. The s-orbitals contribute little to the total orbital character of the VBM and CBM states. The trigonal prismatic configuration of the crystal groups the remaining orbitals according to transformations under symmetry operations into $d \rightarrow \{d_{z^2}\}, \{d_{x^2-y^2}, d_{xy}\}, \{d_{xz}, d_{yz}\}$ and $p \rightarrow \{p_z\}, \{p_x, p_y\}$. [Wil69, Hui71, Mat73a, Fen12b] The VB at the K points is constructed from $\{d_{x^2-y^2}, d_{xy}\}$ with a weak admixture of $\{p_x, p_y\}$, whereas the K-point CB states are formed by $\{d_{z^2}\}$ states. The $\{d_{z^2}\}$ and $\{d_{x^2-y^2}, d_{xy}\}$ states can hybridize, opening up the bandgap at the K points. The involved orbitals are mostly localized at the center of the individual crystal layers, leading to very weak interlayer coupling. The gap at the K points therefore hardly depends on the number of layers. In contrast, the CB states at Σ and the VB states at Γ all have relevant admixture from $\{d_{z^2}\}$, $\{d_{x^2-y^2}, d_{xy}\}$ and $\{p_z\}$ states. The $\{p_z\}$ states, originating from the S atoms instead of the Mo atoms in

the center of the layer and oriented out-of-plane, can couple between layers. [Spl10, Liu15] The Γ-point VB and Σ-point CB states are therefore much more sensitive to layer number and energetically pass the respective states at the K point when transitioning to monolayer thickness.

The high atomic number of the transition metals induces a large spin-orbit-coupling in the electronic states. [Zhu11] This can lead to a large spin splitting in odd-layered TMDs, in particular TMD monolayers: Time-reversal symmetry requires the existence of degenerate states with opposite momentum and spin. [Kra30, Wig32] For example, for every electron state at the K point with spin-up orientation ($|\uparrow\rangle$), there is an energy-degenerate spin-down ($|\downarrow\rangle$) state at K'. If the system is moreover inversion symmetric (which, as discussed above, is true for even-numbered TMD few-layers), the existence of degenerate states with opposite momentum but equal spin orientation follows. Then, each spin-up state at K requires a degenerate spin-up state at K'. In total, inversion- and time-symmetric systems therefore feature pairs of energy-degenerate states at the same quasi-momentum but with flipped spin. This is not the case for systems with broken inversion symmetry, e.g. TMD monolayers: Here, the bands are spin-split with opposite signs of the spin splitting in the opposite K valleys.

The spin splittings are generally larger in the VB than in the CB (e.g. 150 meV vs. < 3 meV for MoS_2 [Xia12, Kor13, Koś13, Liu15, Lat15, Mar17]). In $MoSe_2$, the splittings in the bands are such that the lowest-energy CB state and the highest-energy VB state have the same spin orientation in the same K valley, giving rise to a large transition dipole moment between the two states. [Kor15, Liu15] In MoS_2, WSe_2, and WS_2, on the other hand, the sign of the spin-orbit-coupling in the CB is reversed such that the transition from the highest VB state to the lowest CB state is dark. [Kor15, Liu15, Zha17c] The band splitting at the K points also occurs in even-numbered layers, such as bilayers. However, in this case the spin and valley degree are not coupled due to the restored inversion symmetry. [Mak12]

2.3 Excitons in TMD monolayers

In the main experimental methods employed in this thesis, photoluminescence and white-light reflectivity, electrons and holes are created pairwise via the absorption of a photon. These charge-carrier pairs are typically tightly bound during the optical process, unlike in many established semiconductor platforms, where electrons and holes can propagate through the crystal independently. These tightly bound electron-hole pairs are called *excitons*. Clear excitonic signatures can be found in the reflectivity and absorption spectra of monolayers TMDs, which exhibit a series of discrete peaks instead of absorption plateaus that might be expected with the 2D joint density of states. [Mak13, Che14]

While excitons also exist in other semiconductors, TMDs exhibit exceptionally high exciton binding energies of several hundred meV, e.g. 0.55 eV in $MoSe_2$. [Uge14] GaAs, for comparison, only has an exciton binding energy of (4.20 ± 0.03) meV.[2] [Nam76] As a result of these high binding energies, excitonic effects remain relevant even at room temperature. There are two main reasons for the high binding-energy values: Firstly, due to the two-dimensional geometry of the monolayers, the spatial separation between electron and hole is reduced. Secondly, the lack of a dielectric material outside the monolayer leads to a weaker screening of the electric field since the effective dielectric permittivity is much smaller. [Che14] Due to this nonlocal and weaker screening, the Rytova-Keldysh potential is frequently used to describe the electron-hole interactions: [Ryt65, Kel79]

$$V_{RK}(r) = \frac{e^2}{8\pi\epsilon_0\epsilon_r l_s}\left[H_0\left(\frac{r}{l_s}\right) - Y_0\left(\frac{r}{l_s}\right)\right] \tag{2.1}$$

Here, r is the distance between electron and hole, e is the elementary charge, ϵ_0 is the vacuum permittivity, ϵ_r is the relative permittivity of the medium (average of the medium above and below the TMD), l_s is the screening length (related to the TMD [Cud11]) and H_0 and Y_0 are the Struve and

[2] The most technologically relevant semiconductors tend to have small exciton binding energies. However, strongly bound excitons are also found outside of TMDs, e.g. in cuprous oxide (Cu_2O) with $E_B \sim 150$ meV. [Gro56, Kaz14]

the second-order Bessel functions, respectively. This potential approaches a Coulomb potential for large distances. The screening only has a major impact at shorter distances, where the potential diverges logarithmically, i.e. more weakly than a Coulomb potential.

Charge-neutral excitons of very different energies can occur within the same material. The electron and hole states can stem from various bands. For example, if they stem from the highest-lying VB and the lowest-lying CB, we will refer to them as A excitons. If the hole is in the energetically unfavorable spin state of the spin-split valence band, i.e. an energetically deeper-lying band, the exciton is referred to as a B exciton. The energetic difference between A and B excitons is evidently then on the order of the VB spin splitting, e.g. 220 meV in $MoSe_2$.[3] [Wan15b] Moreover, in analogy to hydrogen atoms, excited states of the same species of excitons exist based on different relative electron and hole wavefunctions. As in the atomic case, they are referenced by principal and angular-momentum quantum number, e.g. 1s, 2s and 2p. [Che14, Wan15b]

Besides neutral excitons, other particle complexes can be formed. In the presence of free electrons or holes, one of these charge carriers can bind to an exciton and form a negatively or positively charged trion. The trion binding energy (energetic difference between trion and isolated exciton plus third charge carrier; not between trion and all three particles isolated) in TMD monolayers is typically 20 meV–30 meV. We present schematic depictions of neutral excitons and both types of charged trions in Fig. 2.3a. At high exciton densities, also biexcitons, bound states of two electrons and two holes, and other few-particle complexes can form.

As an example for excitonic signatures in optical spectra of TMD mono- and few-layers, we present the low-temperature PL spectrum recorded from a $MoSe_2$ monolayer in Fig. 2.3b, excited using a laser at 2.33 eV. The monolayer is encapsulated by a few layers of hBN above and below to provide a homogeneous dielectric environment and improve the homogeneity and

[3] The split-off VB and therefore the B exciton are also present in even-numbered and bulk $MoSe_2$ samples [Ane80] but spin and quasimomentum are not coupled in these cases.

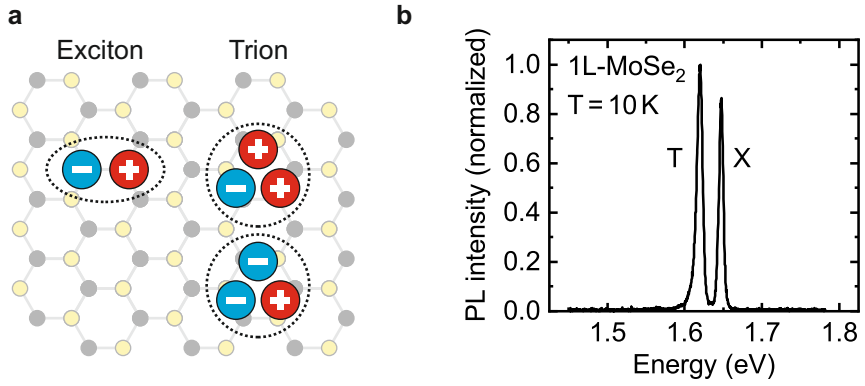

Figure 2.3: **Excitonic particle complexes in monolayer TMDs. (a)** Schematic illustrations of neutral exciton and the positively and negatively charged trion. **(b)** Normalized low-temperature PL spectrum of an encapsulated monolayer of $MoSe_2$. The two distinct peaks correspond to exciton and trion emission.

stability of the emission. [Wie17, Aja17, Cad17] The two distinct peaks correspond to emission of A excitons and trions. There is no emission at the single-particle bandgap at 2.16 eV (not shown).

The peak positions of exciton (1.648 eV) and trion (1.620 eV) and accordingly the trion binding energy (28 meV) correspond well to literature values. [Ros13] The measured linewidth (FWHM) of the neutral exciton of 7 meV is close to the homogeneous limit (3.4 meV at $T = 10$ K [Dey16]) but still surpasses it by a factor of two. This indicates that despite the high-quality dielectric environment provided by the hBN cladding layer, there are still inhomogeneities within the sample, likely from contaminants trapped between the layers that give rise to inhomogeneous broadening. The same conclusions can be drawn from the slightly broader (9 meV) trion peak.

2.4 Excitons in artificial TMD bilayers

As stated earlier in this chapter, a key feature of van-der-Waals materials is the possibility to easily combine different materials into heterostructures. If two semiconducting monolayers of different TMD materials are stacked

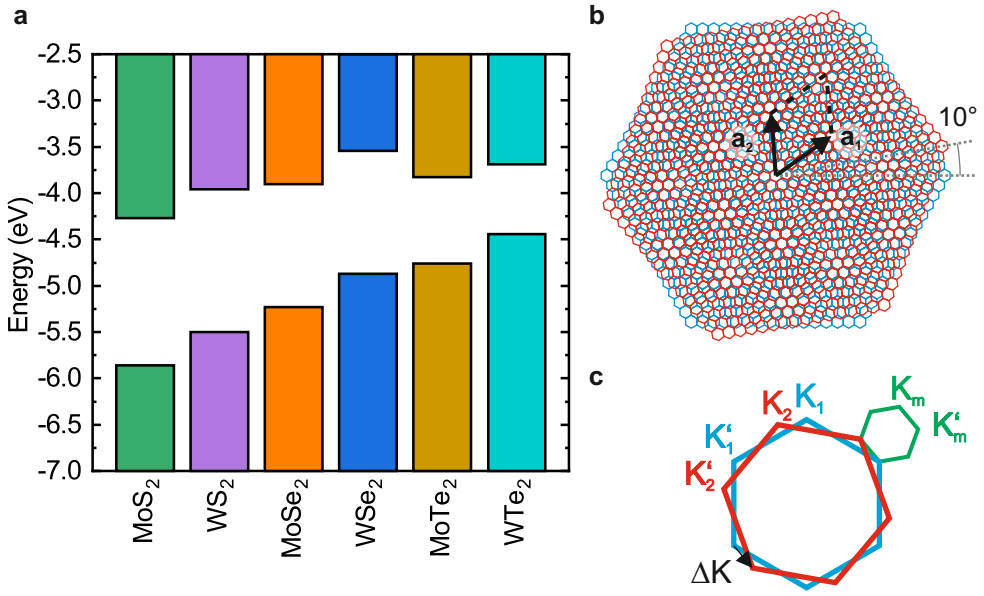

Figure 2.4: **Band alignments and lattice alignment in artificial TMD bilayers.** **(a)** Conduction-band and valence-band edges of selected monolayer TMDs. Reprinted from Cheng Gong, Hengji Zhang, et al.: Band alignment of two-dimensional transition metal dichalcogenides: Application in tunnel field effect transistors, Applied Physics Letters **103**, 53513 (2013) [Gon13], with the permission of AIP publishing. **(b)** Schematic depiction of the moiré superlattice of twisted honeycomb lattices. The blue and the red lattice have the same lattice constant but are twisted by 10° relatively. The moiré lattice vectors are depicted in black. **(c)** Schematic depiction of the first Brillouin zones of two individual honeycomb lattices with a relative twist angle of 20° (red and blue) and the moiré supperlatice they span (green).

vertically, forming a heterobilayer (HBL), the resulting structure generally exhibits a type-II band alignment in which the global CBM and VBM are located in opposite layers. [Kan13, Gon13, Koś13, Ter13] In particular, the energies of the VBM increase from sulfides over selenides to tellurides as illustrated in the band-edge diagram in Fig. 2.4a. Within these groups of TMDs, they are higher for W-based materials than for the Mo-based counterparts. The CBM mostly follows this trend, barring some exceptions for the tellurides. [Kan13, Gon13, Koś13, Ter13] As a consequence, the lowest-energy exciton in most TMD heterobilayers is formed by an electron and a hole residing in different layers. These quasiparticles, called interlayer excitons (IXs), still have exceptionally high binding energies of more than 100 meV despite the spatial separation of the charge carriers. [Lat17, Wil17, Ove19, Mer19]

The vertical displacement of electrons and holes results in two major differences compared to *intra*-layer excitons: Firstly, due to the reduced wavefunction overlap, the optical transition dipole of the interlayer exciton is strongly reduced. This increases the radiative recombination times into the nanosecond regime [Riv15, Nag17b, Mil17, Jau19, Riv18] compared to the intralayer exciton lifetimes that have been reported to be in the picosecond regime. [Yan14, Wan14, Rob16] Secondly, the charge-carrier separation gives rise to a static electric dipole moment in the out-of-plane direction. Due to this dipole moment, the IX energy [Riv15, Jau19, Kie20] and lifetime [Jau19, Kie20] are strongly tunable by applied electric fields. Moreover, repulsive diploar interactions are induced between IXs which leads to pronounced blueshifts for increasing exciton densities, as seen in experiments with varied excitation-power densities. [Riv15, Nag17b, Mil17] The picture of the strict type-II band alignment does not hold for all material combinations. The VBs in MoS_2-WS_2 [Kie20] and the CBs in $MoSe_2$-WS_2 [Ale19] heterobilayers are energetically so close that, depending on parameters such as twist angle and out-of-plane electric field, the lowest-energy excitons can be *intra*layer excitons, *inter*layer excitons or hybridized excitons, in which at least one of the charge carriers is not fully localized within one layer. [Kie20, Ale19]

The vertical stacking of vdW materials may well be possible for a range of twist angles between consecutive layers, but the mutual orientation greatly influences the electronic and excitonic properties of the combined system. A twist angle between layers in real space equally well translates to a rotation of the Brillouin zones in reciprocal space. With the band extrema located at the K points at the edges of the Brillouin zone, this introduces a momentum mismatch for IXs in TMD-HBLs. This is illustrated in Fig. 2.4c, where the blue and red hexagons denote the edges of the Brillouin zones of the consituent TMD monolayers of a bilayer with a twist angle of 20°. For the $MoSe_2$-WSe_2 HBL, it has therefore been observed that only twist angles close to the commensurate angles of 0° and 60° result in bright IXs. [Nay17] For chalcogen-mismatched combinations of TMDs, the lattice constants of the two layers also differ notably, leading to a slight momentum mismatch of the lowest-energy IXs even in the absence of rotational misalignment. [Riv18] The IX energy, brightness and degree of hybridization are still expected to be strongly tunable by the twist angle in these systems. [Heo15, Ale17, Ale19]

As depicted schematically in Fig. 2.4b, the lattice-constant mismatch and rotational misalignment give rise to moiré patterns that can exhibit long-range periodicity [Li10, Dec11, Yan12] or quasi-periodicity [Ahn18, Moo19] in real space. The figure depicts two honeycomb lattices (red and blue) of a TMD bilayer constructed from materials sharing the same lattice constant and a mutual twist angle of 10°. This results in the formation of a visible moiré pattern on the length scale of six unit cells of the individual lattices, for which a modulation of the local stacking order of the two layers exists. The local atomic registry is strongly linked to the local electronic bandgap in the HBL system, such that the moiré lattice defines a periodic potential landscape for interlayer excitons. [Yu17] In combination with disorder, this can give rise to locally trapped IX states [Sey19, Tra19, Jin19] that can act as quantum-light emitters. [Bae20] These superlattice effects have been observed in hBN-encapsulated HBL samples at low excitation powers. [Sey19, Tra19, Jin19] It is not currently clear whether the trapping of IXs that we observe in chapters 4 and 5 is driven purely by the induced inhomogeneous strain profile or an interplay of strain and superlattice effects. We will

present a more detailed discussion of stacking orders in moiré superlattices in the appendix, section A.2.

The new periodicity given by the moiré superlattice also determines the size of the Brillouin zones of the hybrid material, which is generally smaller than those of the constituent materials. [Bis11] The electronic (and phononic) bandstructures are folded into the new moiré Brillouin zone. This is illustrated in Fig. 2.4c, where the Brillouin zones of two honeycomb lattices with a twist angle of 20° are outlined in blue and red. The Brillouin zone of the resulting moiré superlattice is outlined in green. The length of one edge corresponds to the (reciprocal) distance between K points of the different layers.

The creation of artificial bilayers is of course not limited to different materials. One can assemble an artificial homo-bilayer from two monolayers of the same material, which might differ from its natural counterpart greatly based on the stacking angle. Since the individual layers are identical, the electronic states can in principle couple and hybridize very well, as seen for the indirect bandgap of bilayers with 2H stacking (see section 2.2). Both the twist angle and the local stacking order can modulate the strength of this coupling. [vdZ14, Liu14, Hua14, Yan19] This can lead to much more pronounced twist-angle dependencies of excitonic properties in homobilayers compared to heterobilayers. We will present our findings on the twist-angle-dependent properties of $MoSe_2$ homobilayers in chapter 6.

CHAPTER 3

Localized excitons in monolayer WSe_2

In this chapter, we discuss localized excitons in monolayers of WSe_2, which have been studied intensely since initial reports in 2015 due to their prospects for use as deterministic single-photon sources for integrated quantum photonics. We begin by reviewing the pertinent literature, giving an overview of the properties of the localized excitons and describing methods to control their occurrence and characteristics. In a more general context, we extend our discussion to explore other quantum emitters in monolayer TMD materials and their heterostructures.

We continue by discussing our findings on site-selectively generated localized exciton states in monolayer WSe_2. After outlining our fabrication routine, we present photoluminescence studies of the observed emitters. In particular, we cover photoluminescence-excitation (PLE) experiments and the impact of substrates on spectral stability.

3.1 Single-photon emitters in monolayer WSe_2

Fully confined electronic states (i.e. states for which the spatial extent of the wave function in all three dimensions is small compared to the De Broglie wavelength) have been an active research topic in semiconductor physics for decades. The localization results in a transition from the quasi-continuous (dispersive) band structure towards discrete, well-separated energy levels. Systems in which full electronic confinement is achieved are therefore often referred to as artificial atoms in the solid state. [McE97] Established examples of such systems include self-assembled InGaAs quantum dots (QDs) in GaAs, [Dre94] GaAs QDs in AlAs, [Gam96, Wat00] gate-defined QDs in 2D electron gases in semiconductor heterostructures, [Ang07] and color centers, such as the nitrogen-vacancy center [Doh13] and the silicon-vacancy center in diamond. [Neu13] For an overview of these systems, we refer interested readers to one of many specialized reviews. [Aha16].

If the confinement is realized in both the conduction band (CB) and the valence band (VB), and transitions between these states are optically allowed, the system can act as a single-photon emitter, a central component needed for many proposed protocols for quantum key distribution. [Ben84, Bru98]

The existence of single-photon emitters in monolayer WSe_2 was first reported in early 2015, by five groups simultaneously. [Ton15, Sri15a, He15, Kop15, Cha15] All five papers describe localized sharp emission peaks redshifted by 20 meV–200 meV from the free exciton transition. The single-photon character of the emission was demonstrated using Hanbury Brown Twiss experiments. [Han56, Kim77] The occurence of the single-photon emitters was seemingly random with an increased formation probability at the edges of the exfoliated monolayers. Other preferential sites for localized excitons include morphological defects such as scratches and wrinkles of the flakes.

With structural deformations being correlated with the emergence of localized exciton states, strain perturbations were quickly linked to their occurrence. This can be explained well with the finding that the energies of free excitons are tuned strongly via applied strain, [Fri17] with monolayer WSe_2

excitons redshifting by 54 meV/% under application of uniaxial tensile strain at room temperature. [Sch16] Consequently, several groups demonstrated that emitters could be generated site-selectively using patterned substrates: The quantum emitters were shown to emerge at indentations [Ker16, Kum15] and dielectric pillars. [Bra17, PB17] This simple creation approach is also advantageous for the use of these emitters in integrated photonics, since WSe_2 monolayers can be placed over waveguides [Bla18, Dut18, Pey19, EH20] or plasmonic resonators [Iff18, Luo18, Cai18]. The induced strain not only creates emitters at the position of these elements, but the spatial proximity facilitates optical coupling between the emitters and the photonic or plasmonic structures. We recommend [Blu21] for a review on the impact of strain on the properties of 2D materials and in particular strain-induced exciton localization.

Besides the progress on strain-induced SPEs in monolayer WSe_2, many analogous findings in other TMD materials have been published: It has been demonstrated that the energy of excitons in MoS_2 monolayers coating nanocones can be reduced by ~ 50 meV at the tip of the cone, where the local strain is maximized, [Li15] and discrete emitters in strained regions of monolayer $MoSe_2$ have been reported.[1] [Bra16, Yu21, Pet22] However, it is not clear whether strain is the only cause for the local confinement potentials or whether other factors, such as atomic-scale point defects, local symmetry breaking or non-local dielectric screening, play a role in all of these findings. [Bra17]

For the work presented in this chapter, we fabricated dielectric nanopillars to generate exciton localization. There are, however, alternative approaches to confine excitons in TMDs, which we will briefly summarize: Atomic defects can bind electronic states, as known from e.g. diamond, which has a plethora of optically active defects (color centers), such as the nitrogen-vacancy [Doh13] or the silicon-vacancy complex. [Neu13] Such defects are also present in 2D materials and have been most widely studied in hBN.

[1] Another manuscript published almost simultaneously to [Bra16] also reported localized emitters in $MoSe_2$ but did not correlate the emission to strain perturbations. [Cha16]

[Tra16a, Tra16b] It was found that point defects can be induced in a controlled way. For example, helium-ion treatment can generate single-photon emitters in monolayer MoS_2 site-selectively. [Kle20] Heterobilayers of TMDs provide even further possibilities to locally control exciton energies: The moiré superlattice of two mismatched crystal lattices can give rise to a confinement potential for interlayer excitons (IXs) and thus host single-photon emitters. [Bae20] Both the helium-ion-induced emitters in MoS_2 and the moiré-trapped IXs suffer from long lifetimes of more than 1 µs and 10 ns, respectively, and thus cannot produce comparable brightness to established single-photon sources in III-V materials, such as those based on III-V quantum dots.

The most straight-forward approach to limit the spatial extent of excitons in TMD monolayers may however be to limit the dimensions of the monolayer itself. Small monolayer crystals can be prepared e.g. by ultra-sonication [Ste13, Gan15, Lua17] or partial etching. [Wei17] In contrast to all previously discussed methods, in which excitons are trapped within an area of reduced energy, the excitons confined to small crystals have an increased energy compared to free excitons in larger crystals, approximately following the expected trend of higher energies for smaller crystal sizes.[2] [Gan15, Lua17, Wei17] In principle, the exciton energy can be tuned from the near-infrared to the ultraviolet spectrum using this method. [Lua17] However, such extreme bandgap modulations require crystal sizes on the level of single nanometers, for which deterministic fabrication has not yet been demonstrated. Moreover, although the effects of strong confinement in these systems are apparent, the confirmation of single-photon emission has not yet been forthcoming, to the best of our knowledge.

[2] Quantitatively, the spectral shifts are much stronger than predicted with simple models, such as particle-in-a-box calculations using the effective masses of the charge carriers. Such calculations are also presented in [Gan15] and [Lua17], where the authors claim agreement between model and experiment. However, we were not able to replicate the results of either publication using the parameters and equations given in the papers themselves. The authors of [Gan15] have admitted errors in their calculations in personal correspondence. We have also contacted the authors of [Lua17] but have not received a reply yet.

3.2 Sample structure

We used two types of samples for the measurements presented in this chapter, to which we will refer as HSQ-based and AlGaAs-based. For the HSQ-based substrates, as depicted in Fig. 3.1a, we start with pieces of a Si wafer covered by 285 nm of SiO_2. We spin-coat the pieces with hydrogen silsesquioxane (HSQ) and write a disk pattern with electron-beam (e-beam) lithography. The unexposed HSQ is removed using tetramethylammoniumhydroxid (TMAH), such that only the exposed areas remain. This substrate preparation has been demonstrated to be suited for SPE generation in WSe_2 with HSQ [PB17] and other resists. [Bra17] After e-beam exposure, HSQ adopts a SiO_2-like structure. For a near-complete conversion, annealing at temperatures exceeding 1000 °C would be necessary, [Hol07] to which we did not have access. We therefore expect that our HSQ-based pillars differ from SiO_2 (and thereby the substrate outside the pillars) regarding their refractive indices and defect densities. Despite the compound nature of the substrate surface, we will refer to these samples as HSQ-based for the remainder of the chapter for the purpose of simplicity. Moreover, this nomenclature is intended to emphasize differences to the sample used in chapters 4 and 5, which was prepared by etching pillars directly into the SiO_2 substrate.

The wafers for the AlGaAs-based substrates were prepared using molecular-beam epitaxy (MBE). A commercially available [001]-GaAs wafer was overgrown with a buffer layer of GaAs, a GaAs-AlAs distributed Bragg reflector (DBR) with a stopband centered at 755 nm (= 1.64 eV, in the typical spectral range of WSe_2 emitters) and finally capping layers of GaAs and $Al_{0.41}Ga_{0.59}As$. We included Al in the top layer in order to increase the bandgap and thus mitigate effects of free-carrier generation in the substrate. However, we limited the Al content to prevent oxidation and maintain high crystalline quality with a low defect density. Finally, we etched into the $Al_{0.41}Ga_{0.59}As$ capping layer outside the pillar areas (outlined by e-beam lithography) with a reactive-ion etching (RIE) process. The top layers of the finished samples are illustrated in Fig. 3.1b.

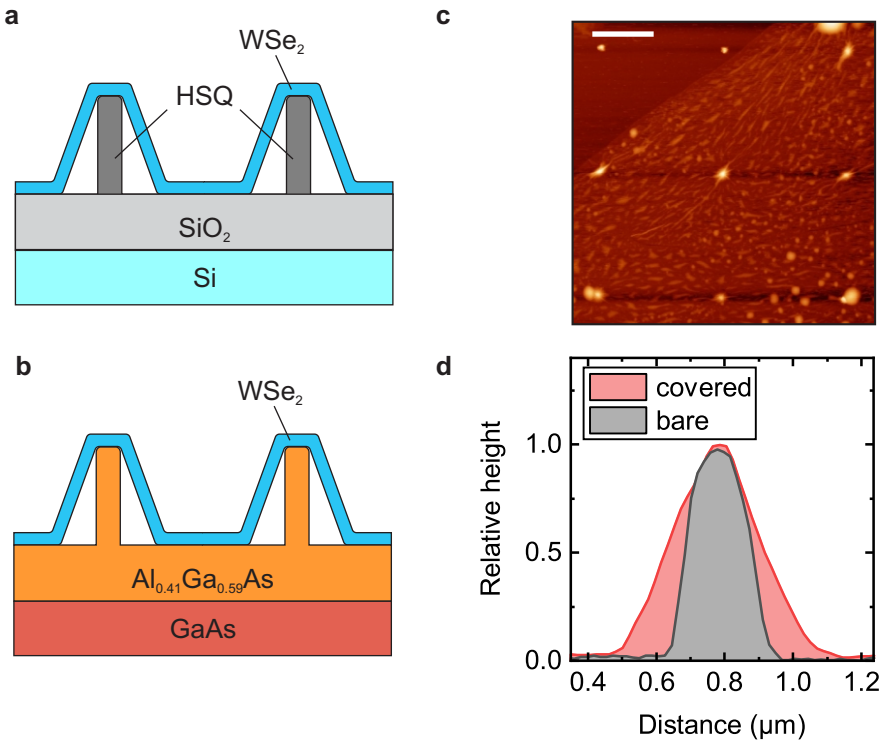

Figure 3.1: **Sample structures for site-selective trapping of excitons in monolayer WSe_2.** **(a)** HSQ-based nanopillars are lithographically defined on top of a Si/SiO_2 substrate before they are covered with a WSe_2 monolayer. **(b)** In AlGaAs-based samples, the pillar grid was etched into a $GaAs/Al_{0.42}Ga_{0.58}As$ substrate before capping with the WSe_2 monolayer. **(c)** Atomic-force microscopy scan of a HSQ pillar array, partially covered by a WSe_2 monolayer. The scale bar corresponds to 2 µm. **(d)** Height profiles of a bare and a covered pillar from the AFM scan in panel (c). We display relative height because the covered pillar was slightly higher (59 nm vs. 45 nm) due to inhomogeneities in the initial resist layer. The data displayed in panels (c) and (d) were analyzed using WSXM. [Hor07]

The WSe_2 monolayers were prepared by micromechanical cleaving with adhesive tape, exfoliated onto polydimethylsiloxane (PDMS) stamps, identified via their optical contrast and finally transferred via viscoelastic stamping. [CG14] A detailed description of the entire fabrication process is presented in appendix sections A.3 and A.5.

Figure 3.1c depicts an atomic-force microscopy (AFM) scan of a HSQ pillar array with a pitch of 4 µm, which is partially covered by a WSe_2 monolayer. The surface of the monolayer features many bubbles or wrinkles, most likely linked to polymer residues from the PDMS stamp or impurities trapped during the transfer process. [Hai12, Roo17] This is increases the surface roughness from $RMS = 1.7$ nm (bare substrate; RMS = root mean square) to $RMS = 3.8$ nm (WSe_2 monolayer on top of unpatterned substrate). Moreover, the nanopillars appear wider when covered by the monolayer. For a more detailed insight, we present height profiles along the pillar apex for a bare and a covered pillar in Fig. 3.1d. We dsplay the relative heights because the covered pillar had a slightly larger absolute height (59 nm vs. 45 nm) due to inhomogeneities in the initial HSQ layer. We measure the apparent diameter (defined as full width at half-maximimum (FHWM)) to be 0.30 µm for the WSe_2-covered and 0.20 µm for the bare nanopillar. This demonstrates that the monolayer does not conform to the substrate topography perfectly but rather forms a "tent" over the pillars, as already indicated in the schematic illustrations in Fig. 3.1a and b. This behavior was analogously observed in previous studies. [Bra17, PB17] There are, however, techniques that result in the monolayer following the shape of the substrate more closely, e.g. by submerging a sample in a solvent, drying it and having the emerging capillary forces press the flake onto the substrate. [Li15]

3.3 Photoluminescence of localized emitters in monolayer WSe_2

We present an optical microscope image of a typical HSQ-based sample in Fig. 3.2a. A WSe_2 crystal with varying layer numbers can be seen in the

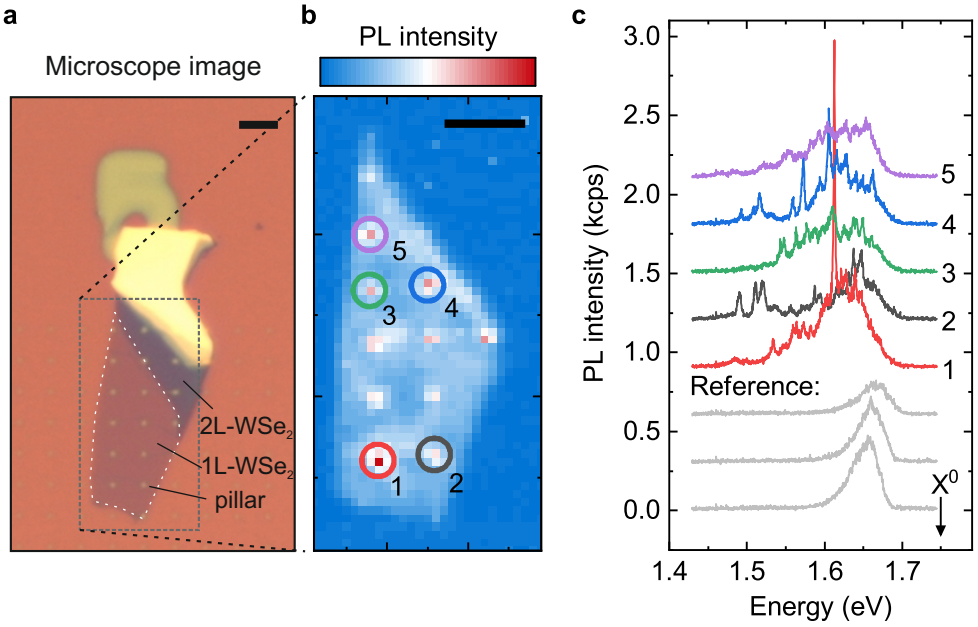

Figure 3.2: **Photoluminescence from strain-defined emitters in monolayer WSe_2.** **(a)** Optical microscope image of a WSe_2 crystal on a HSQ-based pillar substrate. The area framed by the gray dashed lines corresponds to the area measured for panel (b). **(b)** Spatially resolved integrated PL intensity in the spectral range 1.43 eV to 1.75 eV. **(c)** Typical spectra from five pillars (color-matched to the position indicators in panel (b)) and three reference spectra from unstrained regions of the monolayer. The spectra were acquired at $T = 10\,\mathrm{K}$ and with cw excitation at $\lambda = 633\,\mathrm{nm}$ with a power of 300 nW focused to $\sim 1\,\mu\mathrm{m}$. All scale bars are 5 µm.

center of the image. The faint blue region corresponds to a monolayer; a bilayer region adjacent to the monolayer appears as a darker blue. The nanopillars appear as bright dots in the mono- and bilayer regions. The optical contrast of the pillars to the surrounding substrate is weaker in the regions not covered by the WSe_2 crystal. The yellow 5 in the top part of the image is an alignment marker, lithographically written into the HSQ. In Fig. 3.2b, we present spatially resolved low-temperature photoluminescence recorded from the monolayer region in the spectral range 1.43 eV to 1.75 eV. The measured area is outlined in Fig. 3.2a. The PL measurements were

performed at a temperature of 10 K using a HeNe laser ($\lambda = 632.8$ nm) as excitation source focused onto a spot of ~ 1 µm. These parameters constitute standard measurement conditions, under which all data presented in the remainder of the chapter were recorded, unless stated otherwise. We used an excitation power of 300 nW. The scale bars in both panels correspond to 5 µm. An increased PL intensity is observed at all pillar sites. This may already be a sign of excitons being attracted towards the pillar sites by the strain-defined potential gradient. [Fen12a, CG13, Li15, Bra17] However, this could in principle also point towards radiative recombination with a higher quantum or collection efficiency at the pillar sites.

We display examples of PL spectra from different pillar sites in Fig. 3.2c and compare them to reference spectra from outside the pillar regions. The spectra at pillar positions are color-matched to their spatial indicators in Fig. 3.2b. The light-gray reference spectra all display broad, unresolved emission in a band centered around 1.66 eV. At this low excitation power, we observe no emission from the free excitons and trions, which would be at 1.75 eV and 1.72 eV, respectively. We attribute the measured low-energy emission to excitons trapped at crystal defect sites.[3] [Ton13a, Zha17b, Wu17, Wu16, Fan19]

In contrast, the emission spectra at the pillar sites extend to much lower energies (down to ~ 1.5 eV) and feature multiple distinct, narrow (typically 2 meV to 4 meV FWHM) emission peaks. This observation is analogous to previous reports on strain-induced SPEs in monolayer WSe_2 [Bra17, PB17] and the spectral distribution also mimics that of the randomly occurring emitters. [Ton15, Sri15a, He15, Kop15, Cha15] We find a comparable red-shift at pillar sites already at room temperature (see section A.6).

[3] In section 4.2, we attribute emission from a WSe_2 monolayer in the same spectral range to different particle complexes, namely dark excitons and trions, and (charged) biexcitons. These attributions are unlikely in this case: The (bright) neutral exciton and trion should be visible in PL spectra at lower excitation power densities than any of the aforementioned complexes. Low-energy, defect-bound excitons, on the other hand, are visible at low excitation powers but saturate early, after which delocalized excitons become populated. [Wu17, Wu16]

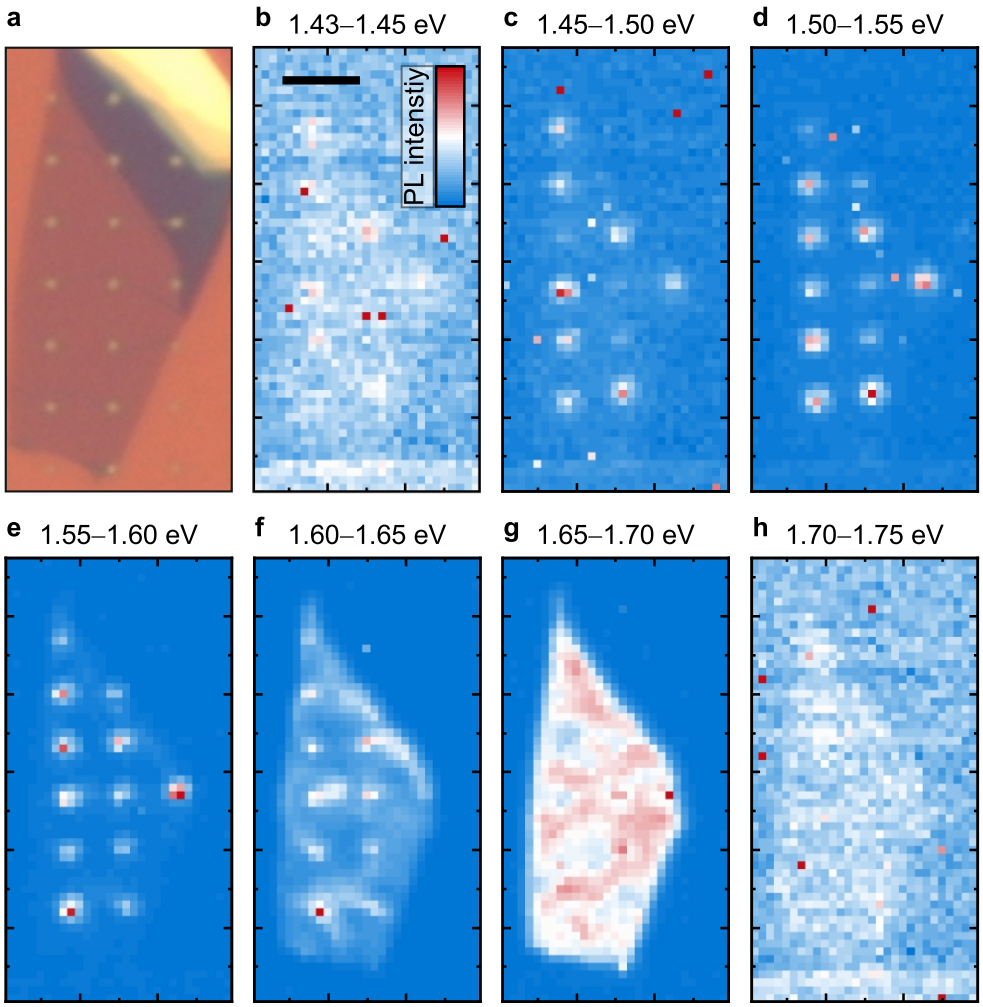

Figure 3.3: **Spatial and spectral distribution of emission of a WSe_2 monolayer on a HSQ-pillar sample.** **(a)** Optical microscope image of the investigated WSe_2 monolayer on a HSQ-pillar substrate. Thicker parts of the crystal are also present but hardly contribute to the photoluminescence. **(b-h)** Spatially resolved PL emission of the monolayer shown in panel (a) integrated over different spectral ranges. The scale bar in panel (b) (and the spacing between major axis ticks) corresponds to 5 µm. The PL is intensity-normalized in each panel. The spectra were acquired at $T = 10\,\mathrm{K}$ and with CW excitation at $\lambda = 633\,\mathrm{nm}$ with a power of 300 nW focused to $\sim 1\,\mu\mathrm{m}$.

The spectral discrepancy between emission on pillars and at flat positions of the monolayers is highlighted in Fig. 3.3. There, we present the spatially resolved PL separately for different spectral ranges. The figure is based on the same dataset as Fig. 3.2. Overall, very little emission is observed in the ranges of the lowest (1.43 eV to 1.45 eV) and the highest (1.70 eV to 1.75 eV) energies. Nonetheless, a slight tendency towards emission at pillar sites can be seen for the lowest energies. All energy ranges up to 1.65 eV (Fig. 3.3b-f) exhibit preferential emission at the pillar sites. Only the range 1.65 eV to 1.70 eV (Fig. 3.3g) displays bright emission over the entire monolayer with the intensity tending to decrease slightly at the pillar positions. The overall intensity in the range 1.70 eV to 1.75 eV is too low to determine how the pillars influence the emission. The spatial variation of the emission illustrates how the strain induced by the pillars locally reduces the bandgap of the WSe_2 monolayer and gives rise to trapping potentials for the optically created excitons.

An overview of the emitter energies is given by the histograms presented in Fig. 3.4. A total of 105 sharp-line emitters were found in a different sample with an AlGaAs-based substrate and analyzed. Their emission energies are plotted in 1 meV and 10 meV binnings in Fig. 3.4a and 3.4b, respectively. We find an average energy of 1.647 eV and a standard deviation of the energy distribution of 27 meV. The emission-energy distribution is asymmetric with a less pronounced decay to the low-energy side. (Skewness: -0.46.[4]) Compared to the reference spectra, centered around 1.66 eV, the emission energy at pillars is reduced by 13 meV. The A exciton of WSe_2 monolayers has been found to shift by 54 meV $\%^{-1}$ with uniaxial strain. [Sch16] The 13 meV of energy reduction therefore correspond to 0.24 % of strain. The standard deviation of emission energies can be converted to a standard deviation of strain of 0.5 %. Experiments with flexible substrates have demonstrated that

[4]The skewness is a measure of asymmetry in a statistical distribution and corresponds to the standardized third moment of the distribution. A distribution of the physical quantity X with mean value μ and standard deviation σ has a skewness of $E\left[\left(\frac{X-\mu}{\sigma}\right)^3\right]$, where E denotes an expectation value.

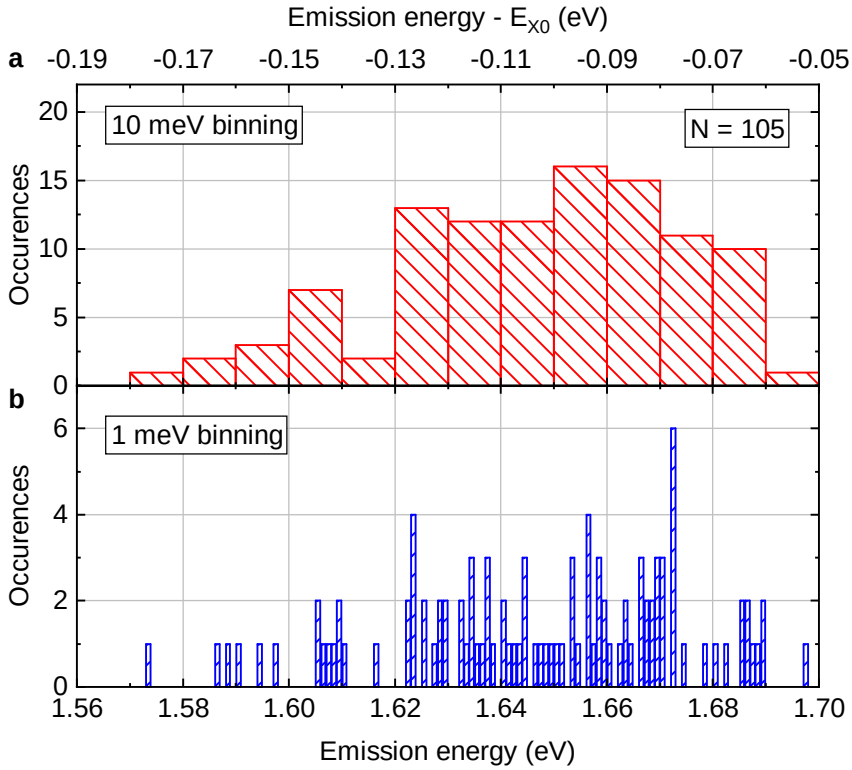

Figure 3.4: **Statistical distribution of WSe_2 emitter energies**. **(a,b)** Histogram of the emission energies of WSe_2 emitters of a single monolayer on an AlGaAs-based substrate. The two panels differ in their spectral binning. In total, 105 emitters were analyzed. The measurements were performed at $T = 10\,\mathrm{K}$.

monolayers of WSe_2 can withstand uniaxial strain of at least 1.4 %. [Sch16] None of the calculated strain values supercede this limit.

We continue by discussing the dependence of the photoluminescence on the excitation conditions, namely excitation power and excitation energy. Figure 3.5a displays typical PL spectra obtained at the same pillar site on an AlGaAs-based substrate for different excitation powers. We measured a narrower spectral range compared to the previously presented spectra in order to achieve a higher spectral resolution. The overall shape of the spectrum (number of peaks, peak positions) is mostly maintained over the two orders of magnitude in excitation power and the PL intensity increases monotonously

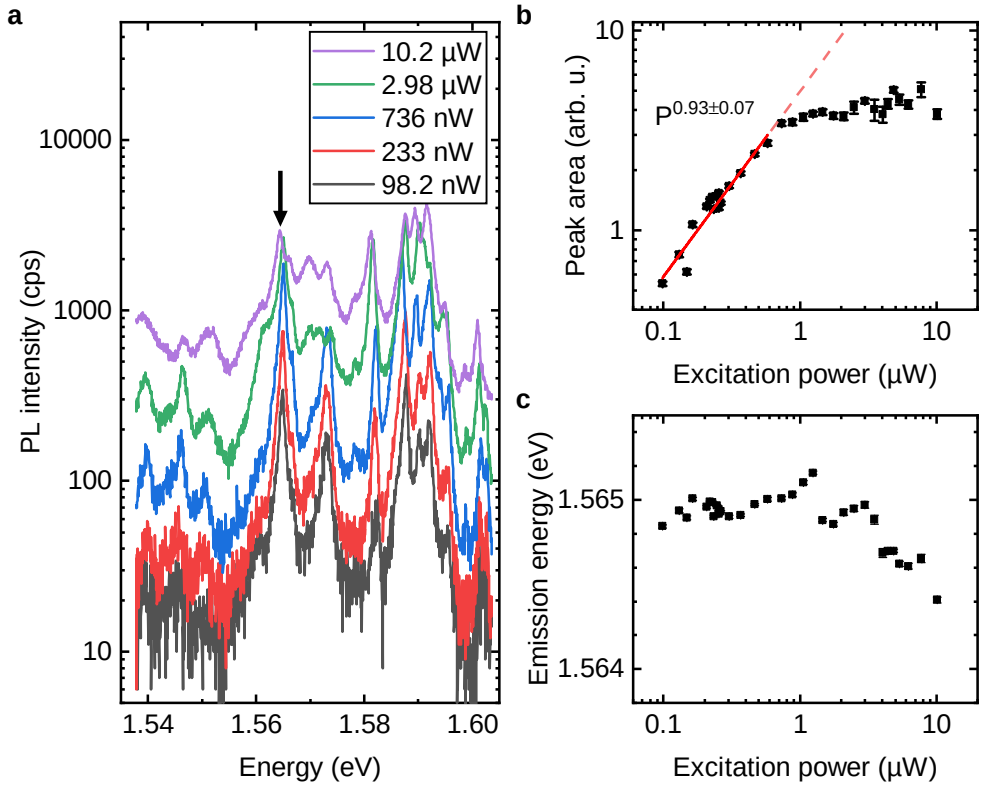

Figure 3.5: **Excitation-power-dependent photoluminescence of WSe_2 emitters.** **(a)** Photoluminescence spectra of the same WSe_2 emitter on an AlGaAs-based substrate under different excitation powers. $T = 10\,\mathrm{K}$ and $\lambda_{exc} = 633\,\mathrm{nm}$. **(b)** Photoluminescence intensity of the peak marked in panel a as a function of excitation power. The solid red line denotes a power-law fit to the low-power data. **(c)** Emission energy of the same peak as a function of excitation power. The data points in panel (b) and (c) were determined from Gaussian fits.

with the excitation power. We fit the different peaks with Gaussian functions, which reproduce the peak shape more accurately than Lorentzian functions. This is a first indication of spectral wandering on a timescale faster than our measurement frequency of 1 Hz, which will be discussed in more detail in section 3.4. We present the extracted peak intensity and emission energy for a typical peak (marked by the arrow in the figure) in Fig. 3.5b and c.

As can be seen from Fig. 3.5b, the intensity of the marked peak first increases with excitation power before it eventually saturates. We fit the low-power behavior with a power law of the form $I(P) = I_0 \cdot P^{\alpha}$. Here, P is the (unitless) excitation power, I is the PL intensity, and I_0 and the power factor α are used as fitting parameters. We find $\alpha = 0.93 \pm 0.7$. The saturation at higher powers occurs once excitons are generated at rate higher than or at least comparable to the radiative decay rate. This linear (or slightly sublinear) increase followed by saturation at higher power is the expected behavior of discrete quantum emitters [Bru94, Zre99] and is typically observed in the emitters in our samples. The emission energy of the analyzed emitter as a function of excitation power is shown in Fig. 3.5c. The energy is reduced by 0.6 meV over the examined power range. The emitters in our samples typically either exhibit similar redshifts (below 1 meV) under increased excitation powers or maintain a constant emission energy, which is independent of excitation power. Note, however, that in either case the emission energy is subject to spectral wandering, which will be discussed in more detail in section 3.4.

Several effects could drive this transition to lower energies: The high excitation power could locally heat the sample, which would reduce the local bandgap. [Var67] Assuming a similar temperature dependence as for free excitons in monolayer WSe_2, [Aro15] a temperature increase from 10 K to 19 K would suffice to reproduce the observed energy shift. Alternatively, an increasing exciton density in the direct vicinity of the trapping potential could reduce the energy of the trapped exciton via attractive interactions. [Sie17]

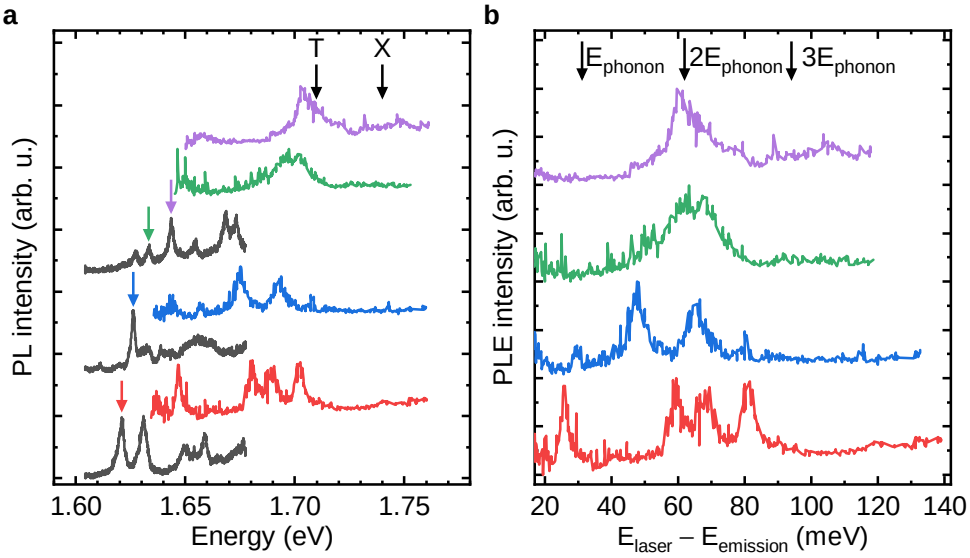

Figure 3.6: **Photoluminescence-excitation spectroscopy of individual WSe_2 emitters.** **(a)** Photoluminescence spectra (gray curves) of WSe_2 emitters at different AlGaAs pillars under excitation at 633 nm (= 1.96 eV). The colored lines represent PLE spectra of individual emission peaks, which are marked by color-matched arrows. **(b)** The PLE spectra presented in panel (a) as a function of the energy difference between excitation laser and the detected peak. All spectra were acquired at $T = 10\,\mathrm{K}$.

Using the parameters measured for free excitons in WS_2,[5] [Sie17] we estimate that moderate exciton densities of $\sim 2 \times 10^{10}\,\mathrm{cm}^{-2}$ (corresponding to a nearest-neighbor distance of $\sim 76\,\mathrm{nm}$) would amount to the observed energy shift. Strain-induced potential gradients could funnel excitons and thus result in a locally increased exciton density even at relatively low excitation powers. Overall, both, the required temperature increase and the required exciton density, could be achieved in experiments and could therefore drive the observed energy reduction.

We continue by discussing the excitation-energy dependence of the PL intensity of various WSe_2 emitters. The gray curves in Fig. 3.6a display

[5] In this system, a redshift of 20 meV was observed for an exciton density of $\sim 0.7 \times 10^{12}\,\mathrm{cm}^{-2}$. The redshift was attributed to electron-hole-pasma-induced bandgap renormalization and screening of the exciton binding energy. [Sie17]

PL spectra recorded at different WSe_2-covered pillar sites from the same AlGaAs-based sample. The presented spectra are already corrected for the substrate emission (see section A.8). We then selected individual, spectrally isolated emission peaks (marked by the colored arrows) and performed photoluminescence-excitation (PLE) measurements on them. For this, we excited the sample with a Ti:sapphire (Ti:Sa) laser, tuned its wavelength (while keeping the excitation power constant) and recorded the PL response of the examined peak. In order to filter out the excitation laser, which was spectrally close to the detected signal, we used a double monochromator with a slit between the two stages, which allowed us to detect only a selected, narrow spectral range.

The colored curves in Fig. 3.6a represent the PLE spectra recorded from the different emitters. The colors match the respective indicators above the PL spectra. We subtracted a background that resulted from detected stray laser light. All four presented PLE spectra exhibit distinct peaks with a FWHM ranging from 2.6 meV to 14 meV. Peaks in PLE spectra correspond to photon energies that are well absorbed by the material and lead to emission at the monitored energies, e.g. by intermediate relaxation of the photogenerated charge carriers into the trapping potential. These resonances appear at different energies for the different emitters. Most notably, we do not observe resonances at the energies of neutral or charged excitons (marked in the figure). This could either indicate that the exciton resonance in the vicinity of the strain maximum is detuned from the relaxed-lattice case or that there is no efficient relaxation channel from the free A exciton to the trapped states.

In Figure 3.6b, we present the same PLE spectra on a relative scale (energy difference between excitation laser and examined emitter) using the same color coding as in Fig. 3.6a. The spectra still exhibit dissimilarities. However, a clustering of PLE resonances around 60 meV above the emitter energy can be seen. It is possible that this clustering at a specific energy difference is linked to phononic or excitonic properties of the system. We marked multiples of the energy of the degenerate, Raman-active A_1 and E' phonon modes at 31 meV = 250 cm^{-1} [Sah13, Zha13a] in order to facilitate comparison with typical phonon energies. The excess energy of 60 meV can-

not be accounted for by a single phonon since single phonons in monolayer WSe_2 have energies below 40 meV. [Sah13] Instead, this energy would require a cascade of at least two phonons. An efficient PLE resonance requires that the total phonon momentum adds up to zero, which also results in a larger available phase space for multi-phonon processes compared to single-phonon processes. Such multi-phonon processes have been observed in monolayer TMDs. [Cho17, Shr18] For example, the free exciton in $MoSe_2$ features a series of PLE resonances at multiples of the $LA(M)$ phonon energy linked to strong exciton-phonon interactions. [Cho17, Shr18] However, our data lack comparable clarity.

On the other hand, if the resonances correspond to discrete excited exciton states, the energy spacing would then be an indicator for the confinement length scale. We model the strain-induced trapping potential as a two-dimensional harmonic potential, which results in the well-known solutions for the equidistant (and in most cases degenerate) energy levels:

$$E_{xy} = (n_x + n_y + 1)\,\hbar\omega + E_0 \tag{3.1}$$

Here, E_0 is the exciton energy in absence of a confinement potential. n_x and n_y are the (integer and non-negative) quantum numbers corresponding to the number of nodes of the wavefunction in x and y direction, respectively. $\hbar$ is the reduced Planck constant and the angular frequency ω can be expressed as $\frac{\hbar}{m\ell^2}$ with the particle mass m and the confinement length ℓ. With electron and hole masses $m_e = 0.39m_0$ [Jin14] and $m_h = 0.45m_0$ [Fal16] in monolayer WSe_2, the total exciton mass amounts to $0.84m_0$. If the energy difference ΔE of 60 meV corresponds to the difference between ground state and first excited state, we find $\ell = \frac{\hbar}{\sqrt{m \cdot \Delta E}} = 1.2\,\text{nm}$. Such a steep confinement potential would also affect the relative electron-hole motion. [Que92, Bai20] Of course, this simple consideration can at most give an order-of-magnitude estimate, however this value is similar to the confinement length scale we find for strain-trapped interlayer excitons ($\sim 3\,\text{nm}$) in chapter 5.

3.4 Spectral stability on different substrates

Spectral stability has been a key problem of WSe_2 emitters since their discovery. All initial reports describe spectral wandering between measurements and linewidths exceeding the lifetime limit by far. [Ton15, Sri15a, He15, Kop15, Cha15] These effects are often linked to charge fluctuations in the vicinity of emission centers. For quantum-optical experiments and applications, a high spectral stability (or in other terms: low inhomogeneous broadening) is necessary and many competing quantum emitters, such as III-V quantum dots [Kuh15, Zha20] or the SiV center in diamond, [Sip14] outperform WSe_2 in this aspect so far.

We present PL time traces of the same emitter on a HSQ substrate at different excitation powers in Fig. 3.7a. 600 PL measurements of 1 s integration time each were performed at the specified powers. The intensities were normalized separately for the three excitation powers. At all three powers, significant spectral wandering is observed between the measurements. Moreover intensity fluctuations occur; most notably, the intensity drops after $\sim$ 500 s in the center subpanel. We fitted the individual spectra with Gaussian peaks and present the extracted peak positions in Fig. 3.7b.

We found emission energies of (1612.9 ± 0.5) meV, (1610.9 ± 0.7) meV and (1610.2 ± 0.9) meV for the excitation powers of 275 nW, 1.65 µW and 12.0 µW, respectively. Here, the value corresponds to the average energy and the uncertainty denotes the standard deviation of the emission energy distribution, which is a measure of spectral wandering between measurements. Analogously to Fig. 3.5, we find a small reduction of the emission energy upon increasing the excitation power. Moreover, we observe a clear trend towards more pronounced spectral wandering for higher excitation powers. In order to obtain a more quantitative insight into the effects, we performed statistical tests, which are only rarely used in the context of solid-state physics. We explain the underlying principle of these tests in section A.7.

Testing the equality of energy variances with an F-test (which corresponds to comparing the spectral wandering in the different measurements), we found an F-value (corresponding to the ratio of variances of emission ener-

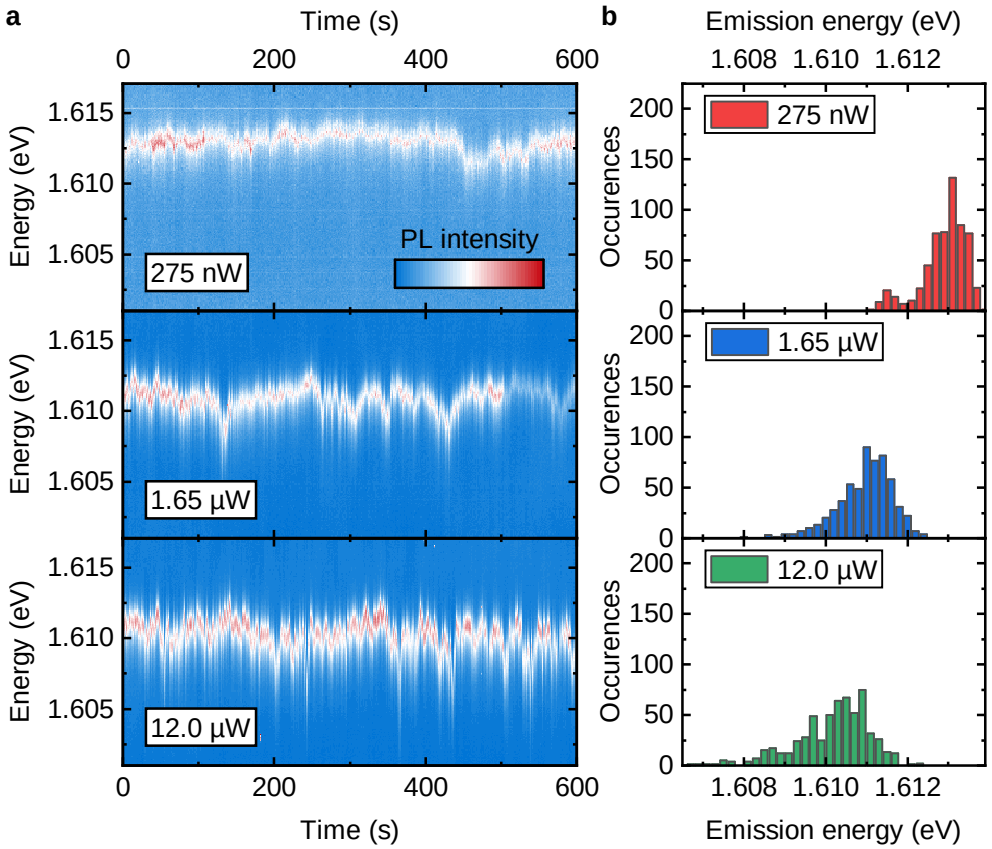

Figure 3.7: **Spectral wandering of a WSe_2 emitter under different excitation powers.** **(a)** False-color maps of PL time traces of the same WSe_2 emitter on a HSQ-based substrate for three different excitation powers. For each power, 600 measurements of 1 s integration time were performed. The color scaling is different for each panel. **(b)** Histograms of the emission energies in the time traces presented in panel (a). The energies were determined from Gaussian fits to the spectra and the histogram binning is 200 µeV.

gies) of 0.64 with an associated p-value of $6.6. \times 10^{-8}$ comparing the datasets for 275 nW and 1.65 µW and an F-value of 0.56 with an associated p-value of 1.1×10^{-12} comparing the datasets for 1.65 µW and 12.0 µW. In both cases, the low p-values indicate a vanishing probability for the observed effects to be based merely on statistical fluctuations. Generally, higher excitation powers lead to more frequent photoactivation of individual charge carriers and to a local heating of the sample. Both can result in more frequent charge-carrier trapping into and release from traps and thus promote spectral jumps of the emission. These observations illustrate the importance of controlling the excitation power when comparing the spectral stability of emitters. We therefore kept the excitation power around 100 nW for the measurements presented in the remainder of this section.

The temporal dynamics of the spectral wandering are illustrated in Fig. 3.8. There, we display the Fourier transforms of the fitted emission energies in logarithmic (a) and double-logarithmic (b) representation. The red curves are power-law fits to the data that yield power factors of -1.70 ± 0.08, -1.51 ± 0.08 and -1.21 ± 0.07 for 275 nW, 1.65 µW and 12.0 µW, respectively. These values are all relatively close to -1, i.e. a frequency dependence of $1/f$. This dependence has been identified as characteristic for charge noise in InGaAs QDs. A higher dependency, closer to -2, could also be attributed to spin noise when subject to an applied magnetic field. [Kuh13]

In the case of WSe_2 emitters, the fluctuations that induce spectral instability could occur inside the monolayer or in the substrate. For this reason, the effect of substrates on the performance of 2D materials has been studied to a great extent. Overall, hexagonal boron nitride (hBN), a wide-bandgap [Hof84] layered material, was found to be a very favorable substrate for various other 2D materials. However, it does not seem to solve the stability problems of WSe_2 emitters, as we will briefly review: As a near-ideal dielectric with few charge traps and dangling bonds, hBN was first found to improve electron mobility in graphene by an order of magnitude compared to SiO_2 substrates. [Dea10] Monolayers of TMDs also benefit from hBN substrates, with free-exciton linewidths reduced almost down to the lifetime limit. [Aja17, Cad17, Wie17]

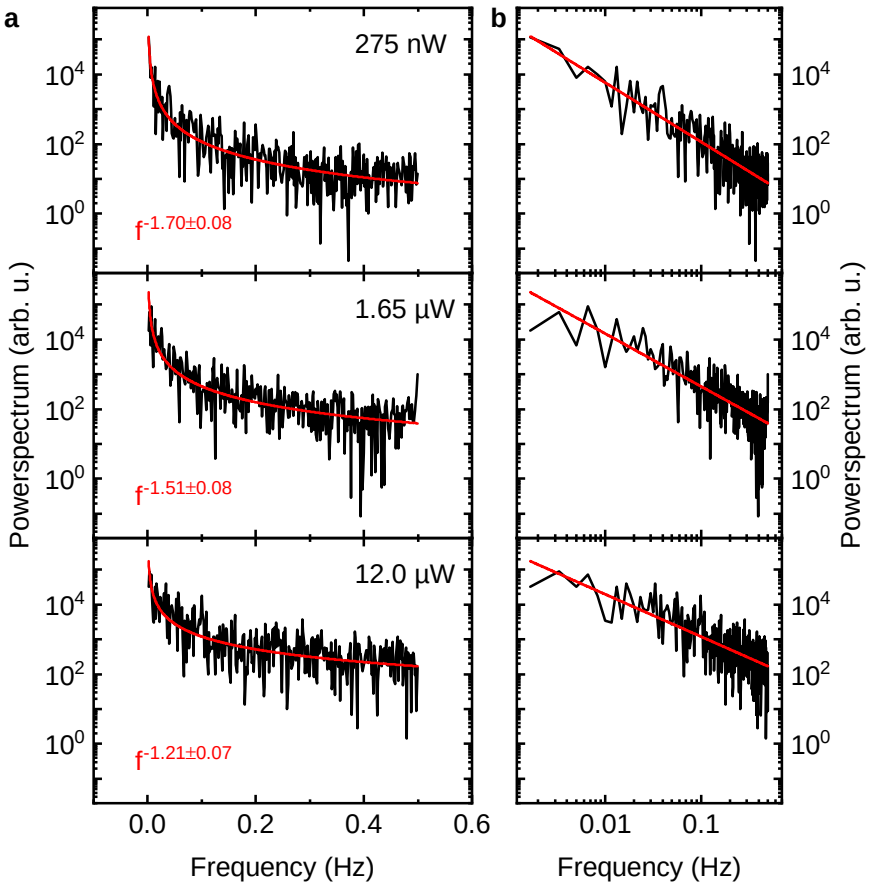

Figure 3.8: **Noise spectrum of the quantum emitter energies presented in Fig. 3.7. (a, b)** Fourier transforms of the emitter energies in the measurements shown in Fig. 3.7 on a linear (a) and logarithmic (b) frequency scale. The red curves are power-law fits. The fit results are indicated in the panels.

A beneficial effect of hBN substrates on the linewidth of WSe_2 emitters, however, has to our knowledge not been demonstrated yet. This may be a consequence of the emitter linewidths being much narrower than free excitons in WSe_2: Free excitons have a radiative lifetime in the few-picosecond range [Yan14] and correspondingly homogeneous linewidths of a few meV. [Moo15, Dey16, Wie17] The localized emitters, on the other hand, have prolonged lifetimes of some nanoseconds up to $\sim 20\,\mathrm{ns}$. Their measured linewidths (down to $\sim 100\,\mu\mathrm{eV}$) are therefore still far above the transform limit of $\sim 1\,\mu\mathrm{eV}$. [Ton15, Sri15a, He15, Kop15, Cha15, Wie19] Thus, the emission is still strongly inhomogeneously broadened. The same absolute broadening would would be much less detrimental (and even hardly notable) in free excitons. Publications using hBN as a substrate for WSe_2 do not necessarily report any linewidth reduction. [Ton15, Wie19] However, there are indications of the beneficial effects of hBN substrates: First, the measured lifetime was found to be slightly longer compared to emitters in WSe_2 on a SiO_2 substrate. [Ton15, Wie19] This is contrary to the expected effect: Since hBN has a higher photonic density of states than SiO_2 due to its larger refractive index, a faster radiative decay would be predicted. The enhanced decay rate in SiO_2 substrate must therefore be linked to additional non-radiative decay options for the emitters, which are not available on hBN substrates. [Ton15] Second, emitters forming over hBN wrinkles tend to have a relatively background-free emission spectrum, which ultimately leads to purer single-photon emission. [Dav20]

While hBN does not seem to influence WSe_2-emitter linewidth systematically, it has been demonstrated that other high-quality substrates, such as epitaxially grown $In_{0.49}Ga_{0.51}P$ can result in emitters with average linewidths of $(75 \pm 12)\,\mu\mathrm{eV}$ and spectral wandering in the few-µeV range. [Iff17] In that study, randomly occurring WSe_2 emitters on flat substrates were examined. We expanded on these experiments by studying site-selectively generated emitters on pillar substrates of different materials, namely SiO_2/HSQ and MBE-grown AlGaAs, as shown in Fig. 3.1a and b.

We present PL time traces (chosen to reflect typical behavior) of WSe_2 on HSQ-based and AlGaAs-based pillar substrates in Fig. 3.9a and c. In both

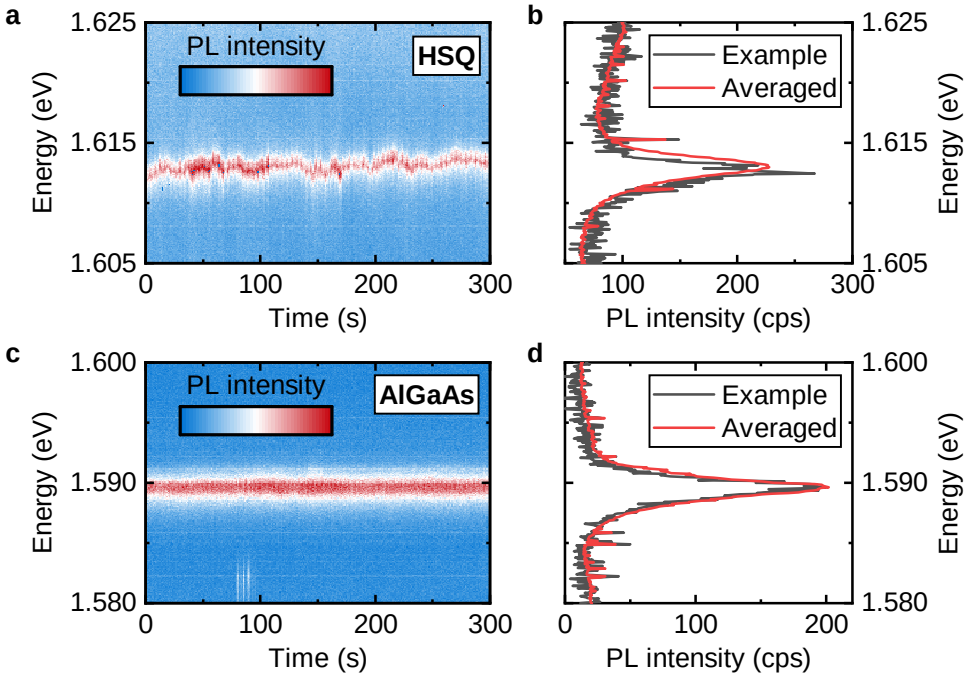

Figure 3.9: **Photoluminescence time traces of WSe_2 emitters on different substrates. (a)** False-color map of PL time trace of a typical WSe_2 emitter on a HSQ-based substrate. **(b)** First (gray) and averaged (red) PL spectrum of the data presented in panel (a). **(c)** False-color map of PL time trace of a typical WSe_2 emitter on an AlGaAs-based substrate. **(d)** First (gray) and averaged (red) PL spectrum of the data presented in panel (c).

cases, 300 measurements of 1 s integration time are displayed. The vertical axis spans 20 meV in both panels. The measurements were performed at $T = 10$ K and with a HeNe laser. The example time trace for HSQ-based samples is the first half of the dataset for 275 nW presented in Fig. 3.7a. The measurements on the AlGaAs-based sample were conducted with an excitation power of 90 nW.

While both substrates feature a single-spectrum linewidth (FWHM) of 1.5 meV, the HSQ dataset features frequent spectral jumps between measurements in a range of 1 meV, which appear to be absent for the AlGaAs sample. The AlGaAs sample still does not guarantee perfectly stable emission, as highlighted by an additional PL peak which blinks on and off shortly

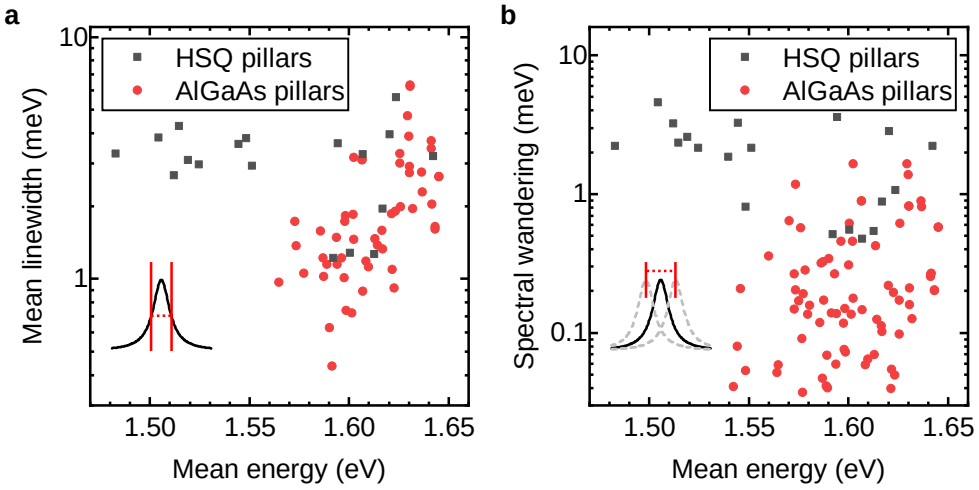

Figure 3.10: **Spectral broadening of WSe_2 emitters on different substrates. (a, b)** Mean linewidth (a) and spectral wandering (b) of WSe_2 emitters on HSQ and AlGaAs pillars. For each emitter, we fitted 300 spectra of 1 s integration time with Gaussians. The mean linewidth denotes the averaged FWHM of the fitted peaks, whereas we define the spectral wandering as the standard deviation of the peak center energies.

before 100 s. However, the individual measurements reflect the time-averaged dynamics of the system more accurately. To illustrate this, we present the first spectrum (gray) and the average spectrum (red) for both measurements in Fig. 3.7b and d. For the AlGaAs substrate, the two spectra are identical except for the different noise levels. The maxima of the example and averaged spectra for the HSQ substrate, on the other hand, are 0.6 meV (a third of the linewidth) apart.

In order to study the influence of the substrate material more systematically, we evaluated PL time traces for multiple emitters on different samples for both material systems and present the results of this analysis in Fig. 3.10. The data points shown in both panels are each based on 300 consecutive PL spectra of one emitter, each with an integration time of 1 s. The data were automatically fitted with Gaussian peaks in manually selected spectral ranges. Fig. 3.10a displays the mean linewidth of the investigated emitters against their mean emission energy. For this, we averaged the fitted FWHM over the

300 spectra. Data points, for which the peak shape was not well captured by the fit, were eliminated. The absence of low-energy emitters on AlGaAs substrates is due to substrate emission overshadowing emitter PL (see Appendix, section A.8). The HSQ-based samples resulted in emitter linewidths of (3.1 ± 1.3) meV. We observed no significant correlation between emission energy and emission linewidth with a Pearson correlation coefficient of -0.15 and a p-value of 0.56.[6] In comparison, the linewidth on AlGaAs-based substrates is reduced to (2.0 ± 1.3) meV. Here, higher emitter energies appear to be linked to higher linewidths with a Pearson correlation coefficient of 0.53 and a p-value of $4.0 \cdot 10^{-5}$. The linewidth reduction in comparison to HSQ samples is significant, based on a two-sample t-test with a Welch-corrected t-value of -3.3 and p-value of 0.0022.

Figure 3.10b depicts the spectral wandering of emitters on HSQ- and AlGaAs-based substrates. Here, we defined spectral wandering as the standard deviation of the distribution of the emission energies as determined by fits to the individual spectra. The HSQ-based samples exhibited a spectral wandering of (2.0 ± 1.2) meV. The emitters at higher energies typically exhibit slightly weaker spectral wandering, with a Pearson correlation coefficient of -0.49 and a p-value of 0.032. The spectral wandering is reduced by almost an order of magnitude to (0.32 ± 0.36) meV in AlGaAs samples. The two-sample t-test yielded a Welch-corrected t-value of -6.0 and p-value of $9.0 \cdot 10^{-6}$. Unlike in HSQ-based samples, higher emitter energies are correlated with stronger spectral wandering in the examined AlGaAs-based samples. The corresponding Pearson coefficient is 0.26 with a p-value of 0.0234.

Overall, we found that AlGaAs substrates significantly improve the spectral stability of strain-induced WSe_2 emitters compared to HSQ substrates, as seen in the linewdith and spectral wandering between measurements. Both of these quantities measure the inhomogeneous broadening. The linewidth gives insight on noise on time scales faster than the integration time, i.e. noise with frequencies above 1 Hz, whereas the spectral wandering is the result of slow, sub-Hz noise. Both quantities are reduced in the AlGaAs

[6] For an explanation of the statistical tests and quantities used here, see section A.7.

samples but this effect is much more pronounced for the spectral wandering, which indicates slow noise. This may be a result of the different natures of the prevalent sources of charge noise in the two materials: HSQ (due to its SiO_2-like structure) is expected to host discrete traps for charge carriers, [Jay89] whereas the MBE-grown AlGaAs is expected to have a greatly reduced defect density, leading to fewer local charge traps. On the other hand, AlGaAs is an optically active semiconductor, that can absorb light from the excitation sources used in our experiments to promote electrons from the valence to the conduction band. These excited carriers can relax back into the valence band, which happens on a sub-ns timescale. [Ros86] The resulting charge noise would then predominantly influence the linewidth observed in our measurements and not be seen in spectral wandering.

The different correlations between emitter energy and spectral instability for the two substrate materials are striking but the reason is not entirely clear. The energy-stability relation could be mediated by the monolayer geometry: The different emitter energies could be related to the local strain, with higher tensile strain values resulting in lower exciton energies. [Sch16] The local strain, on the other hand, can be expected to depend the position of the emitter, relative to the nanopillar. The electric fields of the different noise sources (discrete traps that are randomly charged and discharged vs. delocalized excitons being constantly pumped and randomly decaying) may decay differently with the distance from the material and therefore differently influence emitters at varying positions. However, we do not have any experimental evidence or precise calculations to support this model.

Despite the AlGaAs substrates outperforming the HSQ substrates in terms of spectral stability, various other problems that we encountered make AlGaAs an unfavorable substrate for spectroscopy studies on 2D materials. We will discuss this in detail in the appendix, in section A.8.

Besides engineering the quality of the surrounding material, another approach to emitter stabilization is the electrical control of the environment. [Kuh15, Zha20] However, even in experiments with the emitter embedded in vdW heterostructures that allow to apply electric fields, linewidths on the order of 100 µeV are reported, [Cha17, BG19] which is still well above the life-

time limit and which has also been achieved in randomly occurring emitters on a bare SiO_2 substrate. [Ton15, He15, Kop15, Sri15a] Overall, deterministic fabrication of quantum emitters with transform-limited linewidths in TMDs remains an open challenge.

3.5 Summary

In this chapter, we have discussed strain-induced, localized emitters in monolayer WSe_2. By patterning substrates with nanopillars, we introduced point-like strain perturbations in the monolayers and created associated trapping potentials for excitons. The presence of these trapping potentials is confirmed by localized emission, which is redshifted by up to 200 meV with respect to free excitons and trions, at the pillar sites. The saturating dependence on excitation power is in agreement with reports on single-photon emitters in the material. Photoluminescence-excitation measurements revealed a clustering of excitation resonances $\sim$ 60 meV above the emitter energies for multiple emitters. This energy could either be linked to a multi-phonon process or to discrete excitation levels of the trapped excitons, which would indicate a localization length of 1 nm to 2 nm, similar to the localization length of analogously trapped interlayer excitons, as we will discuss in chapter 5.

We analyzed the spectral instability of the emitters, which manifests itself in the linewidth and in spectral wandering between measurements. We found that higher excitation powers result in stronger spectral wandering, as would be expected from increased charge carrier motion inside the substrate. Illustrating the importance of the substrate material for 2D materials, we compared SiO_2 substrates (with nanopillars based on HSQ) with MBE-grown AlGaAs substrates. The high material quality of the MBE-grown substrates was found to result in a reduction of spectral wandering by almost an order of magnitude, in many cases down to our measurement resolution limit of 70 µeV.

We will apply the fabrication and measurement techniques introduced here to interlayer excitons in TMD heterobilayers in the next chapter, where we will find similar localization effects.

CHAPTER 4

Site-selective traps for interlayer excitons

In this chapter, we will demonstrate that the presence of local strain perturbations, induced by placing 2D crystals on top of a non-planar substrate with a patterned surface, does not only give rise to a localization potential for excitons in TMD monolayers, but also to interlayer excitons in TMD heterobilayers.

In analogy to the previous chapter, we will use a substrate with a grid of dielectric nanopillars. We will present photoluminescence data from a $MoSe_2$-WSe_2 heterobilayer that displays energetically reduced emission at the pillar sites. In order to pinpoint this emission to locally trapped interlayer excitons, we will present analogies between these localized features and free interlayer excitons in the dependence on excitation power and excitation energy, as well as the temporal dynamics of the emission. Further microscopic insights are provided by exploring the Zeeman splitting in an out-of-plane magnetic field and the polarization profile of the emission.

We will use the trapped interlayer excitons to study interactions within few-exciton complexes in the next chapter. The contents of this chapter follow our publication, [Kre20] which has been published under a Creative

Commons Attribute 4.0 International License.[1] Any reused material will be indicated. Many of the findings of this chapter have in the meantime been confirmed by other groups. [Li20, Wan20][2] Furthermore, related reports on strain-trapped IXs in WS_2-WSe_2 HBLs [Mon21] and work-function modulations in non-uniformly strained $MoSe_2$-WSe_2 HBLs [Ale20] have appeared since performing the work documented in this chapter.

4.1 Sample structure

Localization potentials for excitons in monolayer TMDs can be created by introducing local strain perturbations, as described in section 3.1. Tensile strain has also been shown to reduce the energy of interlayer excitons in TMD HBLs, [He16a] presenting the prospect of defining IX trapping potentials in a completely analogous way.

Besides the methods that are known to create localization potentials for excitons in monolayer materials, interlayer excitons offer additional possibilities to define exciton traps via their distinct properties: They have a permanent electric dipole moment on the order of the layer separation of the component materials ($\sim$ 7 Å). This dipole moment can be used to tune the IX energy via the DC Stark effect. [Riv15] In fact, tuning over a range of 200 meV has been demonstrated for IXs in $MoSe_2$-WSe_2-HBLs. [Jau19] Locally varying the out-of-plane electric field with suitable gate geometries can therefore create a trapping potential. This technique is routinely used for indirect excitons in III-V semiconductor heterostructures [Rap05, Ham06, Gär07, Hig09, Sch11] and has very recently been demonstrated in van der Waals heterobilayers with a patterned graphene gate. [Sha21] Another approach that is unique to van der Waals heterostructures is utilizing potentials associated with a moiré superlattice, as introduced in

[1] http://creativecommons.org/licenses/by/4.0/

[2] [Li20] is often cited as a paper on interactions of moiré-trapped IXs. However, the authors do not discuss the origin of the localization potentials in their samples. In the Methods section of the paper, it is confirmed that substrates with nanopillars were used for the work but the role of the pillars is not discussed within the main text.

section 2.4. Specifically for IXs in TMD-HBLs, this moiré superlattice is associated with a potential on the order of 100 meV. [Zha17a] In an ideal HBL, these periodic or quasi-periodic potential modulations would give rise to an array of identical quantum emitters. [Yu17] Interlayer excitons trapped in moiré potential minima have been observed [Tra19, Sey19, Jin19, Bae20] but, probably due to imperfect fabrication, the demonstration of identical emitter arrays has to our knowledge not been reported yet. An actual realization of such an emitter array would be of great benefit for e.g. quantum simulation, and first results pointing towards Hubbard physics with holes (instead of IXs) in the moiré potential have been reported. [Reg20, Tan20] We will explore moiré physics in twisted $MoSe_2$ homobilayers in chapter 6. However, the moiré superlattice by itself is not suited for *site-selective* generation of *individual* trapping potentials. We therefore chose strain-engineering as a method for a proof-of-principle demonstration of IX trapping. This approach also allows to define very steep trapping potentials, as will be discussed in the next chapter.

Our schematic sample structure is depicted in Fig. 4.1a. We place a heterobilayer of WSe_2 and $MoSe_2$ on top of dielectric nanopillars, which induce localized strain perturbations and give rise to trapping potentials for interlayer excitons, as will be discussed in the remainder of this chapter. The pillar grid (disks with 90 nm radius and 4 µm pitch) is defined via electron-beam lithography on a commercially available Si wafer overgrown with 285 nm of SiO_2. A negative resist (AR-N 7520.07) was used in order to minimize writing time. We etched the substrate (apart from the areas covered by resist disks) by 130 nm using fluorine-based reactive-ion etching (RIE) and afterwards removed residues of the resist in an oxygen plasma. Bulk crystals of WSe_2 and $MoSe_2$ were exfoliated onto polydimethylsiloxane (PDMS, Gel-Pak) stamps. We identified monolayers in an optical microscope via their reflectivity contrast and transferred the layers onto a pillar array. Each transfer step was followed by thermal annealing in vacuum (200 °C, 30 min after the WSe_2 transfer; 150 °C, 20 min after the $MoSe_2$ transfer). During the assembly of the HBL, we took efforts to orientate the crystal axes of the two materials by aligning long crystalline edges of the monolayers.

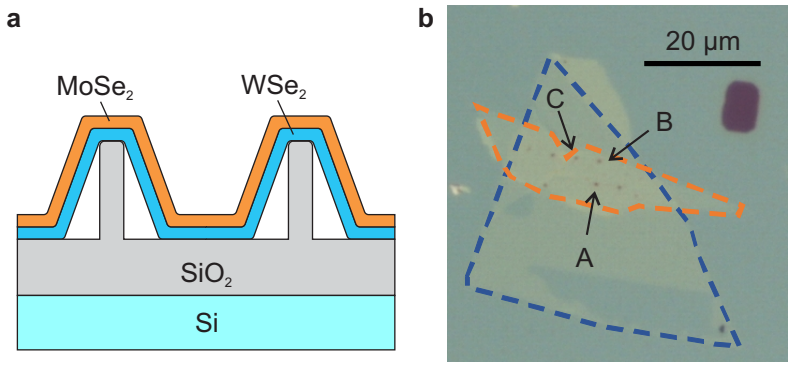

Figure 4.1: **Sample for localization of interlayer excitons in strain-defined trapping potentials. (a)** Schematic sample structure. A heterobilayer of $MoSe_2$ and WSe_2 is placed on top of a Si/SiO_2 substrate patterned with nanopillars. **(b)** Microscope image of the sample used to measure the data presented in this and the next chapter. The monolayers of WSe_2 and $MoSe_2$ are outlined with blue and orange dashed lines, respectively. The nanopillars appear as black dots in the heterobilayer region. Adapted from [Kre20].

Figure 4.1b displays a microscope image of the finished sample. The monolayers of WSe_2 and $MoSe_2$ are outlined with blue and orange dashed lines, respectively, and the nanopillars appear as black dots in the heterobilayer region. The final structure allows us to optically probe regions of unstrained monolayer WSe_2, unstrained monolayer $MoSe_2$, unstrained WSe_2-$MoSe_2$ heterobilayer and WSe_2-$MoSe_2$ heterobilayer strained over nanopillars separately.

4.2 Interlayer excitons in a $MoSe_2$-WSe_2 heterobilayer

We present low-temperature PL spectra of the unstrained monolayer and heterobilayer regions of the sample in Fig. 4.2a. These spectra were recorded at $T = 10\,\mathrm{K}$ with cw excitation at 633 nm and a power of P_{ex}=30 µW focused to $\sim 1\,\mu\mathrm{m}$. Both, WSe_2 and $MoSe_2$, have prominent emission features

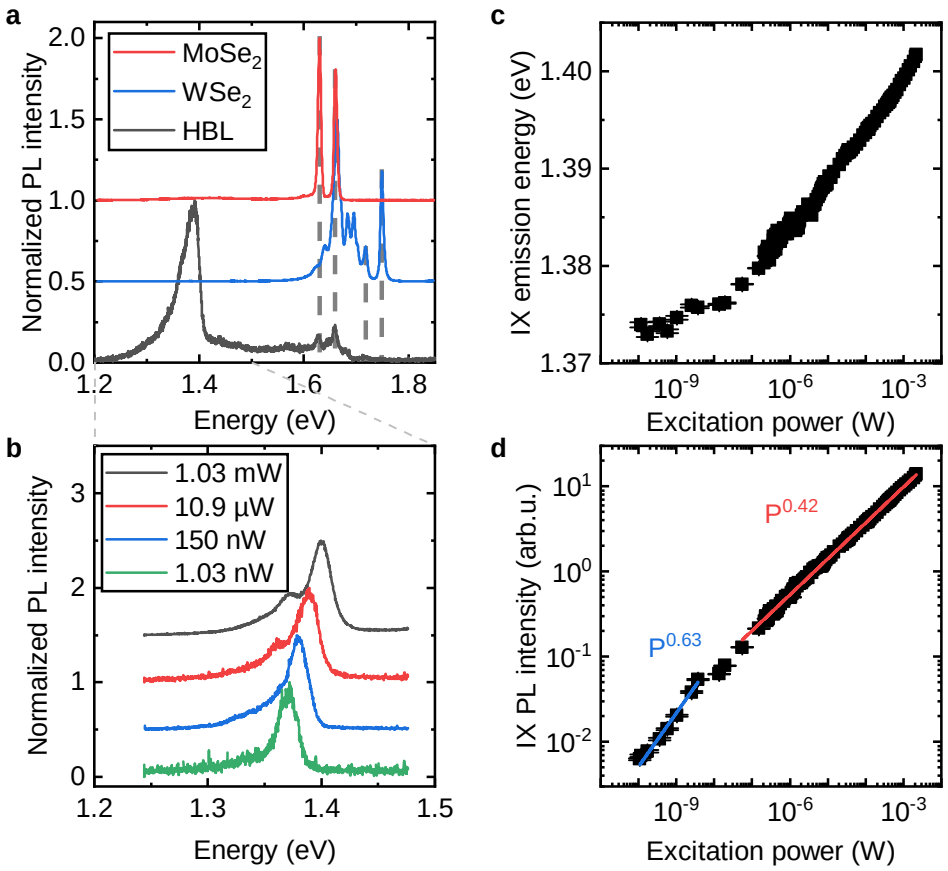

Figure 4.2: **Interlayer-exciton photoluminescence from a $MoSe_2$-WSe_2 heterobilayer. (a)** Normalized low-temperature PL spectra of monolayer $MoSe_2$, monolayer WSe_2 and a $MoSe_2$-WSe_2 heterobilayer. **(b)** Normalized IX PL emission under different excitation powers. **(c, d)** Interlayer-exciton main peak energy (c) and integrated PL intensity (d) as a function of excitation power. All spectra were acquired at $T = 10\,\mathrm{K}$ under cw excitation with a HeNe laser ($\lambda = 632.8\,\mathrm{nm}$) focused to a spot of $\sim 1\,\mu\mathrm{m}^2$. The data presented in panel (a) was recorded at an excitation power of $30\,\mu\mathrm{W}$. Adapted from [Kre20].

at their characteristic exciton and trion energies at 1.75 eV and 1.72 eV, [Jon13] and 1.66 eV and 1.63 eV, [Ros13] respectively. Furthermore, the WSe_2 monolayer exhibits a broader band of unresolved emission at lower energies ($1.60-1.70$eV) that has been identified as stemming from dark excitons [Wan17a, Zho17] and trions, [Zha17c] charged biexcitons [Che18, Ye18, Bar18, Li18, Ste18] and defect-bound excitons. [Ton13a, Zha17b] Each of these emission features is also present in the HBL region, albeit strongly quenched, due to interlayer charge transfer that occurs over sub-picosecond timescales, faster than the exciton lifetime. [Ceb14, Ceb15, Rig15] The most prominent emission feature from the HBL is at $\sim$1.38 eV and is attributed to IXs formed by an electron in the $MoSe_2$ and a hole in the WSe_2. [Riv15] This attribution is supported by the emission energy and the characteristically asymmetric lineshape featuring red-shifted emission from momentum-indirect IXs. [Mil17]

The IX emission in the HBL region is depicted for various excitation powers in Fig. 4.2b. We note a strong blueshift of the IX PL peak with increasing excitation power, which is universally reported in literature. [Riv15, Mil17, Nag17b, Riv18] In fact, this is a direct consequence of the spatial separation of electron and hole in interlayer excitons: The resulting permanent out-of-plane electrical dipole moment gives rise to repulsive interactions between IXs. As a result, the energy of an individual interlayer exciton increases with increasing IX density. In total, we varied the excitation power density by more than seven orders of magnitude and determined the spectral position of the IX main peak and its integrated PL intensity by fitting the data with two Gaussians. The extracted IX energies and intensities as a function of excitation power are displayed in Fig. 4.2c and d, respectively. As can be seen from Fig. 4.2c, the IX energy monotonously increases by almost 30 meV over the examined power range. For high excitation powers, the increase of IX energy with excitation power is approximately logarithmic, confirming previously repoted trends. [Mil17, Nag17b] This trend, however, has an onset at a threshold power of $P_0 \approx 20$ nW. In the low-exciton-density regime below this threshold power, a much weaker dependence of IX energy on the excitation power is observed. Figure 4.2d shows the IX PL intensity, as determined from

the Gaussian fits to the spectra, as a function of excitation power. We fit the dependence with a power law of the form $I(P) = I_0 \cdot P^{\alpha}$ with PL intensity I, excitation power P and fitting parameters I_0 and α. For powers above P_0, we find a power factor α of 0.42, close to a $\sqrt{P}$ dependence. This dependence is, again, in accordance with previous reports. [Mil17, Nag17b] The low-density regime below P_0 exhibits a slightly steeper increase of $\alpha = 0.63$. In conclusion, the interactions between IXs appear to influence the properties of the IX ensemble less strongly below P_0. The emission energy has only a weak dependence on excitation power and the PL intensity increases more linearly with the excitation. Above P_0, on the other hand, a strong blueshift related to dipolar repulsion is visibile and the $\sqrt{P}$-dependence of the PL intensity hints at the population dynamics being dictated by nonlinear processes, such as Auger recombination, as we will discuss now.

Assuming that excitons are generated at a rate of G and can either radiatively recombine over a characteristic timescale of τ or can undergo an Auger process with another nearby exciton with a probability proportional to the Auger constant A, the temporal evolution of the exciton density n follows: [O'H99, Hul80]

$$\frac{dn}{dt} = \frac{-n}{\tau} - An^2 + G \tag{4.1}$$

In an experiment with cw excitation (G is constant and the measurement times exceed τ by far), the exciton population will mostly be at a steady state. Setting eq. 4.1 equal to zero, we find:

$$n_{1/2} = -\frac{1}{2A\tau} \pm \sqrt{\frac{1}{4A^2\tau^2} + \frac{G}{A}} \tag{4.2}$$

Here, only the plus sign yields a positive exciton density. For low generation rates, we can expand the square-root term in a Taylor series (in terms of the dimensionless quantity $A\tau^2 G$), truncating at the linear term, and find that $n \approx \tau G$. For large generations rates, we can approximate $n \approx \sqrt{G/A}$ (up to terms independent of G or terms that decay with G). As can be seen, from these calculations, the observed $\sqrt{P}$ dependence of the IX PL signal at high powers and the transition to a stronger dependence on the

excitation power in the low-power regime could be explained by nonlinear process depopulating the excitons, such as Auger recombination. However, a clear conclusion about this power-dependence transition cannot be drawn from the available data. Other studies (typically centering around electro-optical measurements) have probed the role of nonlinear processes in TMDs more directly: Auger proceses can cause electroluminescence upconversion, as seen in MoS_2-WSe_2-HBLs [Bin19] or photoluminescence upconversion, as reported for WS_2 monolayers. [Lin20a] Moreover, they can facilitate transport of photogenerated charge carriers into regions that would normally not be accessible considering the photon energies of the optical driving. [Lin20b]

Overall, the interlayer excitons in the $MoSe_2$-WSe_2-HBL region, which we observe via their PL emission at distinctly lower energies, display exactly the previously reported and expected characteristics. In the remainder of the chapter, we will demonstrate that these IXs can be localized in strain-induced trapping potentials and discuss the similarities and differences of free and localized IXs.

4.3 Photoluminescence signatures of localized interlayer excitons

We compare the low-temperature PL spectra of the unstrained HBL and the strained HBL at different pillar sites (labelled A, B and C in accordance with Fig. 4.1b) in Fig. 4.3a. The flat HBL (black curve) features IX emission at 1.375 eV with a pronounced, broad low-energy tail, as discussed in the previous section. We also observe this PL signature at all pillar sites. This is to be expected, since the dimensions of the pillar are much smaller than the diffraction-limited probed sample area of $\sim 1\,\mu m^2$. The spectra at the pillar sites therefore always contain a background from unstrained sample regions. However, additional peaks emerge at the pillar sites. These peaks are redshifted by several tens of meV, up to 100 meV, from the IX main peak. Moreover their linewidths (down to a FWHM of 6 meV, only considering peaks shown in the figure) are distinctly lower than the linewidth of the IX

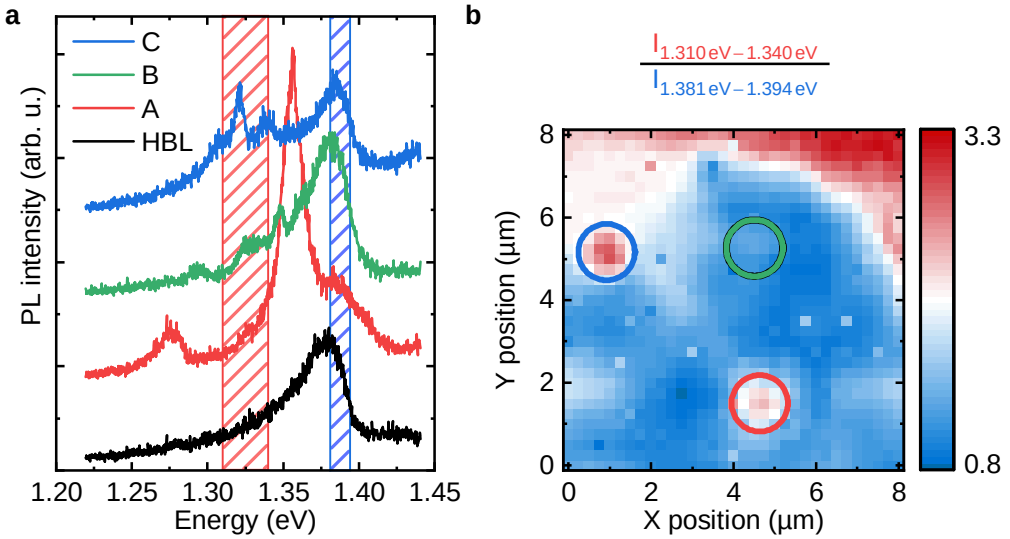

Figure 4.3: **Photoluminescence from localized interlayer-exciton states at pillar sites. (a)** Low-temperature PL spectra from the $MoSe_2$-WSe_2 region of the sample shown in Fig. 4.1b. The upper three spectra were taken at different pillar sites (labelled as in Fig. 4.1b) whereas the lowest spectrum is a reference from a flat HBL region. **(b)** Spatially resolved ratio of the integrated PL intensities in the ranges 1.310 eV to 1.340 eV (associated with localized IXs) and 1.381 eV to 1.394 eV (associated with free IXs). These spectral ranges are marked by the colored boxes in panel (a). The three pillar sites are framed by circles, color-matched to the curves in panel (a). All spectra were recorded at $T = 10\,\mathrm{K}$, under cw excitation with a HeNe laser ($\lambda = 633\,\mathrm{nm}$) with a power of $30\,\mu\mathrm{W}$ focused to an area of $\sim 1\,\mu\mathrm{m}^2$. Adapted from [Kre20].

main peak (FWHM of 20 meV). These observations are very similar to the localized excitons in monolayer WSe_2 trapped in strain-defined potentials, [Kum15, Bra17, PB17] which we discussed in the previous chapter. Analogously, we attribute these peaks to localized interlayer excitons (LIXs). The exact energies of the LIXs vary between the pillars, as is already known from strain-induced quantum emitters in WSe_2, [Bra17, PB17] and are altered by thermal cycling (see section A.9). Therefore, even spectra from the same pillar may not quantitatively agree over different figures. We will however only present LIX data from the same set of measurements within individual figures.

The spatially resolved ratio of integrated PL intensities in the ranges 1.310 eV to 1.340 eV and 1.381 eV to 1.394 eV is depicted in Fig. 4.3b. These two ranges, which we also marked in Fig. 4.3a, are associated with localized and free-IX emission, respectively. The three pillar sites are framed by circles (color-matched to the data curves in Fig. 4.3a). We note a local increase of the intensity ratio around the pillars, indicating favored emission in the LIX spectral range. In the flat HBL region, this ratio is mostly uniform, staying at a lower value. The regions of increased intensity ratio in the upper half of the figure are due to transitions to regions with no $MoSe_2$ or only bilayer $MoSe_2$ present, i.e. the emission cannot be attributed to a $MoSe_2$-WSe_2 HBL anymore. The spatial extent of the PL features at the pillar site corresponds to the diffraction-limited resolution of our setup ($\sim$ 1 µm), indicative of a point-like emission source. This demonstrates the *localized* nature of the LIX peaks.

The experimental results presented in the following will mostly showcase analogous behavior of the LIX peaks and free-IX emission, substantiating our assignment of the LIX peaks as trapped *interlayer* excitons (and in particular excluding deep defect states within *one* of the monolayers as a possible cause of the emission).

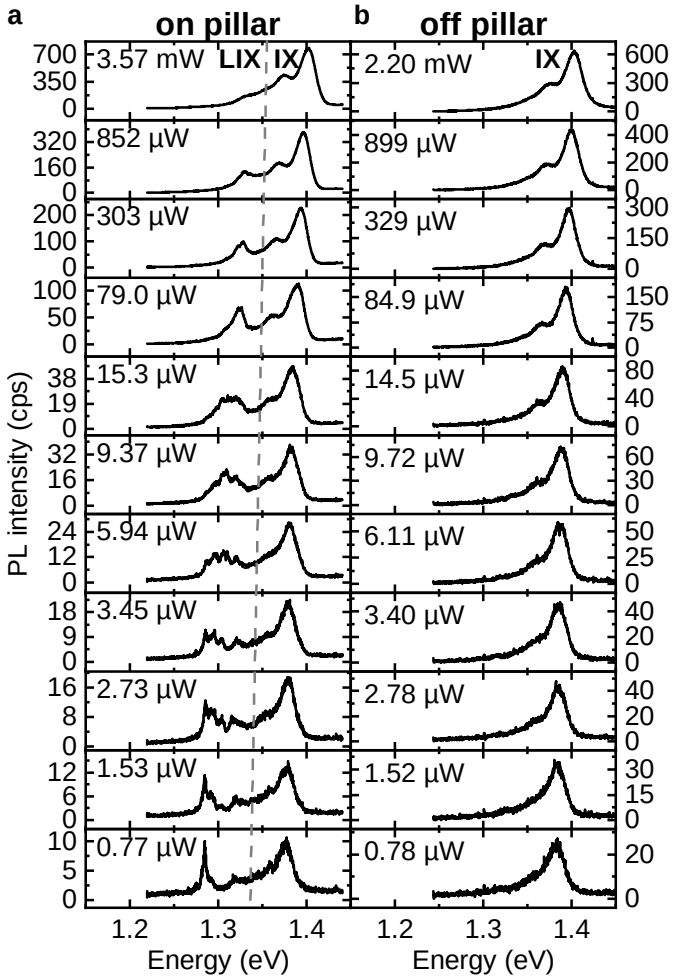

Figure 4.4: **Excitation-power dependence of free and localized interlayer-exciton emission. (a, b)** Interlayer-exciton PL spectra at pillar site A (a) and at a flat reference position (b). All spectra were recorded at $T = 10\,\mathrm{K}$, under cw excitation with a HeNe laser ($\lambda = 633\,\mathrm{nm}$) focused to an area of $\sim 1\,\mu\mathrm{m}^2$. Adapted from [Kre20].

4.3.1 Excitation-power dependence

We present PL spectra over more than three orders of magnitude of excitation power in Fig. 4.4a (at pillar site A) and Fig. 4.4b (flat reference position). In both cases, the free-IX peak can be seen clearly. At the lowest powers, the emission is centered around 1.375 eV but it blueshifts by 25 meV over the displayed excitation power range. Only small differences between the free IX emission on the pillar and at the reference position are visible. Again, this strong resemblance of the free-IX signatures is expected since the probed sample volume (limited by the resolution of our setup, $\sim 1\,\mu m^2$) is much larger than the extent of the strain-induced trapping potential.

In contrast to the free-IX peak, the LIX signatures *individually* do not spectrally shift under changes of the excitaiton-power density. For example, the strong LIX peak seen at the lowest excitation power, centered at 1.285 eV remains at that energy over the entire excitation-power range over which it is observable. However, as the excitation power is increased, new LIX peaks emerge at higher energies compared to the ones previously present. At the same time, the overall LIX emission intensity is redistributed towards the higher-energy peaks. We interpret these contrasting behaviors of the *continuously* shifting free-IX peak and the *discrete* spectral jumps of the LIX emission as a result of the spatial extent of the LIX confinement potential: The free IX are distributed over an extended plane, in which the exciton density can be tuned continuously. The discrete energy shifts of the LIX emission correspond to individual excitons being added to a nanoscale confinement potential. A more thorough analysis of numbers of excitons contributing to certain emission peaks and a discussion of the confinement length scale will be given in the next chapter.

We calculate the spectral centers of mass of the free-IX and the LIX emission in order to compare their spectral shifts upon excitation-power variation. Our analysis procedure is illustrated in Fig. 4.5a: We fit the PL spectra at the pillar position outside the LIX spectral range. This fitting region is indicated in the figure by the gray background. We use three Gaussians to fit each spectrum. We have confirmed that this model reproduces the off-pillar spectra,

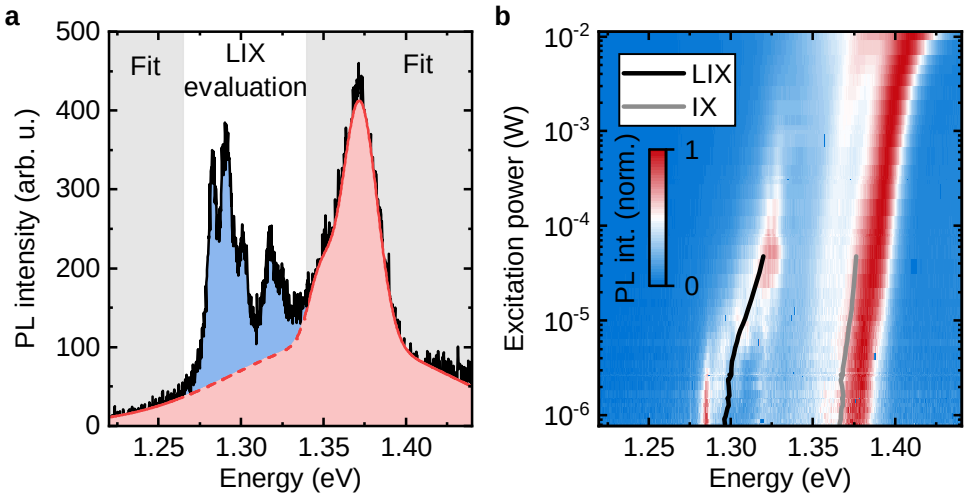

Figure 4.5: **Spectral centers of mass of free and localized interlayer exciton emission under different excitation powers.** **(a)** Example PL spectrum at pillar site A to illustrate the fitting procedure and calculation of spectral center of mass, as described in the text. **(b)** False-color plot of the normalized, excitation-dependent PL spectra at the pillar site. The overlayed solid lines indicate the calculated spectral centers of mass. This figure is based on the same dataset as Fig. 4.4a. Adapted from [Kre20].

which should only be governed by free-IX emission, even when restricting the fitting range analogously. Therefore, this fitting procedure is expected to predict the free-IX emission within the LIX spectral range, as indicated by the red dashed line in Fig. 4.5a. Everything that is not accounted for by the fit is attributed to LIX emission, as indicated by the blue area in the figure. We then determine the spectral center of mass for the LIX arithmetically from these remaining data, whereas it is extracted from the fit for the free IXs. Figure 4.5b contains a false-color plot of power-dependent, intensity-normalized emission spectra at pillar A (same dataset on which Fig. 4.4a is based) with the centers of mass for LIX and free IX overlayed for nearly two orders of magnitude of excitation power. Both exhibit a similar, increasing trend for higher excitation powers but the shift is more pronounced for the LIXs. This is to be expected since a confinement potential would drive

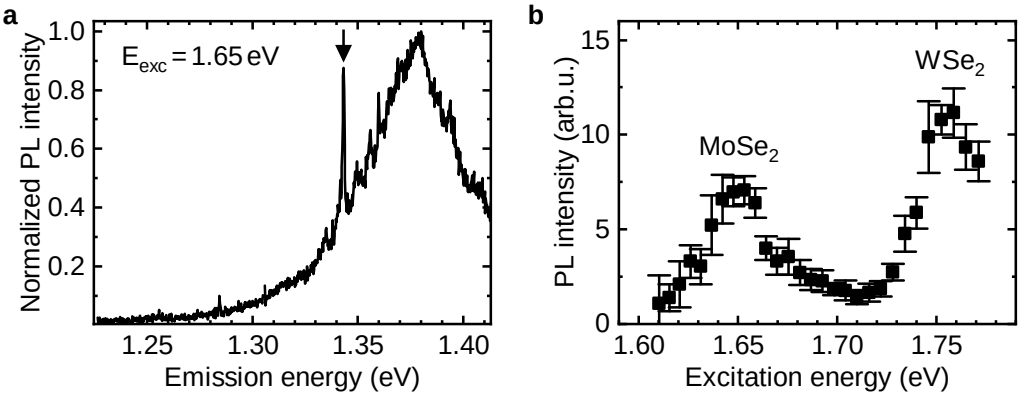

Figure 4.6: **Photoluminescence-excitation spectroscopy of localized interlayer excitons. (a)** Emission spectrum at pillar site A under cw excitation at an excitation energy of 1.65 eV. **(b)** PL intensity of the LIX peak marked in panel (a) as a function of excitation energy. All spectra were recorded at $T = 10\,\mathrm{K}$, under cw excitation with a tunable Ti:Sa laser at a power of 1 µW focused to an area of $\sim 1\,\mu\mathrm{m}^2$. Adapted from [Kre20].

the repulsively interacting particles towards each other, thus increasing the exciton density and the interaction energy.

4.3.2 Excitation-energy dependence

We performed photoluminescence-excitation (PLE) measurements, in which the wavelength/energy of the excitation laser is tuned, on the LIX peaks. Again, there is a clear consensus of the behavior of free IX in the literature: Interlayer excitons in HBLs of $MoSe_2$ and WSe_2 exhibit clear PLE resonances in the spectral range of free excitons of their component monolayers: $\sim$ 1.65 eV for $MoSe_2$ and $\sim$ 1.75 eV for WSe_2. [Riv15, Nag17b, Riv18, Sey19] At these resonances, photons are efficiently absorbed to create excitons within the respective layer. This is followed by rapid tunneling of one charge carrier (hole in the case of $MoSe_2$, electron in the case of WSe_2) into the other material, caused by the type-II band alignment. [Ceb14, Ceb15, Rig15]

Figure 4.6a displays an example spectrum recorded at pillar A with a pronounced LIX peak marked by an arrow. The excitation energy used to

record that particular spectrum was 1.65 eV, in resonance with $MoSe_2$ excitons. We monitored the PL intensity of the marked LIX peak as a function of excitation energy (keeping the excitation power constant at 1 µW), which is presented in Fig. 4.6b. Most notably, only negligible signal is present for energies below the $MoSe_2$ resonance. The intensity increases for higher energies with very pronounced resonances at the monolayer exciton energies at 1.65 eV and 1.75 eV. This behavior is in complete analogy to free IXs, supporting our interpretation of the localized peaks as stemming from trapped interlayer excitons (as opposed to deep, defect-bound states within one of the materials). We performed PLE measurements for multiple LIX peaks and generally observed this dependence.

4.3.3 Time-resolved photoluminescence

Interlayer excitons display much longer radiative lifetimes than intralayer excitons (which recombine over $\sim$ 2 ps [Rob16, Yan14, Wan14]) due to the strongly reduced wavefunction overlap of electron and hole. This effect may even be enhanced by a momentum mismatch between the two charge carriers induced by the twist angle between the two layers. [Nay17, Riv18] Due to this twist-angle dependence (and possible sample inhomogeneities and imperfections) a large range of lifetimes spanning between a few ns [Riv15] and more than 100 ns [Mil17, Nag17b] has been reported.

Figure 4.7a depicts the PL emission at pillar site A at $T = 10$ K under pulsed excitation at 640 nm, with 90 ps pulse length, 2.5 MHz repetition rate and a pulse energy of 17.2 pJ (cw power equivalent of 43 µW). This power was chosen such that there would be a high ratio of LIX emission to free-IX background over a spectral range that can be reliably selected using optical bandpass filters. A band of multiple, partially resolved LIX features between $\sim$ 1.32 eV and $\sim$ 1.36 eV is clearly distinguishable from the free-IX background. A reference spectrum from a flat part of the HBL is depicted in Fig. 4.7b. We selected luminescence from spectral ranges associated with LIXs (around 1.33 eV, red area in Fig. 4.7a, green area in Fig. 4.7b) and free IXs (around 1.39 eV, blue area in Fig. 4.7a, purple area in Fig. 4.7b) using

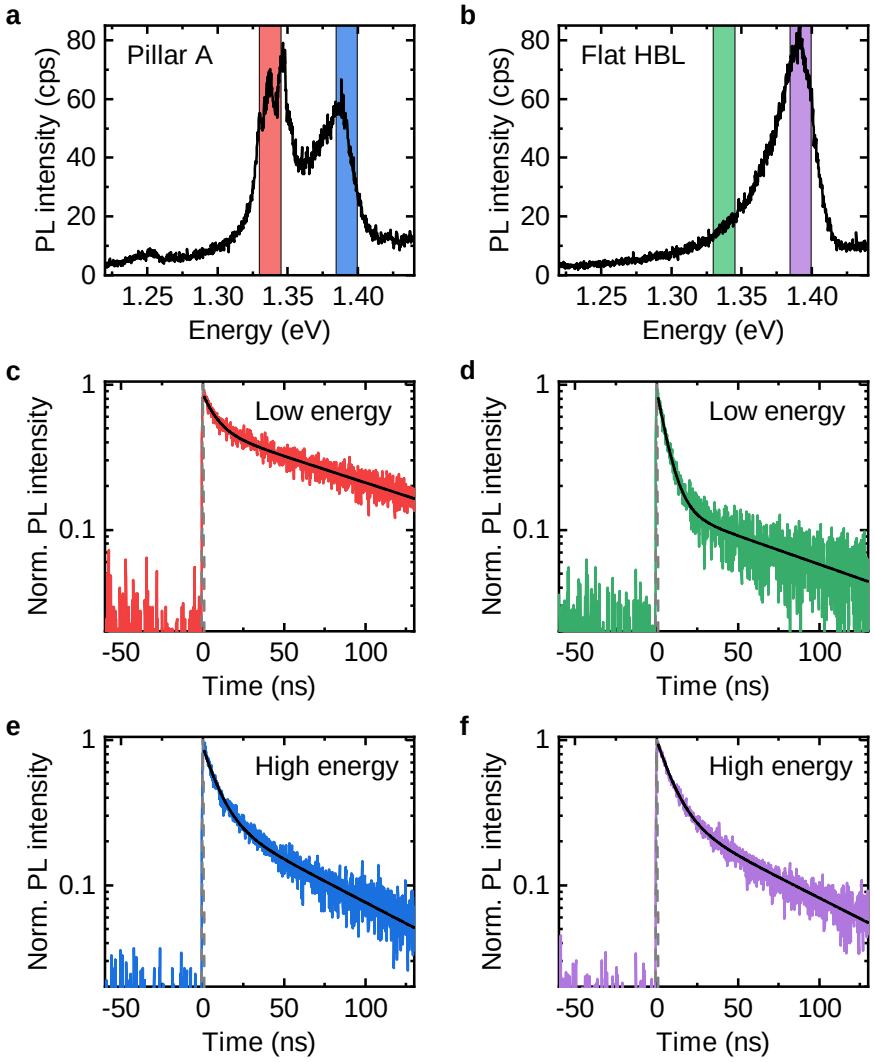

Figure 4.7: **Time-resolved photoluminescence of free and localized interlayer excitons. (a, b)** PL spectra at pillar A (a) and a flat HBL reference position (b) under pulsed excitation (90 ps pulses at 640 nm with a pulse energy of 17.2 pJ and 2.5 MHz repition rate). **(c-f)** Time-resolved photoluminescence at different sample positions and spectral ranges. The colors of the curves match the spectral indicators in panels (a) and (b). The gray dashed lines denote the instrument response (which is hardly visible over the displayed timescale) and the black solid lines represent biexponential fits to the data. Adapted from [Kre20].

Position	Pillar A		Flat HBL	
Spectral range	Low (LIX)	High (IX)	Low (LIX)	High (IX)
Slow timescale (ns)	118.8 ± 2.1	74.5 ± 1.5	111 ± 4	76.5 ± 1.4
Slow proportion (%)	95 ± 3	80 ± 3	76 ± 5	78 ± 3
Fast timescale (ns)	8.1 ± 0.5	9.0 ± 0.3	6.16 ± 0.12	9.48 ± 0.16
Fast proportion (%)	5 ± 3	20 ± 3	24 ± 5	22 ± 3

Table 4.1: Parameters extracted from biexponential fits to the time-resolved PL data presented in Fig. 4.7. The fitted model $I(t) = A_{slow}e^{-t/\tau_{slow}} + A_{fast}e^{-t/\tau_{fast}}$ directly includes the slow/fast timescale $\tau_{slow/fast}$. The slow/fast proportion is calculated as $\frac{A_{slow/fast}\cdot\tau_{slow/fast}}{A_{slow}\cdot\tau_{slow}+A_{fast}\cdot\tau_{fast}}$. Adapted from [Kre20].

suitable filters (Thorlabs FB930-10 / FB890-10; Center wavelength: 930 nm / 890 nm; Transmission FWHM: 10 nm).

We present the time-resolved response in these spectral ranges for the two sample positions in Fig. 4.7c-f, where we match the data color coding with the spectral indicators in Fig. 4.7a and b. In all four graphs, the instrument response is denoted by a gray dashed curve. We fit the data with a biexponential decay of the form $I(t) = A_{slow}e^{-t/\tau_{slow}} + A_{fast}e^{-t/\tau_{fast}}$. The fitted time-dependeces are represented by solid black lines. In all four cases, this fit function captures the signal decay over the measured 130 ns fairly well.

The parameters extracted from the fits are summarized in Table 4.1. Instead of giving the direct fit parameter of the fast/slow amplitude, we calculate what proportion of the signal belongs to the fast or the slow decay. The slow/fast proportion is calculated as $\frac{A_{slow/fast}\cdot\tau_{slow/fast}}{A_{slow}\cdot\tau_{slow}+A_{fast}\cdot\tau_{fast}}$.

The time dependence of the free-IX part of the signal is described by the same set of parameters (within the uncertainties) at the pillar site and at the reference position. Again, this is to be expected, since even at the pillar site, a large part of our probed sample volume corresponds to the unstrained HBL. The time-dependent signal decay within the LIX spectral range looks different at the pillar site and at the reference position, at first glance. However, the fits reveal very similar decay timescales: In both cases

a quick decay over ~ 7 ns is followed by a long decay over ~ 115 ns. The two curves only appear very different because the slow decay accounts for most of the signal (95%) at the pillar position whereas only 74% of the signal at the reference position stem from the slow decay channel.

The presence of several decay channels with different timescales could indicate nonlinear mechanisms, e.g. density-dependent Auger recombination. However, no definite conclusions about these non-linear dynamics can be drawn from the dataset presented here. Additional measurements, such as time-resolved PL measurements for different pulse energies, would have to be performed. Nonetheless, the very similar timescales for free-IX and LIX decay again substantiate our original assignment of the LIX peaks as stemming from trapped interlayer excitons.

4.3.4 Polarization profile of the emitted light

Many localized excitons in semiconductor nanostructures, including III-V quantum dots [Gam96, Fin02, Bay02] and quantum emitters in WSe_2, [He15, Cha15, Sri15a] exhibit fine-structure splitting of the exciton emission. This usually reflects asymmetries in the confinement potential and is mediated by the electron-hole exchange interaction. [Bay02] As a result, two energetically slightly detuned emission lines with perpendicular linear polarization can be detected.

We typically do not observe such fine-structure doublets in the LIX emission. We present LIX PL spectra with perpendicular detection polarizations in Fig. 4.8a. We show the polarization profile for each of the marked LIX peaks in Fig. 4.8b-d. While each of the peaks exhibits preferential orientation of the polarization in some direction, we do not observe a full linear polarization for any of the peaks: The highest degree of polarization (DOP) is at merely 68 %. More importantly, we could not find two lines with perpendicular orientation to each other, which could be considered a fine-structure doublet.

It should be noted that due to the sample geometry (HBL forming a tent over the pillar) we probably do not probe the material in normal incidence.

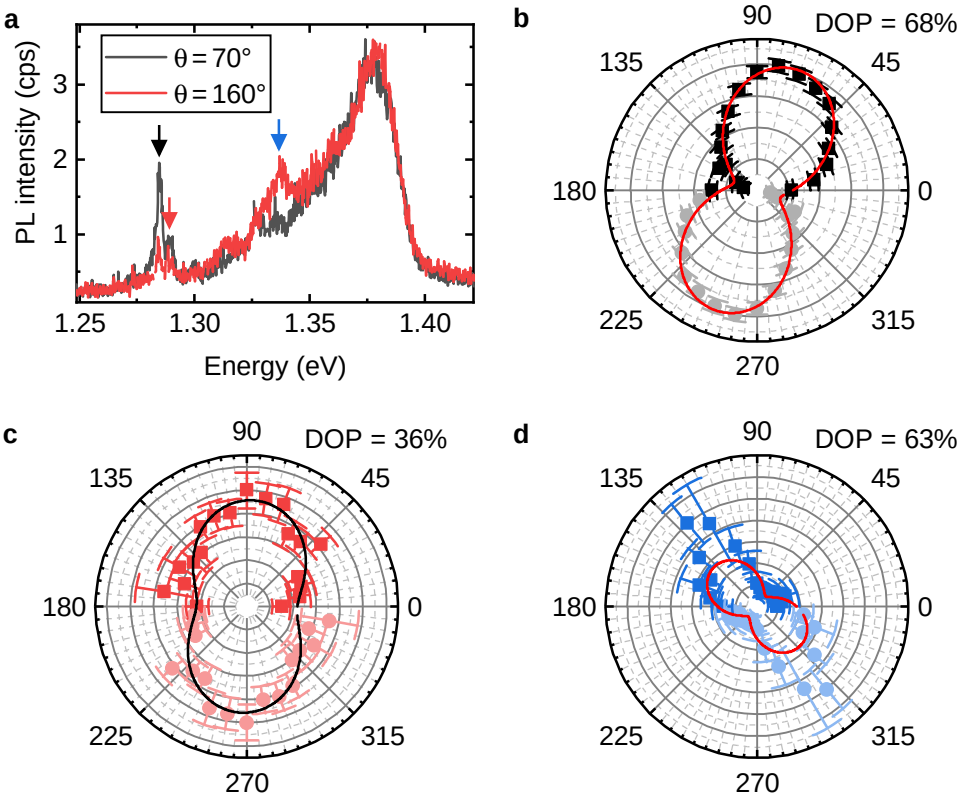

Figure 4.8: **Linear-polarization dependence of the LIX emission. (a)** Photoluminescence spectrum at a pillar site for two perpendicular polarizations. **(b-d)** Dependence of the LIX peaks marked in panel (a) on the angle of the detected polarization. The faint points are mirrored from the actual dataset as a guide to the eye. The solid lines are fits to the data from which the degree of polarization is extracted. Adapted from [Kre20].

Nonetheless, the absence of any exciton fine structure stands in clear contrast to the observations in localized emitters in WSe_2. In fact, this may again be traced back to the interlayer character of the emission lines: The spatial separation of electron and hole should strongly reduce the electron-hole exchange interaction and thus also fine-structure splitting.

4.3.5 Zeeman splitting in an out-of-plane magnetic field

In order to study the orbital contributions to the LIX states, we performed magneto-PL measurements in Faraday geometry (magnetic field in out-of-plane direction) and studied the observed Zeeman splitting. Fig. 4.9a depicts the polarization-resolved PL emission from an example LIX peak (the single localized interlayer exciton LIX_1, which will be discussed in the next chapter) as the magnetic field increases from 0 T to 8 T. The peak clearly splits into an oppositely circularly polarized doublet at elevated magnetic fields. Fig. 4.9b presents the Zeeman splitting of these peaks as function of the magnetic field. This was evaluated from spectra acquired without polarization filtering to counteract spectral wandering between measurements. Due to the linewidth of $\sim 600\,\mu eV$, the splitting is only clearly visible at $B \gtrsim 2\,T$. The linear fit to the data, shown as a red line in the figure, yields a g factor of -6.43 ± 0.13. This g factor differs from values reported for the Zeeman splitting of interlayer excitons in WSe_2-$MoSe_2$-HBLs [Sey19, Nag17a] and thus strongly suggests different orbital or spin contributions to the trapped states. This is akin to quantum emitters in monolayer WSe_2 [He15, Sri15a, Kop15, Cha15] that also do not share their g factor with free WSe_2 excitons or trions. [Sri15b, Wan15a, Mit15] There, intervalley defect states have been proposed as the origin of this behavior. [Lin19]

The lower panel of fig. 4.9c displays the polarization-resolved emission from pillar A over a wider spectral range at $B = 4\,T$. It can be seen that several features within the detection volume display the same Zeeman splitting behavior as the previously discussed LIX_1 peak. This included localized bi- and triexciton states (as will be discussed in the next chapter) as well as other peaks that most likely stem from other proximal potential traps. We

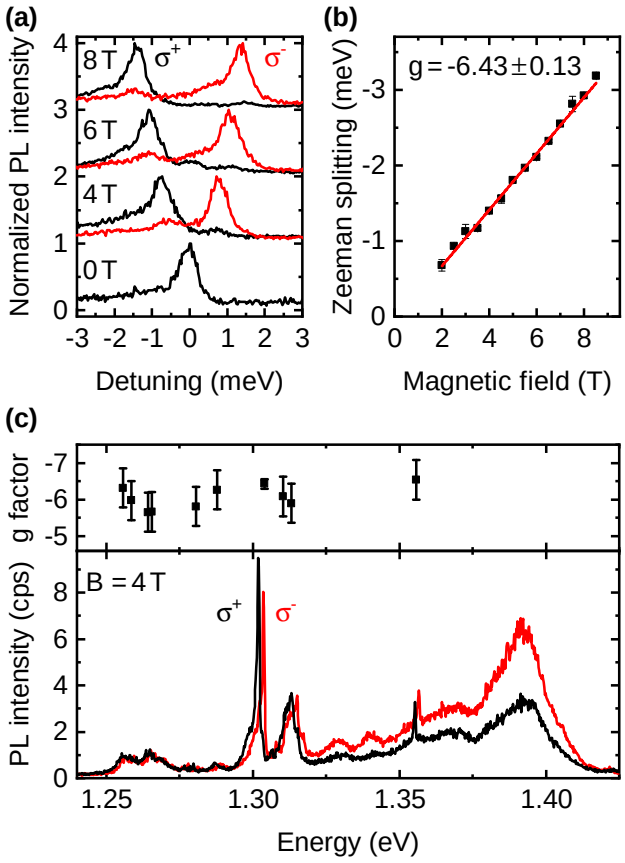

Figure 4.9: **Zeeman splitting of the LIX emission in an out-of-plane magnetic field.** **(a)** PL spectra of an LIX peak for different magnetic fields and different circular detection polarizations. **(b)** Zeeman splitting of the LIX peak presented in panel (a) as a function of magnetic field. The solid line depicts a linear fit yielding a g-factor of -6.43 ± 0.13. **(c)** Lower panel: PL spectra at pillar site A for the two perpendicular circular detection polarizations. Upper panel: Extracted g-factors for different LIX peaks observed at pillar site A.

evaluated the g-factors of the features with linewidths below 1.5 meV and present them in the upper panel of fig. 4.9c. Within the statistical errors, the g-factors of all ten features overlap. This strongly hints at a shared orbital origin of all of these localized states. Moreover, our data do not indicate magnetic-field-induced mixing of orbital states, suggesting that the orbital energy splitting of the trapped states exceeds the magnetic energies in our experiment.

4.4 Summary

In this chapter, we have demonstrated that nanoscale patterning of substrates can be utilized in order to trap interlayer excitons in TMD hetero-bilayers in strain-defined confinement potentials. Localized, spectrally narrow features, red-shifted by up to 100 meV from the free-IX emission emerge at the pillar sites in low-temperature photoluminescence measurements. The interlayer character of these localized emitters becomes apparent in excitation-power-dependent measurements, PLE spectroscopy, time-resolved and polarization-resolved measurements: Upon increasing excitation power, the LIX emission monotonously blueshifts because of repulsive dipolar interaction, as is known from free IXs. In contrast to free IXs, this blueshift does not happen continuously but via discrete spectral jumps. This is due to discrete changes in the trapping-potential occupation as opposed to the quasi-continuous tuning of the IX density in an extended HBL. In excitation-energy-dependent measurements, the LIXs exhibit clear resonances at the $MoSe_2$ and WSe_2 exciton energies, as known for free IXs. The radiative decay timescales ((118.8 ± 2.1) ns and (8.1 ± 0.5) ns) observed in time-resolved PL measurements also coincide with the ones measured for free IXs. Finally, the absence of any fine-structure splitting, as would have been observed in polarization-resolved measurements, stands in clear contrast to localized emitters that reside in only one TMD layer and can be explained by the reduced electron-hole exchange interaction in spatially separated excitons. However, the g-factors around -6 that were determined via magnetic-field-dependent PL measure-

ments do not match the commonly reported values for IXs in $MoSe_2$-WSe_2-HBLs. This strongly suggests that the orbital contributions to the LIX states differ from the previously reported free IXs.

In the following chapter, we will utilize the strain-induced trapping potentials in order to stabilize complexes of a few interlayer excitons that would otherwise dissociate. This enables us to study the energy scales involved in both, direct and exchange dipolar interactions between multiple LIXs. Moreover, we will obtain insight into the steepness of the induced confinement potential.

CHAPTER 5

Discrete interactions between localized interlayer excitons

In this chapter, we will discuss the interactions between interlayer excitons in a $MoSe_2$-WSe_2 HBL localized within a strain-defined potential. Confining the IXs to a nano-scale volume enhances interaction effects drastically, giving rise to a substantial interaction energy of several meV even for only two IXs present. We will first demonstrate that excitation-power-dependent PL measurements enable us to differentiate between emission from states with different numbers of IXs (N_{IX}) present in the confinement potential. Specifically, we will identify emission from single excitons ($N_{IX} = 1$) up to quintexcitons ($N_{IX} = 5$). This allows us to directly measure the hierarchy of dipolar interactions between localized dipolar excitons in a common trapping potential. We find that the energy cost to add one IX to the trap increases with the number of IXs already present in the trapping potential and compare the numerical values to predictions based on a model of point dipoles in a harmonic trapping potential. Moreover, we observe that some states energetically split into a doublet. We interpret the observed splitting of the localized biexciton ($N_{IX} = 2$) in terms of exchange interaction between

the two constituent excitons and reproduce the observed value via numerical modeling using realistic material parameters.

Comparing the observed energy scales with theoretical models, we find that the particular trapping potential we examine in this chapter is characterized by a confinement length of only a few nm. The strong interaction energies we observe in this chapter render interlayer excitons in TMD-HBLs a promising system for the realization of exotic quantum phases of matter, quantum simulation or nonlinear optical elements. The contents of this chapter follow our publication on the topic, [Kre20] which has been published under a Creative Commons Attribute 4.0 International License.[1] Any reused material will be indicated. Many of the findings of this chapter have in the meantime been confirmed by another group. [Li20]

5.1 Identifying few-exciton states in optical spectroscopy

We have discussed the excitation-power dependence of LIX emission already in section 4.3.1. There, we found that discrete spectral jumps to higher emission energies occur upon increasing the excitation power. We interpreted this as individual IXs being added to the trap, which results in a blueshift due to the repulsive dipolar interactions between the LIXs. In order to verify this hypothesis and give a more quantitative analysis of this phenomenon, we shift our attention to a specific dataset recorded at pillar A, which features only a small emission background from free IXs. (Note that thermal cycling can result in spectral shifts of the LIX emission; hence the energy mismatch between data presented in this and the previous chapter.)

Figure 5.1a displays LIX emission spectra for different excitation powers. These spectra were acquired in a different measurement setup, compared to the data presented in the previous chapter (apart from section 4.3.5) In particular, the temperature was 4 K, the excitation wavelength was 532 nm and the excitation spot was defocused due to the chromatic aberration of the

[1] http://creativecommons.org/licenses/by/4.0/

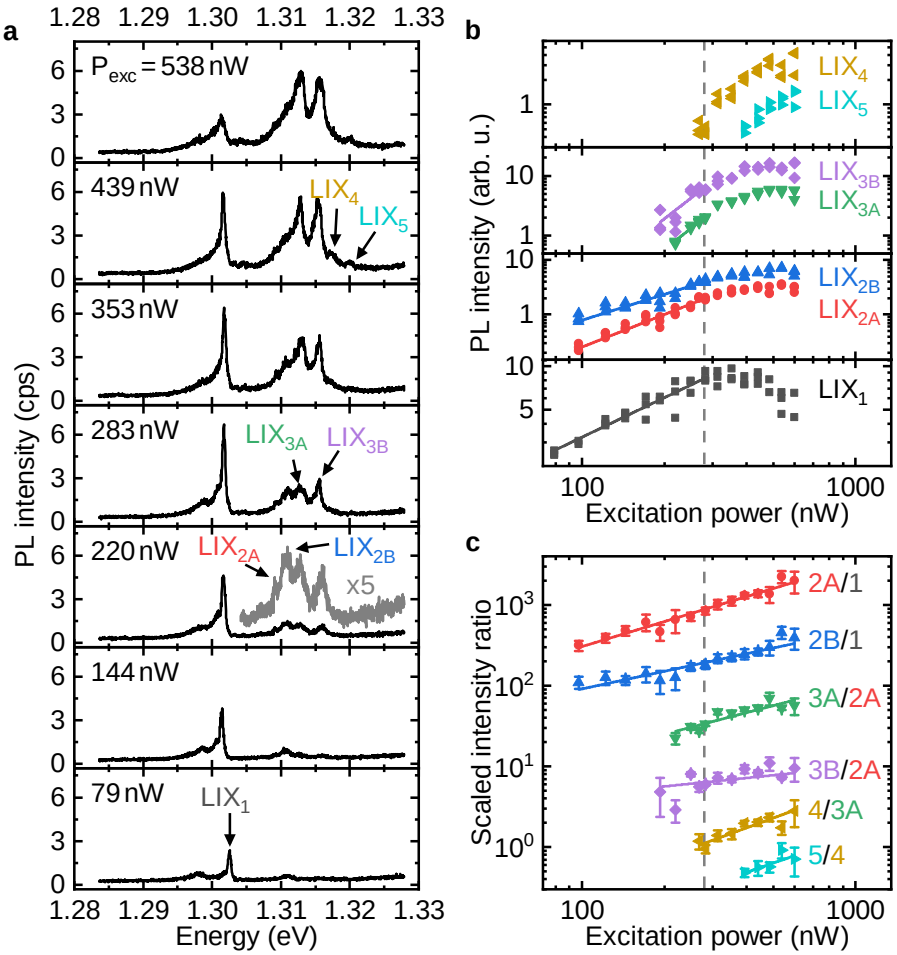

Figure 5.1: **Sequential filling of an IX trapping potential in excitation-power-dependent PL measurements.** **(a)** Example PL spectra at pillar site A for different excitation powers at $T = 4\,\mathrm{K}$ under defocused cw excitation with $\lambda = 532\,\mathrm{nm}$ (unlike the power-dependent data discussed in the previous chapter). **(b)** Photoluminescence intensities of the individual LIX peaks marked in panel (a). **(c)** Selected ratios of the intensities presented in panel (b). In panels (b) and (c), the gray dashed lines mark the onset of saturation effects and the solid lines indicate power law fits to the data. The respective power-law exponents for panels (b) and (c) are given in Tables 5.1 and 5.2. Adapted from [Kre20].

objective which was optimized for signal collection. (In this experiment, excitation and signal were detuned by 400 nm.) Therefore, the given excitation powers and the signal strength cannot be compared quantitatively to the the values given in the previous chapter.

At the lowest excitation power of 79 nW, a single sharp line (labelled LIX_1 in the figure) at 1.303 eV dominates the spectrum, in a similar manner to the spectra in Fig. 4.4. The FWHM of this peak is 550 meV, more than 35 times narrower than the free-IX emission ($\sim$ 20 meV). As the excitation power is increased towards 283 nW, the intensity of this process rises. For higher excitation powers, however, the intensity exhibits a clear saturation behaviour and eventually even decreases. Simultaneously, new emission peaks at higher energies emerge. Among these new peaks, a doublet labelled as LIX_{2A} and LIX_{2B} are the brightest in the low-power regime. The overall emission is redistributed towards higher-energy peaks (LIX_{3A}, LIX_{3B}, LIX_4 and LIX_5) with increasing excitation power. This behavior is in complete analogy to the data presented in Fig. 4.4.

Our original explanation for these discrete spectral jumps was that the increasing excitation power leads to a successive filling of the trapping potential, with the repulsive dipolar interactions giving rise to successively stronger blueshift. In order to substantiate this interpretation, we analyzed the PL intensities of the various LIX peaks observed in the spectra. The intensity of LIX_1, as determined from a Gaussian fit to the data, is depicted in the lowest panel of Fig. 5.1b. A clear transition from the low-power regime, in which the signal monotonously increases, to the saturation regime is visible and marked by a gray dashed line. We fitted a power law of the form $I(P) = I_0 \cdot P^{\alpha}$ to the data in the non-saturated regime, where I is the PL intensity, P is the excitation power, and I_0 and the power-law exponent α are fitting parameters. The fitted α of 0.9 ± 0.1 indicates a close-to-linear dependence of the signal on the excitation power. This is the expected behavior for single confined excitons.

The intensities of the remaining LIX peaks are presented in the upper three panels of Fig. 5.1b. Due to the broader linewdiths of these peaks and their spectral proximity, we were not able to determine intensities of the in-

Peak	LIX_1	LIX_{2A}	LIX_{2B}	LIX_{3A}	LIX_{3B}
α	0.90 ± 0.10	1.96 ± 0.15	1.57 ± 0.12	3.48 ± 0.27	3.6 ± 0.7

Table 5.1: Power-law exponents of the excitation-power dependence of the LIX peaks before saturation, as presented in Fig. 5.1b. Adapted from [Kre20].

dividual peaks via fitting over the whole excitation-power range. Instead, we integrated the signal in a range of 120 µeV around their respective center energies. The intensisties of all peaks increase monotonously with excitation power in the low-power regime. As for the LIX_1, all of these power dependencies exhibit a kink that occurs at the same excitation power. This simultaneous saturation behavior is a clear indicator that the peaks are directly correlated, i.e. are different states within the same trapping potential and are not independent states from various traps inside the detection volume. We fitted the low-power dependence of LIX_{2A}, LIX_{2B}, LIX_{3A} and LIX_{3B} with a power law analogous to LIX_1. The extracted power-law exponents are summarized in Table 5.1. For LIX_{2A} and LIX_{2B}, we find a clear superlinear dependence with a power-law exponent close to 2. This is characteristic of biexcitons. [Mil82, Bru94, He16b] LIX_{3A} and LIX_{3B} exhibit near-cubic dependencies. However, the uncertainties of their power-law exponents are relatively large due to the small number of available data points in the non-saturated regime. For LIX_4 and LIX_5, we do not have any data that could be used for a power-law fit. In order to incorporate also the data from the saturated regime into our analysis, we consider the ratios of intensities of different peaks and compare this to predicitions from an independent-capture model.

We consider excitons which are randomly captured by a potential trap at a rate G, which (like the exciton generation rate) is proportional to the excitation power. These excitons decay with a radiative lifetime τ. Both parameters could in principle depend on the occupation number N of the trap. The occupation probabilities n_N of the N-exciton states are then described by the following set of rate equations:

$$\frac{dn_N}{dt} = \frac{(N+1)n_{N+1}}{\tau_{N+1}} - \frac{Nn_N}{\tau_N} + G_{N-1}n_{N-1} - G_N n_N \tag{5.1}$$

If trapping and recombination rate are independent of N, the steady-state solution for these equations is known to be the Poissonian distribution:

$$n_N = \frac{(G\tau)^N}{N!} e^{-G\tau} \tag{5.2}$$

For a more general case, the exact distribution can take various different forms. Focusing only on the ratio of populations of two states with occupation numbers $N+1$ and N, a quick, induction-based proof can show that:

$$\frac{n_{N+1}}{n_N} = \frac{G_N \tau_{n+1}}{N+1} \propto P_{exc} \tag{5.3}$$

This linear dependence persists even into the saturated power regime. More generally, it follows that $\frac{n_{N+M}}{n_N} \propto P_{exc}^M$.

Figure 5.1c displays intensity ratios of selected pairs of LIX peaks. We scaled the individual curves by constant factors for better visibility. In stark contrast to the individual intensities, these ratios do not have a kink in their excitation-power dependence upon transitioning into the saturated power regime (marked by the gray dashed line), as the model predicts. We fit the data with power laws over the entire power range. The fits are shown as solid lines in the figure and the extracted power-law exponents are summarized in Table 5.2.

Intensity ratio	I_{2A}/I_1	I_{2B}/I_1	I_{3A}/I_{2A}
α	1.03 ± 0.05	0.72 ± 0.07	0.89 ± 0.15
Intensity ratio	I_{3B}/I_{2A}	I_4/I_{3A}	I_5/I_4
α	0.34 ± 0.17	1.24 ± 0.24	1.17 ± 0.46

Table 5.2: Power-law exponents of the excitation-power dependence of the LIX intensity ratios presented in Fig. 5.1c. Adapted from [Kre20].

We compared the intensities of both, LIX_{2A} and LIX_{2B}, to that of the single exciton LIX_1. Both ratios were found to depend linearly on the excitation

power, clearly supporting the assignment of these two peaks as biexcitons. The ratio of LIX_{3A} to LIX_{2A} exhibits a linear power dependence as well. This implies that LIX_{3A} consists of one more exciton than LIX_{2A} and thus corresponds to a triexciton. Fully analogously, we identify LIX_4 as a quadexciton and LIX_5 as a quintexciton because of the linear power dependence of the intensity ratios of LIX_4 to LIX_{3A} and LIX_5 to LIX_4, respectively. The least clear case is that of the LIX_{3B}, for which the uncertainty of the PL intensity dataset is the highest. As a result, the power law for the low-power regime has an exponent with a large uncertainty (3.6 ± 0.7), which could be interpreted as a triexciton or a quadexciton. Conversely, the intensity ratio of LIX_{3B} to LIX_{2A} has the most sublinear dependence ($\alpha = 0.34 \pm 0.17$) among the presented ones. Based on that intensity ratio, one would conclude that LIX_{3B} is either a biexciton or a triexciton. Both of these observations are, however, compatible with the interpretation of the LIX_{3B} as a triexciton.

Overall, the intensities of the various LIX peaks that emerge successively upon increasing the excitation power offer detailed insight into the associated states. We find complexes of one to five excitons which have spectrally clearly separated emission. In the remainder of this chapter, we will analyze the emission energies of the states which we have identified in this section in order to examine interactions between localized interlayer excitons.

5.2 Direct dipolar interactions between localized interlayer excitons

We fit the LIX emission spectra shown in Fig. 5.1a with Gaussian peaks (which, as stated before, works for some peaks only in a limited power range) and present the extracted emission energies of the various LIX features as a function of excitation energy in Fig. 5.2a. No systematic spectral shift with excitation power is observed for any of the peaks. Some random spectral wandering is observed, in particular for LIX_1, for which jumps of up to $\sim 1\,\mathrm{meV}$ occurred between measurements. Comparing the different emission peaks, we find that a higher number of excitons generally results in a

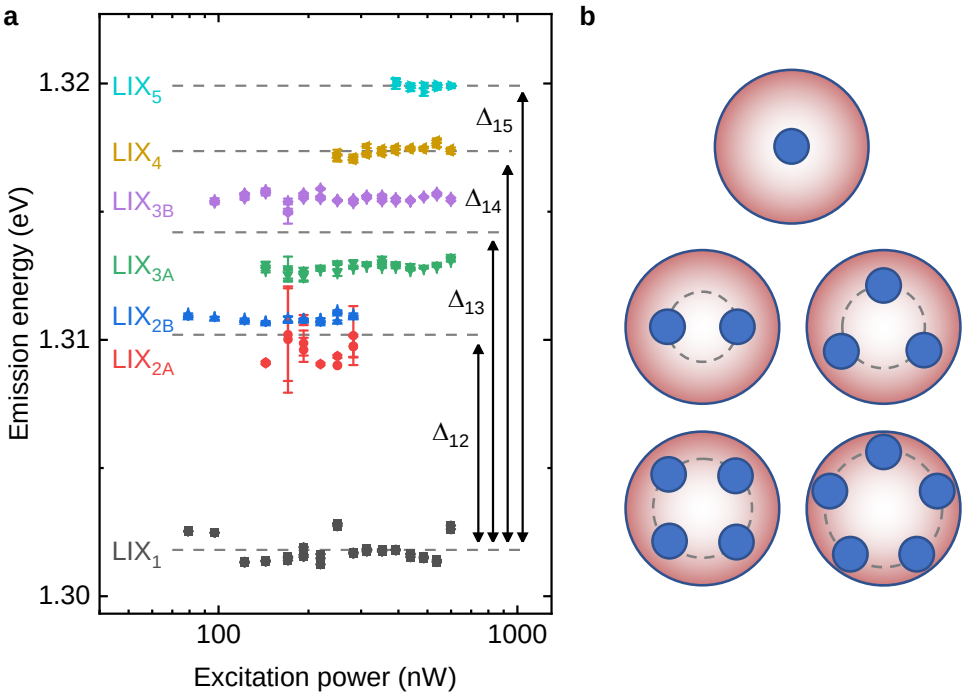

Figure 5.2: **Direct dipolar interactions between localized interlayer excitons.** **(a)** Emission energies of various LIX peaks as a function of excitation power. The values are determined from Gaussian fits to the data presented in Fig. 5.1a. Error bars denote fit uncertainties and gray dashed lines indicate mean energies for the multi-excitonic states. **(b)** Schematic illustration of the spatial configurations of one to five dipolar excitons trapped in a harmonic potential. Adapted from [Kre20].

higher emission energy. This is qualitatively expected since the IXs interact repulsively with each other via dipole-dipole interaction.

More specifically, we find that the biexciton is blueshifted by (8.4 ± 0.6) meV with respect to the single exciton. This large value is already a first indication of the small confinement length scale. For comparison, a similar experiment on dipolar excitons in InGaAs double quantum wells with (calculated) lateral distances of ~ 35 nm yielded a much smaller blueshift of less than 2 meV despite the larger dipole moment of $e \cdot 17$ nm. [Sch13] This discrepancy can only be explained by much shorter distances between the excitons in our

experiments. The triexciton blueshift amounts to (12.4 ± 0.4) meV, whereas the quadexciton and quintexciton blueshift are given by (15.5 ± 0.6) meV and (18.2 ± 0.8) meV, respectively. For the biexciton (triexciton) value, we averaged over LIX_{2A} and LIX_{2B} (LIX_{3A} and LIX_{3B}).

For a quantitative insight into the successively increasing interactions, we calculated the binding energies of trapped multi-excitonic states classically in terms of point-like dipoles in an isotropic 2D harmonic potential. This model has been applied analogously to dipolar excitons in double quantum wells and has described the experimental findings well. [Sch13] Note that we define positive binding energies as an increase of the multi-particle-state energy compared to the energy of the well-separated constituent particles. We parametrize the confinement potential in terms of a confinement lengthscale ℓ such that the energy of a single exciton with total mass M in the trap, displaced by a distance x from the potential minimum, reads:

$$U_{harm} = \frac{1}{2}\frac{\hbar^2}{M\ell^4}x^2 \tag{5.4}$$

Moreover, the potential energy of two IXs at a distance $\Delta\rho$ from the mutual dipole repulsion is given by:

$$U_{dip} = \frac{(ed)^2}{4\pi\epsilon}\left(\Delta\rho\right)^{-3} \tag{5.5}$$

Here, ed denotes the electric dipole moment composed of the elementary charge e and the distance d between electron and hole, and $\epsilon = \epsilon_0\epsilon_r$ is the effective, absolute permittivity of the surrounding medium given by the product of vacuum permittivity ϵ_0 and relative permittivity ϵ_r. In order to minimize dipole-dipole repulsion, the IX reside maximally spaced around an equipotential of the harmonic trap. The constellations that arise from this condition are a line (biexciton), an equilateral triangle (triexciton), a square (quadexciton) and a regular pentagon (quintexciton), all centered around the minimum of the harmonic potential, as illustrated in fig. 5.2b. As a function

of the nearest-neighbor distance $\Delta\rho$, the harmonic and dipole-dipole potential energies are then given by:

$$U^{2X} = 2 \cdot \frac{1}{2}\frac{\hbar^2}{M\ell^4}\left(\frac{\Delta\rho}{2}\right)^2 + \frac{(ed)^2}{4\pi\epsilon}(\Delta\rho)^{-3} \tag{5.6}$$

$$U^{3X} = 3 \cdot \frac{1}{2}\frac{\hbar^2}{M\ell^4}\left(\frac{\Delta\rho}{\sqrt{3}}\right)^2 + 3\frac{(ed)^2}{4\pi\epsilon}(\Delta\rho)^{-3} \tag{5.7}$$

$$U^{4X} = 4 \cdot \frac{1}{2}\frac{\hbar^2}{M\ell^4}\left(\frac{\Delta\rho}{\sqrt{2}}\right)^2 + 4\frac{(ed)^2}{4\pi\epsilon}(\Delta\rho)^{-3} + 2\frac{(ed)^2}{4\pi\epsilon}\left(\sqrt{2}\Delta\rho\right)^{-3} \tag{5.8}$$

$$U^{5X} = 5 \cdot \frac{1}{2}\frac{\hbar^2}{M\ell^4}\left(\frac{\sqrt{50+10\sqrt{5}}\Delta\rho}{10}\right)^2 + 5\frac{(ed)^2}{4\pi\epsilon}(\Delta\rho)^{-3} + \tag{5.9}$$

$$+5\frac{(ed)^2}{4\pi\epsilon}\left(\frac{1}{2}\left(1+\sqrt{5}\right)\Delta\rho\right)^{-3}$$

We minimize each of these expressions to find the equilbrium interparticle separation (e.g. $\Delta\rho = \sqrt[5]{\frac{6(ed)^2}{4\pi\epsilon}\frac{M\ell^4}{\hbar}}$ for the biexciton) and equilibrium potential energy U_0. Introducing $\tilde{E} = \left(\frac{(ed)^2}{4\pi\epsilon}\right)^{2/5}\left(\frac{\hbar^2}{M\ell^4}\right)^{3/5}$, we find:

$$U_0^{2X} = \frac{5}{2\cdot 6^{3/5}}\tilde{E} \approx 0.853\tilde{E} \tag{5.10}$$

$$U_0^{3X} = \frac{5\cdot 9^{2/5}}{6}\tilde{E} \approx 2.007\tilde{E} \tag{5.11}$$

$$U_0^{4X} = \frac{5\left(8+\sqrt{2}\right)^{4/5}}{2^{2/5}3^{3/5}}\tilde{E} \approx 3.642\tilde{E} \tag{5.12}$$

$$U_0^{5X} \approx 5.796\tilde{E} \tag{5.13}$$

We emphasize that other spatial configurations of the excitons can easily be shown to be less favorable than the ones discussed above. For example, arranging three excitons in a line would result in $U_{0,\text{line}}^{3X} \approx 2.650\tilde{E} > U_0^{3X}$, a quadexciton with three excitons on a triangle and the fourth one in the center would give $U_{0,\text{triangle}}^{4X} \approx 4.163\tilde{E} > U_0^{4X}$ and a quintexciton consisting of four excitons on a square surrounding the fifth in the trap center would have

$U^{5X}_{0,\text{square}} \approx 5.945\tilde{E} > U^{5X}_0$. Combined with the energy of a single exciton inside the trap E^X, the transition energies of the multi-exciton states can then be expressed as:

$$E^{2X\to 1X} \approx E^X + 0.853\tilde{E} \tag{5.14}$$

$$E^{3X\to 2X} \approx E^X + 1.154\tilde{E} \tag{5.15}$$

$$E^{4X\to 3X} \approx E^X + 1.635\tilde{E} \tag{5.16}$$

$$E^{5X\to 4X} \approx E^X + 2.154\tilde{E} \tag{5.17}$$

As can be seen from above equations, the blueshifts of all states show universal scaling with all system parameters. The ratios of blueshifts of different emission peaks therefore eliminate the dependency on the precise parameters and take fixed values. We denote the blueshift of the N-exciton peak with respect to the single LIX as Δ_{1N}, as depicted in Fig. 5.2a. Table 5.3 summarizes the ratios of Δ_{1N} for $N = 3,4,5$ to Δ_{12}, as predicted by the model above and as calculated from the experimentally determined emission energies.

Blueshift ratio	Model prediction	Experimental value
Δ_{13}/Δ_{12}	1.354	1.48 ± 0.12
Δ_{14}/Δ_{12}	1.918	1.85 ± 0.15
Δ_{15}/Δ_{12}	2.526	2.17 ± 0.18

Table 5.3: Ratios of the blueshifts of various LIX peaks with respect to the single LIX.

Overall, we find good agreement between the theoretical predictions and our experimentally observed values, especially considering the simplicity of the model, which considers the excitons as classical point particles and assumes a harmonic potential despite us having no microscopic insight into the spatial dependence of the potential energy. Deviations from the model become apparent for the quintexcitons. This can be expected: As the excitons reside farther away from the potential minimum, any anharmonicities of the

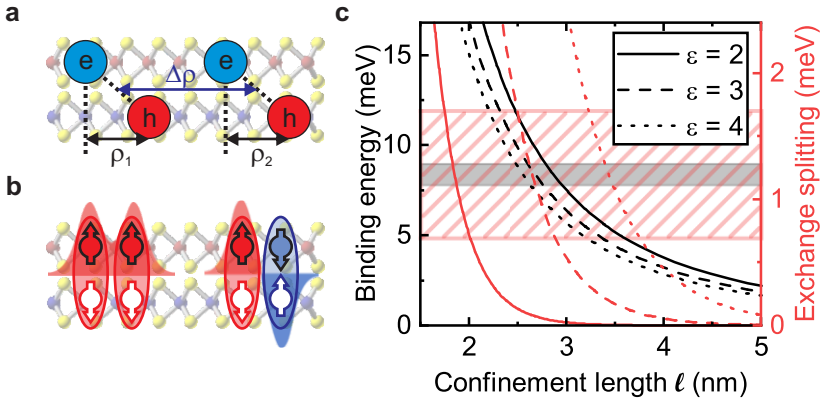

Figure 5.3: **Theoretical model for the observed biexciton splitting.** **(a)** Sketch of the interlayer biexciton complex and the coordinate conventions used in the main text. **(b)** Schematic illustration of biexciton states with different symmetries of spatial and spin wavefunction. **(c)** Binding energy (gray curves) and exchange splitting (red curves) of the trapped biexciton as a function of the confinement length of the harmonic potential. Positive binding energies correspond to an increase in energy. The gray-shaded (red-shaded) energy range indicates the measured biexciton blueshift (splitting). We assume $d = 0.7\,\mathrm{nm}$ and $m_{e/h} = 0.8/0.45 m_0$. Adapted from [Kre20].

potential (which one can assume to be present but which are not included in the model) will have a stronger impact on the observed energies.

5.3 Exchange splitting of the localized interlayer biexciton

In the discussion of dipolar interactions, we have neglected the existence of multiple biexciton and triexciton peaks so far. In this section, we will demonstrate how exciton-exciton exchange interaction can give rise to such a sub-structure and model the biexciton complex to reproduce the observed splitting of $(1.2 \pm 0.5)\,\mathrm{meV}$. All calculations were performed by our collaborator at the Max Planck Institute of Quantum Optics, Johannes Knörzer.

We modified the method outlined in [Bon18] and start with a Hamiltonian describing the biexciton complex of the following form:

$$H = H_0 + H_{\text{int}}, \tag{5.18}$$

where

$$H_0 = \sum_{i=1,2} \Bigg[- \frac{\hbar^2}{2\mu}\frac{1}{\rho_i}\frac{\partial}{\partial\rho_i}\left(\rho_i\frac{\partial}{\partial\rho_i}\right) + \frac{1}{2}\mu\Omega_0^2\rho_i^2 - \tag{5.19}$$

$$- \frac{e^2}{4\pi\varepsilon}\left(\frac{1}{\sqrt{\rho_i^2+d^2}} + \frac{1}{\sqrt{(\rho_i+(-)^i\Delta\rho)^2+d^2}}\right)\Bigg]$$

describes non-interacting excitons exposed to the weak harmonic confinement potential and

$$H_{\text{int}} = \frac{e^2}{\pi\varepsilon}\Bigg[\frac{1}{|\rho_1-\rho_2+2\Delta\rho|} + \frac{1}{|\rho_1-\rho_2-2\Delta\rho|} - \tag{5.20}$$

$$-\frac{1}{\sqrt{(\rho_1+\rho_2+2\Delta\rho)^2+d^2}} - \frac{1}{\sqrt{(\rho_1+\rho_2-2\Delta\rho)^2+d^2}}\Bigg]$$

represents the Coulomb interactions between the excitons. In equations 5.19 and 5.20, the coordinates ρ_1 and ρ_2 are in-plane projections of the relative electron-hole coordinates of the interlayer excitons, as depicted in Fig. 5.3a, and $\Delta\rho$ is the exciton-exciton distance, as introduced before. Moreover, $d \approx 0.7\,\text{nm}$ is the interlayer separation of the HBL that determines the strength of the dipole-dipole repulsion and $\epsilon = \epsilon_0\epsilon_r$ describes the effective dielectric screening by the surrounding vacuum (upper) and SiO_2 (lower) media. We note that, in the simplest picture in which we average the values for vacuum (upper cladding) and SiO_2 (lower substrate), the effective dielectric constant would be $\epsilon_r = (\epsilon_{vac} + \epsilon_{SiO_2})/2 \sim 2.45$. For the effective masses m^*, we use $m^* = 0.8m_0$ ($0.45m_0$) for the $MoSe_2$ electrons[Lar18] (WSe_2 holes[Fal16]). In the formula, the reduced mass $\mu = \frac{m_e^* m_h^*}{m_e^*+m_h^*}$ appears in terms related to the relative electron-hole motion. We characterized the strength of the harmonic potential by the level splitting Ω. This level splitting and the localization length (used in the previous section) are related via $\Omega = \frac{\hbar}{m\ell^2}$.

For each individual exciton, the confinement potential acts separately on the center-of-mass motion and the relative motion: $\frac{1}{2}m_e\Omega^2 r_e^2 + \frac{1}{2}m_h\Omega^2 r_h^2 = \frac{1}{2}M\Omega^2 R_{com}^2 + \frac{1}{2}\mu\Omega^2\rho^2$. In this, M is the sum of the particle masses and R_{com} is the center-of-mass coordinate. Analogous to [Bon18], we use an adiabatic approximation, in which the center-of-mass positions of the individual excitons are assumed to be static. In particular, we use $\Delta\rho$ as a fixed parameter, which we deduce following the steps of the previous section. We therefore do not write out terms that only influence the center-of-mass motion explicitly, anymore.

In order to be able to follow the procedure in [Bon18], we need to determine if and how the presence of the confinement potential impacts the relative electron-hole motion within an exciton. For weak confinement potentials (characterized by a confinement length larger than the exciton Bohr radius), the exciton ground-state wavefunction still decays exponentially. The effect of the confinement potential on the wavefunction extent can be accounted for by replacing the layer distance d by an effective layer distance $\tilde{d} = \frac{d}{\sqrt[3]{1+\frac{4\pi\epsilon_0\epsilon_r\hbar^2}{2e^2\mu\ell^4}d^3}}$. We evaluated the denominator of this expression for $\epsilon_r = 3$, $\mu = 0.25m_e$ and $\ell = 3\,\mathrm{nm}$ and obtained a value of 1.00045. This small correction using realistic parameter values verifies a negligible influence of the confinement potential on the extent of the single-exciton wavefunction. The confinement potential therefore merely dictates the equilibrium inter-exciton distance $\Delta\rho$ and we can continue to follow the steps in [Bon18].

The indistinguishability of the two LIX composite bosons forming the biexciton implies that the total wavefunction must be symmetric with respect to IX exchange. This condition can only be satisfied when both spin and spatial parts of the two-exciton wavefunction are simultaneously *symmetric* or simultaneously *antisymmetric*, as illustrated schematically in Fig. 5.3b. Thus, the spatial part of the two-IX (biexciton) wavefunction can take the form $\Psi \sim \frac{1}{\sqrt{2}}[\psi_{IX,1}(\rho_1)\psi_{IX,2}(\rho_2) \pm \psi_{IX,1}(\rho_2)\psi_{IX,2}(\rho_1)]$, giving rise to two, ener-

getically distinct biexciton states separated by the exchange energy $2J(\Delta\rho)$. Here, $J(\Delta\rho)$ is given by [Bon11]

$$J(\Delta\rho) = \frac{1}{3}\int_{-\Delta\rho/\sqrt{2}}^{\Delta\rho/\sqrt{2}} \mathrm{d}y \left|\Psi(x,y)\frac{\partial\Psi(x,y)}{\partial x}\right|_{x=0}, \tag{5.21}$$

where $\Psi(x,y)$ is the ground state of eqn. (5.18) that has been transformed to the coordinate system $x = (\rho_1 - \rho_2 - \Delta\rho)/\sqrt{2}$ and $y = (\rho_1 + \rho_2)/\sqrt{2}$. This expression can be calculated and written out explicitly: [Bon18]

$$\begin{aligned} J &= \frac{2N^4}{3}\Delta\rho\left(\frac{\alpha\Delta\rho}{\sqrt{\Delta\rho^2+4d^2}} + \frac{1}{3(\alpha\Delta\rho-1)}\right)\cdot \\ &\cdot\left(\frac{e}{3}\right)^{2\Delta\rho/(\alpha\Delta\rho-1)}\cdot\exp\left[-2\alpha\left(\sqrt{\Delta\rho^2+4d^2}-2d\right)\right] \end{aligned} \tag{5.22}$$

In this expression, we use atomic units (modified for the exciton). In particular, all lengths are expressed in units of the Bohr radius $a_B = \frac{4\pi\epsilon_0\epsilon_r\hbar^2}{\mu e^2}$ (where e is the elementary charge, unlike in equation (5.22), where it is Eurler's number) and energies are given as multiples of the Rydberg energy $R = \frac{\mu e^4}{8c\epsilon_0^2 h^3}$. We furthermore use the abbreviations $N = \frac{4}{\sqrt{1+4\sqrt{d}+8d\left(1+\sqrt{d}\right)}}$ and $\alpha = \frac{2}{1+2\sqrt{d}}$. We numerically evaluate equation (5.22) for the value of $\Delta\rho$ that minimizes the center-of-mass energy (as discussed in section 5.2) and obtain the absolute energies of the two biexciton states:

$$\begin{aligned} E_{\mathrm{LIX2B/A}} &= 2E_{\mathrm{LIX1}} + \frac{2d^2}{4\pi\varepsilon(\Delta\rho)^3} + \frac{\hbar^2\left(\Delta\rho\right)^2}{4m^* l^4} \pm J\left(\Delta\rho\right) = \\ &= 2E_{\mathrm{LIX1}} + E_{\mathrm{binding}} \pm J\left(\Delta\rho\right) \end{aligned} \tag{5.23}$$

Again, a positive binding energy refers to an increase in energy of the biexciton state compared to two isolated excitons. Representative results of our calculations are presented in fig. 5.3c that depicts the numerically evaluated biexciton binding energy and exchange splitting as a function of the effective confinement lengthscale ℓ. The three curves presented on the figure correspond to effective dielectric constants $\epsilon_r = 2 - 4$. The experimentally

observed blueshift of LIX_2 of (8.4 ± 0.6) meV is consistent with a confinement length scale in the range $\ell = 2.5$ nm to 3.0 nm, with relatively weak sensitivity to the effective dielectric constant. We interpret the existence of two biexciton states, split by (1.2 ± 0.5) meV, as reflecting the existence of two distinct spatial wavefunctions with even and odd symmetry with respect to IX exchange, as discussed above. The red curves presented in fig. 5.3c denote the calculated exchange splittings $2J(\ell)$ for the same range of effective dielectric constants. The red-shaded region indicates the measured splitting of the biexciton peak. Remarkably, our model calculations simultaneously reproduce *both* the observed biexciton binding energy and the exchange splitting for a dielectric constant in the range $\epsilon \approx 3$, very close to the average dielectric constant of the environment $\epsilon_{vac-SiO_2} = 2.45$, and an effective confinement length scale of $\ell \lessapprox 3$ nm. Thus, we conclude that the strain-induced trapping potentials in the vicinity of the nanopillars give rise to nanometer-scale confinement traps in which the LIX interact via direct and exchange Coulomb interactions in the range of a few meV.

5.4 Summary

In this chapter, we have covered the direct and exchange dipolar interactions between localized interlayer excitons. We have identified states from single excitons up to quintexcitons based on the characteristic excitation-power dependence of their emission. Overall, we found that an increased particle number results in higher-energy emission, in accordance with the repulsive, dipolar interaction between IXs. In the dataset analyzed in this chapter, we find that the localized biexciton is blueshifted by (8.4 ± 0.6) meV from the single localized exciton, a value greater than what is observed in comparable systems like III-V double quantum wells. The relative shift of complexes of multiple excitons are well captured by a model of point-like, classical dipoles in a harmonic trapping potential.

Moreover, we found that some of the peaks (biexciton and triexciton) are split into doublets. Interpreting this splitting as arising from exciton-

exciton exchange interaction, we reproduced the observed biexciton splitting of (1.2 ± 0.5) meV modelling interactions with realistic parameter values. Taking into account dipolar and exchange interactions, we deduce a confinement length of 3 nm for the examined potential trap. In summary, we find good quantitative agreement between spectroscopic data of 1 to 5 localized interlayer excitons and their modelled direct and exchange dipolar interactions. The magnitude of the observed interaction energies renders IXs in TMD-HBLs a promising platform for the exploration of novel interacting phases of matter and for non-linear optical elements.

CHAPTER 6

Excitons in twisted bilayer $MoSe_2$

In the previous chapters, we have investigated interlayer excitons in a $MoSe_2$-WSe_2 heterobilayer, which have been localized to a nanometer-sized area by strain-induced potentials, to explore an extreme regime of repulsive interactions between excitons. For applications in quantum technologies, a system with similar interaction effects but a higher degree of controllability would be highly desirable. Twisted $MoSe_2$ bilayers may fulfill these requirements. The lowest-energy excitons in $MoSe_2$ with a twist angle of 0° have recently been demonstrated to have a considerable dipolar character, potentially facilitating strong exciton-exciton interactions. [Sun20] Moreover, the twist angle in TMD bilayers offers control over the superlattice period, which can define exciton confinement lengths, as seen in moiré-trapped excitons in heterobilayers. [Tra19, Sey19, Jin19]

In this chapter, we present the first systematic study of excitonic properties of artificial $MoSe_2$ bilayers as a function of twist angle. We produce samples with twist angles spanning the relevant parameter range of 0° to 60° using the *tear-and-stack* technique. [Kim16] By combining PL and reflectivity measurements, we examine A excitons and trions, as well as momentum-

indirect excitons. The A-exciton energy exhibits relatively weak sensitivity to the twist angle in the range 10° to 50° but abruptly decreases in the vicinity of 0° or 60°, indicating enhanced interlayer coupling at these angles. The hypothesis of reduced interlayer coupling between 10° and 50° is further supported by the lack of clear indirect-exciton features and the brightening of the A exciton in the according samples. Finally, we present continuum-model calculations of excitons in the moiré potential of a twisted $MoSe_2$ bilayer, which reproduce and explain our experimental findings.

The contents of this chapter follow our publication on these topics.[1] [Vil23] Any reused material will beindicated.

6.1 Fabrication of twisted $MoSe_2$ bilayers

For the studies presented in this chapter, we produced a series of samples featuring artificial $MoSe_2$ bilayers with varying twist angles. Each of these bilayers is encapsulated in layers of hBN (typically 10 nm to 30 nm thick) and placed on a Si-SiO_2 substrate. In order to fabricate the bilayers with optimal control over the twist angle, we employed the tear-and-stack technique, [Kim16] a version of the hot-pick-up method, [Wan13, Piz16] which we show schematically in Fig. 6.1. Microscope images from the fabrication of a sample containing a $MoSe_2$ bilayer with a twist angle of 20° are presented in Fig. 6.2.

Fig. 6.1a shows the design of the stamps that we used for the tear-and-stack process. We place transparent PDMS pillars with a dome-shaped top onto a glass slide, which allows us to mechanically manipulate the whole stamp and to view the fabrication process through the stamp. A thin layer of poly-carbonate (PC) is stretched over the dome. Depending on temperature, the adhesion of vdW materials to the PC film is stronger than to SiO_2 substrates, such that flakes can be picked up in the desired order before we deposit the entire stack onto a substrate in a final step. [Piz16]

[1] https://doi.org/10.1103/PhysRevLett.130.026901

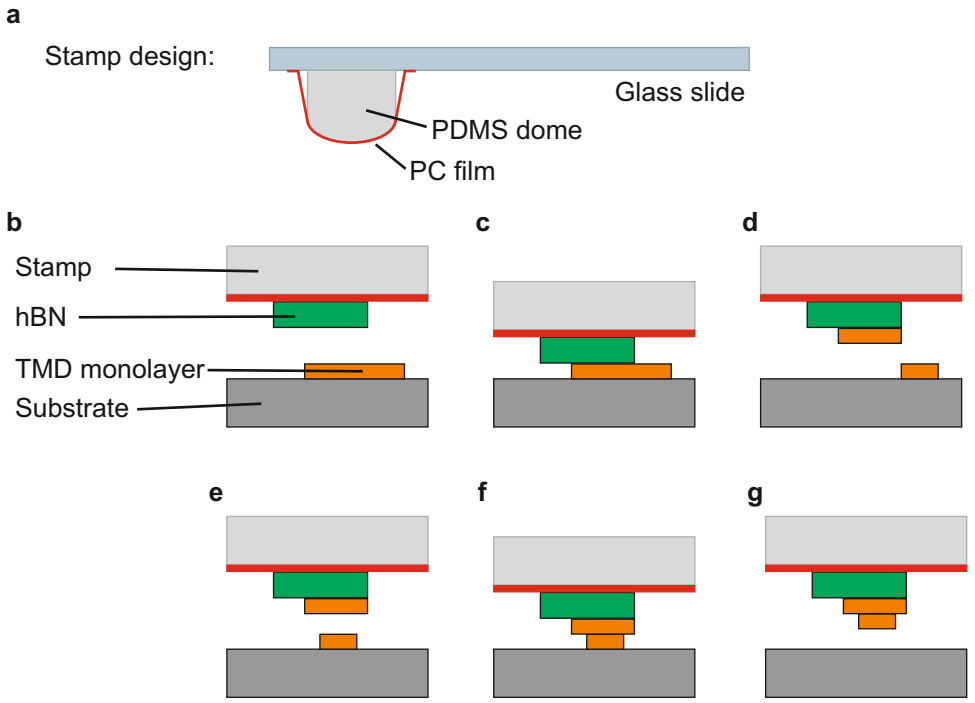

Figure 6.1: **Tear-and-stack fabrication of twisted TMD bilayers. (a)** Design of the PC-based stamps used in tear-and-stack fabrication. **(b-g)** Schematic illustration of the fabrication steps. More detailed description in the main text.

As a first step, we exfoliate all materials separately onto Si-SiO_2 substrates and identify suitable flakes. The final heterostructure is assembled from the top to the bottom layer. We choose a designated top hBN flake, which ideally features a long straight edge, and bring the tip of the stamp into contact with the substrate in the vicinity of this hBN layer, as seen in Fig. 6.2a. There, substrate and stamp are already in contact on the left edge of the picture. Where stamp and substrate are close, but not yet in contact, colorful Newton rings can be seen. As the stamp is lowered further, the contact area expands until also the hBN flake touches the stamp. After waiting for one minute, we retract the stamp in order to lift the hBN off the substrate.

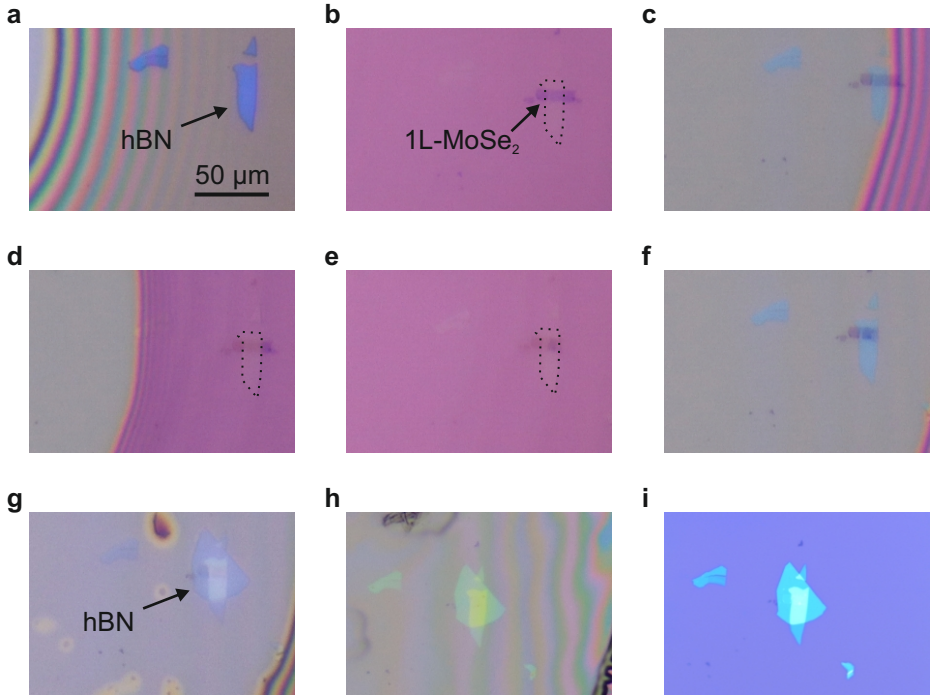

Figure 6.2: **Fabrication of a twisted $MoSe_2$ bilayer sample.** More detailed description in the main text. The scale bar in panel (a) applies to all panels.

The hBN adhering to the stamp is then partially aligned with a monolayer of $MoSe_2$, as seen in Figs. 6.1b and 6.2b. In the latter, the contours of the hBN flake are outlined with dashed lines to enhance visibilty despite the faint contrast. Only a part of the monolayer, outlined by the hBN flake, is supposed to be lifted off. The straight edge of the hBN helps to define this part more clearly. We lower the stamp again, having the contact edge between substrate and stamp only progress until the end of the hBN flake, as shown in Figs. 6.1c and 6.2c. The contact edge often still advances after the lowering of the stamp has been stopped, possibly due to imperfections in the mechanics or due to thermal expansion. We therefore aimed to pick up less than half of the monolayer, such that enough material remained even if too much was picked up accidentally. We lift the stamp again, picking up only the material that was in contact with the PC or the hBN, as depicted in

Figs. 6.1d and 6.2d. In particular, comparison of Figs. 6.2b and 6.2d reveals that the parts of the $MoSe_2$ monolayer which were within the contact region now have a reduced contrast to their surroundings, since they do not sit on top of the substrate anymore. We then rotate the substrate by the desired twist angle and align the lifted-off part of the monolayer with the remaining part on the substrate (Figs. 6.1e and 6.2e). We bring stamp and substrate into contact (Figs. 6.1f and 6.2f), such that the two parts of the monolayer form a bilayer. Since they were part of the same crystal, their crystal axes were aligned before the substrate was rotated. Their mutual twist angle therefore corresponds to the angle by which the substrate was rotated. The stamp is lifted again (Fig. 6.1g) and now carries the top hBN and the twisted bilayer.

In order to complete the vdW heterostructure, we pick up a bottom hBN layer, as shown in Fig. 6.2g. During the entire assembly of the heterostructure, we heat the substrates to 110 °C to promote adhesion of the vdW materials to the stamp. We keep the stamp in proximity to the heated stage such that its temperature also stays close to that value. Otherwise, the PC would contract and could ripple or detach from the PDMS dome. We deposit the entire heterostructure on a clean Si-SiO_2 substrate at a temperature of 180 °C. This higher temperature melts the PC, such that it remains on the substrate, as the stamp is retracted again. Moreover, many impurities trapped between the layers become mobile at this temperature, such that they can be pushed out as substrate and stamp are pressed together. [Pur18] After the stamp has been removed, the heterostructure remains on the substrate, covered by the melted PC film, as seen in Fig. 6.2h. The substrate is left to cool down to room temperature. In order to remove the PC residue, the sample is left in choloroform for 1 hour, followed by rinsing in fresh chloroform for four hours, acetone for four hours and IPA for twelve hours. A microscope image of the finished and cleaned sample is presented in Fig. 6.2i. The visibility of the $MoSe_2$ layers in this sample is reduced without the surrounding PC film. In total, we produced samples with nine different twist angles: 0°, 3°, 8°, 12°, 20°, 30°, 40°, 54° and 60°. We were able to reproduce the results for the twist angles 0° and 8° by creating one additional sample for both angles

and repeating the measurements (detailed in the following sections) on them. For reference, we also made a sample containing a natural (2H) bilayer with pristine and encapsulated areas.

6.2 Optical spectroscopy of the A exciton in $MoSe_2$ bilayers

Since $MoSe_2$ monolayers are direct-bandgap semiconductors in contrast to few-layer and bulk $MoSe_2$, which have an indirect bandgap, pronounced differences in the PL intensity of the monolayer and bilayer regions of the samples are expected. We demonstrate this with the sample shown in the microscope image in Fig. 6.3a. The two main parts of the original $MoSe_2$ monolayer are outlined by black (top) and red (bottom) dashed lines. In the overlap region, they form a bilayer with a twist angle of 30°. Figure 6.3b depicts the spatially resolved PL signal in the spectral range 1.5 eV to 1.7 eV, which includes the $MoSe_2$ A exciton, at $T = 10\,\mathrm{K}$. The monolayer regions clearly display brighter emission than the bilayer region, as expected.

We present example spectra from the monolayer and bilayer region in Figs. 6.3c and d, respectively. Both regions exhibit emission from neutral excitons and trions. Besides the PL intensity reduction, the bilayer region displays a redshift of the emission: In the example spectra, the neutral exciton is shifted from 1.644 eV to 1.626 eV and the trion is shifted from 1.615 eV to 1.600 eV. The energetic reduction in the bilayer region has two major contributions: Hybridization of electronic states between the layers [Li07, Spl10] and dielectric effects. [Uge14, Raj17, Flo18, Cho18] In principle, the A-exciton energy has a rather small sensitivity to its dielectric environment because the bandgap and the exciton binding energy are both reduced as the surrounding dielectric constant is increased, leaving only small net changes. [Lin14, Sti16, Flo18] However, the contrast in dielectric constant between hBN and $MoSe_2$ is very pronounced: $MoSe_2$ has a static dielectric constant of 7.2 (16.8) in in-plane (out-of-plane) direction, whereas hBN only has a static dielectric constant of 6.93 (3.76) in in-plane (out-of-plane) di-

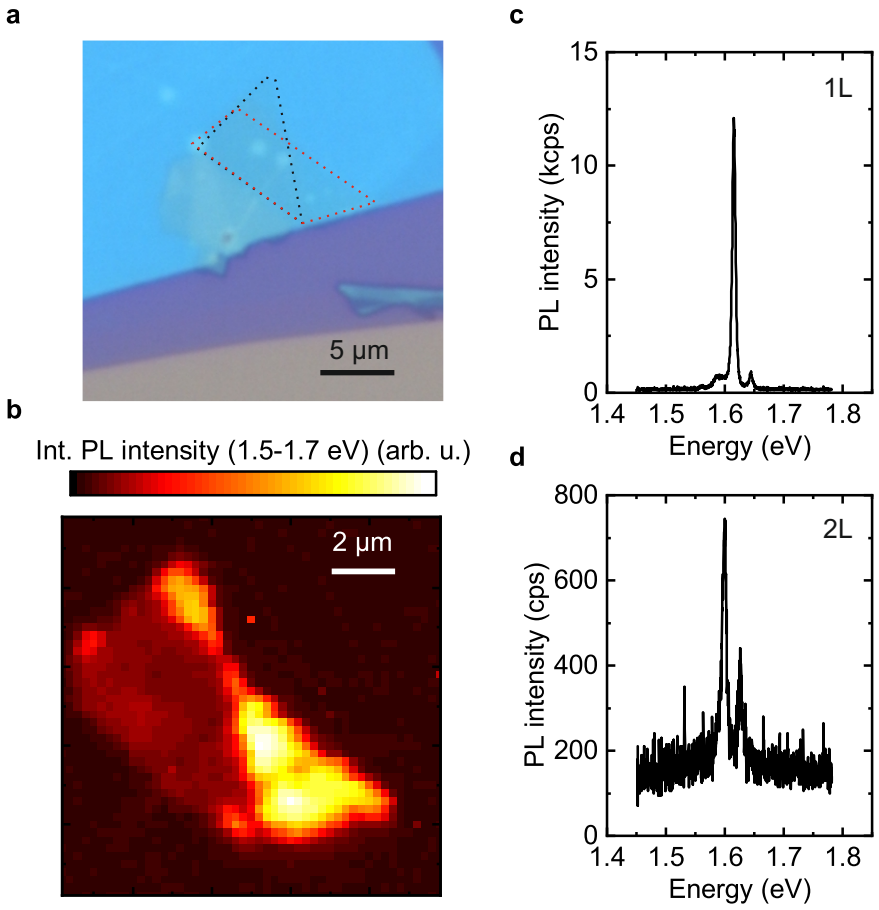

Figure 6.3: **Photoluminescence from monolayer and twisted bilayer $MoSe_2$. (a)** Microscope image of a vdW heterostructure consisting of hBN, bilayer $MoSe_2$ with a twist angle of 30° and hBN on top of a Si-SiO_2 substrate. The two partially overlapping $MoSe_2$ monolayers are outlined with dashed lines. **(b)** Spatially resolved integrated PL signal of the sample depicted in panel (a) between 1.5 eV and 1.7 eV, revealing the bright monolayer and the darker bilayer regions. **(c, d)** Example spectra from the monolayer (c) and the bilayer (d) regions of the sample. The data presented in panels (b-d) was acquired at $T = 10\,\mathrm{K}$ with excitation at $\lambda = 532\,\mathrm{nm}$ and an excitation power of 500 nW. Adapted from [Vil23].

rection. [Lat18] This discrepancy can already account for redshifts up to the order of $\sim 15\,\mathrm{meV}$. [Cho18]

We compared PL emission from monolayer and bilayer regions in samples containing $MoSe_2$ bilayers with twist angles ranging from 0° to 60° in order to probe the impact of the twist angle on the properties of the A exciton. Figures 6.4a-i display PL spectra at $T = 10\,\mathrm{K}$ from samples with bilayer twist angles as indicated in the top right corner of each panel. The dashed lines are monolayer spectra, which we give for reference and to which we normalize the PL intensity in each panel. The twist angle in the bilayer region should not impact the excitonic properties of the monolayer region. However, we observe slight variations of the A-exciton energies between samples, even in the monolayer regions, which most likely stem from strain variations. [Fri17] The solid curves are spectra from the bilayer region, which we scale up by a factor of eight w.r.t. the respective monolayer spectra for better visibility. Overall, we see a clear reduction in PL intensity. The bilayers with twist angles of 0° and 60° feature no discernible PL in the depicted range. The samples at 3°, 8° and 54° show some PL signal but it is at the same energy as the respective monolayer emission. In these samples, the bilayer region also turned out to be narrow (in the range of 1 µm to 2 µm), such that the most likely origin of these feature is that we probed the adjacent monolayers region at the edge of our excitation spot. In conclusion, we find no evidence for bright bilayer A-exciton emission for twist angles in the ranges 0° to 8° and 54° to 60°. This behavior is analogous to natural bilayers with 2H stacking order. For comparison, we present the PL spectra from a pristine (not encapsulated) $MoSe_2$ monolayer and a natural (2H) bilayer in Fig. 6.4j in the same manner as the previous plots. Again, no bilayer emission can be seen in the depicted range. Instead, excitons relax into momentum-indirect states at lower energies, as we will discuss in section 6.3.

The emission patterns of samples with larger twist angles (12° to 40°) differ notably from this behavior, as seen in Figs. 6.4d-g. There, the bilayer spectra always exhibit PL features, whose center energies are also distinctly

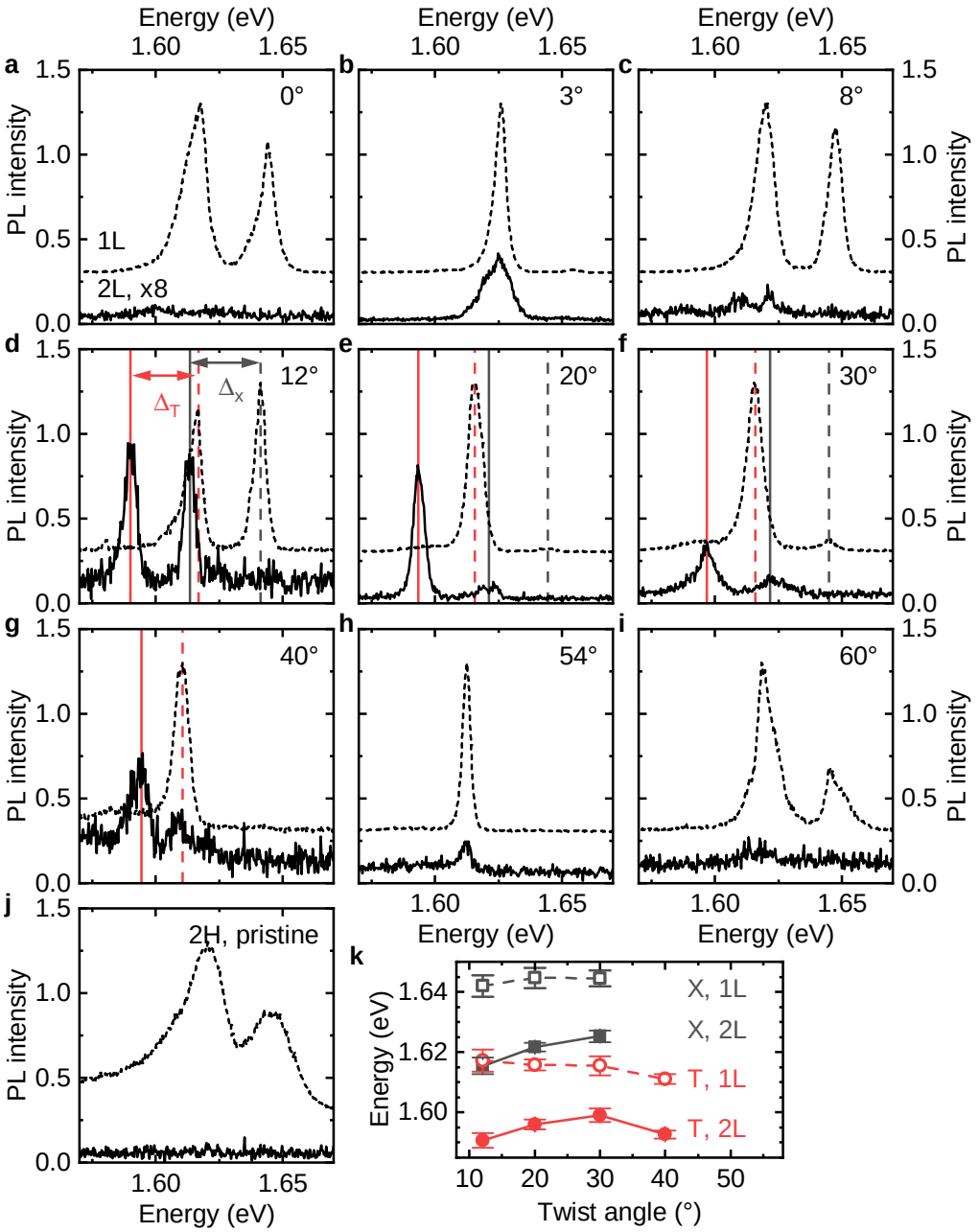
a
b
c
d
e
f
g
h
i
j
k
Energy (eV)
1.60
1.65
PL intensity
0.0
0.5
1.0
1.5
0°
3°
8°
12°
20°
30°
40°
54°
60°
1L
2L, x8
Δ_T
Δ_X
2H, pristine
Energy (eV)
1.60
1.62
1.64
X, 1L
X, 2L
T, 1L
T, 2L
10
20
30
40
50
Twist angle (°)

Figure 6.4: **Direct-exciton photoluminescence of twisted $MoSe_2$ bilayers.** (Figure on page 97.) **(a-i)** Photoluminescence spectra from samples containing $MoSe_2$ bilayers with different twist angles (denoted in the top right corner of each panel) recorded at $T = 10\,\mathrm{K}$. For reference, we present normalized spectra from the monolayer regions of each sample as a dashed line. The bilayer spectra are shown as solid lines and scaled with a factor of eight relative to their respective monolayer spectrum. The monolayer spectra are offset by 0.3 for visibility. If an exciton (trion) peak was identified in both regions, we indicated it with a gray (red) line. Again, dashed (solid) indicators are used for the monolayer (bilayer) spectra. **(j)** Spectra from an unencapsulated sample containing a natural (2H) $MoSe_2$ bilayer, showcased analogously to panels (a-i). **(k)** Exciton and trion transition energies for samples, in which the respective feature could be identified in monolayer and bilayer regions. Gray squares (red circles) indicate excitons (trions). Empty (full) data points and dashed (solid) lines represent monolayer (bilayer) data. Adapted from [Vil23].

different from those of the monolayer. The bilayer spectra typically consist of two peaks with intensity ratios which vary between the samples. This behavior is well-known in $MoSe_2$ monolayers, which can exhibit varying ratios of emission from the neutral exciton (1.65 eV) and the charged trion (1.62 eV) depending on the individual free-carrier density of the flake. [Ros13] In fact, the ratios of the higher-energy and lower-energy peak in the bilayer regions in our samples mimic those of the neutral exciton and charged trion in the respective monolayer regions. This can be seen most clearly when comparing Fig. 6.4d, which features two equally large peaks in bilayer and monolayer region, and Fig. 6.4f, in which the lower-energy peak is much more pronounced in monolayer and bilayer region. We therefore conclude that the two peaks in the bilayer emission spectra also correspond to neutral excitons and trions, whose relative intensities depend on the free-carrier density of the $MoSe_2$ flakes.

If the neutral exciton (charged trion) was visible in monolayer and bilayer regions of the same sample, we marked it with a gray (red) line in Figs. 6.4d-g as a guide to the eye. The monolayer (bilayer) feature was denoted by a dashed (solid) line. In order to quantify the energy shift between the different sample regions, we fitted both features with Gaussian peaks, individually for each sample position (on a grid of 250 nm), which we could unambiguously identify as monolayer or bilayer. For each position j, we determined the integrated PL intensity A_j and the center energy E_j of neutral exciton and trion. We calculated the weighted average of the emission energy $\bar{E} = \frac{\sum_j A_j E_j}{\sum_j A_j}$ and the respective standard deviation $\Delta E = \sqrt{\frac{\sum_j A_j E_j^2}{\sum_j A_j} - \left(\frac{\sum_j A_j E_j}{\sum_j A_j}\right)^2}$. In Fig.6.4k, we plot the obtained average energies of the neutral exciton in gray and of the trion in red. Open data points and dashed lines represent monolayer data, whereas bilayer data are depicted with filled data points and solid lines. The error bars indicate the weighted standard deviation, as defined above. We noticed sample-to-sample variation in the monolayer data, most notably when comparing the trion energies of the 12° sample and the 40°. These variations are comparable to the statiscal fluctuations within the samples. There is a consistent redshift from the monolayer to the bilayer data in the range of 15 meV to 30 meV, which we will discuss in more detail after presenting the reflectivity data.

We were not able to probe the A exciton resonances of samples with small twist angles (0° to 8° and 54° to 60°) using non-resonant PL experiments, presumably because the A-exciton population relaxes into states of lower energies before radiative recombination can occur, in analogy to natural $MoSe_2$ bilayers. (This will be discussed in sections 6.3 and 6.4.) However, these (momentum-direct) transitions can be detected in white-light-reflectivity measurements due to their large optical dipole moment. [Eva71, Ane80] The overall (spectrally resolved) reflected light intensity, however, does not only depend on the exciton resonance: The excitation source already features a characteristic emission spectrum and the detection efficiency of the

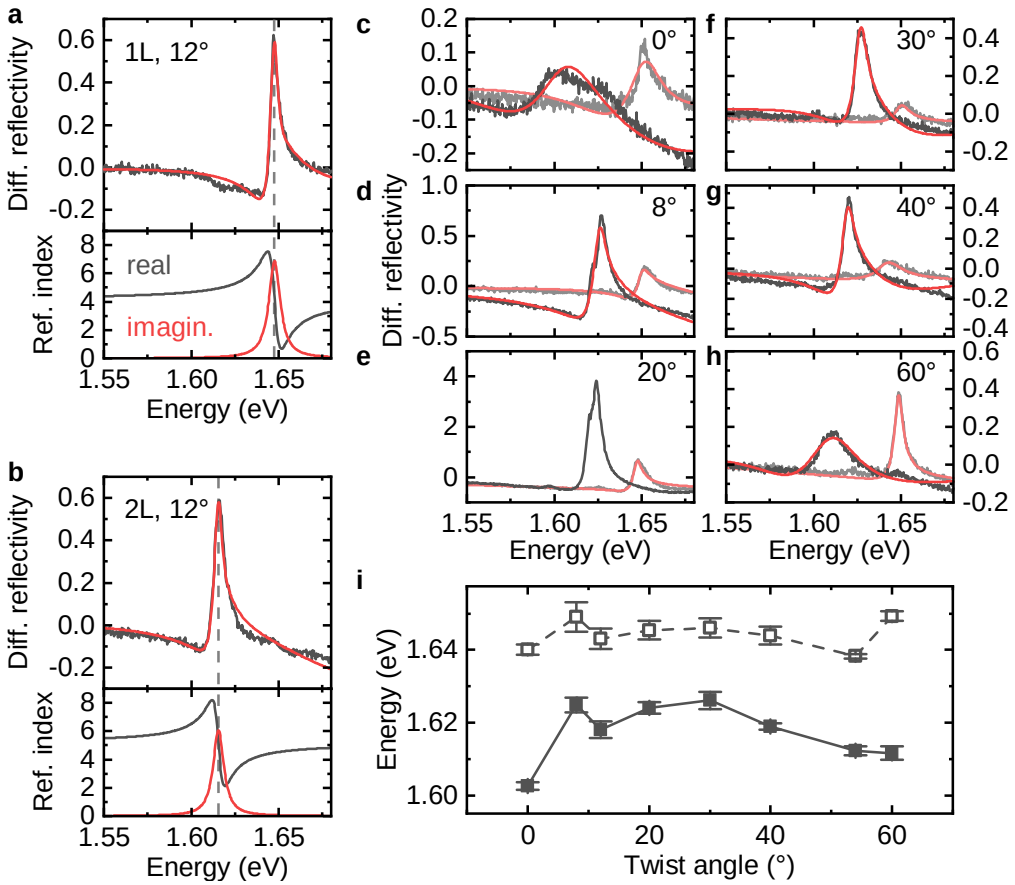

Figure 6.5: **Direct-exciton reflectivity of twisted $MoSe_2$ bilayers. (a, b)** Top: Differential reflectivity spectrum (gray) of a $MoSe_2$ monolayer (a) and a bilayer with 12° twist angle (b), and Lorentz-oscillator fits to the data (red). Bottom: Real (gray) and imaginary (red) part of the refractive index obtained from the Lorentz-oscillator fit. **(c-h)** Differential reflectivity spectra (gray) and Lorentz-oscillator fits (red) of samples containing $MoSe_2$ bilayers with the twist angles denoted in the upper right corner. The faint curves are monolayer spectra from the respective sample for reference, whereas the bilayer spectra are plotted in stronger shades. The 20° bilayer spectrum could not be fitted sufficiently well and is therefore displayed without a fit curve. **(i)** A-exciton energies as function of the bilayer twist angle as extracted from Gaussian fits to the reflectivity data. Open (filled) data points and dashed (solid) lines denote data from the monolayer (bilayer) regions of the sample.

setup depends on the wavelength. To suppress the impact of emission spectrum and detection efficiency, we only show the spectrally resolved differential reflectivity $DR = \frac{R_{on}-R_{off}}{R_{off}}$. Here, R_{on} is the reflected intensity on the area of interest, i.e. the full heterostructure in either the $MoSe_2$ monolayer or the bilayer region, and R_{off} is a reference spectrum of the heterostructure without any $MoSe_2$ but including top and bottom hBN layers. Moreover, optical interference effects within the thin-film sample can modulate its reflectivity. These effects are also taken into account by our theoretical model using the transfer-matrix method (see below and section A.10 of the appendix).

We present the differential-reflectivity spectrum of the monolayer region in the 12° sample in the upper panel of Fig. 6.5a as a gray line. The spectrum exhibits a very pronounced peak in the general vicinity of the A-exciton energy but the maximum of the curve does not have to coincide with the center energy of the resonance. (We have also performed these reflectivity experiments at higher energies, in the range of the $MoSe_2$ B exciton. These data are discussed in section A.11 of the appendix.) For a quantitative analysis of the data, we modelled the refractive index of the $MoSe_2$ monolayer as a single Lorentz oscillator and calculated the differential reflectivity based on the transfer-matrix method (see section A.10 for more details). We leave the parameters (amplitude, resonance energy, width and offset of the real part) of the Lorentz oscillator as well as the thicknesses of the hBN layers undefined and fit this model to the differential-reflectivity data. The fit results are depicted as a red line in the top panel of Fig. 6.5a. The fit agrees very well with the experimentally obtained differential-reflectivity spectrum.

The fitted models for the differential reflectivity include the energy-dependent complex refractive index, which we present in the bottom panel of Fig. 6.5a. This fitted refractive index can be compared to literature values, which were measured using more direct methods, such as ellipsometry. [Par18, Liu20b] Before approaching the A-exciton resonance, the real part of the refractive index is $\sim$ 4, agreeing well with previous reports. [Par18, Liu20b] The amplitude of the resonance, on the other hand, seems to be a little overestimated by our model: The imaginary part of the refractive index rises above six whereas reported values are instead close to or slightly

above one. [Par18, Liu20b] At the same time, the real part of the refractive index drops below one for a small spectral range, which is not physically impossible but an extreme result.

There are several possible reasons for this discrepancy: The A exciton is spectrally close to the B exciton such that the single-oscillator model may be an over-simplified model. In fact, direct measurements of the complex refractive index reveal that the imaginary part, which is associated with absorption, only decreases to half of the maximum value at the A-exciton resonance between A and B exciton, [Par18, Liu20b] whereas it is allowed to decrease to zero in our model. Analogously for the real part of the refractive index, the influence of other resonances cannot be assumed to be a constant value in the fitted region. Moreover, leaving the hBN and SiO_2 layer thicknesses as a fit parameter could result in the model assuming a wrong heterostructure geometry, which could lead to errors in the obtained dielectric function.

We present the differential-reflectivity spectrum from the bilayer region (twist angle 12°) in the top panel of Fig. 6.5b, accompanied by a fit with the previously described model as a red curve. Again, the model reproduces the spectrum well. The extracted refractive indices shown in the bottom panel once again take reasonable values below the A-exciton energy but overestimate the amplitude of the resonance. Comparing the obtained resonance energies for the monolayer and the bilayer (marked by dashed lines in their respective panels), we find a redshift of $\sim 25\,\mathrm{meV}$ in agreement with the results of our PL measurements.

Differential-reflectivity spectra from samples with other bilayer twist angles are given in Figs. 6.5c-h with the twist angles specified in the top right corners. Each panel includes a reference monolayer spectrum in light gray and a bilayer spectrum in dark gray. We plot Lorentz-oscillator fits to the data in red, except for the 20° bilayer, where the measured data could not be reproduced by our model. In all other cases, good agreement between data and fits is observed. Only the 0° bilayer spectrum features a broad peak with hints of a substructure that was not resolved in the experiments. Again, the bilayer spectra exhibit consistent redshifts when compared to their mono-

layer counterparts. This effect is most pronounced for the twist angles of 0° and 60°.

The weighted average resonance energies and their uncertainties for the different samples are presented in Fig. 6.5i. For this, we analyzed the reflectivity spectra in many spots (between 53 and 178) for each sample and averaged as described before for the PL. This procedure could not be applied to the 54° sample since the bilayer region in that sample was too small. Many of the spots didn't allow proper fitting with the Lorentz-oscillator model. Since the spot size is enhanced compared to the PL experiments, most spots do not exhibit pure mono- or bilayer character (like the spectra showcased in Figs. 6.5a-h) but feature both mono- and bilayer regions or have reduced exciton features because parts of the excitation spot do not contain any $MoSe_2$ at all. These constellations could only be described by combining different reflectivity spectra, each obtained from an individual resonance, which would have introduced a multitude of parameters to the model. Instead, we fitted the reflectivity peaks locally with Gaussian peaks after verifying with the pure mono- and bilayer spectra that this analysis method can be used equivalently (see appendix, section A.10). Using this Gauss-fit method (and accounting for its introduced offset), we obtain the energies shown in Fig. 6.5i.

Figure 6.6 summarizes our findings on A-exciton energies from PL and reflectivity spectroscopy at low temperatures. Signatures from the neutral A exciton appeared in the bilayer PL for large twist angles between 8° and 30°. (The 40° sample featured mostly trion emission, most likely due to a high free-carrier density.) The neutral-exciton energies (bilayer and monolayer for reference) obtained from PL measurements are presented in Fig. 6.6a. Reflectivity measurements contain signatures from the neutral exciton in the bilayer region independent of twist angle. The extracted values are summarized in Fig. 6.6b. Where the neutral exciton also appeared in PL, the energies from PL and from reflectivity measurements match well, validating the simplified analysis method for the reflectivity spectra. Trion signatures only appeared in PL experiments and are limited to the range of high twist angles (12° to 40°). The obtained energy values are given in Fig. 6.6c. In all

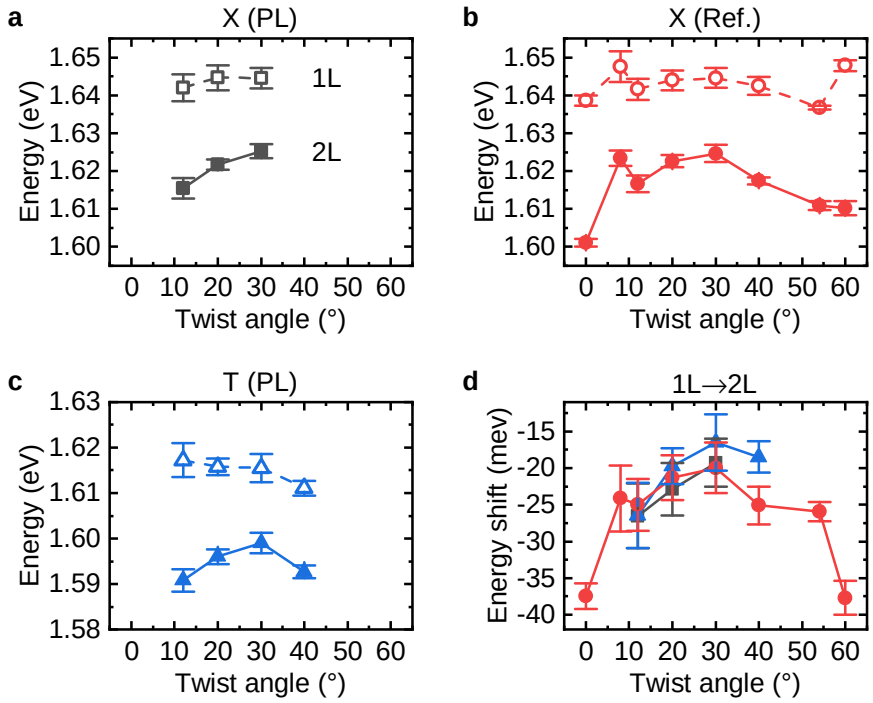

Figure 6.6: **A-exciton energies in bilayer $MoSe_2$ as a function of twist angle. (a-c)** Energies of the neutral A exciton obtained from PL (a) and reflectivity (b) measurements and trion energies obtained from PL measurements (c) as a function of bilayer twist angle. The solid lines and filled data points represent the bilayer data whereas the data of the monolayers in the corresponding sample are given for reference as open data points and dashed lines. The error bars give the standard deviation of the resonance energies across the samples. **(d)** Energy shift between monolayer and bilayer regions for excitons and trions calculated from the data presented in panels (a-c). The color coding matches the color coding in the other panels. Negative shifts correspond to an energy reduction in the bilayer region with respect to the monolayer region. Adapted from [Vil23].

cases, we evaluated the monolayer energy of the samples as well in order to account for general spectral shifts in the individual $MoSe_2$ flake.

We present the energy shift from monolayer to bilayer region as a function of bilayer twist angle in Fig. 6.6d. Here, we combine the data from the neutral exciton as obtained from PL (gray squares) and reflectivity (red circles) as well as data from the trion as obtained from PL (blue triangles). In the large-angle regime, where we have data from all three cases, they exhibit matching behaviors: The redshift in the bilayer region is between 15 meV and 25 meV. The dependence on the twist angle is not pronounced but the redshift appears to be weakest for the maximum twist angle of 30°. The reflectivity data from the samples with twist angle 0° and 60° reveal a significant increase of the redshift to $\sim$ 38 meV.

The dependence of the bilayer A exciton energy on the bilayer twist angle has been studied in other TMD systems as well. Some reports on WS_2 [Yan19] and MoS_2 [vdZ14, Liu14] state that the A-exciton energies as obtained from PL were independent of the twist angle.[2] However, the same reports contain density-functional-theory (DFT) calculations that predict a slightly lower A exciton energy at 0° and 60° on the order of 10 meV related to an enhanced layer separation at larger twist angles, [Yan19, vdZ14, Liu14] which is the exact behavior observed in our experiments.

There have also been some recent reports on artificial $MoSe_2$ bilayers, although, to our knowledge, no comprehensive study on the excitonic properties as a function of twist angle outside of ours is available. Marcellina *et al.* present photoluminescence spectra of bilayers with twist angles close to 0° and 60°, which exhibit emission bands, which they interpret as stemming from moiré-trapped trions. [Mar21] Comparing spectra from monolayer and bilayer regions within their samples, they do not observe any systematic exciton-energy reduction, in stark contrast to our findings. On the other

[2]For completeness, it should be mentioned that also reflectivity measurements are presented in [vdZ14]. There, the top and bottom monolayer are spectrally detuned by $\sim$ 40 meV due to the fabrication process. The homobilayers display a feature, which is energetically between the individual monolayers. There are indications that this feature redshifts for twist angles close 0° but the data is not fully conclusive.

hand, Sung *et al.* present a detailed study of $MoSe_2$ bilayers with a twist angle of 0°, addressing the static electric dipole moment of different excitonic features. [Sun20] In analogy to our results, they see an energetic reduction of the A exciton in the bilayer region by several tens of meV. We cannot offer any conclusions on what causes the discrepancy between the findings by Sung *et al.* and in this thesis on one side and Marcellina *et al.* on the other side. However, we will present a theoretical description of excitons in twisted MoSe2 bilayers in terms of a continuum model in section 6.4, which is in agreement with our findings.

Finally, we examined the photoluminescence of the A exciton in monolayer and twisted bilayer at different excitation-power densities in order to probe possible non-linear dynamics. As a reference, we first present PL spectra of monolayer $MoSe_2$ at different example excitation powers in Fig. 6.7a. The spectra feature prominent emission peaks from the neutral exciton, marked X, and from the trion, marked T. The PL intensity increases with the excitation power but no qualitative differences between the spectra are observed. We fitted the neutral-exciton and the trion peak with Gaussian functions in order to quantify the influence of the excitation power. Figure 6.7b displays the energies of the neutral exciton and trion in gray and red, respectively, as function of the excitation power. At powers below $\sim 200\,\mathrm{nW}$, the PL intensity of the neutral exciton is low compared to the measurement noise, resulting in a larger uncertainty of the fitted energy. Apart from that, no influence of the excitation power on the resonance energies is observed.

We give the integrated PL intensity of both peaks in Fig. 6.7c, where gray and red data points represent the neutral exciton and the trion, respectively. In both cases, the slope in double-logarithmic representation remains constant, indicating that a single power law of the form $I(P) = I_0 \cdot P^{\alpha}$ can describe the data. Here I denotes the integrated PL intensity, P the excitation power and I_0 and the power-law exponent α can be used as free parameters. Fitting these power laws to the data, we find exponents of $\alpha_X = 0.905 \pm 0.011$ for the neutral exciton and $\alpha_T = 0.985 \pm 0.005$ for the trion. Both are close to one, indicating a linear dependence. The population dynamics of both states therefore appear to be governed by linear processes, such as radiative

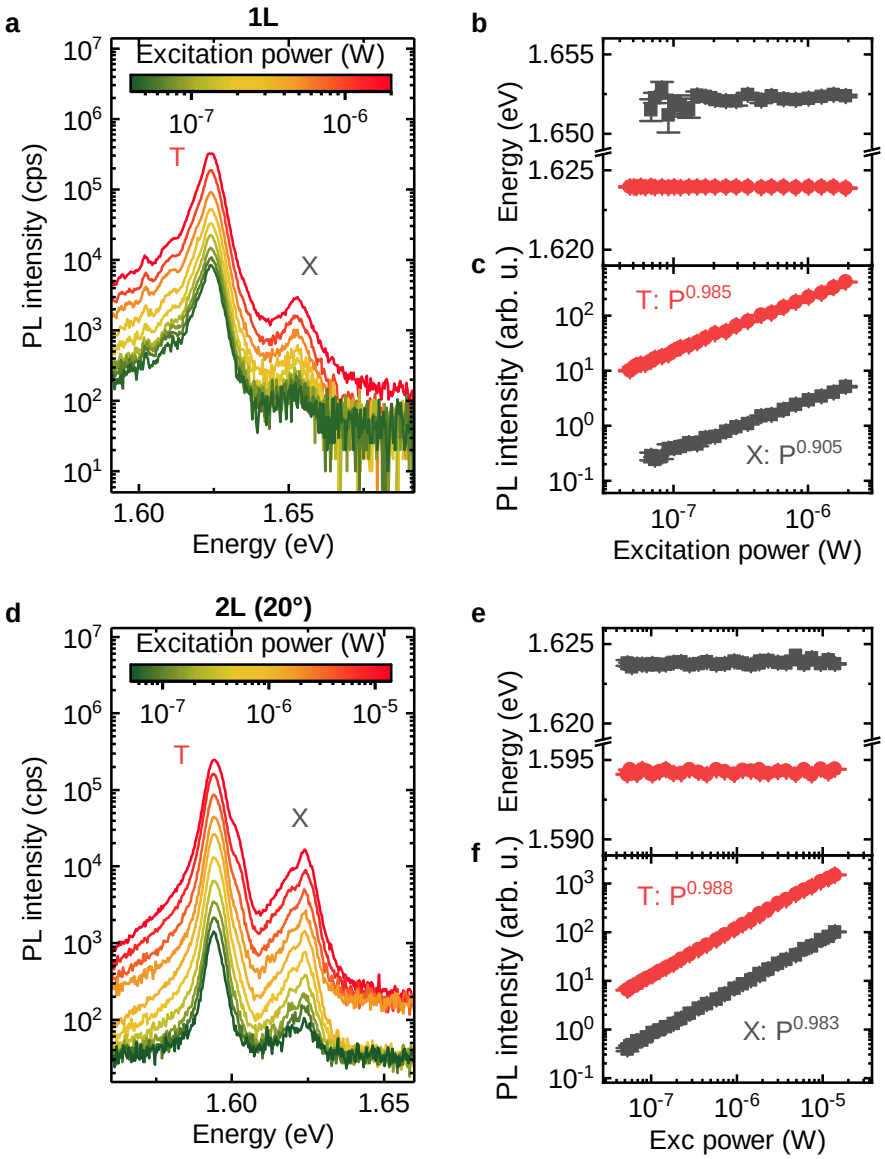

Figure 6.7: **Excitation-power-dependent PL from A excitons and trions in monolayer and twisted bilayer $MoSe_2$.** **(a)** PL spectra of monolayer $MoSe_2$ at different excitation powers. **(b, c)** Emission energy (b) and integrated PL intensity (c) of A excitons (gray) and trions (red) as a function of excitation power. **(d-f)** The same quantities as in panels (a-c) for a bilayer of $MoSe_2$ with a twist angle of 20°. The offset between the groups of curves in panel (d) is due to data with different exposure times of the camera being used. All spectra were aquired at $T = 10\,\mathrm{K}$ with an excitation laser at $\lambda = 532\,\mathrm{nm}$.

recombination or energetic relaxation into a continuum of states. This is in complete agreement with previous studies on monolayer $MoSe_2$.[3] [Bar17]

Photoluminescence spectra from a $MoSe_2$ bilayer with a twist angle of 20° at different excitation powers are given in Fig. 6.7d. As in the monolayer case, we observe emission from the neutral exciton and the trion. Both are at lower energies compared to the monolayer. The PL intensity of both peaks increase as the excitation power is increased, without any changes in the overall shape of the spectrum. At the high-energy end of the depicted spectral range, two groups of spectra can be identified via their distinct baselines. This contrast is due to different acquisition times of the camera for the different measurements. Again, we evaluated resonance energies and integrated PL intensities of both major features for each spectrum by fitting a Gaussian function to the data. The obtained resonance energies are presented in Fig. 6.7e. Gray (red) points denote the neutral exciton (trion) data. Over the two and a half orders of magnitude of excitation power which we examined, no change in the resonance energy is found. The dependence of the integrated PL intensities on excitation power, given in Fig. 6.7f with the same color coding as before, can be described by single power laws again. We find $\alpha_X = 0.983 \pm 0.004$ and $\alpha_T = 0.988 \pm 0.004$. In complete analogy to the monolayer case, the population dynamics of neutral A excitons and charged trions in twisted $MoSe_2$ bilayers are entirely linear within the studied range of excitation powers. The same behavior was found for the other bilayer twist angles which featured A-exciton emission.

[3] Older studies will often report strong photodoping for Mo-based TMDs, meaning that strong laser illumination increases the free-carrier density and thus the trion-to-exciton ratio. [Cad16, Lun18, Wie19] However, these experiments were conducted on monolayers without hBN encapsulation. The encapsulation was later found to suppress the photodoping effects. [Cad17, Wie17]

6.3 Indirect excitons in twisted $MoSe_2$ bilayers

Natural bilayer $MoSe_2$ is known to have an indirect bandgap with the VBM at the Γ point and the CBM at the Σ point. [Hon17] This contrast to the $MoSe_2$ monolayer, which features a direct bandgap at the K point, [Ros13] stems from the interlayer coupling, which is more pronounced for the VB states at Γ and the CB states at Σ than for their respective K-point counterparts and therefore makes them energetically more favorable in a bilayer. [Li07, Spl10, Mak10] Interlayer coupling between electronic states generally has a strong dependence on twist angle, as commonly predicted by theory [Lop07, Tra10, Wan17b] and observed in experiments on various twisted homo-bilayer [vdZ14, Liu14, Yan19] and hetero-bilayer systems. [Ale19] We therefore expect pronounced changes of the indirect bandgap of bilayer $MoSe_2$ with the twist angle. Apart from the natural bilayer, only bilayers at 0° have been studied in that regard so far. There, momentum-indirect ΓK excitons occupying the AB domains and displaying a static out-of-plane dipole moment of 0.23 nm were found to be the lowest-energy states. [Sun20] We studied the low-energy photoluminescence spectra of our twisted $MoSe_2$ bilayer samples (0°, 3°, 8°, 12°, 20°, 30°, 40°, 54° and 60°) and of a natural $MoSe_2$ bilayer in order to reveal signatures of the indirect bandgap.

Figures 6.8a-d display low-energy PL spectra from four $MoSe_2$ bilayer samples. The spectral range extends almost to A-exciton energies. The twist angles of the selected samples are given in the top left corner of each panel. None of the twist angles deviate strongly from 0° or 60°, corresponding to almost parallel or anti-parallel alignment of the two layers. All spectra were recorded at a relatively low excitation power of 1 µW to promote visibility of indirect excitons, as will become clear after the discussion of the excitation-power-dependent data in Fig. 6.9. In each of these spectra, the lowest-energy PL feature is marked by an arrow. The twist angles included in Fig. 6.8 are the ones for which we observed the corresponding low-energy emission over

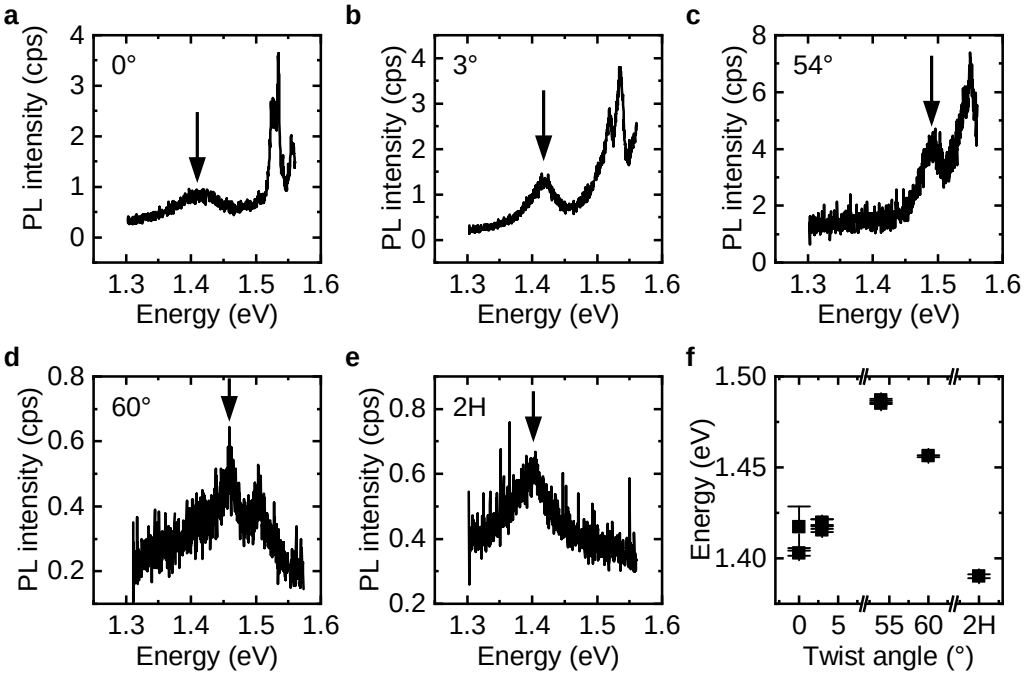

Figure 6.8: **Photoluminescence from indirect excitons in $MoSe_2$ bilayers. (a-e)** Low-energy PL spectra of twisted bilayers (a-d, twist angle in upper left corner) and a natural bilayer (e) of $MoSe_2$ acquired at $T = 10\,\mathrm{K}$ with an excitation laser at $\lambda = 532\,\mathrm{nm}$ and a power of $1\,\mu\mathrm{W}$. The displayed samples were the ones to consistently show a low-energy feature (marked by arrows) over the entire bilayer region, which we interpret as emission from momentum-indirect excitons. **(f)** Energy of the indirect exciton as a function of twist angle. Adapted from [Vil23].

the entire bilayer. We did not observe clear indications of indirect-exciton emission in the remaining samples with twist angles in the range 8° to 40°.

The indirect-exciton PL emission from a natural 2H bilayer of $MoSe_2$ is depicted in Fig. 6.8e. As can be seen from comparing the spectra of samples with various twist angles and of the natural bilayer, the energy of the lowest-energy feature (marked by black arrows in the respective panel) varies strongly from sample to sample. We present the obtained indirect-exciton energies as a function of twist angle in Fig. 6.8f.

To our knowledge, the dependence of the $MoSe_2$-bilayer indirect bandgap on the twist angle has neither been calculated nor been determined experimentally before. Similarly, no literature known to us discusses that only near-aligned samples feature PL signatures of indirect excitons. A simple explanation for this fact would be that the associated transition dipole moment decreases with the twist angle, making the excitons dark in all other samples. However, we do not have direct experimental measurements supporting this modulation of the transition dipole moment.

An alternative explanation for our observations would be that direct and indirect gap are spectrally close at larger twist angles. This hypothesis is supported by findings of our continuum-model description (see section 6.4) and is similar to findings in other materials. The indirect bandgap of bilayer MoS_2 has been observed to vary by 200 meV with twist-angle variations, [vdZ14, Liu14] which corresponds to the energy difference of indirect and direct excitons in our $MoSe_2$ bilayer sample with a twist angle of 0°. The energetic proximity of direct and indirect bandgap can prevent detection of indirect excitons by two mechanisms: Firstly, the PL of the direct transition would overshadow that of the indirect transition due to the larger transition dipole moment. Secondly, fewer excitons would relax to momentum-indirect states if they are not as clearly energetically favorable.

We performed excitation-power-dependent PL measurements on all samples, which exhibited indirect-exciton emission. As an example, we showcase the excitation-power-dependent behavior of indirect excitons in the 60° sample in Fig. 6.9. We will comment on the generalizability of the results to other twist angles after the discussion of this figure. We plot PL spectra for different excitation powers at $T = 10\,\mathrm{K}$ and using an excitation source with $\lambda = 532\,\mathrm{nm}$ in Fig. 6.9a. All spectra consist of two prominent peaks, labelled "P1" ($E \sim 1.459\,\mathrm{eV}$) and "P2" ($E \sim 1.506\,\mathrm{eV}$), and a broad background, which increases towards higher energies. P1 appears consistently over the entire bilayer area as the lowest-energy feature and we therefore attribute it to excitons at the indirect bandgap. Comparing the individual spectra in Fig. 6.9a, we find that P1 stands out above the background more clearly at lower powers. This indicates that the background grows more strongly with

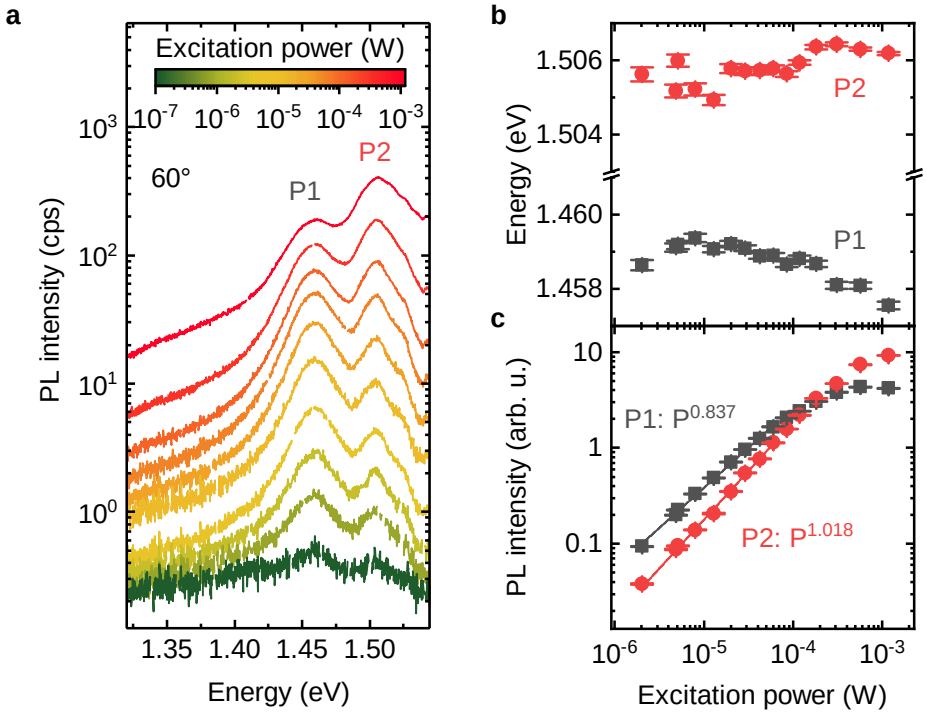

Figure 6.9: **Excitation-power-dependent PL from indirect excitons in a twisted $MoSe_2$ bilayer. (a)** Photoluminescence spectra of $MoSe_2$ bilayer with a twist angle of 60° for excitation powers between 118 nW and 1.2 W. The two main emission features are labelled P1 and P2. **(b, c)** Emission energies (b) and integrated PL intensities (c) of features P1 (gray) and P2 (red) as functions of excitation power. Power-law fits to the power-dependent PL intensity of the form $I(P) = I_0 \cdot P^{\alpha}$ yield a clearly sublinear dependence ($\alpha = 0.837 \pm 0.014$) for P1 and a linear dependence ($\alpha = 1.018 \pm 0.018$) for P2.

the excitation power than P1. This does not hold for P2, which is more clearly visible in the high-power spectra.

All spectra were fitted by interpolating the emission background with a spline and fitting P1 and P2 with Gaussian functions. The results of this analysis are presented in Fig. 6.9b and c. We plot the obtained emission energy as a function of excitation power in Fig. 6.9b. The emission energy of P1 (gray data points) is 1.459 eV at intermediate powers and seems to decrease slightly for lower and higher powers. The most reliable data points, however, stem from the intermediate power range: At lower excitation powers, the peak amplitude of P1 is only slightly higher than the noise level of the spectrum. At high powers, on the other hand, the amplitude of P1 becomes smaller in comparison to the PL background, such that errors in the estimation of the background lead to higher errors of the obtained resonance energy. Overall, we observed no clear signatures of an excitation-power-dependent shift of the energy of P1. P2 does not exhibit pronounced energy shifts as a function of excitation power either.

The PL intensities of P1 and P2 as functions of excitation power are depicted in Fig. 6.9c in double-logarithmic scaling. At low powers, the data points of either peak form a line, indicating the intensity I as a function of excitation power P can be described by a power law of the form $I(P) = I_0 \cdot P^{\alpha}$. Fitting this power law to the data, we find $\alpha = 0.837 \pm 0.014$ for P1 and $\alpha = 1.018 \pm 0.018$ for P2. The population of excitons corresponding to P2 seems to be mainly defined by linear processes, whereas the sublinear power dependence of P1 indicates a non-negligible impact of nonlinear processes, such as Auger recombination, on the population dynamics of excitons at the indirect bandgap.

Performing analogous experiments on bilayers with different twist angles, we found a similar behavior of all indirect excitons to P1. All peaks exhibited a sublinear intensity increase with excitation power. The power factors α ranged from 0.38 ± 0.02 in the 54°-sample to 0.84 ± 0.02 in the 3°-sample. Consequently, all indirect excitons suffered from a poor signal-to-background ratio at high excitation powers, since the background increased linearly with excitation power. All indirect excitons also seemed to exhibit spectral shifts

in the meV range towards higher excitation powers. Excitation-power dependent shifts may be linked to dipolar interactions: Indirect excitons in $MoSe_2$ bilayers with a twist angle of 0° have been measured to possess an out-of-plane dipole moment, as evidenced by their linear Stark shift. [Sun20] Calculations for bilayers with twist angles close to 60° predict a spatial in-plane displacement between VBM and CBM, [Fer21] which would result in an in-plane electric dipole moment. However, the bright background emission introduces large uncertainties in the obtained exciton energies and therefore prevents us from drawing any definitive conclusions.

The reduction of A-exciton emission intensity in (twisted) $MoSe_2$ bilayers compared to monolayers and the emergence of emission from indirect excitons in natural bilayers or bilayers with twist angles close to 0° or 60° suggest energy transfer from the direct to the indirect bandgap. We employed PLE spectroscopy in order to probe this energy transfer more directly for the samples with bilayer twist angles of 0° and 3°. Figure 6.10a displays the low-energy emission from the 0°-bilayer sample under excitation with a laser at $E = 1.610\,\mathrm{eV}$ in black. In analogy to Fig. 6.8a, we find a broad emission feature centered at $\sim 1.42\,\mathrm{eV}$. We varied the energy of the excitation laser (tunable cw Ti:Sa laser SOLSTIS by M Squared), maintaining a constant power of $2\,\mu\mathrm{W}$, and recorded spectra for each excitation energy. We fitted the indirect-exciton emission with two Gaussians and plot the total obtained intensity as a function of excitation energy in red in Fig. 6.10a. For reference, we present a PL spectrum from the monolayer region of the sample in gray. The PLE spectrum (red) has a clear resonance around the A-exciton energy of the monolayer spectrum. This illustrates that excitons excited at the direct (K-K) bandgap can efficiently relax to the indirect bandgap. The resonance exhibits a double-peak structure that requires further investigation. The energy separation of the two peaks of 18 meV is lower than the typical trion binding energy in $MoSe_2$ of 30 meV. [Ros13] The peak separation would spectrally match the longitudinal-acoustic phonons of $MoSe_2$ at the M point. These phonons have been found to couple well to the A

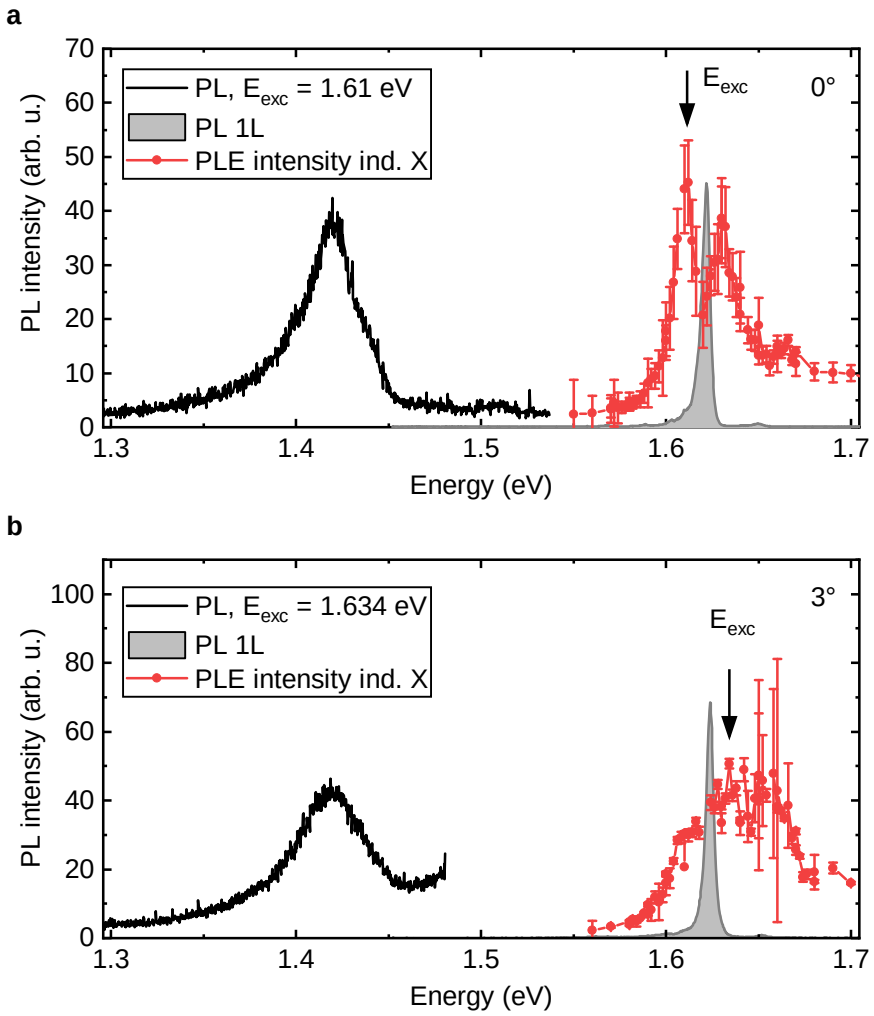

Figure 6.10: **Photoluminescence-excitation spectra of indirect excitons in twisted $MoSe_2$ bilayers. (a, b)** Low-energy PL spectra (black) of $MoSe_2$ bilayers with twist angles of 0° (a) and 3° (b) displaying emission from momentum-indirect excitons. The integrated PL intensity of the indirect-exciton feature as a function of excitation-laser energy (PLE spectrum) is depicted in red. For reference, the (rescaled) PL spectrum of the $MoSe_2$ monolayers is presented in gray. The excitation energy at which the black PL spectrum was obtained is marked by an arrow. The data were aquired at $T = 10\,\mathrm{K}$ and the excitation power was maintained at $2\,\mu\mathrm{W}$ for the PLE measurements.

exciton, leading to multiple peaks in the PLE spectra of the A exciton in monolayer $MoSe_2$. [Cho17] However, the precise origin of the double-peak structure remains to be explored.

We present data for the anologous measurement on a $MoSe_2$ bilayer with a twist angle of 3° in Fig. 6.10b. The black curve represents the low-energy PL spectrum under excitation with $E = 1.634\,\mathrm{eV}$ at $T = 10\,\mathrm{K}$. The red data points denote the integrated PL intensity as a function of excitation photon energy at a constant excitation power of $2\,\mu\mathrm{W}$. We show the PL emission spectrum of the monolayer region in gray for comparison. Again, we find a PLE resonance around the A-exciton energy. Towards higher energies, the PL intensity decreases again. At lower energies than the A exciton, the PL intensity vanishes completely. In comparison to the 0°-bilayer, the PLE resonance appears broadened and does not exhibit any identifiable substructure. In both cases, we find resonant enhancement of the PL intensity when exciting around the A-exciton energy, illustrating the efficient energy transfer from the direct to the indirect bandgap. We have, however, not explored the precise shape of the PLE spectra further.

6.4 Continuum model for moiré excitons in $MoSe_2$ homobilayers

We applied a low-energy continuum model to gain insights into the states involved in the observed optical transitions and their evolution with bilayer twist angle. Computational details can be found in the Supplemental Material (SM) of our publication on the topic. [Vil23] All calculations were performed by our collaborators at the University of Michigan, Matthias Florian, and at the University of Bremen, Ruven Hübner and Alexander Steinhoff. As a general strategy, we will use that the moiré supercell corresponds to a smooth variation of stacking orders, as visualized in Fig. 6.12a. We calculate the bandstructure of a $MoSe_2$ homobilayer at different stacking orders via density-functional theory (DFT), as shown in Fig. 6.12c. We will treat moiré supercells by generating an effective potential for the center-of-mass Hamil-

tonian for each exciton species from the energetic variations for different stacking orders. The twist angle of the homobilayer enters these calculations as a scaling factor for the periodic moiré potential.

Figure 6.12a displays two identical honeycomb lattices at a relative twist angle of 5°. A moiré pattern, of which we outline a unit cell with black lines, forms. We marked the path between two vertices of the moiré superlattice. Along this path, the stacking order of the two layers varies smoothly, as illustrated in the bottom part of Fig. 6.12a. (See Fig.A.1 for illustrations of a homobilayer close to 60° twist angle.) In a first step, we calculate the band structures of $MoSe_2$ homobilayers without a twist angle between the two layers for different translations between the two layers. For R-stacking, we use the six positions marked in Fig. 6.12a, i.e. we calculate the band structure for the high-symmetry stacking order AA, the low-symmetry stacking orders AB and BA, as well as the stacking orders halfway between each two of these.

For our calculations, we consider conduction-band states at the K points and valence-band states at the K and Γ points. This covers the lowest-energy direct transitions $X_{1,2,3,4}$ and the lowest indirect transition X_{ind}, as illustrated in Fig. 6.12b. The results for the stacking-order-dependent energies of these states are presented in Fig. 6.12c. There, upward-pointing (downward-pointing) triangles correspond to spin-up (spin-down) states. (At the Γ point, the different spin states are degenerate. The K point features a splitting of the different spins. The energies for the different spin states would be interchanged at the −K point.) The color encodes layer contribution. The Γ-VB states are always spread out over the two layers due to strong interlayer hopping. The states at the K points are highly localized for mirror-symmetry breaking stacking orders, i.e. for AB and BA stacking. At the mirror-symmetric AA stacking, both layers contribute equally to each state. For homobilayers close to 60° (not shown here), all stacking orders in the moiré supercell preserve inversion symmetry. Therefore, there is no energetic splitting between the spin states. However, the different spin states are localized in different layers, see SM of [Vil23]. The energies of all states

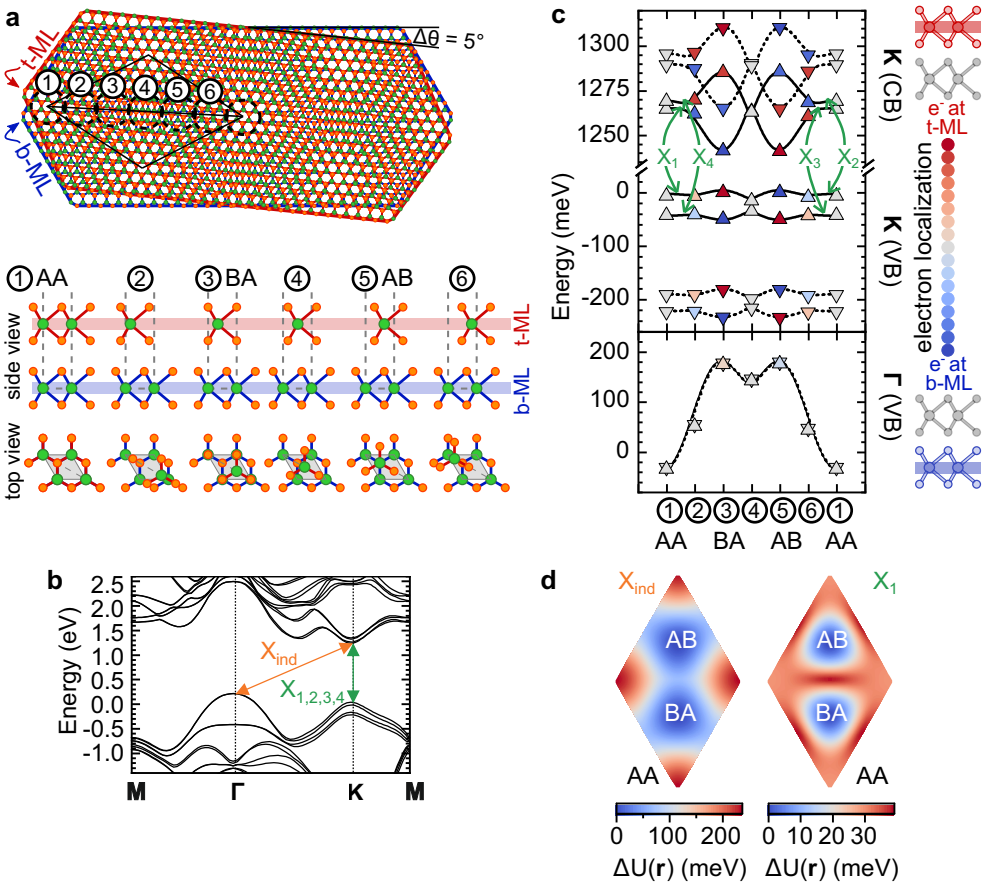

Figure caption on page 119. Reprinted figure with permission from Viviana Villafañe, Malte Kremser et al., Physical Review Letters, 130, 026901, 2023. [Vil23] Copyright (2023) by the American Physical Society. Original creators: R. Hübner, M. Florian and A. Steinhoff.

vary with stacking order. However, this effect is most pronounced for the Γ VB states. Due to their high interlayer-hopping terms, the change of layer distance between different stacking orders has the strongest impact on them.

The DFT calcualtions carried out so far assume homobilayers with a constant stacking order. To apply this to twisted bilayers, we use the energy variations seen in Fig. 6.12c to construct an effective potential for each exciton species across the moiré unit cell. [Wan17b, Hag21] The resulting potential for X_{ind} and X_1 are depicted in Fig. 6.12d. The Hamiltonian describing the center-of-mass (COM) motion of the exciton then reads:

Figure 6.12: **Potential energies and layer localization of excitons in a $MoSe_2$-bilayer moiré superlattice.** (Figure on page 118.) **(a)** Top: Visualization of a moiré superlattice of two hexagonal layers with no lattice mismatch and a twist angle of 5°. Bottom: Various stacking sequences occuring in the moiré supercell. The position of the stacking orders is marked via numbers in the upper panel. **(b)** Band structure of a $MoSe_2$ homobilayer for AB stacking order including spin-orbit coupling, determined via density-functional theory calculations. **(c)** Energy variation of the conduction-band minimum at the **K**-point as well as the valence-band maxima at the **K**- and **Γ**-point as a function of interlayer translation. Upward-pointing (downward-pointing) triangles correspond to spin up (down) bands. The color encodes the layer contribution to Bloch states. The solid (dashed) lines denote the result of our fit model for the variation of spin up (down) bands. **(d)** Moiré potentials $\Delta U(\mathbf{r})$ for the indirect exciton X_{ind} and the direct exciton X_1 relative to the potential minimum within the moiré unit cell.

$$\hat{H}_0 = E^0_{\mathrm{gap}} + \frac{\hbar^2 \hat{\boldsymbol{Q}}^2}{2M} + U(\hat{\boldsymbol{r}})\,, \tag{6.1}$$

Here, E^0_{gap} is the local band gap corresponding to $\boldsymbol{r} = 0$ and M is the total effective mass of electron and hole combined. $\boldsymbol{Q}$ and $\boldsymbol{r}$ are the COM wavevector and position vector, respectively. Within our model, the evolution of potential energy over the moiré supercell only depends on the type of stacking (R-type close to 0° and H-type close to 60°). The exact twist angle enters the model only via the size of the moiré supercell, i.e. as a scaling factor on $\boldsymbol{r}$ in the periodic potential energy. Close to 0°, the moiré supercell scales with $1/\sin(\theta/2)$ whereas it scales with $1/\sin((\frac{\pi}{3} - \theta)/2)$ close to 60°. A central limitation of our model is that we extend these considerations also to larger twist angles (close to 30°) where the moiré approximation does not hold anymore. For more accurate results, one would have to consider the entire moiré supercell for DFT calculations, which would have been computationally unfeasible.

The exciton energies as a function of twist angle are depicted as lines in Fig. 6.13a. The data points denote our experimental data. The calculated energies have been shifted by 554 meV in order to match experimental and calculated values for the indirect excitons. This is in agreement with expected GW corrections. [He14] The discontinuity at 30° is a result of our model that considers the stacking order as strictly R-type (H-type) for angles below (above) 30°. The color coding of the line indicates whether the transitions have an intralayer or an interlayer character. This character is linked to the twist-angle dependent energy shifts: The strongest shifts are seen for the indirect excitons X_{ind}. There, the energies of holes at the Γ point vary strongly with stacking order (and therefore also twist angle) due to the large interlayer hopping terms. For direct transitions, which feature layer-localized states, interlayer transitions react more sensitively than intralayer transitions to variations in the interlayer distance and therefore display a larger energy shift with twist angle.

For R-stacking, the energetically lowest direct excitons, X_2 and X_3, are split by 12 meV at 0°, followed by the interlayer exciton X_1. The twist-angle dependence of the energy of the intralayer excitons matches our experimental results and we can identify the lowest-energy exciton X_2 as the neutral-exciton peak seen in PL in Fig. 6.4. The calculations for 0° also match electric-field dependent reflectivity data for almost-aligned $MoSe_2$ homobilayers. [Sun20] For H-stacking, there are only two direct transition energies because the two intralayer (interlayer) transitions are degenerate due to inversion symmetry. The double-peak structure in the reflectivity data for 0°, 8° and 20° in Fig. 6.5 might be due to contributions from X_2 and X_3. It is possible that the full description of our direct-exciton data requires layer hybridaztion effects between X_2 and X_3, [RT19] which our model does not take into consideration. (These two transitions have intra-layer character but the states are localized in opposite layers.) Lattice reconstruction effects [Wes20] have also been neglected.

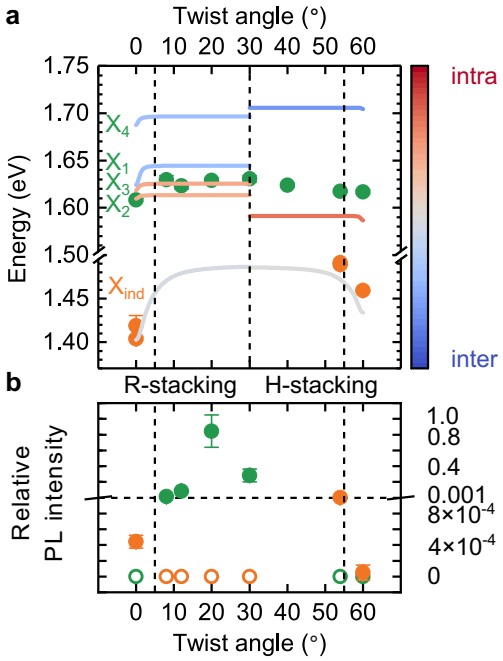

Figure 6.13: **Twist-angle dependent properties of excitons in twisted bilayers of $MoSe_2$ (a)** Angle-dependent exciton energies. Solid lines denote the result of our continuum model based on DFT calculations. Each line corresponds to an individual exciton species, while the color encodes the layer character. The intermediate case (gray color) indicates delocalization of electron and/or hole over both layers. The green and orange data points are taken from Fig. 6.5 (DR, X^0), Fig. 6.4 (PL, X^0) and Fig. 6.8 (PL, X_{ind}). **(b)** Integrated PL intensity for X^0 and X_{ind} relative to the corresponding monolayer intensity as a function of twist angle. Reprinted with permission from [Vil23]. Original creators: R. Hübner, M. Florian and A. Steinhoff.

Finally, Fig. 6.13b displays the measured integrated PL intensity for intralayer and interlayer transitions relative to the monolayer PL intensities of the same samples. Close to 0° and close to 60°, we observe a reduction of direct-exciton PL accompanied by an increase of indirect-exciton PL. This agrees with an increase of the energetic splitting between direct and indirect excitons from 150 meV to 200 meV, which favors population transfer from direct to indirect excitons.

6.5 Summary

We have produced artificial bilayers of $MoSe_2$ with a variety of twist angles and studied different excitonic states with PL and reflectivity spectroscopy. Moreover, we described excitons in the moire superlattices of twisted MoSe2 bilayers in terms of a continuum model, which reproduced our experimental findings. The neutral A exciton was found to be energetically reduced by at least 15 meV in the bilayers compared to their constituent monolayers. For twist angles between 10° and 50°, we observed only a minor modulation of the exciton energy with the twist angle. Approaching the parallel (0°) or antiparallel (60°) alignment, the redshift abruptly increased to 38 meV. Very similar behaviors have been reported for bilayers of MoS_2 and WS_2. [Liu14, vdZ14, Yan19] The trion was only observed in PL measurements at twist angles around 30° but it appears to follow the same trend as the neutral exciton.

For samples with twist angles close to 0° or 60°, we were able to identify indirect excitons in low-energy PL spectra. The sublinear dependence of their PL intensity on excitation power suggest nonlinear decay dynamics, such as Auger recombination. We were not able to identify indirect excitons in samples with higher twist angles but instead observed a brightening of the direct-exciton PL, which indicates the indirect bandgap energetically shifting towards the direct bandgap, as predicted by our continuum-model calculations.

Twisted $MoSe_2$ bilayers are a promising system to realize controllable potential landscapes for bright excitons with dipolar interactions. [Sun20, Fer21] Our findings represent a strong starting point for continued studies on this hitherto largely unexplored platform.

CHAPTER 7

Summary

In this thesis, we studied the excitonic properties of different devices featuring monolayers or artificial bilayers of semiconducting transition metal dichalcogenides. We probed the influence of substrates (topography and dielectric properties) and TMD layer sequences (materials and twist angle) on the electronic excitations of the studied systems. In the following, we will review our most important findings and suggest future studies that could expand our understanding of TMD monolayer and few-layer structures.

Substrate engineering for strain-trapped excitons in monolayer tungsten diselenide

In chapter 3, we studied localized excitons in WSe_2 monolayers, trapped at sites of dielectric nanopillars on top of the substrate. The tensile strain induced by the pillar leads to a reduction of the bandgap and therefore creates localized states with energies below the optical bandgap of the unstrained material. These states have been demonstrated to act as single-photon emitters. [Bra17, PB17] In analogy to previous studies, we found clear indications of the discrete nature of the emitters, such as saturation at high excitation

powers. A common disadvantages of these single-photon emitters is their poor spectral stability. [Ton15, Cha15, He15, Kop15, Sri15a, Kum15, Bra17, PB17] We therefore built on previous research on the influence of substrate material on the optical quality of unstrained TMDs [Iff17] and compared nanopillar substrates based on different materials. Nanopillars based on HSQ (resist for e-beam lithography that takes a SiO_2-like structure after development) resulted in emitters with broad linewidths ((3.1 ± 1.3) meV) and pronounced spectral wandering ((2.0 ± 1.2) meV) on sub-Hz timescales. In comparison to this established substrate choice, [PB17] we observed clear improvements using substrates with pillars etched into MBE-grown GaAs-AlGaAs heterostructures: The linewidths of WSe_2 emitters in these samples were only (2.0 ± 1.3) meV and the sub-Hz spectral wandering was reduced by almost an order of magnitude to (0.32 ± 0.36) meV.

At the time of our studies discussed above, several groups reported that hBN can act as an ideal substrate for TMD monolayers, resulting in emission linewidths of free excitons close to the lifetime limit. [Cad17, Aja17, Wie17] Surprisingly, such beneficial effects have not been reported for the WSe_2 emitters. However, hBN encapsulation allows to integrate the WSe_2 into a capacitor structure based solely on 2D materials. [BG19] In analogy to GaAs quantum dots, [Zha20] control over the applied electric field is expected to reduce electrical noise and thus reduce linewidth broadening. Moreover, such devices can facilitate manipulation of the charge state of the trap, allowing control over the emission spectrum. [BG19] Overall, the optical quality of WSe_2 emitters still needs to be enhanced strongly to make them appealing for quantum-photonic applications, which may be done through combined efforts of substrate engineering and electrical control.

Strain-defined potential traps for interlayer excitons in TMD heterobilayers

In chapter 4, we applied the established technique of defining strain perturbations through patterned substrates to TMD heterobilayers. The PL spectrum of a $MoSe_2$-WSe_2 HBL featured additional peaks redshifted from free

interlayer excitons by up to 100 meV. These localized peaks shared various characteristics with free interlayer excitons, substantiating our assignment of these features as localized interlayer excitons: The enhanced radiative decay time of (118.8 ± 2.1) ns compared to intralayer excitons can be explained by the reduced electron-hole wavefunction overlap and matches the temporal dynamics of free interlayer excitons in the sample. Photoluminescence-excitation resonances at the $MoSe_2$ and WSe_2 monolayer exciton energies demonstrate decay paths originating in the separate monolayer materials to the monitored states. Finally, increasing the excitation power and thus the exciton density results in a strong blueshift of the emission due to the repulsive dipolar interactions, as studied in more detail in chapter 5.

To our knowledge, our work represents the first realization of site-selective traps for interlayer excitons in TMD heterobilayers. Following publication of our work, several groups have presented analogous works that largely confirm our findings. [Li20, Wan20] The approach has also been demonstrated using WS_2-WSe_2 HBLs, where even longer radiative lifetimes of up to 4 µs have been observed. [Mon21] In addition, the electric dipole moment of IXs offers the possibility to define traps electrostaticaly, which has in the meantime been demonstrated using a graphene layer patterned on a ~ 30 nm length-scale. [Sha21] The prospect of creating long-lived and strongly interacting Bosonic ensembles continues to drive reasearch on optimal methods to trap and control interlayer excitons. [Mor21]

Dipolar interactions of interlayer excitons in nano-scale confinement potentials

We investigated the excitation-power-dependent blueshift of localized interlayer excitons, which occurs via discrete jumps as opposed to a continuous shift, in more detail in chapter 5. By analyzing the different dependencies on excitation power of various peaks (and their ratios), we were able to assign the PL features to complexes of one to five excitons. We reproduced the successive blueshifts for increasing particle numbers with a model of classical point dipoles in a two-dimensional harmonic trapping potential. The biexci-

ton blueshift of (8.4 ± 0.6) meV and splitting of (1.2 ± 0.5) meV allowed for a more detailed modelling of the trapping potential: Interpreting the splitting as arising from exchange interactions between the two excitons and incorporating exchange interactions into our calculations, we found a confinement length of 3 nm while simultaneously reproducing a realistic effective dielectric constant of 3.

After the initial publication of our manuscript on the topic, [Kre20] another group confirmed most of our findings. [Li20] Overall, dipolar excitons in TMD bilayers have thereby been demonstrated to exhibit strong interaction phenomena when confined to short length scales. These interaction effects could be utilized for quantum-simulation purposes or for nonlinear optical elements. Our work represents an important proof-of-concept but also calls for systems with a higher degree of reproducibility and controllability of the confinement potentials, such as the moiré potential in twisted bilayers.

Excitons in twisted molybdenum diselenide bilayers

In chapter 6 we studied the influence of the twist angle on the excitonic properties of artificial $MoSe_2$ bilayers. We examined a series of fully hBN-encapsulated bilayers with twist angles spanning the entire parameter range from 0° to 60° with different optical-spectroscopy techniques. Differential reflectivity and PL spectra revealed that the A exciton is always energetically reduced by at least 15 meV in bilayers compared to monolayers. The energetic difference is particularly large for twist angles of 0° or 60°, where we observed a redshift of 38 meV. We evaluated the trion energies in bilayers in the twist-angle range 12° to 40° from PL measurements and observed energy shifts equivalent to the case of neutral A excitons.

Bilayers with twist angles close to 0° or 60° furthermore featured low-energy PL emission related to the indirect bandgap of the material. The sublinear power dependencies of the intensities of these peaks indicate nonlinear processes contributing to the population dynamics. We did not observe discernible PL from indirect excitons at larger twist angles, which indicates energetic proximity of the momentum-direct and indirect exciton species.

We applied a continuum model to excitons moving through the moiré superlattice of a twisted bilayer, based on DFT calculations for different stacking orders occuring in the moiré supercell. These calculations predicted the same twist-angle dependencies that were experimentally observed for momentum-direct excitons and deduced for momentum-indirect excitons from the relative PL intensities of the different exciton species.

While other materials, such as MoS_2 [vdZ14, Liu14] and WS_2, [Zhe15, Yan19, Sha20] have been studied extensively, twisted bilayers of $MoSe_2$ are still relatively unexplored. Our studies examined central properties of the system, in particular different exciton energies. With temporal dynamics, interactions between excitons and interactions with external electric and magnetic fields not yet examined, this promising material system still features many unknown parameters to be the subject of future studies.

Outlook

Using patterned substrates and thereby creating site-selective confinement potentials, we have demonstrated that dipolar excitons in artificial TMD bilayers can exhibit strong (direct and exchange) interaction effects. However, a higher degree of control over the confinement potential is required to utilize these effects in quantum simulation or for optical devices. The moiré potential in twisted bilayers could offer such a well-defined potential landscape. Near-aligned bilayers of $MoSe_2$ have been demonstrated to host long-lived excitons with a static electric dipole moment on the same order of magnitude as interlayer excitons in $MoSe_2$-WSe_2 heterobilayers. [Sun20, Bae20] At the same time, homobilayers offer high control over the twist angle via the tear-and-stack fabrication technique [Kim16] and access to a large range of moiré periods. As we have discussed, the indirect excitons persist with only minor energy shifts to twist angles of at least 3°, which are already associated with moiré periods below 10 nm, where strong interactions are expected to occur. We expect that this system will offer complex interaction physics that can be strongly tuned via the moiré period and external electric fields.

APPENDIX A

Appendix

A.1 List of abbreviations

- 1L: Monolayer
- 2D: Two-dimensional
- 2L: Bilayer
- AFM: Atomic-force microscopy
- BZ: Brillouin zone
- CB: Conduction band
- CBM: Conduction band minimum
- CCD: Charge-coupled device
- CVD: Chemical vapor deposition
- CW: Continuous wave
- DBR: Distributed Bragg reflector
- DC: Direct current

- DFT: Density-functional theory
- DOP: Degree of polarization
- e-beam: Electron beam
- FWHM: Full width at half maximum
- HBL: Heterobilayer
- hBN: Hexagonal boron nitride
- HIM: Helium-ion microscope
- HSQ: Hydrogen silsesquioxane
- IPA: Isopropyl alcohol
- IX: Interlayer exciton
- LIX: Localized interlayer exciton
- low-T: Low-temperature
- MBE: Molecular-beam epitaxy
- PC: Polycarbonate
- PDMS: Polydimethylsiloxane
- PL: Phtotoluminescence
- PLE: Photoluminescence excitation
- QD: Quantum dot
- RF: Radio frequency
- RIE: Reactive-ion
- RMS: Root mean square
- SPE: Single-photon emitter
- T: Trion
- Ti:Sa: Titanium-sapphire
- TMAH: Tetramethylammoniumhydroxid
- TMD: Transition metal dichalcogenide

- VB: Valence band
- VBM: Valence band maximum
- vdW: Van der Waals
- WSC: Wigner-Seitz cell
- X: Exciton

A.2 Stacking order in moiré superlattices

We visualize the different high-symmetry stacking orders in a moiré superlattice in Fig. A.1. Panel (a) shows two identical TMD monolayers rotated by an angle of 4°. With the twist angle being close to 0°, the local symmetry of the bilayer system is rhombohedral. The precise atomic alignment varies over the moiré supercell. We will refer to the fully aligned stacking order, in which the transition-metal atoms of both layers sit on top of each other, as AA stacking. If the transition-metal (chalcogen) atoms of the top layer are aligned with the chalcogen (transition-metal) atoms of the bottom layer, we will refer to this stacking as AB (BA). We also noted another popular nomenclature of these stacking orders of the form R^i_h. Here, R stands for "rhombohedral" and the top index i can take the values h, X or M, indicating whether the "hole" of the honeycomb structure of the bottom layer is aligned with a top-layer "hole", chalcogen atom or transition-metal atom, respectively. Fig. A.1c illustrates the stacking orders for a twist angle of 56°, close to 60°. Here, the local symmetry is hexagonal. The notation H^i_h works analogously to the rhombohedral case, with the H standing for "hexagonal". The H^h_h stacking resembles the 2H stacking of the most common TMD polytypes. The stacking orders MM and XX denote that the transition-metal and the chalcogen atoms of the two layers are aligned, respectively.

The picture of the rigid moiré superlattice breaks down for twist angles very close to 0° or 60°. If the deviations are smaller than $\sim 6°$, the atomic lattice will undergo reconstruction in order to promote energetically more favorable stacking. [Car18, Ros20, Qua21] The AB and BA stacking close to

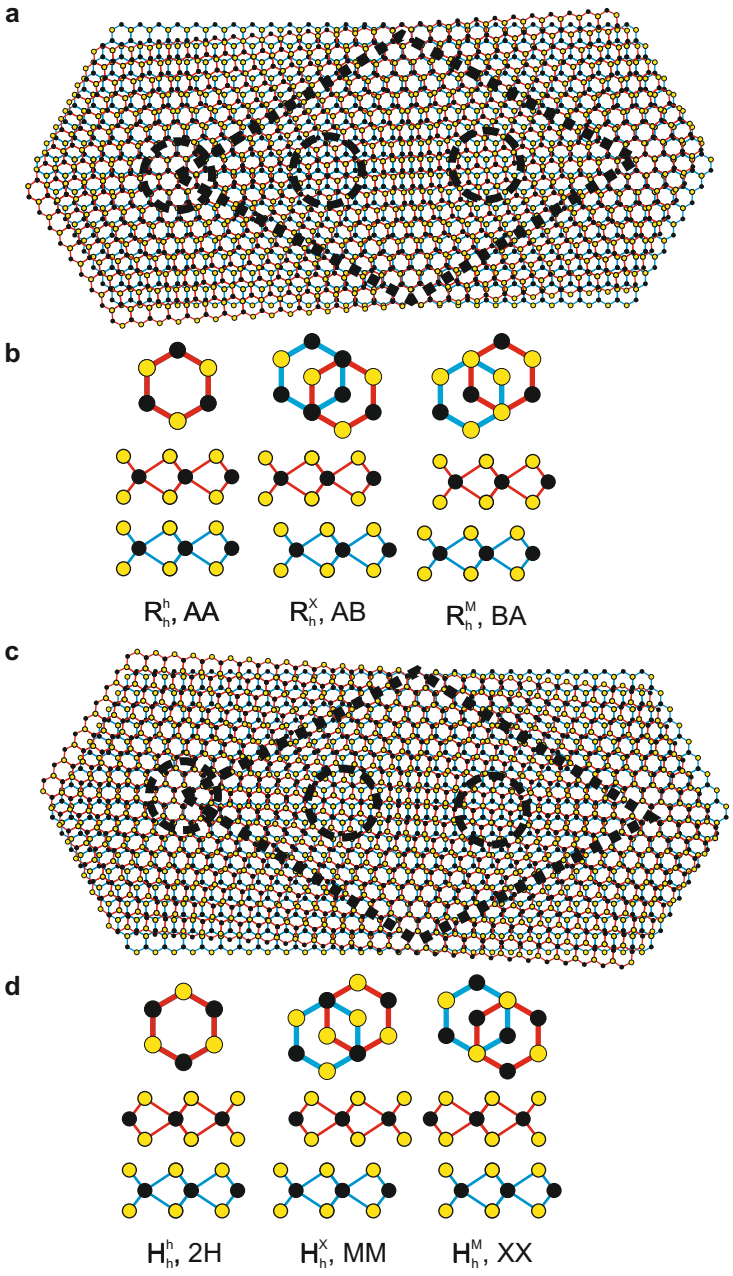

Figure A.1: **Stacking orders in twisted bilayers of TMDs. (a)** Two identical honeycomb lattices (edges colored blue and red for better visibility) with a twist angle of 4°. The unit cell of the moiré superlattice is outlined by the dashed rhombus. Dashed circles mark points of high-symmetry stacking orders. **(b)** Top and side views of the stacking orders outlined in panel (a). **(c, d)** The same as panels (a) and (b) for a twist angle of 56°.

0° are mirror images of each other and therefore energetically equivalent. The AA stacking is energetically less favorable in comparison, mostly because it requires a higher interlayer distance and consequently reduces the electronic hybridization between the layers. A marginally twisted bilayer will therefore form large, alternating, triangular domains of AB and BA stacking, whereas the AA domains will be compressed and sit at the vertices of the AB and BA domains. Close to 60°, the energetically most favorable stacking order is also the one with the shortest interlayer distance, namely the 2H stacking. To minimize the energy, large, hexagonally shaped 2H domains will form, with small spots of MM and XX stacking at the vertices, which, in turn, span a honeycomb lattice. Both types of reconstruction have been directly imaged via electron microscopy [Wes20, And21] and piezoresponse force microscopy. [McG20]

For homobilayers, the stacking order strongly defines the electronic structure: Close to 0°, the only stacking order with mirror symmetry between the two layers is the AA stacking. The AB and BA stacking, on the other hand, break this symmetry, such that the two layers are locally not equivalent. These stacking orders are the energetically more favorable ones and they typically contain the global VBM and CBM of the bilayer. [Fer21] In near-aligned $MoSe_2$ bilayers, this leads to the lowest-energy exciton having a dipolar character, with the electrons localized mostly in the top (bottom) layer for AB (BA) stacking. [Sun20] Since the two stacking orders are mirror images of each other, they also mirror physics of each other, with the exciton dipole exactly flipped.

For twist angles in the vicinity of 60°, inversion symmetry between top and bottom layer is always locally preserved. Unless this symmetry is broken by external factors, such as applied electric fields or different dielectric environments, the layers are equivalent and, consequently, excitons should not have an out-of-plane dipole moment. The VBM for $MoSe_2$ is always located within the 2H domain but it is dragged towards the borders to XX domain for very small angles. [Fer21] The MM domains, on the other hand, feature the CBM, at least for deviations $\leq 3°$ from twist angles of 60°. [Fer21] These distinctly different potential landscapes for electrons and holes may lead to

confinement of excitons along domain boundaries and possibly to in-plane dipole moments.

A.3 Fabrication of pillar substrates

We used three types of pillar substrates in this thesis. The first two, SiO_2 substrates with HSQ-based pillars and AlGaAs substrates with etched pillars, are used in chapter 3 and compared with each other in terms of spectral stability in section 3.4. The third kind, for which the pillar structures were etched into the SiO_2 substrate, was used for the sample in chapters 4 and 5. In the following, we will describe the fabrication steps for the three types of substrates in the order in which they were mentioned here.

For the SiO_2 substrates with HSQ-based pillars, we start with a commercially available Si-[100] wafer with 285 nm of thermally grown oxide. The wafer is cleaved into smaller pieces (6 mm to 10 mm), cleaned (ultrasonic bath in acetone, then IPA; finally subjected to oxygen plasma) and spin-coated with HSQ (Dow Corning) with 6000 rpm. We then bake the wafer pieces at 80 °C for 4 min and write disk patterns in e-beam lithography with a dose of 2000 $\mu C\,cm^{-2}$. The resist is developed by submersion in 25 % TMAH at 80 °C for 30 s followed by a thorough rinse with flowing deionized water.

For the AlGaAs substrates, we start with a commercially available GaAs-[100] wafer. We then grow additional layers of various AlGaAs compounds with molecular beam epitaxy. First, a GaAs buffer layer of 300 nm is grown to ensure a high-quality substrate for the subsequent growth steps. We then grow 15 pairs of alternating layers of 72.4 nm AlAs and 59.4 nm GaAs, which form a DBR at typical WSe_2 emitter wavelengths. The last layer consists 325.6 nm of $Al_{0.41}Ga_{0.59}As$ which will be directly beneath the WSe_2 monolayer. This height was chosen such that the layer hosts 1.5 wavelengths of typical WSe_2 emitters ($\sim$ 750 nm vacuum wavelength) and, as a consequence, there would be an electric-field maximum at the substrate surface. (The thicknesses were initially determined for a flat substrate and not corrected for the pillar geometry.)

The pillars are then etched into the top layer. For this, we first deposit 70 nm of Si_3N_4 as a hardmask via plasma-assisted chemical-vapor deposition (CVD). Si_3N_4 was chosen as a mask material because we can selectively etch Si_3N_4 or AlGaAs using Cl-based or F-based RIE processes, respectively. We spin-coat the samples with AR-N 7520.07 (new version; by Allresist), a negative e-beam resist, at 4000 rpm and pre-bake it at 85 °C for 5 min. This was found to result in a resist thickness of (92.2 ± 1.7) nm. We use a dose of $25\,\mu C\,cm^{-2}$ to write the disk pattern. We develop the resist in 66 % AR300-47 (Allresist) for 90 s and bake the sample at 125 °C for 5 min, after which only pillars of the resist remain. This pattern is transferred into the Si_3N_4 by F-based RIE. We remove resist residues in an oxygen plasma. This removes the resist and leaves the MBE-grown wafer covered with pillars of Si_3N_4. We etch into the wafer with a Cl-based RIE process, typically to depths ≤ 200 nm. The Si_3N_4 pillars are finally removed by F-based RIE. Before the WSe_2 transfer, the substrate is dipped into HCl in order to remove the oxide at the surface that could have formed from the oxygen plasma.

The fabrication of the etched SiO_2 pillar samples starts with Si-[100] wafers with 285 nm of oxide. The lithography is carried out with the AR-N 7520.07, as described above. Afterwards, F-based RIE was carried out to etch into the SiO_2. We compared different etch recipes, which turned out to produce similar results, as described in the next section. Finally, we removed resist residues with an oxygen plasma.

A.4 Reactive-ion etching

In preparation for the pillar etching process used for the sample in chapters 4 and 5, we determined SiO_2 etching rates of different RIE recipes and also compared them in terms of selectivity versus the favored e-beam resist AR-N 7520.07 new (AllResist).

The used substrates were pieces of a p-Si-[100] wafer covered by 285 nm of SiO_2. Pieces of 5 mm edge length were cleaved out of the wafer and cleaned in an ultrasonic bath at 50 °C at the highest power for at least 10 minutes, first

Recipe name	eSAE	RT3	EK
Temperature (°C)	25	25	5
Pressure (mTorr)	10	7	17
RF forward (W)	80	50	80
ICP forward (W)	0	0	150
Helium backing	8	5	10
C_4F_8 (sccm)	8	10	18
SF_6 (sccm)	0	0	0
O_2 (sccm)	2	0	2
Ar (sccm)	58	30	0

Table A.1: Parameters of the tested RIE recipes for SiO_2 etching.

in acetone and then in IPA. To remove residual dirt, we exposed the samples to an oxygen plasma (recipe: "waferclean long") with a microwave power of 550 W for 10 min. To test selectivity against the resist, some of the samples were spin-coated with AR-N 7520.07 new at 4000 rpm for 1 min, resulting in a film of (92.2 ± 1.7) nm thickness. The resist was then hard baked on a hot plate at 125 °C for 5 minutes.

We compared the following RIE recipes: "Ruhstorfer SiO2 eSAE" (eSAE), "Ruhstorfer RecTest3" (RT3) and "SiO2 Etch Kremser" (EK). The relevant parameters for these processes are summarized in Table A.1. For the eSAE and RT3 recipes, a pressure strike step, during which the plasma was ignited, was added before the etching step. The pressure strike step shared the parameters of the respective recipe, except for the chamber pressure (18 mTorr) and the RF forward power(140 W (eSAE) or 180 W (RT3)). All of the recipes were tested for continuous etching over 1 min. Additionally, EK was also tested with the etching time divided into six parts of 10 s each with 30 s waiting time in between. eSAE was also tested with an etching time of 2 min.

To monitor the effect of the RIE, we covered half of each sample with an AlGaAs wafer piece acting as an etching mask. The resulting step in

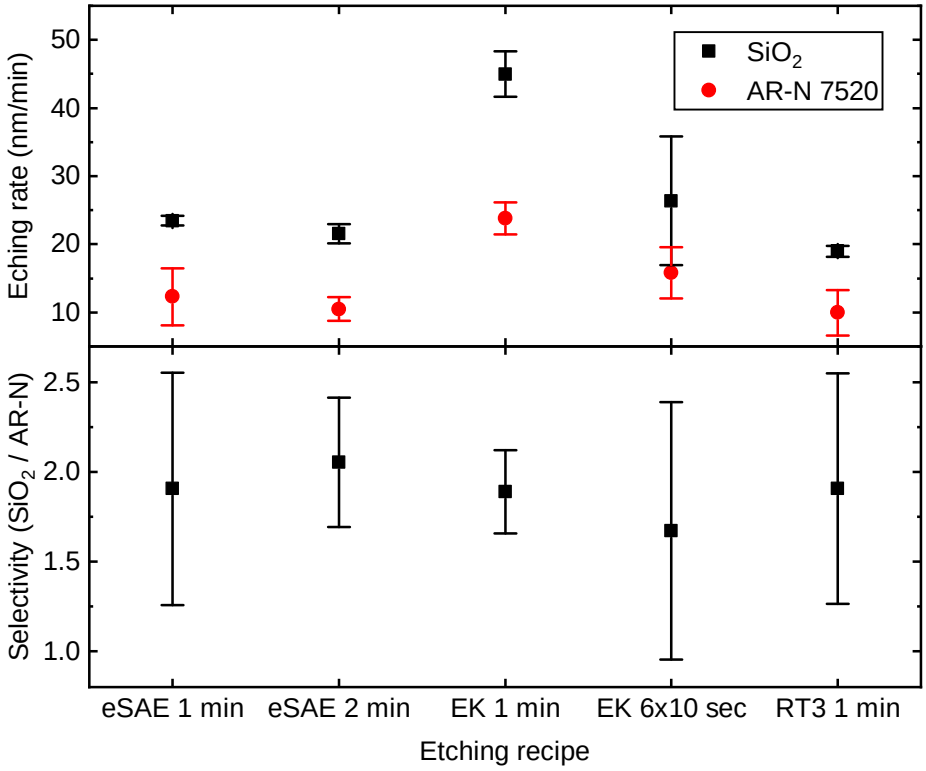

Figure A.2: **SiO_2 etching rates and selectivity versus AR-N 7520.07 new of the RIE protocols defined in table A.1.**

height was analyzed with a profilometer (DekTak, Bruker). We performed every measurement four times and averaged over these measurements. The extracted etching rates are displayed in the upper part figure A.2. We computed the ratio of the etching rates of SiO_2 and AR-N 7520.07. This selectivity is plotted in the lower part of figure A.2. It can be seen that this selectivity hardly varies between the recipes, so one can focus on factors such as etching rate and surface roughness. The selectivity values around 2 imply that, with the use of only the resist as etching mask, only structures with a height of up to twice the initial resist thickness can be realized.

A.5 Exfoliation and transfer of 2D crystals

By now, a multitude of techniques for the deterministic placement of vdW crystals of desired thickness on selected substrate regions have been developed. [Fri18] The samples used in chapters 3-5 have been fabricated by micromechanical exfoliation ("Scotch tape method") of monolayers from bulk crystals [Nov04, Tan14] and subsequent viscoelastic stamping with PDMS. [CG14]

For the exfoliation, we place bulk crystals (from hq graphene) with edge lengths of $\sim 1\,\mathrm{cm}$ on adhesive tape (Nitto Lensguard 7568, "Nitto white"). Upon removal of the bulk crystal, a thin layer remains on the tape. Pushing another piece of tape onto the first one (sticky side to sticky side) and pulling apart, we thin this "seed crystal" down and produce copies of it. This procedure is repeated until the layers on the tape appear thin enough (red-brown color). The tape is then brought into contact with a prepared PDMS stamp and peeled off again. Crystals with varying layer numbers remain on the stamp and we identify monolayers via their optical contrast under a microscope.

The PDMS stamp consists of a PDMS film (Gel-Pak, P/N DGL-30-X4 or P/N DGL-30/17-X8) on a glass slide. After the exfoliation, we mount this stamp in a mask aligner, with the crystal side facing down, over the final substrate. The stamp is transparent and thus allows us to align identified monolayers and structures on the substrate. We slowly bring substrate and stamp into contact and retract again, leaving the crystal on the substrate. Unfortunately, the exfoliation is highly non-deterministic and the transfer, despite allowing for precise positioning, still has a non-negligible failure chance, such that often, several attempts are required for successful sample fabrication.

The samples for chapter 6 were fabricated in an entirely different way, which is already covered in section 6.1 in detail.

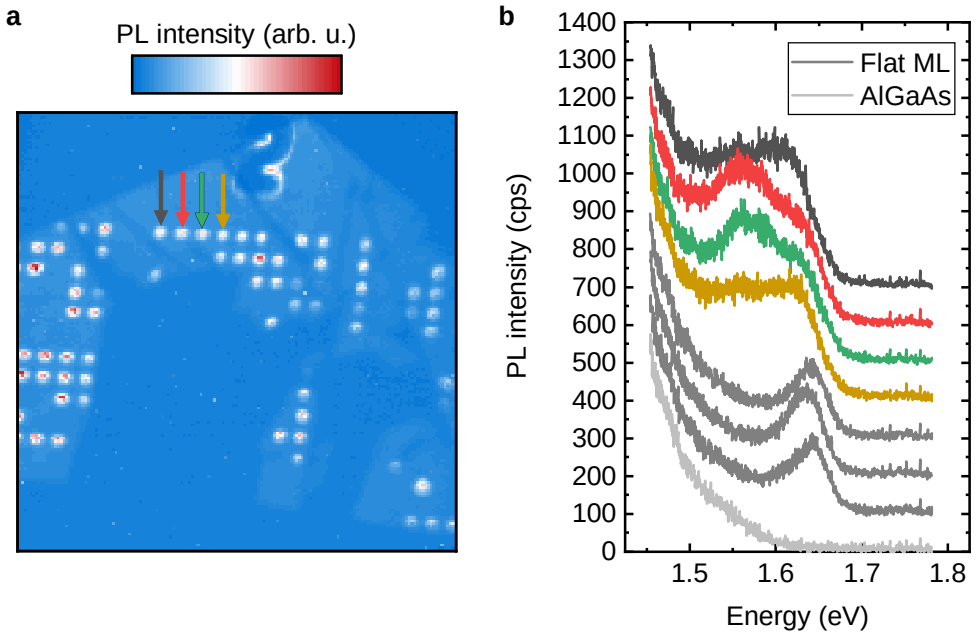

Figure A.3: **Room-temperature photoluminescence of a WSe_2 emitter array on an AlGaAs substrate.** **(a)** Spatially resolved photoluminescence in the range 1.56 eV to 1.60 eV. **(b)** Photoluminescence spectra from four pillar positions (colored according to the indicators in panel (a)), three flat monolayer reference positions (dark gray; positions were between the shown pillars) and from the bare substrate (light gray). All spectra were acquired at $T = 300\,\mathrm{K}$ with 5 µW from a HeNe laser ($\lambda = 633\,\mathrm{nm}$) focused to $\sim 1\,\mu\mathrm{m}$.

A.6 Room-temperature PL of WSe_2 emitter arrays

We recorded the photoluminescence of a WSe_2 emitter array on an AlGaAs substrate at room temperature. The spatially resolved PL in the spectral range 1.56 eV to 1.60 eV is shown in Fig. A.3a. The contours of the (slightly ripped) monolayer, the pillar grid and a lithographical marker are clearly visible. The PL intensity is strongly enhanced at the pillar sites compared to the flat parts of the monolayer. We present spectra from individual pillars

in Fig. A.3b. The colors of the curves match the respective position markers in panel (a). For reference, we also give spectra from three monolayer positions with a flat substrate topography (between the four presented pillars; dark gray curves) and from the bare AlGaAs substrate (light gray curve). All spectra feature a background from the GaAs emission, which becomes stronger for lower energies. The flat WSe_2 monolayer emits around 1.64 eV, which is the expected value for room-temperature excitons. At the pillar sites, the monolayer features additional emission features in the range from 1.5 eV to 1.6 eV. These features are much broader than at low temperatures (the data presented in chapter 3 were typically acquired at 10 K) but nonetheless demonstrate that the pillars create regions of strongly reduced exciton energies, also at room temperature.

A.7 Statistical quantities and tests

In this section, we will give a brief introduction into the statistical quantities and tests used in the substrate material comparison in section 3.4, since these are rarely covered in physics classes or employed in physics research despite being standard practice in many other disciplines, particularly social sciences. The following explanations are not technically precise (e.g. in explicitly discriminating between a quantity and a sample of the quantity) but they are only intended to make this thesis easier to follow. For more information, consult any textbook on statistics, e.g. [Sir05].

The aim of many statistical tests is to determine whether an observed effect could be the result of pure coincidence. This is formulated as a hypothesis test, in which the null hypothesis is that no underlying effect exists, e.g. "The two variables are not correlated" or "The two groups of samples have the same average for some variable". These tests have an associated **p-value**, the probability to observe the measured or a more extreme result under the assumption that the null hypothesis is true. In order to "prove" an effect (which is not a strict proof in the mathematical sense, but rather a proof "beyond reasonable doubt"), one seeks to test the associated null

hypothesis and find a small p-value. A common limit in social sciences is a p-value of 0.05 which implies only a 1-in-20 chance of randomly producing the observed results. The 5-sigma limit, which is often used e.g. in particle physics, corresponds to a p-value of $3 \cdot 10^{-7}$. (The name "5 sigma" refers to the part of a normal distribution which is more than five standard deviations above the mean value.) This large discrepancy between the disciplines is a result of the different levels of controllability in the respective experiments.

The **Pearson correlation coefficient** is a normalized quantity that measures the linear correlation between two variables, [Pea95] e.g. WSe_2 emitter energy and linewidth. This requires a set of data pairs, in our case n pairs of energies E_i and linewidths L_i. (L is not a common symbol for linewidth but chosen here for simple notation.) First, the mean values and standard deviation are calculated separately for the two quantities:

$$\overline{E} = \sum_{i=0}^{n} E_i \tag{A.1}$$

$$\sigma_E = \sqrt{\frac{1}{n-1} \sum_{i=0}^{n} \left(E_i - \overline{E}\right)^2} \tag{A.2}$$

Analogously $\overline{L}$ and σ_L. Next, determine the covariance of the two variables:

$$\mathrm{cov}(E,L) = \sum_{i=0}^{n} \left(E_i - \overline{E}\right)\left(L_i - \overline{L}\right) \tag{A.3}$$

Finally, for the Pearson correlation coefficient (or "Pearson's r") normalize the covariance with respect to the standard deviations:

$$r_{E,L} = \frac{\mathrm{cov}(E,L)}{\sigma_E \sigma_L} \tag{A.4}$$

This coefficient can take values between -1 and $+1$. A positive sign implies a positive correlation between the two quantities. In our example, higher energies would typically have higher linewidths associated. A negative sign, on the other hand would suggest that higher emission energies are

associated with lower linewidths. If r is ± 1, the relation of the two variables can be described perfectly with a linear function, i.e. $L_i = a + bE_i$ with some constants a and b. Deviations from this linear relation (or small b compared to the scattering of the data points) reduce the absolute value of r. Note that r is only a measure of linear correlation! Even strongly correlated quantities, whose relation can be described by other functions, e.g. parabolic or sinusoidal functions, can produce $r = 0$.

Pearson's r can randomly be high even for uncorrelated quantities, in particular for small sample sizes. We therefore always gave a p-value accompanying correlation coefficients in the main text, indicating with what probability this (or a more extreme) coefficient could have been produced by an equally sized sample under the assumption of uncorrelated variables.

A **two-sample t-test** examines whether two samples (in the statistical sense), e.g. WSe_2 emitters on SiO_2 and AlGaAs substrates, differ in a quantity, e.g. linewidth, significantly. [Stu08] For this purpose, the mean value and standard deviations for both samples ($\overline{L}_{SiO2}$, $\overline{L}_{AlGaAs}$, $\sigma_{L,SiO2}$, $\sigma_{L,AlGaAs}$) are calculated. The associated t-value is calculated as:

$$t = \frac{\overline{L}_{SiO2} - \overline{L}_{AlGaAs}}{\sqrt{\frac{\sigma^2_{L,SiO2}}{n_{SiO2}} + \frac{\sigma^2_{L,AlGaAs}}{n_A lGaAs}}} \tag{A.5}$$

In principle, it represents the difference of the two mean values in units of the standard deviations with an additional weighting for the sample sizes. (The t value becomes larger for larger sample sizes.) This formulation of the t-value is already generalized for inequal sample sizes and standard distributions. The associated statistical test is called "Welch's t-test". [Wel47] In order to dismiss the null hypothesis, a large t-value is desired. However, a more refined statistical analysis of the degrees of freedom (in the statistics, not the physics sense) also factors into the final p-value.

Lastly, an **F-test** is a hypothesis test that compares the variances of a quantity in two statistical samples. We used it to compare spectral wandering (which we generally define as the standard deviation of emission energies) in the same emitter under different excitation powers. The associated effect size is given by F, the ratio of the variances of the samples. In our example, where

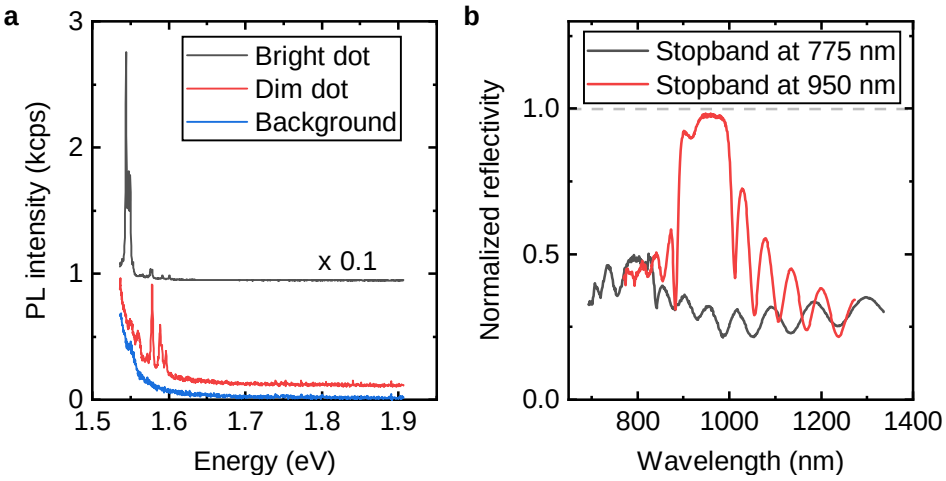

Figure A.4: **Influence of AlGaAs substrates on optical device performance.** **(a)** Low-temperature PL spectra of two WSe_2 emitters on an AlGaAs pillar substrate and the background spectrum from the substrate. The spectra are vertically offset for better visibility. **(b)** Normalized reflectivity of GaAs-AlAs DBRs with the stopband center set at 775 nm and at 950 nm.

we performed 600 measurements of the emission energy for each excitation power, F would be:

$$F = \frac{\sigma^2_{E,P1}}{\sigma^2_{E,P2}} \tag{A.6}$$

The null hypothesis is that $F = 1$. The F-test is only one of several tests that examine equality of variances and it is particularly sensitive to non-normality. [Box53] However, due to the clarity of the data, we refrained from employing more complicated tests.

A.8 AlGaAs as a substrate for 2D materials

In section 3.4, we demonstrated that WSe_2 emitters on AlGaAs-based pillar substrates exhibit a higher spectral stability than the ones on SiO_2-based substrates. This stability is, of course, a desirable property but the AlGaAs

material system brings its unique challenges when used as substrate, which ultimately led to our decision to discontinue the work on these samples. All of the problems presented in the following are, in principle, a result of AlGaAs not being an ideal insulator (unlike SiO_2) but an optically active semiconductor. Figure A.4a displays example PL spectra from two WSe_2 emitters on an AlGaAs pillar substrate and compares them to the emission from the bare substrate. The background emission is centered at 1.52 eV, which corresponds to the bandgap of GaAs at $T = 10$ K. We did not include these photon energies in the measured range in order to prevent saturation of the CCD detector. The remaining background may seem negligible in the case of brighter emitters but it accounts for a considerable part of the PL at the sites of the (much more common) dimmer emitters. This is also the reason why we do not present any photon-correlation measurements for these samples. Even with spectral filtering, the strong background emission makes it impossible to demonstrate photon antibunching for these emitters.

A clear advantage of the AlGaAs material system are the well-developed epitaxial growth and top-down fabrication methods. In other branches of semiconductor research, such as most notably III-V quantum dots, AlGaAs-based substrates have been structured into photonic elements, e.g. to spatially guide emitted light [Rei14] or achieve strong light-matter coupling with cavities. [Pet05] The suitability of AlGaAs for these application, however, highly depends on the wavelength of the light emitted by the investigated system. WSe_2 quantum dots typically emit around 750 nm (= 1.65 eV), which is above the GaAs bandgap at 1.52 eV. Any DBR containing GaAs will therefore absorb light at that wavelength and thus not act as an efficient mirror. This can be seen from Fig. A.4b, where the gray curve shows the reflectivity spectrum of a sample with a GaAs-AlAs DBR nominally centered at 775 nm. The maximum reflectivity is at 0.5, in clear contrast to a GaAs-AlAs DBR at 950 nm (red curve), as it would be used for self-assembled InGaAs QDs. Here, the maximum reflectivity at the center of the stopband is close to one. Both spectra are normalized w.r.t. to the reflectivity of a gold mirror, which has a reflectivity above 95 % in the entire displayed spectral range. Overall, the beneficial properties of AlGaAs, which is generally an established plat-

form for on-chip optics, cannot be harnessed, when it serves as a substrate for TMDs, which have exciton energies in the red or near-infrared regime. A combination of materials, from which a decent DBR compatible with TMDs could be constructed, is SiO_2 and TiO_2. [Lun16]

A property of substrates based on the AlGaAs material system, which merely makes them less convenient for use with 2D materials, is that they offer only a limited optical contrast for monolayers placed on top. This is demonstrated in Fig. A.5, where we present micrographs of two WSe_2 crystals as seen on PDMS stamps and on different final substrates. Fig. A.5a and b show the same crystal, which was transferred onto a GaAs-$Al_{0.65}Ga_{0.35}As$ substrate. The multilayer regions can still be seen reasonably well on the AlGaAs substrate. The monolayer, however, has only a very faint contrast. We outline the monolayer contours in the lower panel as a guide to the eye. Still, very close inspection of the image is required to actually notice the monolayer. This faint contrast may not limit the performance of such devices in experiments but it clearly makes them less convenient to work with. Fig. A.5c and d show a different WSe_2 crystal which was transferred onto a Si-SiO_2 substrate (with an oxide thickness of 285 nm) patterned with HSQ pillars and markers. Mostly the monolayer region was transferred and it partially ripped during the transfer process, as can be seen by comparing the two panels. Much unlike on the AlGaAs substrate, the monolayer including all edges and ripples can be easily seen.

To understand the difference between the substrates, one must consider that the visibility of TMD monolayers is mostly related to interference of light reflected at different interfaces, as illustrated in Fig. A.6. The absorption inside the monolayer of $\sim 2\,\%$ to $5\,\%$ [Ber13, Li14] in the visible range plays only a minor role. The bare substrate can reflect light at its surface or, if it consists of different materials, at any interface between the various media. Depending on the thicknesses of the different layers, these reflected parts of the light can interfere constructively or destructively. When a monolayer of a TMD is placed on top of the substrate, two things are modified: Firstly, a part of the light is already reflected at the top surface of the TMD. Secondly, the surface of the substrate is not in contact to vacuum (or the re-

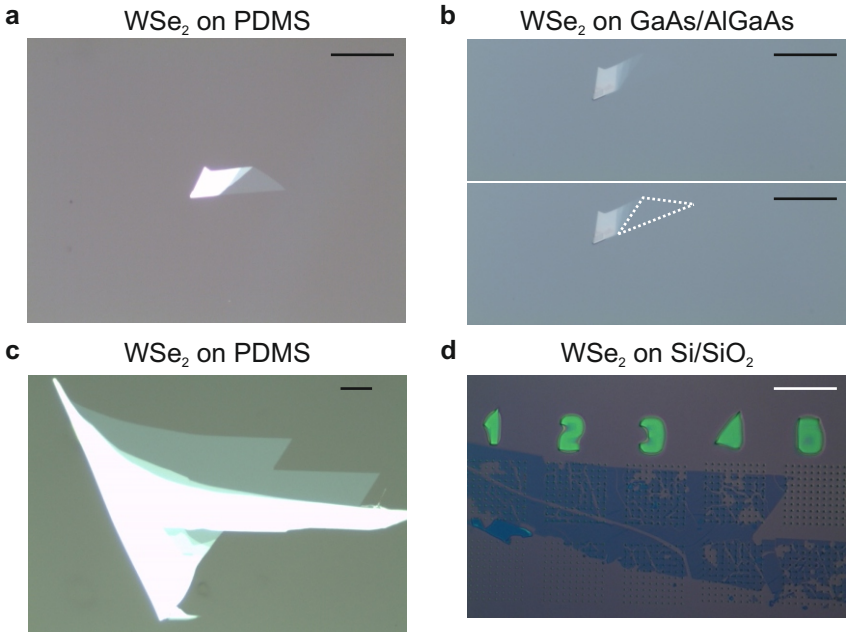

Figure A.5: **Microscope images of WSe_2 monolayers and multilayers on different substrates. (a)** WSe_2 crystal with a monolayer and multilayer regions on a PDMS stamp. **(b)** The WSe_2 crystal from panel (a) after transfer onto a flat GaAs-AlGaAs substrate. The two panels show the same image but the monolayer region (which is present in the image) is outlined in the lower panel. **(c)** A second WSe_2 crystal with a monolayer and multilayer regions on a PDMS stamp. **(d)** The monolayer region of the crystal in panel (c) (and some residues) after transfer onto a Si-SiO_2 substrate with HSQ pillars and markers. The scale bars correspond to 20 µm.

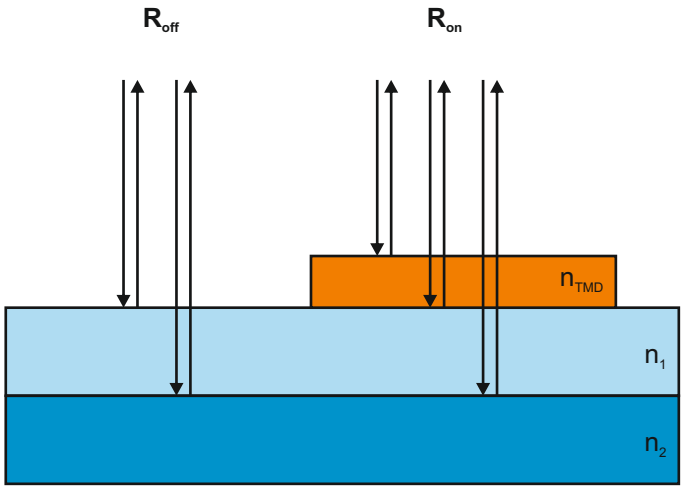

Figure A.6: **Schematic illustration of light being reflected by a multilayered substrates, both bare and covered with a TMD**. Adapted from [Kle15].

spective ambient medium) anymore but to the TMD, changing transmission and reflection at that interface. In particular, if the refractive index of the top layer is between the ambient refractive index and that of the TMD (as is the case for e.g. SiO_2), placing the TMD on top of the substrate suppresses the phase change that the light reflected at the substrate surface would normally experience. More generally, light reflected from all different interfaces of the system interferes and the presence of the TMD can modify the resulting reflected light strongly. This depends not only on the materials of the substrate but also to a large extent on the thicknesses of the different layers.

We simulated the Michelson contrast of WSe_2 monolayers on different substrates using the transfer matrix method. This method is outlined in detail below as part of our routine to fit differential reflectivity spectra. We define the Michelson contrast as $C = \frac{R_{off}-R_{on}}{R_{off}+R_{on}}$ where $R_{on/off}$ is the reflectivity in and outside the monolayer region, respectively. Unlike the standard definition of the Michelson contrast ($\frac{R_{max}-R_{min}}{R_{max}+R_{min}}$ with maximum and minimum reflectivity), we allow for negative values, which indicate that the monolayer-covered regions appear brighter than the bare substrate; The absolute values of the contrast match the standard definition. We present the calculated

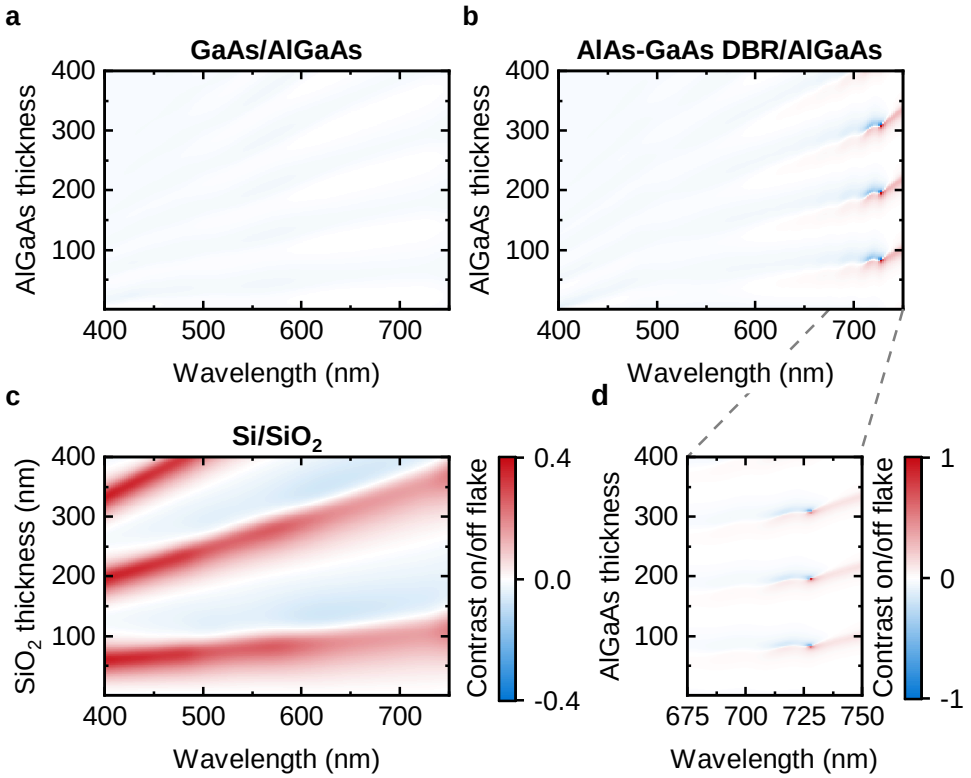

Figure A.7: **Simulated contrast of WSe_2 monolayers on different substrates.** **(a)** Michelson contrast for a substrate with a $Al_{0.7}Ga_{0.3}As$ layer of variable thickness covering a thick GaAs layer. **(b)** Michelson contrast for a substrate with a $Al_{0.7}Ga_{0.3}As$ layer covering a 20-pairs AlAs-GaAs DBR. Singular contrast values are outside of the depicted range of -0.4 to 0.4. **(c)** Michelson contrast for a substrate with a SiO_2 layer of variable thickness covering a thick Si layer. The depicted color bar applies to panels (a-c). **(d)** Zoom-in of panel (b) with a different color scaling.

contrast values as a function of the incident wavelength and as a function of the thickness of the top substrate layer for different substrates in Fig. A.7a-c. The color coding of the data is the same in all three panels. Fig. A.7a shows simulations for a GaAs wafer capped with $Al_{0.7}Ga_{0.3}As$. The contrast values are only in the single-percent regime. The values for Si wafers capped with SiO_2 can reach tens of percent, as seen in Fig. A.7c, which is one order of magnitude higher than the AlGaAs substrates. There are two reasons for this discrepancy: Firstly, AlGaAs can efficiently absorb light in the visible spectrum, unlike SiO_2. More detrimentally, however, the low refractive-index contrast between GaAs and AlGaAs (compared to Si and SiO2) results in only small fractions of the light being reflected inside the substrate. (The reflection coefficient under normal incidence is given by $R = \left(\frac{n_1-n_2}{n_1+n_2}\right)^2$ with the refractive indices n_1 and n_2 of the different media.) Overall, the intensity of the light reflected from within the sample is too low to interfere with the light reflected at the substrate surface in a meaningful way and, as a result, the presence of the monolayer cannot influence this interference strongly.

Introducing a DBR into the sample structure at first seems like a viable approach to circumvent this problem. However, even if the material system was well suited for DBRs in the visible regime, this idea would have several shortcomings: The DBR would significantly alter the optical performance of the device. This can be beneficial for measurements but that would require the DBR stopband to match the investigated system (e.g. WSe_2 emitters) spectrally and the top layer thickness would have to be chosen such that the investigated sample part is at an anti-node of the electric field to ensure good coupling. Overall, the sample paramters have to be optimized for good optical performance of the device, which might not be the optimal values for good contrast. To provide further insight, we show simulations for a substrate consisting of a GaAs wafer topped by 20 pairs of AlAs and GaAs layers with thicknesses of 52.4 nm and 63.9 nm and capped with an $Al_{0.7}Ga_{0.3}As$ layer of variable thickness in Fig. A.7b. The DBR is optimized for WSe_2 emitters around 750 nm. Indeed, high contrast values (even outside the plotted range of -0.4 to 0.4) are recorded in that spectral range for certain capping layer

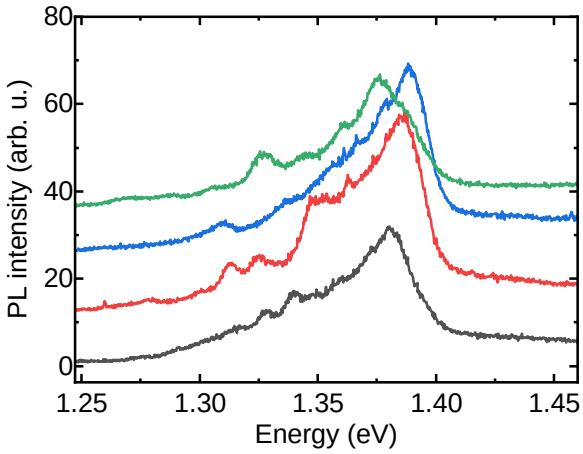

Figure A.8: **Photoluminescence spectra from localized interlayer excitons in a $MoSe_2$-WSe_2 HBL obtained from the same pillar under the same excitation conditions ($T = 10\,\mathrm{K}$, HeNe laser, $30\,\mu\mathrm{W}$ focused to $\sim 1\,\mu\mathrm{m}$) after thermal cycling.** Adapted from [Kre20].

thicknesses. We show the interesting spectral range with a different color-coding in Fig. A.7d. Near-perfect contrast values are observed, however only for very specific wavelengths (at which the human eye also happens to have very low sensitivity). A slight variation of the wavelength near these optimal points can invert the contrast. When using broadband illumination and a detector with low spectral selectivity, much lower contrast values will be observed, effectively nullifying the benefits of the DBR in terms of contrast of TMD monolayers.

A.9 Impact of thermal cycling on LIX emission

We investigated the effect of thermal cycling on localized IXs by repeatedly cycling the sample temperature between 10 K and 300 K. Each time, we performed PL measurements at 10 K under the same excitation conditions (cw excitation with a HeNe laser at 633 nm, 30 µW focused to a spot of 1 µm). Figure A.8 compares typical emission spectra from the same pillar follow-

ing successive cooldowns. We observe a clear change in the energy at which the LIX features appear. This effect was found to be even more pronounced than with typical strained WSe_2-monolayer samples tested under similar conditions. In order to mitigate the effects of thermal cycling, we performed the comprehensive studies on discrete exciton interactions presented in chapter 5 with the sample placed inside a closed-cycle cryostat that facilitated all measurements during a single cooldown. Under these conditions, we found the absolute energy of the LIX states to be stable over several weeks.

A.10 Modelling differential reflectivity

In section 6.2, we presented differential reflectivity spectra of hBN-encapsulated $MoSe_2$ monolayers and twisted bilayers and compared them to calculations, which we will discuss here in more detail. In short, we describe the complex refractive index of the $MoSe_2$ layer as a single Lorentz oscillator. We then compute the reflectivity of our full sample structure (bottom to top: Si, SiO_2, hBN, $MoSe_2$, hBN) and the heterostructure without the $MoSe_2$ with the transfer-matrix method. Using the differential reflectivity calculated from these two regions, we eliminate the influence of the incident light spectrum and the wavelength-dependent detection efficiency in our measurements. We leave the properties of the Lorentz function describing the $MoSe_2$ refractive index and the thicknesses of the hBN and SiO_2 layers as open parameters and fit the data to the model. After explaining these steps in detail, we will also show that this more rigorous treatment of the reflectivity data gives very similar results to a simple peak-fit routine.

The description of the refractive index as a Lorentz oscillator comes from the Lorentz-oscillator model, an expansion of the Drude model, which can be found in most standard books on solid-state-physics, e.g. [Kop89]. In this model, electrons, which are dislocated from their respective nucleus by a distance $\vec{x}$, experience a spring-like restoring force with spring constant $m\omega_0^2$, where m is the (effective) electron mass and ω_0 has the unit of a frequency. Additionally, moving electrons are slowed down by a frictional force of $-m\gamma\dot{\vec{x}}$

with the electron velocity $\dot{\vec{x}}$ and a constant γ. An incident light wave leads to an oscillatory force $-eE_0e^{-i\omega t}$ on the electron with elementary charge e and the electric-field amplitude and frequency given by E_0 and ω, respectively. The equation of motion for the electron is then given by:

$$m\ddot{\vec{x}} + m\gamma\dot{\vec{x}} + m\omega_0^2\vec{x} = -eE_0e^{-i\omega t} \tag{A.7}$$

This equation for a driven harmonic oscillator is solved by:

$$\vec{x}(t) = -\frac{e}{m}\frac{1}{\omega_0^2 - \omega^2 - i\gamma\omega}E_0e^{-i\omega t} \tag{A.8}$$

This dislocation $\vec{x}(t)$ leads to a dipole moment $\vec{p} = -e\vec{x}(t)$. With the volume density of the atoms in the crystal n and the vacuum permittivity ϵ_0, we finally arrive at the dielectric function:

$$\epsilon(\omega) = 1 + \frac{ne^2}{\epsilon_0 m}\frac{1}{\omega_1^2 - \omega^2 - i\gamma\omega} \tag{A.9}$$

The shifted resonance frequency in the dielectric function is given by $\omega_1^2 = \omega_0^2 - \frac{1}{3}n\frac{e^2}{\epsilon_0 m}$. Generally, the refractive index in weakly magnetic materials is given by $n = \sqrt{\epsilon}$. If the second summand in eq. (A.9) is small, we can approximate n by a linear Taylor expansion around 1:

$$n(\omega) = 1 + \frac{ne^2}{2\epsilon_0 m}\frac{1}{\omega_1^2 - \omega^2 - i\gamma\omega} \tag{A.10}$$

This approximation is usually carried out for a thin gas but may be an oversimplification for solid-state materials. The second term describes refractive indices close to resonances well for many gases and solid-state systems. The magnitude of this Lorentz resonance, however, also depends on the transition dipole moment, which is entirely absent in this model. We therefore introduced the amplitude A as a free parameter in our model. Separating the complex refractive index into its real and imaginary part $n = \tilde{n} + i\kappa$ and introducing an offset $\tilde{n}_0$, we set:

$$\tilde{n} = 1 + \tilde{n}_0 + A\frac{\omega_1^2 - \omega^2}{\left(\omega_1^2 - \omega^2\right)^2 + \gamma^2\omega^2} \tag{A.11}$$

$$\kappa = A\frac{\gamma\omega}{\left(\omega_1^2 - \omega^2\right)^2 + \gamma^2\omega^2} \tag{A.12}$$

We were able to describe materials that only feature a single resonance fairly well without the introduced offset $\tilde{n}_0$ in the real part of the refractive index. However, resonances can influence the refractive index over a wide frequency range and, in consequence, several resonance features can overlap. This is particularly true for the real part of the refractive index, for which the resonance term does not decay as sharply, especially towards lower frequencies. If two different resonances are far enough apart, we can account for the influence of one on the other one by the introduced offset terms. If they are too close, however, a more explicit treatment of both resonances is necessary.

The complex refractive index is now modelled in terms of four parameters, which are later used as fit parameters: $A, \omega_1, \gamma, \tilde{n}_0$, which represent the amplitude of the resonance, the resonance energy, the electron damping / width of the resonance and an offset induced by distant resonances. Using this refractive index, we determine the frequency-dependent reflectivity for our full sample structure. We use the transfer-matrix method, outlined in many optics books including [Yeh05], which we restrict to normal incidence. We treat the problem as one-dimensional, since the in-plane extent of all relevant regions is larger than the spot size in our experiment. At any point within or above our sample, we can write the electric field as the sum of a downward (towards the Si substrate) travelling and an upward (towards the objective) travelling component. We can define a two-dimensional vector that contains the downward and upward travelling electric-field amplitudes A and B as its components:

$$\begin{pmatrix} A(z) \\ B(z) \end{pmatrix} \tag{A.13}$$

We can track the evolution of this vetor with a small set of matrices. Moving downward by a distance d within a medium with constant (complex) refractive index n is described by a propagator matrix $P(n,d)$:

$$\begin{aligned}\begin{pmatrix} A(z+d) \\ B(z+d) \end{pmatrix} &= P(n,d) \begin{pmatrix} A(z) \\ B(z) \end{pmatrix} = \\ &= \begin{pmatrix} \exp(i\frac{2\pi nd}{\lambda}) & 0 \\ 0 & \exp(-i\frac{2\pi nd}{\lambda}) \end{pmatrix} \begin{pmatrix} A(z) \\ B(z) \end{pmatrix} \end{aligned} \tag{A.14}$$

Here, λ is the vacuum wavelength of the light. For real refractive indices, this only induces a phase evolution. Otherwise, it also includes absorption in the medium. Entering and leaving a medium are described by the dynamic matrix $D(n)$ and $D^{-1}(n)$:

$$D(n) = \begin{pmatrix} 1 & 1 \\ n & -n \end{pmatrix} \qquad D^{-1}(n) = \frac{1}{2} \begin{pmatrix} 1 & 1/n \\ 1 & -1/n \end{pmatrix} \tag{A.15}$$

We can describe the entire stack of dielectric materials, which we will index with l, with these matrices and can then relate the light above the sample ($z = 0$) with the light that is transmitted into the substrate ($z = z_s$), as follows:

$$\begin{aligned}\begin{pmatrix} A(0) \\ B(0) \end{pmatrix} &= \begin{pmatrix} M_{11} & M_{12} \\ M_{21} & M_{22} \end{pmatrix} \begin{pmatrix} A(z_s) \\ B(z_s) \end{pmatrix} = \\ &= D^{-1}(n_0) \prod_l \left[D(n_l) P(n_l,d_l) D^-1(n_l) \right] \begin{pmatrix} A(z_s) \\ B(z_s) \end{pmatrix} \end{aligned} \tag{A.16}$$

Since the silicon substrate is very thick and absorbs light in the wavelength range of our experiment, we can safely assume that no interfaces after the silicon play a role in the optical processes. This also means that there is no upward-travelling part of the light in the substrate, i.e. $B(z_s) = 0$. It quickly follows then that since $A(0) = M_{11}A(z_s)$ and $B(0) = M_{21}A(z_s)$, the reflectivity (ratio between incident and reflected intensity) is given by $|\frac{M_{21}}{M_{11}}|^2$.

This gives us an analytic way to calculate the reflectivity of a stack of dielectric materials if all refractive indices and thicknesses are known. The measured reflected spectrum, however, also depends on the sensitivity of the measurement setup on the specific wavelength and the emission spectrum of the whitelight source. In order to cancel these dependencies we analyze the differential reflectance spectra $R_{diff} = \frac{R_{on}-R_{off}}{R_{off}}$, which compare R_{on}, the reflected spectrum on the full heterostructure (top to bottom: hBN, $MoSe_2$, hBN, SiO_2, Si), and R_{off}, the reflected spectrum away from the TMD layer (top to bottom: hBN, hBN, SiO_2, Si). In that case, working with measured reflected spectra and calculated reflectivities are equivalent (as long as the measured signal is bright enough). We fit the differential reflectivity as obtained from the transfer-matrix method and assuming the Lorentz-oscillator refractive index to our data. For this, we leave the parameters of the Lorentz oscillator and the hBN and SiO_2 thicknesses, which vary across samples, as open parameters. The fit results can be seen in Fig. 6.5a-h.

The single-oscillator fits worked well for A-exciton spectra that were chosen from the center of the respective region. We wanted to analyze the spatial homogeneity of the exciton resonance and therefore consider spectra from various points on the sample. Due to the large spot size in our reflectivity measurements, we often recorded spectra in which features from the monolayer and the bilayer region overlapped, which prevented us from using the model explained above. We were therefore looking for a method that allows us to obtain resonance energies from analyzing smaller spectral ranges within our data, where the overlap of the different features is not as pronounced. We demonstrate this approach in Fig. A.9a, where we plot a differential-reflectivity spectrum of a $MoSe_2$ monolayer as black data points and the fitted spectrum using the oscillator model described above as a green curve. The fit captures the relevant features over the depicted spectral range well. The obtained resonance energie of $E_{osc} = 1.6428\,\mathrm{eV}$ is shown as a green dashed line. Additionally, we show local peak fits to the data using a Gaussian and a Lorentzian function in red and blue, respectively. We limit the fit range rather strongly on the low-energy side in order to avoid any influence of the dip around 1.637 eV. As expected, the Lorentzian reproduces the

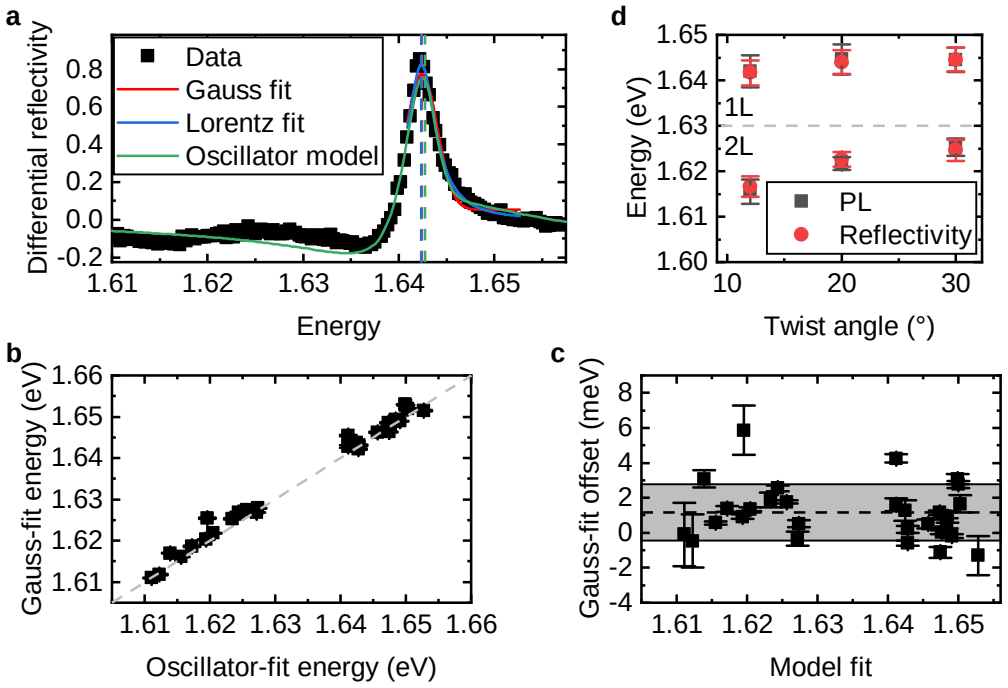

Figure A.9: **Comparison of reflectivity-data analysis using the oscillator model or local peak fitting.** **(a)** Example differential reflectivity spectrum of a $MoSe_2$ monolayer. The green curve shows the oscillator model fit to the spectrum. The red and blue curve denote local Gauss and Lorentz peak fits, respectively. The resonance energy from the oscillator fit is marked by the green dashed line, whereas the (overlapping) red and blue dashed lines give the center energies of the Gauss and Lorentz fits. **(b)** Scatter plot of the center energy of the Gauss fit versus the resonance energy from the oscillator-model fit to 29 spectra from $MoSe_2$ monolayers and bilayers. The gray dashed line marks points for which the two energies are identical. **(c)** Offset between Gauss-fit center energy and resonance energy from the oscillator fit of the same 29 spectra. The black dashed line denotes the mean offset and the gray area indicates offsets less than a standard deviation away from the mean. **(d)** Average A-exciton energies for various samples, obtained from PL (gray data) and from a corrected Gauss-fit analysis to the reflectivity data (red).

shape of the peak better but the center energies $E_{Gauss,Lorentz} = 1.6424\,\mathrm{eV}$ are virtually identical and differ only slightly from the energy obtained from the oscillator model.

We analyzed 29 individual A-exciton reflectivity spectra from $MoSe_2$ monolayers and twisted bilayers independently with the oscillator model and with local Gauss peak fits. Figure A.9b compares the resonance energies within the oscillator model and the center energy of the fitted Gauss peaks. The gray dashed line indicates where the two methods would give identical results. Overall, we see only small deviations. To quantify this better, we show the difference of the two energies (plotted over the energy obtained from the oscillator fit) in Fig. A.9c. On average (as indicated by the black dashed line), the center energy of the Gauss fit overestimates the resonance energy by 1.2 meV. The standard deviation of the offset distribution (indicated by the gray rectangle in the figure) is 1.6 meV. If we try to reconstruct the resonance energy from local peak fits, this standard deviation takes the role of an additional uncertainty in our analysis. However, this uncertainty is small compared to the typical energy variation across a sample, which makes this method viable for the analysis of average resonance energies within samples.

The suitability of the local-peak-fit analysis is demonstrated in Fig. A.9d. There, we make use of the fact that we have "redundant" data for the A exciton in some samples because it appears in photoluminescence and reflectivity measurements. The gray data points denote the average A-exciton energies per sample as obtained from PL measurements. Data above 1.63 eV stems from the monolayer region of the respective sample whereas the data points below that limit correspond to values from the bilayer regions. We also analyzed reflectivity data from the same samples by only fitting the A-exciton peaks in the reflectivity spectra with a Gaussian function and correcting the result by $-1.2\,\mathrm{meV}$, the results of which we display with red data points. The advantage of this analysis is that we only fit a small range of the spectrum, allowing us to use spectra which have overlapping features from different sample regions. The excellent overlap of the gray and the red data points confirms the validity of our analysis. We are therefore confident that it is also reliable for other samples, in which we did not have PL data to verify

the energies, namely samples with twist angles close to 0° or 60°. We used this analysis method to produce the data presented in Fig. 6.5i and Fig. 6.6b and the red data in Fig. 6.6d.

A.11 B excitons in $MoSe_2$ bilayers

We present differential reflectivity spectra in the B-exciton spectral range of seven $MoSe_2$ bilayer samples in Fig. A.10. The twist angle of the bilayer is given in the top right corner of each panel. For each sample, we show the bilayer spectrum in black and a spectrum from the monolayer region in light gray. We already find strong deviations in the shape of the monolayer spectra between different samples. Since in all cases we probe a $MoSe_2$ monolayer encapsulated in hBN, the observed differences are unlikely to stem from variations of the electronic structure of the TMD layer. However, the hBN and SiO_2 layer thicknesses vary across samples, giving rise to the different differential reflectivity spectra. (This effect of the layer thicknesses is considered within the fit model we introduced to reproduce the data from Fig. 6.5, see Appendix, section A.10.)

Comparing the monolayer and the bilayer reflectivity spectra for each sample individually, we find that the bilayer spectrum imitates the general shape of the monolayer spectrum, as seen e.g. in the sample with a twist angle of 0° in Fig. A.10a. All distinctive features, in particular local maxima and minima, are shifted towards lower energies in the bilayer region. This is clearly observed in all samples excluding the 20°-sample in Fig. A.10d, which overall features less pronounced peaks and dips than the other ones. Qualitatively, the B exciton follows the same trend we observed for the A exciton, with the bilayer features redshifted from the monolayer features, most likely due to a combination of electronic coupling and dielectric screening. However, we were unable to draw more quantitative conclusions from our data since fits using the Lorentz-oscillator model did not capture the reflectivity well.

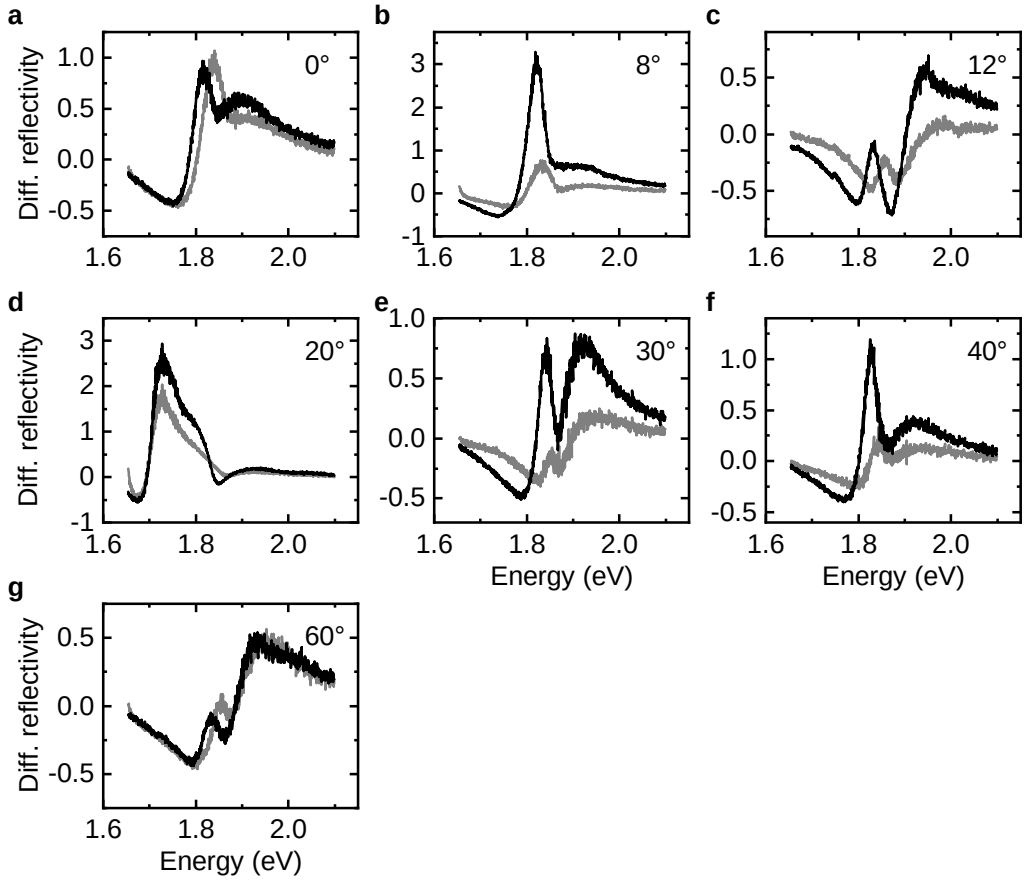

Figure A.10: **B excitons in twisted bilayers of $MoSe_2$ (a-g)** Differential-reflectivity spectra of $MoSe_2$ bilayers (black) of various twist angles (specified in the top right corners) in the spectral range of the B exciton. For reference, monolayer spectra from the respective sample are given in gray. Simple oscillator fits failed to reproduce the exact spectral shape. Generally, all spectral features appear redshifted in the bilayer region although specific resonance energies are not clear. The data were acquired at $T = 10\,\mathrm{K}$.

Assuming a single Lorentz oscillator, the model poses restrictions on the energy-dependent refractive index, which ultimately prevented an appropriate description of the material: As ellipsometry measurements on $MoSe_2$ revealed, the refractive index around the B exciton is also strongly influenced by the distant but broad C-exciton resonance around 2.5 eV. [Par18, Liu20b] With most parts of the C exciton resonance not captured by our experiments due to the emission spectrum of our white-light source, we approximate this influence by a constant offset, which is likely to be an oversimplification.

Two approaches could allow us to determine the B-exciton energies as a function of bilayer twist angle in the future. Reflectivity measurements across samples would be more easily comparable if all samples were constructed in an entirely equivalent way apart from the twist angle. Producing another series of samples with constant hBN thicknesses would give the highest-quality samples for this purpose but preparing and identifying suitable hBN layers via exfoliation is practically not feasible. It would most likely be easiest to remove hBN from the sample structure entirely. There have been various demonstrations of artificial TMD-homobilayer [Liu14, vdZ14, Zhe15, Hua16, Pur16, Yeh16, Lin18, Psi19, Yan19, Sha20] and heterobilayer [Wan16, Nay17, Ale19, Yua20] samples (typically based on CVD-grown monolayers) that feature a large variety of twist angles on a single substrate. Alternatively, we could use the already produced samples and employ different spectroscopy techniques. For $MoSe_2$ monolayers, it has been shown that a combination of second-harmonic generation and one-photon or two-photon PLE can reveal higher-energy excitons, such as the B exciton but also exciton Rydberg states. [Wan15b] These (and possibly further) spectroscopic measurements could help to shed more light on the excitonic properties of artificial $MoSe_2$ bilayers.

A.12 Sample overview

Sample name	Description	Figures
HSQ pillar 1	WSe_2 monolayer on top of Si-SiO_2 substrate with HSQ pillars	3.10, A.5d
HSQ pillar 4	WSe_2 monolayer on top of Si-SiO_2 substrate with HSQ pillars	3.2, 3.3, 3.7, 3.8, 3.9a, 3.10
TS3 Olli	Based on wafer TS3 / Epi-0563. Etched AlGaAs pillars. The exfoliated WSe_2 monolayer happened to be large, hence the sample was named after the tall master student Oliver Hartwig.	3.4, 3.5,3.6, 3.9b, 3.10, A.3, A.4a (black curve in A.4b was recorded on the same wafer)
LIX sample / "Dirty Dan"	$MoSe_2$ monolayer on top of WSe_2 monolayer on top of Si-SiO_2 with etched (RIE) SiO_2 pillars	4.1b, 4.2, 4.3, 4.4, 4.5, 4.6, 4.7, 4.8, 4.9, 5.1, 5.2a, 5.3c (shaded regions), A.8
Twisted $MoSe_2$ bilayer series	$MoSe_2$ homo-bilayers produced via tear&stack, encapsulated in hBN on Si-SiO_2 substrate	2.3b, 6.2, 6.3, 6.4, 6.5, 6.6, 6.7, 6.8, 6.9, 6.10, 6.13b, A.9, A.10

Bibliography

[Aha16] I. Aharonovich, D. Englund, M. Toth, *Solid-state single-photon emitters*, Nature Photonics **10**, 631–641 (2016)

[Ahn18] S. J. Ahn, P. Moon, T.-H. Kim, H.-W. Kim, H.-C. Shin, E. H. Kim, H. W. Cha, S.-J. Kahng, P. Kim, M. Koshino, Y.-W. Son, C.-W. Yang, J. R. Ahn, *Dirac electrons in a dodecagonal graphene quasicrystal*, Science **361**, 782–786 (2018)

[Aja17] O. A. Ajayi, J. V. Ardelean, G. D. Shepard, J. Wang, A. Antony, T. Taniguchi, K. Watanabe, T. F. Heinz, S. Strauf, X.-Y. Zhu, J. C. Hone, *Approaching the intrinsic photoluminescence linewidth in transition metal dichalcogenide monolayers*, 2D Materials **4**, 31 011 (2017)

[Ale17] E. M. Alexeev, A. Catanzaro, O. V. Skrypka, P. K. Nayak, S. Ahn, S. Pak, J. Lee, J. I. Sohn, K. S. Novoselov, H. S. Shin, A. I. Tartakovskii, *Imaging of Interlayer Coupling in van der Waals Heterostructures Using a Bright-Field Optical Microscope*, Nano Letters **17**, 5342–5349 (2017)

[Ale19] E. M. Alexeev, D. A. Ruiz-Tijerina, M. Danovich, M. J. Hamer, D. J. Terry, P. K. Nayak, S. Ahn, S. Pak, J. Lee, J. I. Sohn, M. R.

Molas, M. Koperski, K. Watanabe, T. Taniguchi, K. S. Novoselov, R. V. Gorbachev, H. S. Shin, V. I. Fal'ko, A. I. Tartakovskii, *Resonantly hybridized excitons in moiré superlattices in van der Waals heterostructures*, Nature **567**, 81–86 (2019)

[Ale20] E. M. Alexeev, N. Mullin, P. Ares, H. Nevison-Andrews, O. Skrypka, T. Godde, A. Kozikov, L. Hague, Y. Wang, K. S. Novoselov, L. Fumagalli, J. K. Hobbs, A. I. Tartakovskii, *Emergence of Highly Linearly Polarized Interlayer Exciton Emission in $MoSe_2$ /WSe_2 Heterobilayers with Transfer-Induced Layer Corrugation*, ACS Nano **14**, 11 110–11 119 (2020)

[And21] T. I. Andersen, G. Scuri, A. Sushko, K. De Greve, J. Sung, Y. Zhou, D. S. Wild, R. J. Gelly, H. Heo, D. Bérubé, A. Y. Joe, L. A. Jauregui, K. Watanabe, T. Taniguchi, P. Kim, H. Park, M. D. Lukin, *Excitons in a reconstructed moiré potential in twisted WSe_2/WSe_2 homobilayers*, Nature Materials **20**, 480–487 (2021)

[Ane80] A. Anedda, E. Fortin, *Exciton spectra in $MoSe_2$*, Journal of Physics and Chemistry of Solids **41**, 865–869 (1980)

[Ang07] S. J. Angus, A. J. Ferguson, A. S. Dzurak, R. G. Clark, *Gate-Defined Quantum Dots in Intrinsic Silicon*, Nano Letters **7**, 2051–2055 (2007)

[Aro15] A. Arora, M. Koperski, K. Nogajewski, J. Marcus, C. Faugeras, M. Potemski, *Excitonic resonances in thin films of WSe_2: From monolayer to bulk material*, Nanoscale **7**, 10 421–10 429 (2015)

[Bae20] H. Baek, M. Brotons-Gisbert, Z. X. Koong, A. Campbell, M. Rambach, K. Watanabe, T. Taniguchi, B. D. Gerardot, *Highly energy-tunable quantum light from moiré-trapped excitons*, Science Advances **6**, eaba8526 (2020)

[Bai20] A. S. Baimuratov, A. Högele, *Valley-selective energy transfer between quantum dots in atomically thin semiconductors*, Scientific Reports **10**, 16 971 (2020)

[Bar17] M. Baranowski, A. Surrente, L. Klopotowski, J. M. Urban, N. Zhang, D. K. Maude, K. Wiwatowski, S. Mackowski, Y. C. Kung, D. Dumcenco, A. Kis, P. Plochocka, *Probing the Interlayer Exciton Physics in a $MoS_2/MoSe_2/MoS_2$ van der Waals Heterostructure*, Nano Letters **17**, 6360–6365 (2017)

[Bar18] M. Barbone, A. R.-P. Montblanch, D. M. Kara, C. Palacios-Berraquero, A. R. Cadore, D. De Fazio, B. Pingault, E. Mostaani, H. Li, B. Chen, K. Watanabe, T. Taniguchi, S. Tongay, G. Wang, A. C. Ferrari, M. Atatüre, *Charge-tuneable biexciton complexes in monolayer WSe2*, Nature Communications **9**, 3721 (2018)

[Bay02] M. Bayer, G. Ortner, O. Stern, A. Kuther, A. A. Gorbunov, A. Forchel, P. Hawrylak, S. Fafard, K. Hinzer, T. L. Reinecke, S. N. Walck, J. P. Reithmaier, F. Klopf, F. Schäfer, *Fine structure of neutral and charged excitons in self-assembled In(Ga)As/(Al)GaAs quantum dots*, Physical Review B **65**, 195 315 (2002)

[Ben84] C. H. Bennett, G. Brassard, *Quantum cryptography: Public key distribution and coin tossing*, in *International Conference on Computers, Systems & Signal Processing, Bangalore, India, Dec 9-12, 1984*, pages 175–179 (1984)

[Ber13] M. Bernardi, M. Palummo, J. C. Grossman, *Extraordinary Sunlight Absorption and One Nanometer Thick Photovoltaics Using Two-Dimensional Monolayer Materials*, Nano Letters **13**, 3664–3670 (2013)

[BG19] M. Brotons-Gisbert, A. Branny, S. Kumar, R. Picard, R. Proux, M. Gray, K. S. Burch, K. Watanabe, T. Taniguchi, B. D. Gerardot, *Coulomb blockade in an atomically thin quantum dot coupled to a tunable Fermi reservoir*, Nature Nanotechnology **14**, 442–446 (2019)

[Bin19] J. Binder, J. Howarth, F. Withers, M. R. Molas, T. Taniguchi, K. Watanabe, C. Faugeras, A. Wysmolek, M. Danovich, V. I. Fal'ko, A. K. Geim, K. S. Novoselov, M. Potemski, A. Kozikov, *Upconverted electroluminescence via Auger scattering of interlayer excitons in van der Waals heterostructures*, Nature Communications **10**, 2335 (2019)

[Bis11] R. Bistritzer, A. H. MacDonald, *Moiré bands in twisted double-layer graphene*, Proceedings of the National Academy of Sciences **108**, 12 233–12 237 (2011)

[Bla18] M. Blauth, M. Jürgensen, G. Vest, O. Hartwig, M. Prechtl, J. Cerne, J. J. Finley, M. Kaniber, *Coupling Single Photons from Discrete Quantum Emitters in WSe_2 to Lithographically Defined Plasmonic Slot Waveguides*, Nano Letters **18**, 6812–6819 (2018)

[Blu21] E. Blundo, E. Cappelluti, M. Felici, G. Pettinari, A. Polimeni, *Strain-tuning of the electronic, optical, and vibrational properties of two-dimensional crystals*, Applied Physics Reviews **8**, 21 318 (2021)

[Bon11] I. V. Bondarev, *Asymptotic exchange coupling of quasi-one-dimensional excitons in carbon nanotubes*, Physical Review B **83**, 153 409 (2011)

[Bon18] I. V. Bondarev, M. R. Vladimirova, *Complexes of dipolar excitons in layered quasi-two-dimensional nanostructures*, Physical Review B **97**, 165 419 (2018)

[Box53] G. E. P. Box, *Non-normality and tests on variances*, Biometrika **40**, 318–335 (1953)

[Bra16] A. Branny, G. Wang, S. Kumar, C. Robert, B. Lassagne, X. Marie, B. D. Gerardot, B. Urbaszek, *Discrete quantum dot like emitters in monolayer $MoSe_2$: Spatial mapping, magneto-optics, and charge tuning*, Applied Physics Letters **108**, 142 101 (2016)

[Bra17] A. Branny, S. Kumar, R. Proux, B. D. Gerardot, *Deterministic strain-induced arrays of quantum emitters in a two-dimensional semiconductor*, Nature Communications **8**, 15 053 (2017)

[Bro71] R. A. Bromley, *The lattice vibrations of the MoS_2 structure*, The Philosophical Magazine: A Journal of Theoretical Experimental and Applied Physics **23**, 1417–1427 (1971)

[Bru94] K. Brunner, G. Abstreiter, G. Böhm, G. Tränkle, G. Weimann, *Sharp-Line Photoluminescence and Two-Photon Absorption of Zero-Dimensional Biexcitons in a GaAs/AlGaAs Structure*, Physical Review Letters **73**, 1138–1141 (1994)

[Bru98] D. Bruß, *Optimal Eavesdropping in Quantum Cryptography with Six States*, Physical Review Letters **81**, 3018–3021 (1998)

[Cad16] F. Cadiz, C. Robert, G. Wang, W. Kong, X. Fan, M. Blei, D. Lagarde, M. Gay, M. Manca, T. Taniguchi, K. Watanabe, T. Amand, X. Marie, P. Renucci, S. Tongay, B. Urbaszek, *Ultra-low power threshold for laser induced changes in optical properties of 2D molybdenum dichalcogenides*, 2D Materials **3**, 45 008 (2016)

[Cad17] F. Cadiz, E. Courtade, C. Robert, G. Wang, Y. Shen, H. Cai, T. Taniguchi, K. Watanabe, H. Carrere, D. Lagarde, M. Manca, T. Amand, P. Renucci, S. Tongay, X. Marie, B. Urbaszek, *Excitonic Linewidth Approaching the Homogeneous Limit in MoS_2-Based van der Waals Heterostructures*, Physical Review X **7**, 21 026 (2017)

[Cai18] T. Cai, J.-H. Kim, Z. Yang, S. Dutta, S. Aghaeimeibodi, E. Waks, *Radiative Enhancement of Single Quantum Emitters in WSe_2 Monolayers Using Site-Controlled Metallic Nanopillars*, ACS Photonics **5**, 3466–3471 (2018)

[Cao18a] Y. Cao, V. Fatemi, A. Demir, S. Fang, S. L. Tomarken, J. Y. Luo, J. D. Sanchez-Yamagishi, K. Watanabe, T. Taniguchi, E. Kaxiras, R. C. Ashoori, P. Jarillo-Herrero, *Correlated insulator behaviour at*

half-filling in magic-angle graphene superlattices, Nature **556**, 80–84 (2018)

[Cao18b] Y. Cao, V. Fatemi, S. Fang, K. Watanabe, T. Taniguchi, E. Kaxiras, P. Jarillo-Herrero, *Unconventional superconductivity in magic-angle graphene superlattices*, Nature **556**, 43–50 (2018)

[Cao20] Y. Cao, D. Chowdhury, D. Rodan-Legrain, O. Rubies-Bigorda, K. Watanabe, T. Taniguchi, T. Senthil, P. Jarillo-Herrero, *Strange Metal in Magic-Angle Graphene with near Planckian Dissipation*, Physical Review Letters **124**, 76 801 (2020)

[Car18] S. Carr, D. Massatt, S. B. Torrisi, P. Cazeaux, M. Luskin, E. Kaxiras, *Relaxation and domain formation in incommensurate two-dimensional heterostructures*, Physical Review B **98**, 224 102 (2018)

[Cas07] E. V. Castro, K. S. Novoselov, S. V. Morozov, N. M. R. Peres, J. M. B. L. dos Santos, J. Nilsson, F. Guinea, A. K. Geim, A. H. C. Neto, *Biased Bilayer Graphene: Semiconductor with a Gap Tunable by the Electric Field Effect*, Physical Review Letters **99**, 216 802 (2007)

[Ceb14] F. Ceballos, M. Z. Bellus, H.-Y. Chiu, H. Zhao, *Ultrafast Charge Separation and Indirect Exciton Formation in a MoS_2–$MoSe_2$ van der Waals Heterostructure*, ACS Nano **8**, 12 717–12 724 (2014)

[Ceb15] F. Ceballos, M. Z. Bellus, H. Y. Chiu, H. Zhao, *Probing charge transfer excitons in a $MoSe_2$–WS_2 van der Waals heterostructure*, Nanoscale **7**, 17 523–17 528 (2015)

[CG13] A. Castellanos-Gomez, R. Roldán, E. Cappelluti, M. Buscema, F. Guinea, H. S. J. van der Zant, G. A. Steele, *Local Strain Engineering in Atomically Thin MoS_2*, Nano Letters **13**, 5361–5366 (2013)

[CG14] A. Castellanos-Gomez, M. Buscema, R. Molenaar, V. Singh, L. Janssen, H. S. J. van der Zant, G. A. Steele, *Deterministic trans-*

fer of two-dimensional materials by all-dry viscoelastic stamping, 2D Materials **1**, 11 002 (2014)

[Cha15] C. Chakraborty, L. Kinnischtzke, K. M. Goodfellow, R. Beams, A. N. Vamivakas, *Voltage-controlled quantum light from an atomically thin semiconductor*, Nature Nanotechnology **10**, 507–511 (2015)

[Cha16] C. Chakraborty, K. M. Goodfellow, A. Nick Vamivakas, *Localized emission from defects in $MoSe_2$ layers*, Optical Materials Express **6**, 2081 (2016)

[Cha17] C. Chakraborty, K. M. Goodfellow, S. Dhara, A. Yoshimura, V. Meunier, A. N. Vamivakas, *Quantum-Confined Stark Effect of Individual Defects in a van der Waals Heterostructure*, Nano Letters **17**, 2253–2258 (2017)

[Che09] Y. L. Chen, J. G. Analytis, J.-H. Chu, Z. K. Liu, S.-K. Mo, X. L. Qi, H. J. Zhang, D. H. Lu, X. Dai, Z. Fang, S. C. Zhang, I. R. Fisher, Z. Hussain, Z.-X. Shen, *Experimental Realization of a Three-Dimensional Topological Insulator, Bi_2Te_3*, Science **325**, 178–181 (2009)

[Che12] T. Cheiwchanchamnangij, W. R. L. Lambrecht, *Quasiparticle band structure calculation of monolayer, bilayer, and bulk MoS_2*, Physical Review B **85**, 205 302 (2012)

[Che14] A. Chernikov, T. C. Berkelbach, H. M. Hill, A. Rigosi, Y. Li, O. B. Aslan, D. R. Reichman, M. S. Hybertsen, T. F. Heinz, *Exciton Binding Energy and Nonhydrogenic Rydberg Series in Monolayer WS_2*, Physical Review Letters **113**, 76 802 (2014)

[Che18] S.-Y. Chen, T. Goldstein, T. Taniguchi, K. Watanabe, J. Yan, *Coulomb-bound four- and five-particle intervalley states in an atomically-thin semiconductor*, Nature Communications **9**, 3717 (2018)

[Cho17] C. M. Chow, H. Yu, A. M. Jones, J. R. Schaibley, M. Koehler, D. G. Mandrus, R. Merlin, W. Yao, X. Xu, *Phonon-assisted oscillatory exciton dynamics in monolayer $MoSe_2$*, npj 2D Materials and Applications **1**, 33 (2017)

[Cho18] Y. Cho, T. C. Berkelbach, *Environmentally sensitive theory of electronic and optical transitions in atomically thin semiconductors*, Physical Review B **97**, 41 409 (2018)

[Cud11] P. Cudazzo, I. V. Tokatly, A. Rubio, *Dielectric screening in two-dimensional insulators: Implications for excitonic and impurity states in graphane*, Physical Review B **84**, 85 406 (2011)

[Dav20] R. S. Daveau, T. Vandekerckhove, A. Mukherjee, Z. Wang, J. Shan, K. F. Mak, A. N. Vamivakas, G. D. Fuchs, *Spectral and spatial isolation of single tungsten diselenide quantum emitters using hexagonal boron nitride wrinkles*, APL Photonics **5**, 96 105 (2020)

[Dea10] C. R. Dean, A. F. Young, I. Meric, C. Lee, L. Wang, S. Sorgenfrei, K. Watanabe, T. Taniguchi, P. Kim, K. L. Shepard, J. Hone, *Boron nitride substrates for high-quality graphene electronics*, Nature Nanotechnology **5**, 722–726 (2010)

[Dec11] R. Decker, Y. Wang, V. W. Brar, W. Regan, H.-Z. Tsai, Q. Wu, W. Gannett, A. Zettl, M. F. Crommie, *Local Electronic Properties of Graphene on a BN Substrate via Scanning Tunneling Microscopy*, Nano Letters **11**, 2291–2295 (2011)

[Dey16] P. Dey, J. Paul, Z. Wang, C. E. Stevens, C. Liu, A. H. Romero, J. Shan, D. J. Hilton, D. Karaiskaj, *Optical Coherence in Atomic-Monolayer Transition-Metal Dichalcogenides Limited by Electron-Phonon Interactions*, Physical Review Letters **116**, 127 402 (2016)

[Doh13] M. W. Doherty, N. B. Manson, P. Delaney, F. Jelezko, J. Wrachtrup, L. C. L. Hollenberg, *The nitrogen-vacancy colour centre in diamond*, Physics Reports **528**, 1–45 (2013)

[Dre94] H. Drexler, D. Leonard, W. Hansen, J. P. Kotthaus, P. M. Petroff, *Spectroscopy of Quantum Levels in Charge-Tunable InGaAs Quantum Dots*, Physical Review Letters **73**, 2252–2255 (1994)

[Dut18] S. Dutta, T. Cai, M. A. Buyukkaya, S. Barik, S. Aghaeimeibodi, E. Waks, *Coupling quantum emitters in WSe_2 monolayers to a metal-insulator-metal waveguide*, Applied Physics Letters **113**, 191 105 (2018)

[EH20] C. Errando-Herranz, E. Schöll, R. Picard, M. Laini, S. Gyger, A. W. Elshaari, A. Branny, U. Wennberg, S. Barbat, T. Renaud, M. Brotons-Gisbert, C. Bonato, B. D. Gerardot, V. Zwiller, K. D. Jöns, *Resonance fluorescence from waveguide-coupled strain-localized two-dimensional quantum emitters* (2020)

[Eva67] B. L. Evans, P. A. Young, *Exciton spectra in thin crystals*, Proceedings of the Royal Society of London. Series A. Mathematical and Physical Sciences **298**, 74–96 (1967)

[Eva71] B. L. Evans, R. A. Hazelwood, *Optical and structural properties of $MoSe_2$*, Physica Status Solidi (a) **4**, 181–192 (1971)

[Fal16] B. Fallahazad, H. C. P. Movva, K. Kim, S. Larentis, T. Taniguchi, K. Watanabe, S. K. Banerjee, E. Tutuc, *Shubnikov–de Haas Oscillations of High-Mobility Holes in Monolayer and Bilayer WSe_2: Landau Level Degeneracy, Effective Mass, and Negative Comp*, Physical Review Letters **116**, 86 601 (2016)

[Fan19] L. Fang, H. Chen, X. Yuan, H. Huang, G. Chen, L. Li, J. Ding, J. He, S. Tao, *Quick Optical Identification of the Defect Formation in Monolayer WSe_2 for Growth Optimization*, Nanoscale Research Letters **14**, 274 (2019)

[Fen12a] J. Feng, X. Qian, C.-W. Huang, J. Li, *Strain-engineered artificial atom as a broad-spectrum solar energy funnel*, Nature Photonics **6**, 866–872 (2012)

[Fen12b] W. Feng, Y. Yao, W. Zhu, J. Zhou, W. Yao, D. Xiao, *Intrinsic spin Hall effect in monolayers of group-VI dichalcogenides: A first-principles study*, Physical Review B **86**, 165 108 (2012)

[Fer21] F. Ferreira, S. J. Magorrian, V. V. Enaldiev, D. A. Ruiz-Tijerina, V. I. Fal'ko, *Band energy landscapes in twisted homobilayers of transition metal dichalcogenides*, Applied Physics Letters **118**, 241 602 (2021)

[Fin02] J. J. Finley, D. J. Mowbray, M. S. Skolnick, A. D. Ashmore, C. Baker, A. F. G. Monte, M. Hopkinson, *Fine structure of charged and neutral excitons in InAs-$Al_{0.6}Ga_{0.4}As$ quantum dots*, Physical Review B **66**, 153 316 (2002)

[Flo18] M. Florian, M. Hartmann, A. Steinhoff, J. Klein, A. W. Holleitner, J. J. Finley, T. O. Wehling, M. Kaniber, C. Gies, *The Dielectric Impact of Layer Distances on Exciton and Trion Binding Energies in van der Waals Heterostructures*, Nano Letters **18**, 2725–2732 (2018)

[Fri66] R. F. Frindt, *Single Crystals of MoS_2 Several Molecular Layers Thick*, Journal of Applied Physics **37**, 1928–1929 (1966)

[Fri17] R. Frisenda, M. Drüppel, R. Schmidt, S. Michaelis de Vasconcellos, D. Perez de Lara, R. Bratschitsch, M. Rohlfing, A. Castellanos-Gomez, *Biaxial strain tuning of the optical properties of single-layer transition metal dichalcogenides*, npj 2D Materials and Applications **1**, 10 (2017)

[Fri18] R. Frisenda, E. Navarro-Moratalla, P. Gant, D. Pérez De Lara, P. Jarillo-Herrero, R. V. Gorbachev, A. Castellanos-Gomez, *Recent progress in the assembly of nanodevices and van der Waals heterostructures by deterministic placement of 2D materials*, Chemical Society Reviews **47**, 53–68 (2018)

[Gam96] D. Gammon, E. S. Snow, B. V. Shanabrook, D. S. Katzer, D. Park, *Fine Structure Splitting in the Optical Spectra of Single GaAs Quantum Dots*, Physical Review Letters **76**, 3005–3008 (1996)

[Gan15] Z. X. Gan, L. Z. Liu, H. Y. Wu, Y. L. Hao, Y. Shan, X. L. Wu, P. K. Chu, *Quantum confinement effects across two-dimensional planes in MoS_2 quantum dots*, Applied Physics Letters **106**, 233 113 (2015)

[Gär07] A. Gärtner, L. Prechtel, D. Schuh, A. W. Holleitner, J. P. Kotthaus, *Micropatterned electrostatic traps for indirect excitons in coupled GaAs quantum wells*, Physical Review B **76**, 85 304 (2007)

[Gei13] A. K. Geim, I. V. Grigorieva, *Van der Waals heterostructures*, Nature **499**, 419–425 (2013)

[Gon13] C. Gong, H. Zhang, W. Wang, L. Colombo, R. M. Wallace, K. Cho, *Band alignment of two-dimensional transition metal dichalcogenides: Application in tunnel field effect transistors*, Applied Physics Letters **103**, 53 513 (2013)

[Gro56] E. F. Gross, *Optical spectrum of excitons in the crystal lattice*, Il Nuovo Cimento **3**, 672–701 (1956)

[Gut13] H. R. Gutiérrez, N. Perea-López, A. L. Elías, A. Berkdemir, B. Wang, R. Lv, F. López-Urías, V. H. Crespi, H. Terrones, M. Terrones, *Extraordinary Room-Temperature Photoluminescence in Triangular WS_2 Monolayers*, Nano Letters **13**, 3447–3454 (2013)

[Hag21] J. Hagel, S. Brem, C. Linderälv, P. Erhart, E. Malic, *Exciton landscape in van der Waals heterostructures*, Phys. Rev. Research **3**, 043 217 (2021)

[Hai12] S. J. Haigh, A. Gholinia, R. Jalil, S. Romani, L. Britnell, D. C. Elias, K. S. Novoselov, L. A. Ponomarenko, A. K. Geim, R. Gorbachev, *Cross-sectional imaging of individual layers and buried interfaces of graphene-based heterostructures and superlattices*, Nature Materials **11**, 764–767 (2012)

[Ham06] A. T. Hammack, N. A. Gippius, S. Yang, G. O. Andreev, L. V. Butov, M. Hanson, A. C. Gossard, *Excitons in electrostatic traps*, Journal of Applied Physics **99**, 66 104 (2006)

[Han56] R. Hanbury Brown, R. Q. Twiss, *A Test of a New Type of Stellar Interferometer on Sirius*, Nature **178**, 1046–1048 (1956)

[He14] J. He, K. Hummer, C. Franchini, *Stacking effects on the electronic and optical properties of bilayer transition metal dichalcogenides MoS_2, $MoSe_2$, WS_2, and WSe_2*, Phys. Rev. B **89**, 075 409 (2014)

[He15] Y.-M. He, G. Clark, J. R. Schaibley, Y.-M. He, M.-C. Chen, Y.-J. Wei, X. Ding, Q. Zhang, W. Yao, X. Xu, C.-Y. Lu, J.-W. Pan, *Single quantum emitters in monolayer semiconductors*, Nature Nanotechnology **10**, 497–502 (2015)

[He16a] Y. He, Y. Yang, Z. Zhang, Y. Gong, W. Zhou, Z. Hu, G. Ye, X. Zhang, E. Bianco, S. Lei, Z. Jin, X. Zou, Y. Yang, Y. Zhang, E. Xie, J. Lou, B. Yakobson, R. Vajtai, B. Li, P. Ajayan, *Strain-Induced Electronic Structure Changes in Stacked van der Waals Heterostructures*, Nano Letters **16**, 3314–3320 (2016)

[He16b] Y.-M. He, O. Iff, N. Lundt, V. Baumann, M. Davanco, K. Srinivasan, S. Höfling, C. Schneider, *Cascaded emission of single photons from the biexciton in monolayered WSe_2*, Nature Communications **7**, 13 409 (2016)

[Heo15] H. Heo, J. H. Sung, S. Cha, B.-G. Jang, J.-Y. Kim, G. Jin, D. Lee, J.-H. Ahn, M.-J. Lee, J. H. Shim, H. Choi, M.-H. Jo, *Interlayer orientation-dependent light absorption and emission in monolayer semiconductor stacks*, Nature Communications **6**, 7372 (2015)

[Her42] C. Herring, *Character tables for two space groups*, Journal of the Franklin Institute **233**, 525–543 (1942)

[Hig09] A. A. High, A. K. Thomas, G. Grosso, M. Remeika, A. T. Hammack, A. D. Meyertholen, M. M. Fogler, L. V. Butov, M. Hanson,

A. C. Gossard, *Trapping Indirect Excitons in a GaAs Quantum-Well Structure with a Diamond-Shaped Electrostatic Trap*, Physical Review Letters **103**, 87 403 (2009)

[Hof84] D. M. Hoffman, G. L. Doll, P. C. Eklund, *Optical properties of pyrolytic boron nitride in the energy range 0.05–10 eV*, Physical Review B **30**, 6051–6056 (1984)

[Hol07] C. W. Holzwarth, T. Barwicz, H. I. Smith, *Optimization of hydrogen silsesquioxane for photonic applications*, Journal of Vacuum Science & Technology B: Microelectronics and Nanometer Structures **25**, 2658 (2007)

[Hon17] J. Hong, C. Wang, H. Liu, X. Ren, J. Chen, G. Wang, J. Jia, M. Xie, C. Jin, W. Ji, J. Yuan, Z. Zhang, *Inversion Domain Boundary Induced Stacking and Bandstructure Diversity in Bilayer $MoSe_2$*, Nano Letters **17**, 6653–6660 (2017)

[Hor07] I. Horcas, R. Fernández, J. M. Gómez-Rodríguez, J. Colchero, J. Gómez-Herrero, A. M. Baro, *WSXM: A software for scanning probe microscopy and a tool for nanotechnology*, Review of Scientific Instruments **78**, 13 705 (2007)

[Hua14] S. Huang, X. Ling, L. Liang, J. Kong, H. Terrones, V. Meunier, M. S. Dresselhaus, *Probing the Interlayer Coupling of Twisted Bilayer MoS_2 Using Photoluminescence Spectroscopy*, Nano Letters **14**, 5500–5508 (2014)

[Hua16] S. Huang, L. Liang, X. Ling, A. A. Puretzky, D. B. Geohegan, B. G. Sumpter, J. Kong, V. Meunier, M. S. Dresselhaus, *Low-Frequency Interlayer Raman Modes to Probe Interface of Twisted Bilayer MoS_2*, Nano Letters **16**, 1435–1444 (2016)

[Hua17] B. Huang, G. Clark, E. Navarro-Moratalla, D. R. Klein, R. Cheng, K. L. Seyler, D. Zhong, E. Schmidgall, M. A. McGuire, D. H. Cobden, W. Yao, D. Xiao, P. Jarillo-Herrero, X. Xu, *Layer-dependent*

ferromagnetism in a van der Waals crystal down to the monolayer limit, Nature **546**, 270–273 (2017)

[Hui71] R. Huisman, R. de Jonge, C. Haas, F. Jellinek, *Trigonal-prismatic coordination in solid compounds of transition metals*, Journal of Solid State Chemistry **3**, 56–66 (1971)

[Hul80] D. Hulin, A. Mysyrowicz, C. B. à la Guillaume, *Evidence for Bose-Einstein Statistics in an Exciton Gas*, Physical Review Letters **45**, 1970–1973 (1980)

[Iff17] O. Iff, Y.-M. He, N. Lundt, S. Stoll, V. Baumann, S. Höfling, C. Schneider, *Substrate engineering for high-quality emission of free and localized excitons from atomic monolayers in hybrid architectures*, Optica **4**, 669 (2017)

[Iff18] O. Iff, N. Lundt, S. Betzold, L. N. Tripathi, M. Emmerling, S. Tongay, Y. J. Lee, S.-H. Kwon, S. Höfling, C. Schneider, *Deterministic coupling of quantum emitters in WSe_2 monolayers to plasmonic nanocavities*, Optics Express **26**, 25 944 (2018)

[Jau19] L. A. Jauregui, A. Y. Joe, K. Pistunova, D. S. Wild, A. A. High, Y. Zhou, G. Scuri, K. De Greve, A. Sushko, C.-H. Yu, T. Taniguchi, K. Watanabe, D. J. Needleman, M. D. Lukin, H. Park, P. Kim, *Electrical control of interlayer exciton dynamics in atomically thin heterostructures*, Science **366**, 870–875 (2019)

[Jay89] R. Jayaraman, C. G. Sodini, *A 1/f noise technique to extract the oxide trap density near the conduction band edge of silicon*, IEEE Transactions on Electron Devices **36**, 1773–1782 (1989)

[Jin14] Z. Jin, X. Li, J. T. Mullen, K. W. Kim, *Intrinsic transport properties of electrons and holes in monolayer transition-metal dichalcogenides*, Physical Review B **90**, 45 422 (2014)

[Jin19] C. Jin, E. C. Regan, A. Yan, M. Iqbal Bakti Utama, D. Wang, S. Zhao, Y. Qin, S. Yang, Z. Zheng, S. Shi, K. Watanabe,

T. Taniguchi, S. Tongay, A. Zettl, F. Wang, *Observation of moiré excitons in WSe_2/WS_2 heterostructure superlattices*, Nature (2019)

[Joe86] P. Joensen, R. F. Frindt, S. Morrison, *Single-layer MoS_2*, Materials Research Bulletin **21**, 457–461 (1986)

[Jon13] A. M. Jones, H. Yu, N. J. Ghimire, S. Wu, G. Aivazian, J. S. Ross, B. Zhao, J. Yan, D. G. Mandrus, D. Xiao, W. Yao, X. Xu, *Optical generation of excitonic valley coherence in monolayer WSe_2*, Nature Nanotechnology **8**, 634–638 (2013)

[Kan13] J. Kang, S. Tongay, J. Zhou, J. Li, J. Wu, *Band offsets and heterostructures of two-dimensional semiconductors*, Applied Physics Letters **102**, 012 111 (2013)

[Kaz14] T. Kazimierczuk, D. Fröhlich, S. Scheel, H. Stolz, M. Bayer, *Giant Rydberg excitons in the copper oxide Cu_2O*, Nature **514**, 343–347 (2014)

[Kel79] L. V. Keldysh, *Polaritons in Semiconducting Films*, Journal of Experimental and Theoretical Physics Letters **30**, 224 (1979)

[Ker16] J. Kern, I. Niehues, P. Tonndorf, R. Schmidt, D. Wigger, R. Schneider, T. Stiehm, S. Michaelis de Vasconcellos, D. E. Reiter, T. Kuhn, R. Bratschitsch, *Nanoscale Positioning of Single-Photon Emitters in Atomically Thin WSe_2*, Advanced Materials **28**, 7101–7105 (2016)

[Kie20] J. Kiemle, F. Sigger, M. Lorke, B. Miller, K. Watanabe, T. Taniguchi, A. Holleitner, U. Wurstbauer, *Control of the orbital character of indirect excitons in MoS_2/WS_2 heterobilayers*, Physical Review B **101**, 121 404 (2020)

[Kim77] H. J. Kimble, M. Dagenais, L. Mandel, *Photon Antibunching in Resonance Fluorescence*, Physical Review Letters **39**, 691–695 (1977)

[Kim16] K. Kim, M. Yankowitz, B. Fallahazad, S. Kang, H. C. P. Movva, S. Huang, S. Larentis, C. M. Corbet, T. Taniguchi, K. Watanabe,

S. K. Banerjee, B. J. LeRoy, E. Tutuc, *van der Waals Heterostructures with High Accuracy Rotational Alignment*, Nano Letters **16**, 1989–1995 (2016)

[Kle15] J. Klein, *Control of valley polarisation by electric field induced symmetry breaking*, Master's thesis, Technical University of Munich (2015)

[Kle20] J. Klein, L. Sigl, S. Gyger, K. Barthelmi, M. Florian, S. Rey, T. Taniguchi, K. Watanabe, F. Jahnke, C. Kastl, V. Zwiller, K. D. Jöns, K. Müller, U. Wurstbauer, J. J. Finley, A. W. Holleitner, *Scalable single-photon sources in atomically thin MoS_2* (2020)

[Kop89] K. Kopitzki, *Einführung in die Festkörperphysik* (Teubner Studienbücher, 1989), ISBN 3-519-23083-6

[Kop15] M. Koperski, K. Nogajewski, A. Arora, V. Cherkez, P. Mallet, J.-Y. Veuillen, J. Marcus, P. Kossacki, M. Potemski, *Single photon emitters in exfoliated WSe_2 structures*, Nature Nanotechnology **10**, 503–506 (2015)

[Kor13] A. Kormányos, V. Zólyomi, N. D. Drummond, P. Rakyta, G. Burkard, V. I. Fal'ko, *Monolayer MoS_2: Trigonal warping, the Γ valley, and spin-orbit coupling effects*, Physical Review B **88**, 45 416 (2013)

[Kor15] A. Kormányos, G. Burkard, M. Gmitra, J. Fabian, V. Zólyomi, N. D. Drummond, V. Fal'ko, *$k \cdot p$ theory for two-dimensional transition metal dichalcogenide semiconductors*, 2D Materials **2**, 22 001 (2015)

[Koś13] K. Kośmider, J. Fernández-Rossier, *Electronic properties of the MoS_2-WS_2 heterojunction*, Physical Review B **87**, 75 451 (2013)

[Kra30] H. A. Kramers, *Théorie générale de la rotation paramagnétique dans les cristaux*, in *Proceedings of the Royal Netherlands Academy of Arts and Sciences 33 (6–10)*, pages 959–972 (1930)

[Kre20] M. Kremser, M. Brotons-Gisbert, J. Knörzer, J. Gückelhorn, M. Meyer, M. Barbone, A. V. Stier, B. D. Gerardot, K. Müller, J. J. Finley, *Discrete interactions between a few interlayer excitons trapped at a $MoSe_2$–WSe_2 heterointerface*, npj 2D Materials and Applications **4**, 8 (2020)

[Kuh13] A. V. Kuhlmann, J. Houel, A. Ludwig, L. Greuter, D. Reuter, A. D. Wieck, M. Poggio, R. J. Warburton, *Charge noise and spin noise in a semiconductor quantum device*, Nature Physics **9**, 570–575 (2013)

[Kuh15] A. V. Kuhlmann, J. H. Prechtel, J. Houel, A. Ludwig, D. Reuter, A. D. Wieck, R. J. Warburton, *Transform-limited single photons from a single quantum dot*, Nature Communications **6**, 8204 (2015)

[Kum15] S. Kumar, A. Kaczmarczyk, B. D. Gerardot, *Strain-Induced Spatial and Spectral Isolation of Quantum Emitters in Mono- and Bilayer WSe_2*, Nano Letters **15**, 7567–7573 (2015)

[Ky18] D. L. C. Ky, B.-C. Tran Khac, C. T. Le, Y. S. Kim, K.-H. Chung, *Friction characteristics of mechanically exfoliated and CVD-grown single-layer MoS_2*, Friction **6**, 395–406 (2018)

[Lar18] S. Larentis, H. C. P. Movva, B. Fallahazad, K. Kim, A. Behroozi, T. Taniguchi, K. Watanabe, S. K. Banerjee, E. Tutuc, *Large effective mass and interaction-enhanced Zeeman splitting of K-valley electrons in $MoSe_2$*, Physical Review B **97**, 201 407 (2018)

[Lat15] D. W. Latzke, W. Zhang, A. Suslu, T.-R. Chang, H. Lin, H.-T. Jeng, S. Tongay, J. Wu, A. Bansil, A. Lanzara, *Electronic structure, spin-orbit coupling, and interlayer interaction in bulk MoS_2 and WS_2*, Physical Review B **91**, 235 202 (2015)

[Lat17] S. Latini, K. T. Winther, T. Olsen, K. S. Thygesen, *Interlayer Excitons and Band Alignment in MoS_2/hBN/WSe_2 van der Waals Heterostructures*, Nano Letters **17**, 938–945 (2017)

[Lat18] A. Laturia, M. L. Van de Put, W. G. Vandenberghe, *Dielectric properties of hexagonal boron nitride and transition metal dichalcogenides: from monolayer to bulk*, npj 2D Materials and Applications **2**, 6 (2018)

[Leb09] S. Lebègue, O. Eriksson, *Electronic structure of two-dimensional crystals from ab initio theory*, Physical Review B **79**, 115 409 (2009)

[Li07] T. Li, G. Galli, *Electronic Properties of MoS_2 Nanoparticles*, The Journal of Physical Chemistry C **111**, 16 192–16 196 (2007)

[Li10] G. Li, A. Luican, J. M. B. Lopes dos Santos, A. H. Castro Neto, A. Reina, J. Kong, E. Y. Andrei, *Observation of Van Hove singularities in twisted graphene layers*, Nature Physics **6**, 109–113 (2010)

[Li14] Y. Li, A. Chernikov, X. Zhang, A. Rigosi, H. M. Hill, A. M. van der Zande, D. A. Chenet, E.-M. Shih, J. Hone, T. F. Heinz, *Measurement of the optical dielectric function of monolayer transition-metal dichalcogenides: MoS_2, $MoSe_2$, WS_2, and WSe_2*, Physical Review B **90**, 205 422 (2014)

[Li15] H. Li, A. W. Contryman, X. Qian, S. M. Ardakani, Y. Gong, X. Wang, J. M. Weisse, C. H. Lee, J. Zhao, P. M. Ajayan, J. Li, H. C. Manoharan, X. Zheng, *Optoelectronic crystal of artificial atoms in strain-textured molybdenum disulphide*, Nature Communications **6**, 7381 (2015)

[Li18] Z. Li, T. Wang, Z. Lu, C. Jin, Y. Chen, Y. Meng, Z. Lian, T. Taniguchi, K. Watanabe, S. Zhang, D. Smirnov, S.-F. Shi, *Revealing the biexciton and trion-exciton complexes in BN encapsulated WSe_2*, Nature Communications **9**, 3719 (2018)

[Li20] W. Li, X. Lu, S. Dubey, L. Devenica, A. Srivastava, *Dipolar interactions between localized interlayer excitons in van der Waals heterostructures*, Nature Materials **19**, 624–629 (2020)

[Lin14] Y. Lin, X. Ling, L. Yu, S. Huang, A. L. Hsu, Y.-H. Lee, J. Kong, M. S. Dresselhaus, T. Palacios, *Dielectric Screening of Excitons and Trions in Single-Layer MoS_2*, Nano Letters **14**, 5569–5576 (2014)

[Lin18] M.-L. Lin, Q.-H. Tan, J.-B. Wu, X.-S. Chen, J.-H. Wang, Y.-H. Pan, X. Zhang, X. Cong, J. Zhang, W. Ji, P.-A. Hu, K.-H. Liu, P.-H. Tan, *Moiré Phonons in Twisted Bilayer MoS_2*, ACS Nano **12**, 8770–8780 (2018)

[Lin19] L. Linhart, M. Paur, V. Smejkal, J. Burgdörfer, T. Mueller, F. Libisch, *Localized Intervalley Defect Excitons as Single-Photon Emitters in WSe_2*, Physical Review Letters **123**, 146 401 (2019)

[Lin20a] E. Linardy, M. Trushin, K. Watanabe, T. Taniguchi, G. Eda, *Electro-Optic Upconversion in van der Waals Heterostructures via Nonequilibrium Photocarrier Tunneling*, Advanced Materials **32**, 2001 543 (2020)

[Lin20b] E. Linardy, D. Yadav, D. Vella, I. A. Verzhbitskiy, K. Watanabe, T. Taniguchi, F. Pauly, M. Trushin, G. Eda, *Harnessing Exciton-Exciton Annihilation in Two-Dimensional Semiconductors*, Nano Letters **20**, 1647–1653 (2020)

[Liu14] K. Liu, L. Zhang, T. Cao, C. Jin, D. Qiu, Q. Zhou, A. Zettl, P. Yang, S. G. Louie, F. Wang, *Evolution of interlayer coupling in twisted molybdenum disulfide bilayers*, Nature Communications **5**, 4966 (2014)

[Liu15] G.-B. Liu, D. Xiao, Y. Yao, X. Xu, W. Yao, *Electronic structures and theoretical modelling of two-dimensional group-VIB transition metal dichalcogenides*, Chemical Society Reviews **44**, 2643–2663 (2015)

[Liu20a] F. Liu, W. Wu, Y. Bai, S. H. Chae, Q. Li, J. Wang, J. Hone, X.-Y. Zhu, *Disassembling 2D van der Waals crystals into macroscopic monolayers and reassembling into artificial lattices*, Science **367**, 903–906 (2020)

[Liu20b] H.-L. Liu, T. Yang, J.-H. Chen, H.-W. Chen, H. Guo, R. Saito, M.-Y. Li, L.-J. Li, *Temperature-dependent optical constants of monolayer MoS_2, $MoSe_2$, WS_2 and WSe_2: spectroscopic ellipsometry and first-principles calculations*, Scientific Reports **10**, 15 282 (2020)

[Lop07] J. M. B. Lopes dos Santos, N. M. R. Peres, A. H. Castro Neto, *Graphene Bilayer with a Twist: Electronic Structure*, Physical Review Letters **99**, 256 802 (2007)

[Lua17] C.-Y. Luan, S. Xie, C. Ma, S. Wang, Y. Kong, M. Xu, *Elucidation of luminescent mechanisms of size-controllable $MoSe_2$ quantum dots*, Applied Physics Letters **111**, 73 105 (2017)

[Lun16] N. Lundt, S. Klembt, E. Cherotchenko, S. Betzold, O. Iff, A. V. Nalitov, M. Klaas, C. P. Dietrich, A. V. Kavokin, S. Höfling, C. Schneider, *Room-temperature Tamm-plasmon exciton-polaritons with a WSe_2 monolayer*, Nature Communications **7**, 13 328 (2016)

[Lun18] N. Lundt, E. Cherotchenko, O. Iff, X. Fan, Y. Shen, P. Bigenwald, A. V. Kavokin, S. Höfling, C. Schneider, *The interplay between excitons and trions in a monolayer of $MoSe_2$*, Applied Physics Letters **112**, 31 107 (2018)

[Luo18] Y. Luo, G. D. Shepard, J. V. Ardelean, D. A. Rhodes, B. Kim, K. Barmak, J. C. Hone, S. Strauf, *Deterministic coupling of site-controlled quantum emitters in monolayer WSe_2 to plasmonic nanocavities*, Nature Nanotechnology **13**, 1137–1142 (2018)

[Mak10] K. F. Mak, C. Lee, J. Hone, J. Shan, T. F. Heinz, *Atomically Thin MoS_2: A New Direct-Gap Semiconductor*, Physical Review Letters **105**, 136 805 (2010)

[Mak12] K. F. Mak, K. He, J. Shan, T. F. Heinz, *Control of valley polarization in monolayer MoS_2 by optical helicity*, Nature Nanotechnology **7**, 494–498 (2012)

[Mak13] K. F. Mak, K. He, C. Lee, G. H. Lee, J. Hone, T. F. Heinz, J. Shan, *Tightly bound trions in monolayer MoS_2*, Nature Materials **12**, 207–211 (2013)

[Mak16] K. F. Mak, J. Shan, *Photonics and optoelectronics of 2D semiconductor transition metal dichalcogenides*, Nature Photonics **10**, 216–226 (2016)

[Man17] S. Manzeli, D. Ovchinnikov, D. Pasquier, O. V. Yazyev, A. Kis, *2D transition metal dichalcogenides*, Nature Reviews Materials **2**, 17 033 (2017)

[Mar17] K. Marinov, A. Avsar, K. Watanabe, T. Taniguchi, A. Kis, *Resolving the spin splitting in the conduction band of monolayer MoS_2*, Nature Communications **8**, 1938 (2017)

[Mar21] E. Marcellina, X. Liu, Z. Hu, A. Fieramosca, Y. Huang, W. Du, S. Liu, J. Zhao, K. Watanabe, T. Taniguchi, Q. Xiong, *Evidence for Moiré Trions in Twisted $MoSe_2$ Homobilayers*, Nano Letters **21**, 4461–4468 (2021)

[Mat73a] L. F. Mattheiss, *Band Structures of Transition-Metal-Dichalcogenide Layer Compounds*, Physical Review B **8**, 3719–3740 (1973)

[Mat73b] L. F. Mattheiss, *Energy Bands for 2H–$NbSe_2$ and 2H–MoS_2*, Physical Review Letters **30**, 784–787 (1973)

[McE97] P. L. McEuen, *Artificial Atoms: New Boxes for Electrons*, Science **278**, 1729–1730 (1997)

[McG20] L. J. McGilly, A. Kerelsky, N. R. Finney, K. Shapovalov, E.-M. Shih, A. Ghiotto, Y. Zeng, S. L. Moore, W. Wu, Y. Bai, K. Watanabe, T. Taniguchi, M. Stengel, L. Zhou, J. Hone, X. Zhu, D. N. Basov, C. Dean, C. E. Dreyer, A. N. Pasupathy, *Visualization of moiré superlattices*, Nature Nanotechnology **15**, 580–584 (2020)

[Mer19] P. Merkl, F. Mooshammer, P. Steinleitner, A. Girnghuber, K.-Q. Lin, P. Nagler, J. Holler, C. Schüller, J. M. Lupton, T. Korn, S. Ovesen, S. Brem, E. Malic, R. Huber, *Ultrafast transition between exciton phases in van der Waals heterostructures*, Nature Materials **18**, 691–696 (2019)

[Mil82] R. C. Miller, D. A. Kleinman, A. C. Gossard, O. Munteanu, *Biexcitons in GaAs quantum wells*, Physical Review B **25**, 6545–6547 (1982)

[Mil17] B. Miller, A. Steinhoff, B. Pano, J. Klein, F. Jahnke, A. Holleitner, U. Wurstbauer, *Long-Lived Direct and Indirect Interlayer Excitons in van der Waals Heterostructures*, Nano Letters **17**, 5229–5237 (2017)

[Mit15] A. A. Mitioglu, P. Plochocka, Á. Granados del Aguila, P. C. M. Christianen, G. Deligeorgis, S. Anghel, L. Kulyuk, D. K. Maude, *Optical Investigation of Monolayer and Bulk Tungsten Diselenide (WSe_2) in High Magnetic Fields*, Nano Letters **15**, 4387–4392 (2015)

[Mon21] A. R.-P. Montblanch, D. M. Kara, I. Paradisanos, C. M. Purser, M. S. G. Feuer, E. M. Alexeev, L. Stefan, Y. Qin, M. Blei, G. Wang, A. R. Cadore, P. Latawiec, M. Lončar, S. Tongay, A. C. Ferrari, M. Atatüre, *Confinement of long-lived interlayer excitons in WS_2/WSe_2 heterostructures*, Communications Physics **4**, 119 (2021)

[Moo15] G. Moody, C. Kavir Dass, K. Hao, C.-H. Chen, L.-J. Li, A. Singh, K. Tran, G. Clark, X. Xu, G. Berghäuser, E. Malic, A. Knorr, X. Li, *Intrinsic homogeneous linewidth and broadening mechanisms of excitons in monolayer transition metal dichalcogenides*, Nature Communications **6**, 8315 (2015)

[Moo19] P. Moon, M. Koshino, Y.-W. Son, *Quasicrystalline electronic states in 30° rotated twisted bilayer graphene*, Physical Review B **99**, 165 430 (2019)

[Mor10] E. Moreau, F. J. Ferrer, D. Vignaud, S. Godey, X. Wallart, *Graphene growth by molecular beam epitaxy using a solid carbon source*, physica status solidi (a) **207**, 300–303 (2010)

[Mor21] D. J. Morrow, X. Ma, *Trapping Interlayer Excitons in van der Waals Heterostructures by Potential Arrays* (2021)

[Nag17a] P. Nagler, M. V. Ballottin, A. A. Mitioglu, F. Mooshammer, N. Paradiso, C. Strunk, R. Huber, A. Chernikov, P. C. M. Christianen, C. Schüller, T. Korn, *Giant magnetic splitting inducing near-unity valley polarization in van der Waals heterostructures*, Nature Communications **8**, 1551 (2017)

[Nag17b] P. Nagler, G. Plechinger, M. V. Ballottin, A. Mitioglu, S. Meier, N. Paradiso, C. Strunk, A. Chernikov, P. C. M. Christianen, C. Schüller, T. Korn, *Interlayer exciton dynamics in a dichalcogenide monolayer heterostructure*, 2D Materials **4**, 025 112 (2017)

[Nam76] S. B. Nam, D. C. Reynolds, C. W. Litton, R. J. Almassy, T. C. Collins, C. M. Wolfe, *Free-exciton energy spectrum in GaAs*, Physical Review B **13**, 761–767 (1976)

[Nay17] P. K. Nayak, Y. Horbatenko, S. Ahn, G. Kim, J.-U. Lee, K. Y. Ma, A.-R. Jang, H. Lim, D. Kim, S. Ryu, H. Cheong, N. Park, H. S. Shin, *Probing Evolution of Twist-Angle-Dependent Interlayer Excitons in $MoSe_2/WSe_2$ van der Waals Heterostructures*, ACS Nano **11**, 4041–4050 (2017)

[Neu13] E. Neu, C. Hepp, M. Hauschild, S. Gsell, M. Fischer, H. Sternschulte, D. Steinmüller-Nethl, M. Schreck, C. Becher, *Low-temperature investigations of single silicon vacancy colour centres in diamond*, New Journal of Physics **15**, 43 005 (2013)

[Nov04] K. S. Novoselov, A. K. Geim, S. V. Morozov, D. Jiang, Y. Zhang, S. V. Dubonos, I. V. Grigorieva, A. A. Firsov, *Electric Field Effect in Atomically Thin Carbon Films*, Science **306**, 666–669 (2004)

[Nov05] K. S. Novoselov, A. K. Geim, S. V. Morozov, D. Jiang, M. I. Katsnelson, I. V. Grigorieva, S. V. Dubonos, A. A. Firsov, *Two-dimensional gas of massless Dirac fermions in graphene*, Nature **438**, 197–200 (2005)

[O'H99] K. E. O'Hara, J. R. Gullingsrud, J. P. Wolfe, *Auger decay of excitons in CuO_2*, Physical Review B **60**, 10 872–10 885 (1999)

[Ove19] S. Ovesen, S. Brem, C. Linderälv, M. Kuisma, T. Korn, P. Erhart, M. Selig, E. Malic, *Interlayer exciton dynamics in van der Waals heterostructures*, Communications Physics **2**, 23 (2019)

[Par10] J. Park, W. C. Mitchel, L. Grazulis, H. E. Smith, K. G. Eyink, J. J. Boeckl, D. H. Tomich, S. D. Pacley, J. E. Hoelscher, *Epitaxial Graphene Growth by Carbon Molecular Beam Epitaxy (CMBE)*, Advanced Materials **22**, 4140–4145 (2010)

[Par18] H. G. Park, T. J. Kim, F. Ullah, V. L. Le, H. T. Nguyen, Y. S. Kim, Y. D. Kim, *Temperature Dependence of the Dielectric Function of Monolayer $MoSe_2$*, Scientific Reports **8**, 3173 (2018)

[PB17] C. Palacios-Berraquero, D. M. Kara, A. R. Montblanch, M. Barbone, P. Latawiec, D. Yoon, A. K. Ott, M. Loncar, A. C. Ferrari, M. Atatüre, *Large-scale quantum-emitter arrays in atomically thin semiconductors*, Nature Communications **8**, 15 093 (2017)

[Pea95] K. Pearson, *VII. Note on regression and inheritance in the case of two parents*, Proceedings of the Royal Society of London **58**, 240–242 (1895)

[Pet05] E. Peter, P. Senellart, D. Martrou, A. Lemaître, J. Hours, J. M. Gérard, J. Bloch, *Exciton-Photon Strong-Coupling Regime for a Single Quantum Dot Embedded in a Microcavity*, Physical Review Letters **95**, 67 401 (2005)

[Pet22] M. M. Petrić, M. Kremser, M. Barbone, A. Nolinder, A. Lyamkina, A. V. Stier, M. Kaniber, K. Müller, J. J. Finley, *Tuning the Optical Properties of a $MoSe_2$ Monolayer Using Nanoscale Plasmonic Antennas*, Nano Letters **22**, 561–569 (2022)

[Pey19] F. Peyskens, C. Chakraborty, M. Muneeb, D. Van Thourhout, D. Englund, *Integration of single photon emitters in 2D layered materials with a silicon nitride photonic chip*, Nature Communications **10**, 4435 (2019)

[Piz16] F. Pizzocchero, L. Gammelgaard, B. S. Jessen, J. M. Caridad, L. Wang, J. Hone, P. Bøggild, T. J. Booth, *The hot pick-up technique for batch assembly of van der Waals heterostructures*, Nature Communications **7**, 11 894 (2016)

[Psi19] S. Psilodimitrakopoulos, L. Mouchliadis, I. Paradisanos, G. Kourmoulakis, A. Lemonis, G. Kioseoglou, E. Stratakis, *Twist Angle mapping in layered WS_2 by Polarization-Resolved Second Harmonic Generation*, Scientific Reports **9**, 14 285 (2019)

[Pur16] A. A. Puretzky, L. Liang, X. Li, K. Xiao, B. G. Sumpter, V. Meunier, D. B. Geohegan, *Twisted $MoSe_2$ Bilayers with Variable Local Stacking and Interlayer Coupling Revealed by Low-Frequency Raman Spectroscopy*, ACS Nano **10**, 2736–2744 (2016)

[Pur18] D. G. Purdie, N. M. Pugno, T. Taniguchi, K. Watanabe, A. C. Ferrari, A. Lombardo, *Cleaning interfaces in layered materials heterostructures*, Nature Communications **9**, 5387 (2018)

[Qua21] J. Quan, L. Linhart, M.-L. Lin, D. Lee, J. Zhu, C.-Y. Wang, W.-T. Hsu, J. Choi, J. Embley, C. Young, T. Taniguchi, K. Watanabe, C.-K. Shih, K. Lai, A. H. MacDonald, P.-H. Tan, F. Libisch, X. Li, *Phonon renormalization in reconstructed MoS_2 moiré superlattices*, Nature Materials **20**, 1100–1105 (2021)

[Que92] W. Que, *Excitons in quantum dots with parabolic confinement*, Physical Review B **45**, 11 036–11 041 (1992)

[Raj17] A. Raja, A. Chaves, J. Yu, G. Arefe, H. M. Hill, A. F. Rigosi, T. C. Berkelbach, P. Nagler, C. Schüller, T. Korn, C. Nuckolls, J. Hone, L. E. Brus, T. F. Heinz, D. R. Reichman, A. Chernikov, *Coulomb engineering of the bandgap and excitons in two-dimensional materials*, Nature Communications **8**, 15 251 (2017)

[Rap05] R. Rapaport, G. Chen, S. Simon, O. Mitrofanov, L. Pfeiffer, P. M. Platzman, *Electrostatic traps for dipolar excitons*, Physical Review B **72**, 75 428 (2005)

[Reg20] E. C. Regan, D. Wang, C. Jin, M. I. Bakti Utama, B. Gao, X. Wei, S. Zhao, W. Zhao, Z. Zhang, K. Yumigeta, M. Blei, J. D. Carlström, K. Watanabe, T. Taniguchi, S. Tongay, M. Crommie, A. Zettl, F. Wang, *Mott and generalized Wigner crystal states in WSe_2/WS_2 moiré superlattices*, Nature **579**, 359–363 (2020)

[Rei14] T. Reichert, S. Lichtmannecker, G. Reithmaier, M. Zeitlmair, J. Wembacher, A. Rauscher, M. Bichler, K. Müller, M. Kaniber, J. J. Finley, *Highly directed emission from self-assembled quantum dots into guided modes in disordered photonic-crystal waveguides*, Physical Review B **90**, 115 310 (2014)

[Rig15] A. F. Rigosi, H. M. Hill, Y. Li, A. Chernikov, T. F. Heinz, *Probing Interlayer Interactions in Transition Metal Dichalcogenide Heterostructures by Optical Spectroscopy: MoS_2/WS_2 and $MoSe_2/WSe_2$*, Nano Letters **15**, 5033–5038 (2015)

[Riv15] P. Rivera, J. R. Schaibley, A. M. Jones, J. S. Ross, S. Wu, G. Aivazian, P. Klement, K. Seyler, G. Clark, N. J. Ghimire, J. Yan, D. G. Mandrus, W. Yao, X. Xu, *Observation of long-lived interlayer excitons in monolayer $MoSe_2$–WSe_2 heterostructures*, Nature Communications **6** (2015)

[Riv18] P. Rivera, H. Yu, K. L. Seyler, N. P. Wilson, W. Yao, X. Xu, *Interlayer valley excitons in heterobilayers of transition metal dichalcogenides*, Nature Nanotechnology **13**, 1004–1015 (2018)

[Rob16] C. Robert, D. Lagarde, F. Cadiz, G. Wang, B. Lassagne, T. Amand, A. Balocchi, P. Renucci, S. Tongay, B. Urbaszek, X. Marie, *Exciton radiative lifetime in transition metal dichalcogenide monolayers*, Physical Review B **93**, 205 423 (2016)

[Roo17] A. P. Rooney, A. Kozikov, A. N. Rudenko, E. Prestat, M. J. Hamer, F. Withers, Y. Cao, K. S. Novoselov, M. I. Katsnelson, R. Gorbachev, S. J. Haigh, *Observing Imperfection in Atomic Interfaces for van der Waals Heterostructures*, Nano Letters **17**, 5222–5228 (2017)

[Ros86] M. J. Rosker, F. W. Wise, C. L. Tang, *Femtosecond optical measurement of hot-carrier relaxation in GaAs, AlGaAs, and GaAs/AlGaAs multiple quantum well structures*, Applied Physics Letters **49**, 1726–1728 (1986)

[Ros13] J. S. Ross, S. Wu, H. Yu, N. J. Ghimire, A. M. Jones, G. Aivazian, J. Yan, D. G. Mandrus, D. Xiao, W. Yao, X. Xu, *Electrical control of neutral and charged excitons in a monolayer semiconductor*, Nature Communications **4**, 1474 (2013)

[Ros20] M. R. Rosenberger, H.-J. Chuang, M. Phillips, V. P. Oleshko, K. M. McCreary, S. V. Sivaram, C. S. Hellberg, B. T. Jonker, *Twist Angle-Dependent Atomic Reconstruction and Moiré Patterns in Transition Metal Dichalcogenide Heterostructures*, ACS Nano **14**, 4550–4558 (2020)

[RT19] D. A. Ruiz-Tijerina, V. I. Fal'ko, *Interlayer hybridization and moiré superlattice minibands for electrons and excitons in heterobilayers of transition-metal dichalcogenides*, Phys. Rev. B **99**, 125 424 (2019)

[Ryt65] N. S. Rytova, *Coulomb interaction of electrons in a thin film*, Dokl. Akad. Nauk SSSR **163**, 1118–1120 (1965)

[Sah13] H. Sahin, S. Tongay, S. Horzum, W. Fan, J. Zhou, J. Li, J. Wu, F. M. Peeters, *Anomalous Raman spectra and thickness-dependent electronic properties of WSe_2*, Physical Review B **87**, 165 409 (2013)

[Sch11] G. J. Schinner, E. Schubert, M. P. Stallhofer, J. P. Kotthaus, D. Schuh, A. K. Rai, D. Reuter, A. D. Wieck, A. O. Govorov, *Electrostatically trapping indirect excitons in coupled $In_xGa_{1-x}As$ quantum wells*, Physical Review B **83**, 165 308 (2011)

[Sch13] G. J. Schinner, J. Repp, E. Schubert, A. K. Rai, D. Reuter, A. D. Wieck, A. O. Govorov, A. W. Holleitner, J. P. Kotthaus, *Confinement and Interaction of Single Indirect Excitons in a Voltage-Controlled Trap Formed Inside Double InGaAs Quantum Wells*, Phys. Rev. Lett. **110**, 127 403 (2013)

[Sch16] R. Schmidt, I. Niehues, R. Schneider, M. Drüppel, T. Deilmann, M. Rohlfing, S. M. de Vasconcellos, A. Castellanos-Gomez, R. Bratschitsch, *Reversible uniaxial strain tuning in atomically thin WSe_2*, 2D Materials **3**, 21 011 (2016)

[Sey19] K. L. Seyler, P. Rivera, H. Yu, N. P. Wilson, E. L. Ray, D. G. Mandrus, J. Yan, W. Yao, X. Xu, *Signatures of moiré-trapped valley excitons in $MoSe_2/WSe_2$ heterobilayers*, Nature **567**, 66–70 (2019)

[Sha20] G. Shao, X.-X. Xue, X. Liu, D. Zhang, Y. Jin, Y. Wu, B. You, Y.-C. Lin, S. Li, K. Suenaga, X. Wang, A. Pan, H. Li, J. Hong, Y. Feng, S. Liu, *Twist Angle-Dependent Optical Responses in Controllably Grown WS_2 Vertical Homojunctions*, Chemistry of Materials **32**, 9721–9729 (2020)

[Sha21] D. N. Shanks, F. Mahdikhanysarvejahany, C. Muccianti, A. Alfrey, M. R. Koehler, D. G. Mandrus, T. Taniguchi, K. Watanabe, H. Yu,

B. J. LeRoy, J. R. Schaibley, *Nanoscale Trapping of Interlayer Excitons in a 2D Semiconductor Heterostructure*, Nano Letters **21**, 5641–5647 (2021)

[Shr18] S. Shree, M. Semina, C. Robert, B. Han, T. Amand, A. Balocchi, M. Manca, E. Courtade, X. Marie, T. Taniguchi, K. Watanabe, M. M. Glazov, B. Urbaszek, *Observation of exciton-phonon coupling in $MoSe_2$ monolayers*, Physical Review B **98**, 35 302 (2018)

[Sie17] E. J. Sie, A. Steinhoff, C. Gies, C. H. Lui, Q. Ma, M. Rösner, G. Schönhoff, F. Jahnke, T. O. Wehling, Y.-H. Lee, J. Kong, P. Jarillo-Herrero, N. Gedik, *Observation of Exciton Redshift–Blueshift Crossover in Monolayer WS_2*, Nano Letters **17**, 4210–4216 (2017)

[Sip14] A. Sipahigil, K. D. Jahnke, L. J. Rogers, T. Teraji, J. Isoya, A. S. Zibrov, F. Jelezko, M. D. Lukin, *Indistinguishable Photons from Separated Silicon-Vacancy Centers in Diamond*, Physical Review Letters **113**, 113 602 (2014)

[Sir05] R. M. Sirkin, *Statistics for the Social Sciences* (SAGE Publications, Inc, 2005), ISBN 9781412905466

[Spl10] A. Splendiani, L. Sun, Y. Zhang, T. Li, J. Kim, C.-Y. Chim, G. Galli, F. Wang, *Emerging Photoluminescence in Monolayer MoS_2*, Nano Letters **10**, 1271–1275 (2010)

[Sri15a] A. Srivastava, M. Sidler, A. V. Allain, D. S. Lembke, A. Kis, A. Imamoğlu, *Optically active quantum dots in monolayer WSe_2*, Nature Nanotechnology **10**, 491–496 (2015)

[Sri15b] A. Srivastava, M. Sidler, A. V. Allain, D. S. Lembke, A. Kis, A. Imamoğlu, *Valley Zeeman effect in elementary optical excitations of monolayer WSe_2*, Nature Physics **11**, 141–147 (2015)

[Ste13] V. Stengl, J. Henych, *Strongly luminescent monolayered MoS_2 prepared by effective ultrasound exfoliation*, Nanoscale **5**, 3387 (2013)

[Ste18] C. E. Stevens, J. Paul, T. Cox, P. K. Sahoo, H. R. Gutiérrez, V. Turkowski, D. Semenov, S. A. McGill, M. D. Kapetanakis, I. E. Perakis, D. J. Hilton, D. Karaiskaj, *Biexcitons in monolayer transition metal dichalcogenides tuned by magnetic fields*, Nature Communications **9**, 3720 (2018)

[Sti16] A. V. Stier, N. P. Wilson, G. Clark, X. Xu, S. A. Crooker, *Probing the Influence of Dielectric Environment on Excitons in Monolayer WSe_2: Insight from High Magnetic Fields*, Nano Letters **16**, 7054–7060 (2016)

[Stu08] Student, *The probable error of a mean*, Biometrika **6**, 1–25 (1908)

[Sun20] J. Sung, Y. Zhou, G. Scuri, V. Zólyomi, T. I. Andersen, H. Yoo, D. S. Wild, A. Y. Joe, R. J. Gelly, H. Heo, S. J. Magorrian, D. Bérubé, A. M. M. Valdivia, T. Taniguchi, K. Watanabe, M. D. Lukin, P. Kim, V. I. Fal'ko, H. Park, *Broken mirror symmetry in excitonic response of reconstructed domains in twisted $MoSe_2/MoSe_2$ bilayers*, Nature Nanotechnology **15**, 750–754 (2020)

[Tan14] D.-M. Tang, D. G. Kvashnin, S. Najmaei, Y. Bando, K. Kimoto, P. Koskinen, P. M. Ajayan, B. I. Yakobson, P. B. Sorokin, J. Lou, D. Golberg, *Nanomechanical cleavage of molybdenum disulphide atomic layers*, Nature Communications **5**, 3631 (2014)

[Tan20] Y. Tang, L. Li, T. Li, Y. Xu, S. Liu, K. Barmak, K. Watanabe, T. Taniguchi, A. H. MacDonald, J. Shan, K. F. Mak, *Simulation of Hubbard model physics in WSe_2/WS_2 moiré superlattices*, Nature **579**, 353–358 (2020)

[Tar19] G. Tarnopolsky, A. J. Kruchkov, A. Vishwanath, *Origin of Magic Angles in Twisted Bilayer Graphene*, Physical Review Letters **122**, 106 405 (2019)

[Ter13] H. Terrones, F. López-Urías, M. Terrones, *Novel hetero-layered materials with tunable direct band gaps by sandwiching different metal disulfides and diselenides*, Scientific Reports **3**, 1549 (2013)

[Ton13a] S. Tongay, J. Suh, C. Ataca, W. Fan, A. Luce, J. S. Kang, J. Liu, C. Ko, R. Raghunathanan, J. Zhou, F. Ogletree, J. Li, J. C. Grossman, J. Wu, *Defects activated photoluminescence in two-dimensional semiconductors: interplay between bound, charged and free excitons*, Scientific Reports **3**, 2657 (2013)

[Ton13b] P. Tonndorf, R. Schmidt, P. Böttger, X. Zhang, J. Börner, A. Liebig, M. Albrecht, C. Kloc, O. Gordan, D. R. T. Zahn, S. Michaelis de Vasconcellos, R. Bratschitsch, *Photoluminescence emission and Raman response of monolayer MoS_2, $MoSe_2$, and WSe_2*, Optics Express **21**, 4908 (2013)

[Ton15] P. Tonndorf, R. Schmidt, R. Schneider, J. Kern, M. Buscema, G. A. Steele, A. Castellanos-Gomez, H. S. J. van der Zant, S. Michaelis de Vasconcellos, R. Bratschitsch, *Single-photon emission from localized excitons in an atomically thin semiconductor*, Optica **2**, 347 (2015)

[Tra10] G. Trambly de Laissardière, D. Mayou, L. Magaud, *Localization of Dirac Electrons in Rotated Graphene Bilayers*, Nano Letters **10**, 804–808 (2010)

[Tra16a] T. T. Tran, K. Bray, M. J. Ford, M. Toth, I. Aharonovich, *Quantum emission from hexagonal boron nitride monolayers*, Nature Nanotechnology **11**, 37–41 (2016)

[Tra16b] T. T. Tran, C. Zachreson, A. M. Berhane, K. Bray, R. G. Sandstrom, L. H. Li, T. Taniguchi, K. Watanabe, I. Aharonovich, M. Toth, *Quantum Emission from Defects in Single-Crystalline Hexagonal Boron Nitride*, Physical Review Applied **5**, 34 005 (2016)

[Tra19] K. Tran, G. Moody, F. Wu, X. Lu, J. Choi, K. Kim, A. Rai, D. A. Sanchez, J. Quan, A. Singh, J. Embley, A. Zepeda, M. Campbell,

T. Autry, T. Taniguchi, K. Watanabe, N. Lu, S. K. Banerjee, K. L. Silverman, S. Kim, E. Tutuc, L. Yang, A. H. MacDonald, X. Li, *Evidence for moiré excitons in van der Waals heterostructures*, Nature (2019)

[Uge14] M. M. Ugeda, A. J. Bradley, S.-F. Shi, F. H. da Jornada, Y. Zhang, D. Y. Qiu, W. Ruan, S.-K. Mo, Z. Hussain, Z.-X. Shen, F. Wang, S. G. Louie, M. F. Crommie, *Giant bandgap renormalization and excitonic effects in a monolayer transition metal dichalcogenide semiconductor*, Nature Materials **13**, 1091–1095 (2014)

[Var67] Y. P. Varshni, *Temperature dependence of the energy gap in semiconductors*, Physica **34**, 149–154 (1967)

[vdZ14] A. M. van der Zande, J. Kunstmann, A. Chernikov, D. A. Chenet, Y. You, X. Zhang, P. Y. Huang, T. C. Berkelbach, L. Wang, F. Zhang, M. S. Hybertsen, D. A. Muller, D. R. Reichman, T. F. Heinz, J. C. Hone, *Tailoring the Electronic Structure in Bilayer Molybdenum Disulfide via Interlayer Twist*, Nano Letters **14**, 3869–3875 (2014)

[Ver70] J. L. Verble, T. J. Wieting, *Lattice Mode Degeneracy in MoS_2 and Other Layer Compounds*, Physical Review Letters **25**, 362–365 (1970)

[Vil23] V. Villafañe, M. Kremser, R. Hübner, M. M. Petrić, N. P. Wilson, A. V. Stier, K. Müller, M. Florian, A. Steinhoff, J. J. Finley, *Twist-Dependent Intra- and Interlayer Excitons in Moiré $MoSe_2$ Homobilayers*, Physical Review Letters **130**, 026 901 (2023)

[Wan09] X. Wang, H. You, F. Liu, M. Li, L. Wan, S. Li, Q. Li, Y. Xu, R. Tian, Z. Yu, D. Xiang, J. Cheng, *Large-Scale Synthesis of Few-Layered Graphene using CVD*, Chemical Vapor Deposition **15**, 53–56 (2009)

[Wan13] L. Wang, I. Meric, P. Y. Huang, Q. Gao, Y. Gao, H. Tran, T. Taniguchi, K. Watanabe, L. M. Campos, D. A. Muller, J. Guo, P. Kim, J. Hone, K. L. Shepard, C. R. Dean, *One-Dimensional Electrical Contact to a Two-Dimensional Material*, Science **342**, 614–617 (2013)

[Wan14] G. Wang, L. Bouet, D. Lagarde, M. Vidal, A. Balocchi, T. Amand, X. Marie, B. Urbaszek, *Valley dynamics probed through charged and neutral exciton emission in monolayer WSe_2*, Physical Review B **90**, 75 413 (2014)

[Wan15a] G. Wang, L. Bouet, M. M. Glazov, T. Amand, E. L. Ivchenko, E. Palleau, X. Marie, B. Urbaszek, *Magneto-optics in transition metal diselenide monolayers*, 2D Materials **2**, 34 002 (2015)

[Wan15b] G. Wang, I. C. Gerber, L. Bouet, D. Lagarde, A. Balocchi, M. Vidal, T. Amand, X. Marie, B. Urbaszek, *Exciton states in monolayer $MoSe_2$: impact on interband transitions*, 2D Materials **2**, 45 005 (2015)

[Wan16] K. Wang, B. Huang, M. Tian, F. Ceballos, M.-W. Lin, M. Mahjouri-Samani, A. Boulesbaa, A. A. Puretzky, C. M. Rouleau, M. Yoon, H. Zhao, K. Xiao, G. Duscher, D. B. Geohegan, *Interlayer Coupling in Twisted WSe_2/WS_2 Bilayer Heterostructures Revealed by Optical Spectroscopy*, ACS Nano **10**, 6612–6622 (2016)

[Wan17a] G. Wang, C. Robert, M. M. Glazov, F. Cadiz, E. Courtade, T. Amand, D. Lagarde, T. Taniguchi, K. Watanabe, B. Urbaszek, X. Marie, *In-Plane Propagation of Light in Transition Metal Dichalcogenide Monolayers: Optical Selection Rules*, Physical Review Letters **119**, 047 401 (2017)

[Wan17b] Y. Wang, Z. Wang, W. Yao, G.-B. Liu, H. Yu, *Interlayer coupling in commensurate and incommensurate bilayer structures of transition-metal dichalcogenides*, Physical Review B **95** (2017)

[Wan18] R. Wang, Y. Yu, S. Zhou, H. Li, H. Wong, Z. Luo, L. Gan, T. Zhai, *Strategies on Phase Control in Transition Metal Dichalcogenides*, Advanced Functional Materials **28**, 1802 473 (2018)

[Wan20] W. Wang, X. Ma, *Strain-Induced Trapping of Indirect Excitons in $MoSe_2/WSe_2$ Heterostructures*, ACS Photonics **7**, 2460–2467 (2020)

[Wat00] K. Watanabe, N. Koguchi, Y. Gotoh, *Fabrication of GaAs Quantum Dots by Modified Droplet Epitaxy*, Japanese Journal of Applied Physics **39**, L79—-L81 (2000)

[Wat04] K. Watanabe, T. Taniguchi, H. Kanda, *Direct-bandgap properties and evidence for ultraviolet lasing of hexagonal boron nitride single crystal*, Nature Materials **3**, 404–409 (2004)

[Wei17] G. Wei, D. A. Czaplewski, E. J. Lenferink, T. K. Stanev, I. W. Jung, N. P. Stern, *Size-tunable Lateral Confinement in Monolayer Semiconductors*, Scientific Reports **7**, 3324 (2017)

[Wel47] B. L. Welch, *The generalization of 'Student's' problem when several different population variances are involved*, Biometrika **34**, 28–35 (1947)

[Wes20] A. Weston, Y. Zou, V. Enaldiev, A. Summerfield, N. Clark, V. Zólyomi, A. Graham, C. Yelgel, S. Magorrian, M. Zhou, J. Zultak, D. Hopkinson, A. Barinov, T. H. Bointon, A. Kretinin, N. R. Wilson, P. H. Beton, V. I. Fal'ko, S. J. Haigh, R. Gorbachev, *Atomic reconstruction in twisted bilayers of transition metal dichalcogenides*, Nature Nanotechnology **15**, 592–597 (2020)

[Wie17] J. Wierzbowski, J. Klein, F. Sigger, C. Straubinger, M. Kremser, T. Taniguchi, K. Watanabe, U. Wurstbauer, A. W. Holleitner, M. Kaniber, K. Müller, J. J. Finley, *Direct exciton emission from atomically thin transition metal dichalcogenide heterostructures near the lifetime limit*, Scientific Reports **7**, 12 383 (2017)

[Wie19] J. Wierzbowski, *Optical studies on quantum nanosystems built from emergent two-dimensional transition metal dichalcogenides*, Doctoral thesis, Technical University of Munich (2019)

[Wig32] E. Wigner, *Über die Operation der Zeitumkehr in der Quantenmechanik*, Nachr. Akad. Ges. Wiss. Göttingen **31**, 546–559 (1932)

[Wil69] J. A. Wilson, A. D. Yoffe, *The transition metal dichalcogenides discussion and interpretation of the observed optical, electrical and structural properties*, Advances in Physics **18**, 193–335 (1969)

[Wil75] J. A. Wilson, F. J. Di Salvo, S. Mahajan, *Charge-density waves and superlattices in the metallic layered transition metal dichalcogenides*, Advances in Physics **24**, 117–201 (1975)

[Wil17] N. R. Wilson, P. V. Nguyen, K. Seyler, P. Rivera, A. J. Marsden, Z. P. Laker, G. C. Constantinescu, V. Kandyba, A. Barinov, N. D. Hine, X. Xu, D. H. Cobden, *Determination of band offsets, hybridization, and exciton binding in 2D semiconductor heterostructures*, Science Advances **3**, e1601 832 (2017)

[Wu16] Z. Wu, Z. Luo, Y. Shen, W. Zhao, W. Wang, H. Nan, X. Guo, L. Sun, X. Wang, Y. You, N. Zhenhua, *Defects as a factor limiting carrier mobility in WSe_2: A spectroscopic investigation*, Nano Research **9**, 3622–3631 (2016)

[Wu17] Z. Wu, W. Zhao, J. Jiang, T. Zheng, Y. You, J. Lu, N. Zhenhua, *Defect Activated Photoluminescence in WSe_2 Monolayer*, J. Phys. Chem. C **121**, 12 294–12 299 (2017)

[Xi15] X. Xi, L. Zhao, Z. Wang, H. Berger, L. Forró, J. Shan, K. F. Mak, *Strongly enhanced charge-density-wave order in monolayer $NbSe_2$*, Nature Nanotechnology **10**, 765–769 (2015)

[Xia12] D. Xiao, G.-B. Liu, W. Feng, X. Xu, W. Yao, *Coupled Spin and Valley Physics in Monolayers of MoS_2 and Other Group-VI Dichalcogenides*, Physical Review Letters **108**, 196 802 (2012)

[Yan12] M. Yankowitz, J. Xue, D. Cormode, J. D. Sanchez-Yamagishi, K. Watanabe, T. Taniguchi, P. Jarillo-Herrero, P. Jacquod, B. J. LeRoy, *Emergence of superlattice Dirac points in graphene on hexagonal boron nitride*, Nature Physics **8**, 382–386 (2012)

[Yan14] T. Yan, X. Qiao, X. Liu, P. Tan, X. Zhang, *Photoluminescence properties and exciton dynamics in monolayer WSe_2*, Applied Physics Letters **105**, 101 901 (2014)

[Yan19] W. Yan, L. Meng, Z. Meng, Y. Weng, L. Kang, X.-a. Li, *Probing Angle-Dependent Interlayer Coupling in Twisted Bilayer WS_2*, The Journal of Physical Chemistry C **123**, 30 684–30 688 (2019)

[Ye18] Z. Ye, L. Waldecker, E. Y. Ma, D. Rhodes, A. Antony, B. Kim, X.-X. Zhang, M. Deng, Y. Jiang, Z. Lu, D. Smirnov, K. Watanabe, T. Taniguchi, J. Hone, T. F. Heinz, *Efficient generation of neutral and charged biexcitons in encapsulated WSe_2 monolayers*, Nature Communications **9**, 3718 (2018)

[Yeh05] P. Yeh, *Optical Waves in Layered Media* (Wiley & Sons, 2005), ISBN 978-0-471-73192-4

[Yeh16] P.-C. Yeh, W. Jin, N. Zaki, J. Kunstmann, D. Chenet, G. Arefe, J. T. Sadowski, J. I. Dadap, P. Sutter, J. Hone, R. M. Osgood, *Direct Measurement of the Tunable Electronic Structure of Bilayer MoS_2 by Interlayer Twist*, Nano Letters **16**, 953–959 (2016)

[Yu17] H. Yu, G.-B. Liu, J. Tang, X. Xu, W. Yao, *Moiré excitons: From programmable quantum emitter arrays to spin-orbit–coupled artificial lattices*, Science Advances **3**, e1701 696 (2017)

[Yu21] L. Yu, M. Deng, J. L. Zhang, S. Borghardt, B. Kardynal, J. Vučković, T. F. Heinz, *Site-Controlled Quantum Emitters in Monolayer $MoSe_2$*, Nano Letters **21**, 2376–2381 (2021)

[Yua20] L. Yuan, B. Zheng, J. Kunstmann, T. Brumme, A. B. Kuc, C. Ma, S. Deng, D. Blach, A. Pan, L. Huang, *Twist-angle-dependent interlayer exciton diffusion in WS_2-WSe_2 heterobilayers*, Nature Materials **19**, 617–623 (2020)

[Zha13a] W. Zhao, Z. Ghorannevis, K. K. Amara, J. R. Pang, M. Toh, X. Zhang, C. Kloc, P. H. Tan, G. Eda, *Lattice dynamics in mono- and few-layer sheets of WS_2 and WSe_2*, Nanoscale **5**, 9677 (2013)

[Zha13b] Y. Zhao, X. Luo, H. Li, J. Zhang, P. T. Araujo, C. K. Gan, J. Wu, H. Zhang, S. Y. Quek, M. S. Dresselhaus, Q. Xiong, *Interlayer Breathing and Shear Modes in Few-Trilayer MoS_2 and WSe_2*, Nano Letters **13**, 1007–1015 (2013)

[Zha17a] C. Zhang, C.-P. Chuu, X. Ren, M.-Y. Li, L.-J. Li, C. Jin, M.-Y. Chou, C.-K. Shih, *Interlayer couplings, Moiré patterns, and 2D electronic superlattices in MoS_2/WSe_2 hetero-bilayers*, Science Advances **3**, e1601 459 (2017)

[Zha17b] S. Zhang, C.-G. Wang, M.-Y. Li, D. Huang, L.-J. Li, W. Ji, S. Wu, *Defect Structure of Localized Excitons in a WSe_2 Monolayer*, Physical Review Letters **119**, 46 101 (2017)

[Zha17c] X.-X. Zhang, T. Cao, Z. Lu, Y.-C. Lin, F. Zhang, Y. Wang, Z. Li, J. C. Hone, J. A. Robinson, D. Smirnov, S. G. Louie, T. F. Heinz, *Magnetic brightening and control of dark excitons in monolayer WSe_2*, Nature Nanotechnology **12**, 883–888 (2017)

[Zha20] L. Zhai, M. C. Löbl, G. N. Nguyen, J. Ritzmann, A. Javadi, C. Spinnler, A. D. Wieck, A. Ludwig, R. J. Warburton, *Low-noise GaAs quantum dots for quantum photonics*, Nature Communications **11**, 4745 (2020)

[Zhe15] S. Zheng, L. Sun, X. Zhou, F. Liu, Z. Liu, Z. Shen, H. J. Fan, *Coupling and Interlayer Exciton in Twist-Stacked WS_2 Bilayers*, Advanced Optical Materials **3**, 1600–1605 (2015)

[Zho17] Y. Zhou, G. Scuri, D. S. Wild, A. A. High, A. Dibos, L. A. Jauregui, C. Shu, K. De Greve, K. Pistunova, A. Y. Joe, T. Taniguchi, K. Watanabe, P. Kim, M. D. Lukin, H. Park, *Probing dark excitons in atomically thin semiconductors via near-field coupling to surface plasmon polaritons*, Nature Nanotechnology **12**, 856–860 (2017)

[Zhu11] Z. Y. Zhu, Y. C. Cheng, U. Schwingenschlögl, *Giant spin-orbit-induced spin splitting in two-dimensional transition-metal dichalcogenide semiconductors*, Physical Review B **84**, 153 402 (2011)

[Zre99] A. Zrenner, M. Markmann, E. Beham, F. Findeis, G. Böhm, G. Abstreiter, *Spatially resolved spectroscopy on single self-assembled quantum dots*, Journal of Electronic Materials **28**, 542–547 (1999)

List of Publications

1. K. Boos,* F. Sbresny,* S. K. Kim,* M. Kremser, H. Riedl, F. W. Bopp, W. Rauhaus, B. Scaparra, K. D. Jöns, J. J. Finley, K. Müller and L. Hanschke. *Coherent Dynamics of the Swing-Up Excitation Technique.* Under review (2023)

2. E. Zallo, A. Pianetti, A. S. Prikhodko, S. Cecchi, Y. S. Zaytseva, A. Giuliani, M. Kremser, N. I. Borgardt, J. J. Finley, F. Arciprete, M. Palummo, O. Pulci and R. Calarco. *Two-dimensional single crystal monoclinic gallium telluride on silicon substrate via transformation of epitaxial hexagonal phase.* npj 2D Materials and Applications **7**, 19 (2023)

3. V. Villafañe,* M. Kremser,* R. Hübner, M. M. Petrić, N. P. Wilson, A. V. Stier, K. Müller, M. Florian, A. Steinhoff and J. J. Finley. *Twist-Dependent Intra- and Interlayer Excitons in Moiré $MoSe_2$ Homobilayers.* Physical Review Letters **130**, 026901 (2023)

4. M. M. Petrić, M. Kremser, M. Barbone, A. Nolinder, A. Lyamkina, A. V. Stier, M. Kaniber, K. Müller and J. J. Finley. *Tuning the Optical Properties of an $MoSe_2$ Monolayer Using Nanoscale Plasmonic Antennas.* Nano Letters **22**, 561-569 (2022)

5. M. M. Petrić,* M. Kremser,* M. Barbone,* Y. Qin, Y. Sayyad, Y. Shen, S. Tongay, J. J. Finley, A. R. Botello-Méndez and K. Müller. *Raman Spectrum of Janus transition metal dichalcogenide monolayers WSSe and MoSSe.* Physical Review B **103**, 035414 (2021)

6. C. Gustin,* L. Hanschke,* K. Boos,* J. R. A. Müller, M. Kremser, J. J. Finley, S. Hughes and K. Müller. *High-resolution spectroscopy of a quantum dot driven bichromatically by two strong coherent fields.* Physical Review Research **3**, 013044 (2021)

7. D. B. Trivedi, G. Turgut, Y. Qin, M. Y. Sayyad, D. Hajra, M. Howell, L. Liu, S. Yang, N. Hossain Patoary, H. Li, M. M. Petrić, M. Meyer, M. Kremser, M. Barbone, G. Soavi, A. V. Stier, K. Müller, S. Yang, I. Sanchez Esqueda, H. Zhuang, J. J. Finley and S. Tongay. *Room-Temperature Synthesis of 2D Janus Crystals and their Heterostructures.* Advanced Materials **32**, 2006320 (2020)

8. M. Kremser, M. Brotons-Gisbert, J. Knörzer, J. Gückelhorn, M. Meyer, M. Barbone, A. V. Stier, B. D. Gerardot, K. Müller and J. J. Finley. *Discrete interactions between a few interlayer excitons trapped at a $MoSe_2$-WSe_2 heterointerface.* npj 2D Materials and Applications **4**, 8 (2020)

9. K. A. Fischer, L. Hanschke, M. Kremser, J. J. Finley, K. Müller and J. Vučković. *Pulsed Rabi oscillations in quantum two-level systems: beyond the area theorem.* Quantum Science and Technology **3**, 014006 (2018)

10. J. Wierzbowski, J. Klein, F. Sigger, C. Straubinger, M. Kremser, T. Taniguchi, K. Watanabe, U. Wurstbauer, A. W. Holleitner, M. Kaniber, K. Müller and J. J. Finley. *Direct exciton emission from atomically thin transition metal dichalcogenide heterostructures near the lifetime limit.* Scientific Reports **7**, 12383 (2017)

* Authors marked with an asterisk contributed equally to the respective work.

Acknowledgements

This thesis would not have been possible without countless people who directly contributed to the presented findings and who made work at the WSI that much more enjoyable.

I would like to thank my supervisor **Jonathan Finley** who enabled me to spend many years at the institute doing curiosity-driven research on fascinating systems. Your involvement in individual projects despite your immense group size impresses and baffles me. With your deep physics knowledge and intuition, you always gave great guidance when I was more on the lost side.

Along these lines, I also want to thank **Kai Müller** for his supervision and for driving the topic of quantum photonics with 2D materials. Thank you for giving me the freedom to explore the topics that really appealed to me.

I could not have advanced as far in my research without the dedication of my master students, **Janine Gückelhorn** and **Moritz Meyer**. Thank you for the time and effort you invested and for the ideas that you brought into the projects. And thanks for the spontaneity to start completely new projects even as deadlines were approaching. And even if it was never official, **Minsung Kim** was always part of the gang to me and I thoroughly enjoyed the work we did together. I wish the three of you the best for your futures.

I want to thank **Johannes Knörzer**, who has not only contributed the modelling for our interlayer-exciton paper. The discussion we had in Oetz started the entire project and was a turning point for my PhD. Every discussion with you is enjoyable and fruitful!

My short stay at the Heriot-Watt University in Edinburgh resulted in the central measurements for the interlayer-exciton project. On top of that, it was immense fun! I want to thank **Brian Gerardot** for hosting me and being very involved with my measurements, and **Mauro Brotons-Gisbert**, who spent a lot of time with me in the lab and got the experiments running. Thanks to **Willeke Kejsers**, who organised my stay, which thanks to her went smoothly. I felt very welcomed the entire time and want to thank the whole team for that!

I want to thank **Viviana Villafañe**, who has immensely pushed the twisted-bilayer project forward despite always juggling numerous projects at any given time. Thanks in particular for always jumping in when some fabrication runs became necessary on short notice!

Thanks to **Ruven Hübner**, **Matthias Florian** and **Alexander Steinhoff**, who modelled the moiré excitons in twisted $MoSe_2$ bilayers and thereby massively upgraded our study of the material system.

I was lucky to work in lab N107, which was always kept in top shape. First and foremost, I would like to thank **Lukas Hanschke**, **Friedrich Sbresny** and **Katarina Boos** for their tireless efforts! The value of having an orderly lab with equipment that is well looked after cannot be overestimated. Besides that, the time-resolved and PLE measurements would not have been possible without your help and direct involvement. I also want to thank **Jakob Wierzbowski** who, despite being at the end of his own PhD thesis, invested a lot of time into constructing and building up a reliable PL setup. I probably still haven't noticed all the details that you paid attention to.

Thank you, **Marko Petrić**, for our numerous collaborations! I appreciate and am amazed by your dedication and diligence. It was a pleasure to work with you on your well planned-out projects and to benefit from your insights into my research.

Thanks to **Wolfhard Oberhausen** for taking the lead in producing the AlGaAs substrates for WSe_2 emitters.

Some efforts have not led to the scientific breakthroughs we had envisioned. These topics have not found their way into this theis. Nonetheless, I appreciate the efforts that other people have invested to support my research. I want to thank **Martin Hetzl** for producing GaN-nanowire samples, that we tried as substrates for strain-induced WSe_2 emitters, and **Felix Eckmann** for the growth of sapphire layers on top of my samples in an effort to create capacitor structures for WSe_2 emitters.

I want to thank **Daniel Ruhstorfer**, **Fabian Merbeler**, **Florian Sigger**, **Chenjiang Qian**, **Minsung Kim**, **Fabian Flassig** and **Pedro Soubelet** for sharing valuable knowledge of various processing techniques with me.

For the good times in the office, I would like to thank **Lukas Hanschke**, **Tobias Simmet**, **Jakob Wiezbowski** and **Katarina Boos**.

I want to thank the evaporator crew, **Andreas Zeidler**, **Jochen Bissinger**, **Max Kraut**, **Florian Pantle**, **Elise Sirotti Lukas Hanschke** and **Sabrina Artmeier**, who invested a lot of time and work into keeping the evaporators running and thereby limited the time and work I had to invest.

The institue could not work without the technicians. You contribute so much valuable knowledge and so many skills that are just indispensible. To the E24 allrounders **Hubert Riedl** and **Ade Ziegltrum**: Sorry that I mostly came to you with problems and thank you for reliably solving them! Thanks to **Claudia Paulus**, **Peter Weiser** and **Marcus Altzschner** for keeping the clean-room labs running and in a good state. Thanks to **Hannes Seitz** and **Nick Schröder**, who particularly helped with the setup construction by providing us with always perfectly fitting parts. And thanks to **Linda Mora** for being a walking encyclopedia of semiconductor processing!

I want to thank **Irmgard Neuner**, **Daniela Huber**, **Martina Schmidt**, **Petra Mayrhofer** and **Lena Stachel** for all their help with administrative topics and for the fun chats we had during that time.

I found a lot of joy in working at the Walter Schottky Institute and E24. To a large extent, this is due to the wonderful people I got to work with. On top of the people acknowledged so far, I want to thank **Frederik Bopp**,

William Rauhaus, **Bianca Scaparra**, **Lucio Zugliani**, **Mäx Blauth**, **Georg Braunbeck**, **Gwen Vest**, **John Cerne**, **Inci Güler** and the rest of the institute for the shared good times, but also for enduring annoyances together.

The International Max Planck Research School for Quantum Science and Technology did not only provide financial support for my studies but also helped me to collaborate with other people in the Munich area and organized many informative (and fun) events. While there are many people and committees behind this, I want to specifically express my thanks to **Sonya Gzyl** for her great investment of time and effort into the school!

Similarly, the Munich Center for Quantum Science and Technology has enriched my studies with numerous events and programs. I would like to thank **Anca Ionescu**, **Barbara Tautz**, **Christoph Hohmann** and **Tatjana Wilk** for keeping it alive and running.

I am very grateful for the support I have received in my private life. I would like to thank my parents, **Manfred Kremser** and **Sabine Kremser** who have supported my education over decades.

To my wife, **Barbara Gleißl**. You have supported me, motivated me during demanding times and celebrated successes with me. You have shown immense patience when I had to put in some extra time, during and after my active research phase. Thank you!

Statement

With the submission of this thesis, I testify that I have written it independently and did not use other sources than the cited references.

Munich, June 4^{th} 2023 Malte Kremser